2D NANOARCHITECTURES FOR SENSING/BIOSENSING APPLICATIONS

EDITED BY: Muhammad Asif, Yimin Sun, Fei Xiao and Mani Govindasamy

PUBLISHED IN: Frontiers in Chemistry

frontiers Research Topics

ISSN 1664-8714
ISBN 978-2-83250-265-5
DOI 10.3389/978-2-83250-265-5

About Frontiers

Frontiers is more than just an open-access publisher of scholarly articles: it is a pioneering approach to the world of academia, radically improving the way scholarly research is managed. The grand vision of Frontiers is a world where all people have an equal opportunity to seek, share and generate knowledge. Frontiers provides immediate and permanent online open access to all its publications, but this alone is not enough to realize our grand goals.

Frontiers Journal Series

The Frontiers Journal Series is a multi-tier and interdisciplinary set of open-access, online journals, promising a paradigm shift from the current review, selection and dissemination processes in academic publishing. All Frontiers journals are driven by researchers for researchers; therefore, they constitute a service to the scholarly community. At the same time, the Frontiers Journal Series operates on a revolutionary invention, the tiered publishing system, initially addressing specific communities of scholars, and gradually climbing up to broader public understanding, thus serving the interests of the lay society, too.

Dedication to Quality

Each Frontiers article is a landmark of the highest quality, thanks to genuinely collaborative interactions between authors and review editors, who include some of the world's best academicians. Research must be certified by peers before entering a stream of knowledge that may eventually reach the public - and shape society; therefore, Frontiers only applies the most rigorous and unbiased reviews.
Frontiers revolutionizes research publishing by freely delivering the most outstanding research, evaluated with no bias from both the academic and social point of view. By applying the most advanced information technologies, Frontiers is catapulting scholarly publishing into a new generation.

What are Frontiers Research Topics?

Frontiers Research Topics are very popular trademarks of the Frontiers Journals Series: they are collections of at least ten articles, all centered on a particular subject. With their unique mix of varied contributions from Original Research to Review Articles, Frontiers Research Topics unify the most influential researchers, the latest key findings and historical advances in a hot research area! Find out more on how to host your own Frontiers Research Topic or contribute to one as an author by contacting the Frontiers Editorial Office: frontiersin.org/about/contact

2D NANOARCHITECTURES FOR SENSING/BIOSENSING APPLICATIONS

Topic Editors:
Muhammad Asif, Wuhan Institute of Technology, China
Yimin Sun, Wuhan Institute of Technology, China
Fei Xiao, Huazhong University of Science and Technology, China
Mani Govindasamy, Ming Chi University of Technology, Taiwan

Citation: Asif, M., Sun, Y., Xiao, F., Govindasamy, M., eds. (2022). 2D Nanoarchitectures for Sensing/Biosensing Applications. Lausanne: Frontiers Media SA. doi: 10.3389/978-2-83250-265-5

Table of Contents

frontiers in Chemistry

ORIGINAL RESEARCH
published: 23 November 2021
doi: 10.3389/fchem.2021.773519

A Convenient and Label-Free Colorimetric Detection for L-Histidine Based on Inhibition of Oxidation of 3,3′,5,5′-Tetramethylbenzidine-H_2O_2 System Triggered by Copper Ions

Zhikun Zhang[1], *Wenmeng Zhao*[1], *Cuixia Hu*[1], *Yapeng Cao*[1], *Yumin Liu*[1]* and *Qingju Liu*[2]*

[1]School of Chemical and Pharmaceutical Engineering, Hebei University of Science and Technology, Shijiazhuang, China, [2]Beijing Research Center for Agriculture Standards and Testing, Beijing Academy of Agriculture and Forestry Sciences, Beijing, China

L-Histidine (L-His) is an essential amino acid, which is used to synthesize proteins and enzymes. The concentration of L-His in the body is controlled to regulate tissue growth and repair of tissues. In this study, a rapid and sensitive method was developed for colorimetric L-his detection using Cu^{2+} ions to inhibit the oxidation of 3,3′,5,5′-tetramethylbenzidine (TMB)–H_2O_2 system. H_2O_2 can oxidize TMB to oxTMB in the presence of copper, and the change in color from colorless (TMB) to blue (oxTMB) is similar to that observed in the presence of peroxidase. However, because the imidazole ring and carboxyl group of L-His can coordinate with Cu^{2+} ions to form stable L-His–Cu^{2+} complexes, the color of the TMB–H_2O_2 solution remains unchanged after the addition of L-His. Therefore, because L-His effectively hinders the colorimetric reaction of TMB with H_2O_2, this assay can be used to quantitatively determine the concentration of L-His in samples. Under optimized conditions, our colorimetric sensor exhibited two linear ranges of 60 nM to 1 μM and 1 μM to 1 mM for L-His detection and a detection limit of 50 nM (S/N = 3); furthermore, the assay can be performed within 20 min. Moreover, the proposed assay was used to determine the concentration of L-His in urine samples, suggesting that this convenient and label-free colorimetric method presents promising applications in bioanalytical chemistry and clinical diagnosis.

Keywords: colorimetric detection, L-histidine, copper, hydrogen peroxide, artificial enzyme

Edited by:
Muhammad Asif,
Wuhan Institute of Technology, China

Reviewed by:
Ghazala Ashraf,
Huazhong University of Science and Technology, China
Dilshad Hussain,
University of Karachi, Pakistan

***Correspondence:**
Yumin Liu
hslym0214@126.com
Qingju Liu
liuqj@brcast.org.cn

Specialty section:
This article was submitted to Analytical Chemistry, a section of the journal Frontiers in Chemistry

Received: *10 September 2021*
Accepted: *05 October 2021*
Published: *23 November 2021*

Citation:
Zhang Z, Zhao W, Hu C, Cao Y, Liu Y and Liu Q (2021) A Convenient and Label-Free Colorimetric Detection for L-Histidine Based on Inhibition of Oxidation of 3,3′,5,5′-Tetramethylbenzidine-H_2O_2 System Triggered by Copper Ions. Front. Chem. 9:773519. doi: 10.3389/fchem.2021.773519

INTRODUCTION

L-Histidine (L-His) levels in the body are typically controlled because L-His regulates the critical physiological functions, such as tissue growth and the transmission of metal elements (Kong et al., 2011). However, inadequate concentrations of L-his in the body can cause chronic kidney disease, primarily by inducing an impaired nutritional state (Huang and Tseng, 2009; Hu et al., 2014). Furthermore, an L-His deficiency can cause Friedreich ataxia, epilepsy, Parkinson's disease, and abnormal erythropoiesis (Li et al., 2013). Conversely, high concentrations of L-His in physiological fluids (serum and urine) can induce metabolic disorders or histidinemia (Oliveira et al., 2013). Therefore, L-His detection is critical for diseasing diseases. To date, numerous detection methods have been developed for quantifying L-his in biological fluids, including liquid chromatography

(Takeuchi et al., 1985), capillary electrophoresis (Meng et al., 2010), electrochemistry (Nai et al., 2013), resonance light scattering (Chen et al., 2006), surface-enhanced Raman scattering (SERS) (Ye et al., 2013), colorimetery (Hyeokseo and SudeokKim, 2013; Wu et al., 2016), and fluorometry (Karasyova et al., 2004). Although these methods present sensitivity and accuracy, they typically require generally complex equipment and professional operation. Moreover, L-His might be derivatizing and labeling using molecular signaling, which is time consuming and labor intensive. Hence, significant efforts are still required for the development of simple, rapid, highly sensitive, and free label method for L-His detection.

Owing to the change in color induced using a simple and rapid operation, colorimetric assays were designed to quantitatively detect biomolecules *via* naked eye observations and ultraviolet-visible (UV-Vis) spectroscopy (Josephy et al., 1982; Karasyova et al., 2004). Considering its chromogenic characteristics, 3,3′,5,5′-tetramethylbenzidine (TMB) has been extensively used as a colorimetric probe (Zhang et al., 2014; Liang et al., 2020). The change in color of TMB in the presence of H_2O_2 catalyzed by peroxidase, such as horseradish peroxidase, is a widely used chromogenic reaction (Liu et al., 2020). However, the natural enzymes are expensive and present low stability, which restricted their application in clinical diagnosis. There, artificial enzymes with peroxidase properties have received increasing attention. To date, numerous artificial enzymes, such as Fe_3O_4 (Xing et al., 2020), Au nanoparticles (Deng et al., 2016), carbon quantum dots (Chandra et al., 2019), and metal organic frameworks have been extensively investigated (Zheng et al., 2018). The artificial enzymes reported to date exhibited high catalytic efficiency and good stability and were inexpensive. However, most of the reported artificial enzymes presented intrinsic disadvantage such as complex synthesis processes. Recently, Cu^{2+} ions were used to catalyze the oxidation of TMB to oxTMB in the presence of H_2O_2 with high efficiency (Zhang et al., 2014). Inexpensive, stable, and readily available Cu^{2+} ions are good candidates as peroxidase mimetics. Analytical systems comprising TMB, Cu^{2+} ions, and H_2O_2 were used to detect uric acids (Lu et al., 2017), dopamine (Wang et al., 2017), and glucose (Li et al., 2019) in biological samples. During the analytical process, analytes are catalytically oxidized in the presence of enzymes to generate H_2O_2, which induces a color reaction. To the best of our knowledge, the use of a Cu^{2+}-triggered colorimetric assay for L-His detection has not been thoroughly investigated to date.

Because of the presence of the N-coordinating ligands of the imidazole ring and –COOH groups, L-his presents a remarkable affinity for Cu^{2+} ions and can strongly chelate with Cu^{2+} ions to form stable L-His–Cu^{2+} complexes (Elbaz et al., 2008; Zhang et al., 2013; Wang et al., 2017; Cai et al., 2020). Upon adding L-His to the assay, the Cu^{2+} ion-catalyzed TMB oxidation to oxTMB in the presence of H_2O_2 was inhibited. This resulted in a color change from blue (oxTMB) to colorless (TMB). Based on the mechanism, in this study, a rapid, convenient, and sensitive colorimetric method was designed.

EXPERIMENTAL

Materials

All of these reagents were of analytical grade, and all aqueous solutions were prepared with Milli-Q water (>18.2 MΩ·cm). 3,3′,5,5′-Tetramethylbenzidine (TMB) and hydrogen peroxide (H_2O_2) were purchased from Aladdin Biochemical Technology Co., Ltd. (Shanghai, China). $Cu(NO_3)_2 \cdot 3H_2O$ was obtained from Tianjin Bodi Chemical Industry Co. Ltd. (Tianjin, China). $Na_2HPO_4 \cdot 12H_2O$, $NaH_2PO_4 \cdot 2H_2O$, NaCl, and glucose were all purchased from Tianjin Best Chemical Co. Ltd. (Tianjin, China). L-alanine (L-Ala), L-phenylalanine (L-Phe), L-proline (L-Pro), L-histidine (L-His), and urea were all purchased from Beijing Solaibao Technology Co. Ltd. (Beijing, China). The pH of the solution was measured with a PB-10 pH meter (Sartorius, 91 Germany). UV-Vis absorption spectroscopic measurements were carried out on a TU-1900 spectrophotometer (Beijing Pu Analysis General Instrument Co., Ltd.) with an optical path length of 10 mm.

Coordination-driven chemistry of L-His and Cu^{2+} ions for colorimetric reaction of 3,5′,5,5′tetramethylbenzidine–hydrogen peroxide system

The coordination-driven chemistry of L-His and Cu^{2+} ions was studied for colorimetric reaction. First, the TMB–H_2O_2 system was constructed. Two hundred microliters of 420 μM Cu^{2+}ions, 40 μl of 160 mM TMB, and 40 μl of 300 mM H_2O_2 were added to 2 ml of phosphate buffer saline (PBS) solution (C = 0.1 M, pH = 5.7) in the absence and presence of 200 μl of 80 μM L-His. The mixture was incubated at 45°C for 20 min. Finally, the adsorption spectrum of the mixture was measured on UV-Vis spectrophotometer equipped with 1-cm path length quartz cuvettes.

Optimization and performance testing of the detecting system

The coordination-driven chemistry of L-His and Cu^{2+} ions was dramatically influenced by pH. We evaluated the effect of pH on the colorimetric reaction of the TMB–H_2O_2 system. Different pH of phosphate buffer saline (PBS) solution (C = 0.1 M) were prepared, including 4.0, 5.0, 5.3, 5.7, 6.0, 7.0, 8.0, and 9.0. Then, 40 μl of 160 mM TMB and 40 μl of 300 mM H_2O_2 were added to 2 ml of phosphate buffer saline (PBS) solution with various pH.

Then various concentrations of L-His and equal concentration of Cu^{2+} ions were incubated in PBS buffer solution (pH 5.7) at room temperature for 10 min, and the mixture was added into the TMB–H_2O_2 system. The final concentration of Cu^{2+} was 30 μM with various concentration of L-His. The mixture was incubated at 45°C for 20 min and then measured by UV-vis.

Meanwhile, the effect of interferents on the detection system was investigated with the above conditions with the substitution of L-His into the interferents. As urine detection probe, L-Ala, L-Phe, L-Pro, glucose, NaCl, and urea, as main constituents of

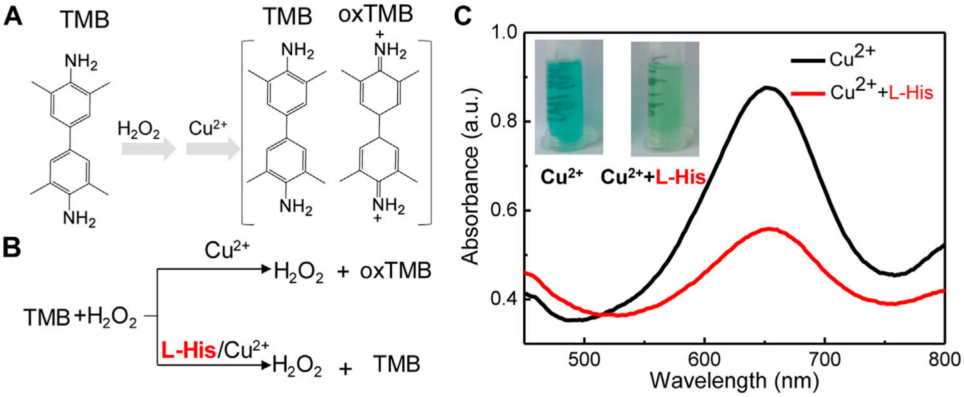

FIGURE 1 | The mechanism and feasibility of the colorimetric platform for L-His detection based on the coordination-driven chemistry of L-histidine (L-His) and Cu^{2+} in the TMB–hydrogen peroxide (H_2O_2) system. **(A)** The oxidation of 3,3′5,5′-tetramethylbenzidine (TMB). **(B)** The mechanism of the coordination-driven chemistry of L-His and Cu^{2+}. **(C)** Absorption spectra of the TMB + H_2O_2 system in the presence of Cu^{2+}, Cu^{2+} + L-His, Inset: Photographs corresponding to the curves.

urine, were evaluated as interferents (Sadighi et al., 2006; Dutta et al., 2014; Zheng et al., 2015). Besides, the main molecules were all added into the solution of PBS (c = 0.1 M, pH 7.4) to prepare the simulated urine for recovery testing.

RESULT AND DISCUSSION

Construction and validation of the coordination-driven chemistry of L-histidine and copper-based biosensing system

Our biosensing system consisted of two critical reactions: the coordination-driven chemistry of L-His and Cu^{2+} ions and the colorimetric TMB–H_2O_2 system (**Figure 1**). TMB, which served as a colorimetric probe, was oxidized by H_2O_2 to oxTMB in the presence of Cu^{2+} ions. During this process, Cu^{2+} ions presented intrinsic catalytic activity for the oxidation of TMB (colorless) to oxTMB (blue) in the presence of H_2O_2 (**Figure 1A**). Upon adding L-His to the biosensing system, the amino groups and hydroxyl groups of L-His chelated with Cu^{2+} ions and formed stable L-His–Cu^{2+} complexes (Zhang et al., 2013). Hence, L-His inhibited the catalytic activity of Cu^{2+} for the oxidation of TMB in the presence of H_2O_2, and the color of the TMB–H_2O_2 system did not change significantly (**Figure 1B**). Therefore, the change in color and decrease in absorbance were directly related to the L-His concentration. During the detecting process for the detecting system, the change in color and the decrease in absorbance were both taken as the detection signal of L-His. Hence, we constructed a colorimetric L-His detection sensor based on this mechanism.

To validate the feasibility of the colorimetric sensor for L-His detection, we compared the color and UV-vis spectra of a pristine state of the probe with those of the probe after exposing the TMB–H_2O_2 system to L-His. The color of the TMB-H_2O_2 was blue, and the highest peak in the UV-vis spectrum of the probe in the presence of Cu^{2+} ions was observed at 652 nm (**Figure 1C**). The color of the TMB–H_2O_2 system changed to light blue in the presence of L-His, indicating that the coordination-driven chemistry of L-His and Cu^{2+} ions affected the oxidation of the TMB–H_2O_2 system. Infrared spectrometry (IR) analysis was utilized to confirm the coordination-driven chemistry of L-His and Cu^{2+} ions, and the results indicated that the proposed method was suitable for L-His detection.

Optimization of experimental conditions

Because the colorimetric reaction and the coordination of Cu^{2+} ions with L-His were significantly affected by pH, we first evaluated the effects of reaction pH on L-His detection (**Figure 2**). The colorimetric reaction of the TMB–H_2O_2 system was significantly affected by pH (**Figure 2A**). The color of the TMB–H_2O_2 system was blue at pH 4, 5, and 6 and changed to yellow and colorless with the increasing pH to 7, 8, and 9. This indicated that the optimum pH for colorimetric reaction ranged between 4 and 6. Therefore, we subsequently evaluated the effect of pH in the range of 4–6 on the detection assay (**Figures 2B–G**). The color-changing rate on the TMB–H_2O_2 system increased rapidly with increasing pH, reached a plateau at pH >5.7, and then it decreased. The UV-vis absorbances of the highest peak (λ_{655}) in the absence and presence of L-His were defined as A_0 and A, respectively. The UV-vis spectra indicated that the absorbance-changing rate of the TMB–H_2O_2 system [(A_0-A)/A_0] was the highest at pH is 5.7 (**Figure 2H**). Therefore, pH 5.7 was used as the optimum pH value of the assay buffer of the sensing system.

Colorimetric assay for L-histidine detection

Owing to the catalytic effect of Cu^{2+} ions on the TMB–H_2O_2 system and the chelating interaction of Cu^{2+} ions and L-His, an assay for rapid and simple L-His detection was fabricated. The change in absorbance at 652 nm of the TMB–H_2O_2 system with increasing L-His concentration was analyzed under the optimized experimental conditions (**Figure 3A**). The absorbance of sensing system decreased with the addition of L-His. Moreover, the photographs of the corresponding solution color were inserted into **Figure 3A**. Upon increasing L-His concentration, the color

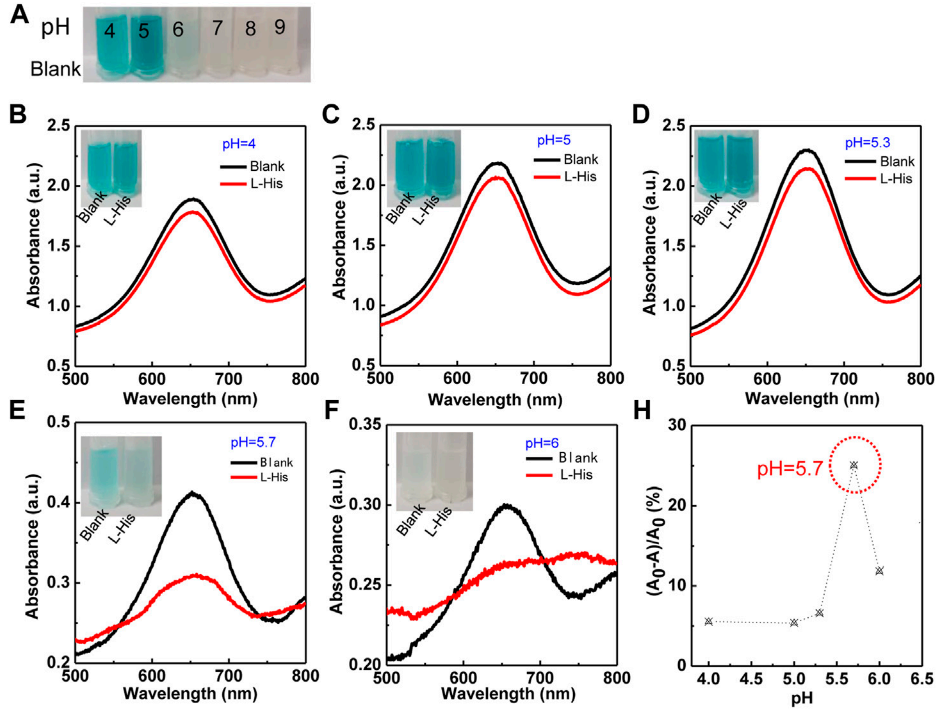

FIGURE 2 | The effect of pH on the colorimetric TMB–H_2O_2 system in the presence of Cu^{2+} ions for L-His detection. **(A)** Colorimetric reaction in different pH (the pH were 4, 5, 6, 7, 8, and 9, respectively). **(B–F)** The colorimetric reaction and absorbance intensity change with pH. The pH values were 4, 5, 5.3, 5.7, and 6. The photographs corresponding to the curves. **(G)** The ratio of absorbance ($(A_0\text{-}A)/A_0$) was changing with pH.

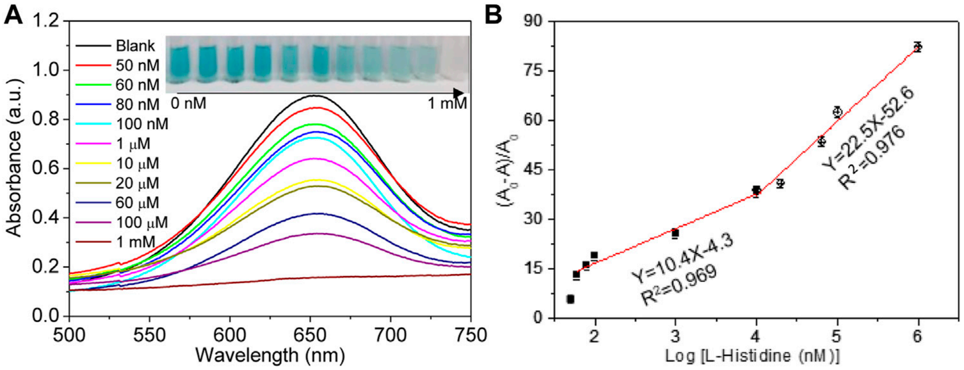

FIGURE 3 | Limit of detection. **(A)** Absorption spectra change in the sensing system with the increasing concentrations of L-his (the concentrations were 0 nM, 50 nM, 60 nM, 80 nM, 100 nM, 1 μM, 10 μM, 20 μM, 60 μM, 100 μM, and 1 mM, respectively). The photographs corresponding to the curves. **(B)** The rate of absorbance changing ($A_0\text{-}A/A_0$) at 655 nm change, with the increase in L-His.

of the TMB–H_2O_2 system changed from deep blue to colorless. Furthermore, the containment level of 10 μM L-His can be clearly distinguished with the naked eye. In addition $(A_0\text{-}A)/A_0$ depended on the concentration of L-His and increased linearly upon increasing L-His concentration in the range of 60 nM to 1 μM and 1 μM to 1 mM, respectively (inset in **Figure 3B**). The limit of detection of the sensing system was 50 nM (S/N = 3), and the linear equations describing the dependence of $(A_0\text{-}A)/A_0$ on the L-His concentration in the aforementioned L-His concentration ranges were y = 22.5 × −52.6 and y = 10.4 × −4.3, respectively (regression coefficient of 0.976 and 0.969, respectively).

To effectively exhibit the proposed method, the method was listed to compare with other methods (colorimetric and fluorescent platform based on nanomaterials) in **Table 1**. Compared with other colorimetric or fluorescent assay, the colorimetric strategy in this study has lower detection and wider analytical range.

TABLE 1 | Comparison of different methods for L-histidine (L-His) detection.

Analytical method	Linear range	LOD	References
Colorimetric probe of TMB-H_2O_2	60 nM–1 μM 1 μM–1 mM	60 nM	This work
Colorimetric probe of DNAzyme cascade	5 μM–100 mM	50 μM	Pan et al. (2018)
Fluorescent probe of azide and alkyne cycloaddition (CuAAC) reaction	0.5–100 μM	76 nM	Qiu et al. (2013)
Fluorescence probes of dopamine functionalized–CdTe quantum dots	1.0–100 μM	500 nM	Shi et al. (2014)
Fluorescent probe of nitrogen-doped carbon nanoparticles	0.5–60 μM	150 nM	Zhu et al. (2016)
Colorimetric probe of G-quadruplex-Cu metalloenzyme	10 nM–1.0 μM	10 nM	Wu et al. (2016)

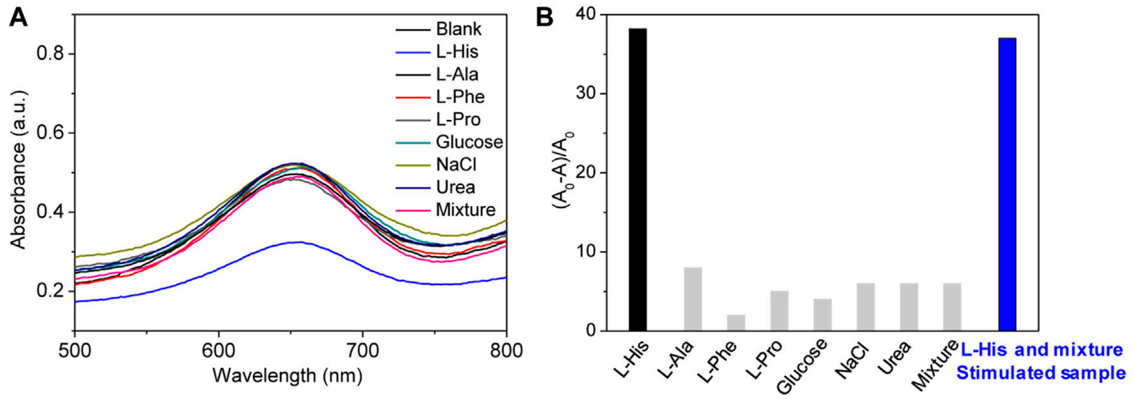

FIGURE 4 | Selectivity and simulated samples detection. **(A)** Absorption spectra of the sensing system in the presence of different molecules, including L-His, L-alanine (L-Ala), L-proline (L-Pro), L-phenylalanine (L-Phe), glucose, NaCl, and urea (the concentrations of the molecules were all 80 μM). **(B)** The rate of absorbance changing (A_0-A/A_0) at 655 nm change with different molecules.

TABLE 2 | The testing result of different L-histidine concentrations in simulated human urine (*N* = 3).

Sample no	Added (μM)	Found (μM)	Recovery (%)	R.S.D. (%, *n* = 3)
1	60	61.2	102.0	3.8
2	80	76.2	95.3	4.2
3	100	98.5	98.5	2.1

Selectivity of the colorimetric detection and artificial urine

The selectivity of the proposed colorimetric sensing system should be evaluated for real or simulated samples because real samples are complex. In particular, amino acids present in real samples can interfere with the quantitative analysis of L-His because their properties and structure are similar to those of L-His. Therefore, we selected L-alanine, L-proline, and L-phenylalanine as interferents to be evaluated because they are the primary components of urine. Meanwhile, the effect of glucose, urea, and NaCl were also studied because they are also the main component in urine (**Figure 4**). The change of absorbance and (A_0-A)/A_0 were presented in **Figures 4A,B**, respectively. Because the tested amino acids and biomolecules did not present significant signals, we concluded that our platform presented good selectivity for L-His, which is the most distinct difference in the structure between L-His and other amino acids. Other amino acids cannot chelate interaction with Cu^{2+} ions and have no effect on the colorimetric reaction of the TMB–H_2O_2 system.

Detection of L-histidine in simulated samples

To illustrate the practical application of colorimetric sensor for L-His detection, the simulated urine was prepared according to the previous literature (Sadighi et al., 2006; Dutta et al., 2014; Zheng et al., 2015). Briefly, L-Ala, L-Phe, L-Pro, glucose, NaCl, and urea were all added into the solution of PBS (c = 0.1 M, pH 7.4). Besides, different L-His concentrations were also added into the simulated urine. We used the standard addition method to obtain the L-His concentrations of simulated samples (**Table 2**). The recovery values were 102.0%, 95.3%, and 98.5%, respectively. Meanwhile, the relative standard deviations (RSDs) were 3.8, 4.2, and 2.1. The recovery values were between 95.3% and 102.0%, and the RSDs were no more than 4.2%. These results demonstrated that the proposed colorimetric sensor had a promising application for glyphosate detection in real samples.

CONCLUSIONS

In conclusion, the proposed platform as a colorimetric sensor can effectively detect L-His with simple and rapid operation. Owing to the coordination-driven chemistry and the strong chelating interaction between Cu^{2+} ions and L-His, the colorimetric sensor presents highly sensitive and selective detection of L-His with a detection limit of 50 μM by the naked eye. Meanwhile, the method did not need any label and is easy to obtain, and can be finished within 20 min. Compared with other TMB–H_2O_2 systems, the sensing platform is simple without enzymes and the complicated operation for biomolecules. In addition, we found that the interferents of urine have no effect on colorimetric platform. The detecting system was successfully used to detect L-His in the simulated samples and exhibited a great promise for practical application in biological and clinical diagnosis fields.

DATA AVAILABILITY STATEMENT

The original contributions presented in the study are included in the article/Supplementary Material, further inquiries can be directed to the corresponding authors.

AUTHOR CONTRIBUTIONS

ZZ and YL designed the experiment. ZZ and WZ carried out the experimental studies and collection, analysis, and interpretation of data. ZZ wrote the manuscript. YF helped to draft and revise the manuscript. All authors read and approved the final manuscript.

FUNDING

This work was supported by the Department of Education of Hebei Province (No. QN2019230), Research Fund for Doctoral Programs of Hebei University of Science and Technology (No. 1181267).

REFERENCES

Cai, Z., Zhu, R., Chen, S., Wu, L., Qi, K., and Zhang, C. (2020). An Efficient Fluorescent Probe for Tetracycline Detection Based on Histidine-Templated Copper Nanoclusters. *ChemistrySelect* 5, 3682–3687. doi:10.1002/slct.202000398

Chandra, S., Singh, V. K., Yadav, P. K., Bano, D., Kumar, V., Pandey, V. K., et al. (2019). Mustard Seeds Derived Fluorescent Carbon Quantum Dots and Their Peroxidase-like Activity for Colorimetric Detection of H_2O_2 and Ascorbic Acid in a Real Sample. *Anal. Chim. Acta* 1054, 145–156. doi:10.1016/j.aca.2018.12.024

Chen, Z., Liu, J., Han, Y., and Zhu, L. (2006). A Novel Histidine Assay Using Tetraphenylporphyrin Manganese (III) Chloride as a Molecular Recognition Probe by Resonance Light Scattering Technique. *Anal. Chim. Acta* 570, 109–115. doi:10.1016/j.aca.2006.04.003

Deng, H.-H., Hong, G.-L., Lin, F.-L., Liu, A.-L., Xia, X.-H., and Chen, W. (2016). Colorimetric Detection of Urea, Urease, and Urease Inhibitor Based on the Peroxidase-like Activity of Gold Nanoparticles. *Anal. Chim. Acta* 915, 74–80. doi:10.1016/j.aca.2016.02.008

Dutta, A. K., Das, S., Samanta, P. K., Roy, S., Adhikary, B., and Biswas, P. (2014). Non-Enzymatic Amperometric Sensing of Hydrogen Peroxide at a CuS Modified Electrode for the Determination of Urine H_2O_2. *Electrochim. Acta* 144, 282–287. doi:10.1016/j.electacta.2014.08.051

Elbaz, J., Shlyahovsky, B., and Willner, I. (2008). A DNAzyme Cascade for the Amplified Detection of Pb^{2+} Ions or L-Histidine. *Chem. Commun.* 13, 1569–1571. doi:10.1039/b716774a

Gu, P., Zhang, G., Deng, Z., Tang, Z., Zhang, H., Khusbu, F. Y., et al. (2018). A Novel Label-free Colorimetric Detection of L-Histidine Using Cu^{2+}-Modulated G-Quadruplex-Based DNAzymes. *Spectrochim. Acta A. Mol. Biomol. Spectrosc.* 203, 195–200. doi:10.1016/j.saa.2018.05.084

Hu, Y., Wang, Q., Zheng, C., Wu, L., Hou, X., and Lv, Y. (2014). Recyclable Decoration of Amine-Functionalized Magnetic Nanoparticles with Ni^{2+} for Determination of Histidine by Photochemical Vapor Generation Atomic Spectrometry. *Anal. Chem.* 86, 842–848. doi:10.1021/ac403378d

Huang, C.-C., and Tseng, W.-L. (2009). Highly Selective Detection of Histidine Using O-Phthaldialdehyde Derivatization after the Removal of Aminothiols through Tween 20-Capped Gold Nanoparticles. *Analyst* 134, 1699–1705. doi:10.1039/b900028c

Hyeokseo, S., and SudeokKim, S. M. (2013). Gold Nanoparticle-Based Colorimetric Chiral Discrimination of Histidine: Application to Determining the Enantiomeric Excess of Histidine. *Anal. Methods* 6, 73–76. doi:10.1039/c3ay41735b

Josephy, P. D., Eling, T., and Mason, R. P. (1982). The Horseradish Peroxidase-Catalyzed Oxidation of 3,5,3',5'-tetramethylbenzidine. Free Radical and Charge-Transfer Complex Intermediates. *J. Biol. Chem.* 257, 3669–3675. doi:10.1016/s0021-9258(18)34832-4

Kong, R.-M., Zhang, X.-B., Chen, Z., Meng, H.-M., Song, Z.-L., Tan, W., et al. (2011). Unimolecular Catalytic DNA Biosensor for Amplified Detection of L-Histidine via an Enzymatic Recycling Cleavage Strategy. *Anal. Chem.* 83, 7603–7607. doi:10.1021/ac2018926

Li, H., Liu, J., Fang, Y., Qin, Y., Xu, S., Liu, Y., et al. (2013). G-quadruplex-based Ultrasensitive and Selective Detection of Histidine and Cysteine. *Biosens. Bioelectron.* 41, 563–568. doi:10.1016/j.bios.2012.09.024

Li, X., Gao, L., and Chen, Z. (2019). Highly Sensitive Colorimetric Detection of Glucose through Glucose Oxidase and Cu^{2+}-Catalyzed 3,3′,5,5′-tetramethylbenzidine Oxidation. *Spectrochim. Acta A: Mol. Biomol. Spectrosc.* 213, 37–41. doi:10.1016/j.saa.2019.01.050

Liang, L., Huang, Y., Liu, W., Zuo, W., Ye, F., and Zhao, S. (2020). Colorimetric Detection of Salicylic Acid in Aspirin Using MIL-53(Fe) Nanozyme. *Front. Chem.* 8, 671. doi:10.3389/fchem.2020.00671

Liu, Q., He, Z., Wang, H., Feng, X., and Han, P. (2020). Magnetically Controlled Colorimetric Aptasensor for Chlorpyrifos Based on Copper-Based Metal-Organic Framework Nanoparticles with Peroxidase Mimetic Property. *Microchim. Acta* 187, 524–533. doi:10.1007/s00604-020-04499-x

Lu, H.-F., Li, J.-Y., Zhang, M.-M., Wu, D., and Zhang, Q.-L. (2017). A Highly Selective and Sensitive Colorimetric Uric Acid Biosensor Based on Cu(II)-Catalyzed Oxidation of 3,3′,5,5′-tetramethylbenzidine. *Sens. Actuators B: Chem.* 244, 77–83. doi:10.1016/j.snb.2016.12.127

Meng, J., Zhang, W., Cao, C.-X., Fan, L.-Y., Wu, J., and Wang, Q.-L. (2010). Moving Affinity Boundary Electrophoresis and its Selective Isolation of Histidine in Urine. *Analyst* 135, 1592–1599. doi:10.1039/c000472c

Metelitza, D. I., Karasyova, E. I., Grintsevich, E. E., and Thorneley, R. N. (2004). Peroxidase-catalyzed Co-oxidation of 3,3',5,5'-tetramethylbenzidine in the Presence of Substituted Phenols and Their Polydisulfides. *J. Inorg. Biochem.* 98, 1–9. doi:10.1016/j.jinorgbio.2003.10.007

Nai, J., Chen, Z., Li, H., Li, F., Bai, Y., Li, L., et al. (2013). Structure-Dependent Electrocatalysis of $Ni(OH)_2$Hourglass-like Nanostructures TowardsL-Histidine. *Chem. Eur. J.* 19, 501–508. doi:10.1002/chem.201203009

Oliveira, E., Santos, C., Poeta, P., Capelo, J. L., and Lodeiro, C. (2013). Turn-on Selective Vitamin B6 Derivative Fluorescent Probe for Histidine Detection in Biological Samples. *Analyst* 138, 3642–3645. doi:10.1039/c3an00324h

Qiu, S., Miao, M., Wang, T., Lin, Z., Guo, L., Qiu, B., et al. (2013). A Fluorescent Probe for Detection of Histidine in Cellular Homogenate and Ovalbumin Based on the Strategy of Clickchemistry. *Biosens. Bioelectron.* 42, 332–336. doi:10.1016/j.bios.2012.10.039

Sadighi, M., Reichman, N., Wilson, K., Carne, A., and Thompson, M. P. (2006). A Nitrogen Balance experiment Using Simulated Urine Samples. *Biochem. Mol. Biol. Educ.* 34, 289–293. doi:10.1002/bmb.2006.494034042632

Shi, F., Liu, S., and Su, X. (2014). Dopamine Functionalized-CdTe Quantum Dots as Fluorescence Probes for L-Histidine Detection in Biological Fluids. *Talanta* 125, 221–226. doi:10.1016/j.talanta.2014.02.060

Takeuchi, T., Asai, H., Hashimoto, Y., Watanabe, K., and Ishii, D. (1985). Application of Micro High-Performance Liquid Chromatography to the Separation of Chiral Amino Acids. *J. Chromatogr. A* 331, 99–107. doi:10.1016/0021-9673(85)80011-x

Wang, H.-B., Li, Y., Dong, G.-L., Gan, T., and Liu, Y.-M. (2017). A Convenient and Label-free Colorimetric Assay for Dopamine Detection Based on the Inhibition of the Cu(ii)-Catalyzed Oxidation of a 3,3′,5,5′-Tetramethylbenzidine-H_2O_2 System. *New J. Chem.* 41, 14364–14369. doi:10.1039/c7nj02710a

Wu, C., Fan, D., Zhou, C., Liu, Y., and Wang, E. (2016). Colorimetric Strategy for Highly Sensitive and Selective Simultaneous Detection of Histidine and Cysteine Based on G-Quadruplex-Cu(II) Metalloenzyme. *Anal. Chem.* 88, 2899–2903. doi:10.1021/acs.analchem.5b04796

Xing, Y., Si, H., Sun, D., and Hou, X. (2020). Magnetic Fe_3O_4@NH_2-MIL-101(Fe) Nanocomposites with Peroxidase-like Activity for Colorimetric Detection of Glucose. *Microchem. J.* 156, 104929–104936. doi:10.1016/j.microc.2020.104929

Ye, S., Xiao, J., Guo, Y., and Zhang, S. (2013). Aptamer-Based SERS Assay of ATP and Lysozyme by Using Primer Self-Generation. *Chem. Eur. J.* 19, 8111–8116. doi:10.1002/chem.201300126

Zhang, J., Yang, C., Chen, C., and Yang, X. (2013). Determination of Nitrite and Glucose in Water and Human Urine with Light-Up Chromogenic Response Based on the Expeditious Oxidation of 3,3′,5,5′-tetramethylbenzidine by Peroxynitrous Acid. *Analyst* 138, 2398–2404. doi:10.1039/c3an00080j

Zhang, L., Li, M., Qin, Y., Chu, Z., and Zhao, S. (2014). A Convenient Label Free Colorimetric Assay for Pyrophosphatase Activity Based on a Pyrophosphate-Inhibited Cu^{2+}-ABTS-H2O2reaction. *Analyst* 139, 6298–6303. doi:10.1039/c4an01415d

Zheng, X., Yao, T., Zhu, Y., and Shi, S. (2015). Cu^{2+} Modulated Silver Nanoclusters as an On-Off-On Fluorescence Probe for the Selective Detection of L-Histidine. *Biosens. Bioelectron.* 66, 103–108. doi:10.1016/j.bios.2014.11.013

Zheng, H.-Q., Liu, C.-Y., Zeng, X.-Y., Chen, J., Lü, J., Lin, R.-G., et al. (2018). MOF-808: A Metal-Organic Framework with Intrinsic Peroxidase-like Catalytic Activity at Neutral pH for Colorimetric Biosensing. *Inorg. Chem.* 57, 9096–9104. doi:10.1021/acs.inorgchem.8b01097

Zhu, X., Zhao, T., Nie, Z., Miao, Z., Liu, Y., and Yao, S. (2016). Nitrogen-Doped Carbon Nanoparticle Modulated Turn-On Fluorescent Probes for Histidine Detection and its Imaging in Living Cells. *Nanoscale* 8, 2205–2211. doi:10.1039/c5nr07826a

Conflict of Interest: The authors declare that the research was conducted in the absence of any commercial or financial relationships that could be construed as a potential conflict of interest.

frontiers in Chemistry

ORIGINAL RESEARCH
published: 24 December 2021
doi: 10.3389/fchem.2021.812503

A Simple Colorimetric Assay for Sensitive Cu^{2+} Detection Based on the Glutathione-Mediated Etching of MnO_2 Nanosheets

Shurong Tang[1]*, Qiao Liu[2,3], Jie Hu[2], Wei Chen[1], Fengping An[2], Hui Xu[2], Hongbo Song[2]* and Yi-Wei Wang[2]*

[1]Faculty of Pharmacy, Fujian Medical University, Fuzhou, China, [2]College of Food Science, Fujian Agriculture and Forestry University, Fuzhou, China, [3]Wuyi University, Wuyishan, China

Edited by:
Fei Xiao,
Huazhong University of Science and Technology, China

Reviewed by:
Abdul Rahman Rahman,
Zhejiang University, China
Tayyaba Iftikhar,
Huazhong University of Science and Technology, China

***Correspondence:**
Shurong Tang
srtang@fjmu.edu.cn
Hongbo Song
sghgbode@163.com
Yi-Wei Wang
ywwangfzu@163.com

Specialty section:
This article was submitted to Analytical Chemistry, a section of the journal Frontiers in Chemistry

Received: 10 November 2021
Accepted: 06 December 2021
Published: 24 December 2021

Citation:
Tang S, Liu Q, Hu J, Chen W, An F, Xu H, Song H and Wang Y-W (2021) A Simple Colorimetric Assay for Sensitive Cu^{2+} Detection Based on the Glutathione-Mediated Etching of MnO_2 Nanosheets. Front. Chem. 9:812503. doi: 10.3389/fchem.2021.812503

In this paper, we developed a quick, economical and sensitive colorimetric strategy for copper ions (Cu^{2+}) quantification via the redox response of MnO_2 nanosheets with glutathione (GSH). This reaction consumed MnO_2 nanosheets, which acted as a catalyst for the oxidation of 3,3′,5,5′-tetramethylbenzidine (TMB) to a blue product (oxTMB). In the presence of Cu^{2+}, the GSH was catalyzed to GSSG (oxidized glutathione), and the solution changed from colorless to deep blue. Under the optimum conditions, the absorption signal of the oxidized product (oxTMB) became proportional to Cu^{2+} concentration in the range from 10 to 300 nM with a detection limit of 6.9 nM. This detection system showed high specificity for Cu^{2+}. Moreover, the system has been efficaciously implemented for Cu^{2+} detection in actual tap water samples. The layered-nanostructures of MnO_2 nanosheets make it possess high chemical and thermal stability. TMB can be quickly oxidized within 10 min by the catalyzing of MnO_2 nanosheets with high oxidase-like activity. There is no need of expensive reagents, additional H_2O_2 and complicated modification processes during the colorimetric assay. Therefore, the strategy primarily based on MnO_2 nanosheets is promising for real-time, rapid and highly sensitive detection of Cu^{2+} under practical conditions.

Keywords: colorimetric system, MnO_2 mimetic enzyme, copper ions, rapid detection, water sample

INTRODUCTION

Copper is an essential microelement for the human body and an important component of human proteins and enzymes. Lack of copper ions (Cu^{2+}) will hinder the physiological activities of human body and easily cause various diseases (Scheiber et al., 2013; Chowdhury et al., 2018). On the other hand, copper is a heavy metal widely discovered in the environment, and excessive copper will produce severe toxic effects on humans, plants and microorganisms (Lee et al., 2016; Zhou et al., 2020). With the extensive utility of copper in industry and agriculture, it has become one of the main pollutants of social concern. Therefore, developing sensitive strategies to detect Cu^{2+} in environmental and biological samples is essential.

The detection techniques of Cu^{2+} have been greatly developed, such as atomic absorption spectroscopy (AAS) (Lima et al., 2012), inductively coupled plasma mass spectrometry (ICP-MS) (Dai et al., 2012; Khan et al., 2014), electrochemical techniques (Flavel et al., 2011; Zhu et al., 2017), fluorescence methods (Lan et al., 2010; Zhang et al., 2014; Zhang et al., 2020) and colorimetric assays

(Ma et al., 2011; Weng et al., 2013; Le et al., 2014; Wang et al., 2017; Luo et al., 2020). Some of these methods suffer from the drawbacks of requirements for large instruments, special operators, complex sample pretreatment process, or poor reproducibility and reliability, which limits their on-side rapid detection and practical application (Du et al., 2014; Wang et al., 2019a). Among them, colorimetric analysis is concerned because of its simple and quick operation, low cost, visualization and no need for professional operators, which makes it widely applied.

Colorimetric assays are generally based on peroxidase or some nanomaterials as the mimic enzyme to initiate chromogenic reactions that produce colored compounds (Jangi et al., 2020; Wang et al., 2020; Xia et al., 2021). Many chromogenic reactions are carried out via catalyzing the peroxidase substrates, usually TMB or 2, 2′-azinobis (3-ethylbenzothiazoline-6-sulfonic acid) (ABTS) (Tang et al., 2016). These reactions generally need additional hydrogen peroxide as the oxidant, which complicates the operation and increase the background signal. Strict time-controlling is necessary to improve the signal to noise ratio. There is also some other special color reactions, such as the etching of gold nanorods showing various color changes (Lin et al., 2016), the pink-blue transition caused by the aggregation of gold nanoparticles (Deng et al., 2013), and other methods generating colored compounds (Yin et al., 2015). Several colorimetric assays based on the nanomaterials of gold, silver and platinum nanoparticle have been developed for sensitive detection of Cu^{2+} (Ma et al., 2011; Le et al., 2014; Wang et al., 2017). The scarcity, high cost and easily poisoned of these precious noble metals, have hindered their large-scale use in practical colorimetric system (Kuo et al., 2014; Asif et al., 2017b). As a result, the creation of more economical and environment-friendly materials for colorimetric detection of Cu^{2+} is of significant importance.

In current years, some non-precious metals oxides-based nanosheets and nanosphere has been synthesized for electrochemical detection of various pollutants, such as MnO_2, CuO and graphene (Asif et al., 2017a; Asif et al., 2017b; Asif et al., 2018; Asif et al., 2019a; Aziz et al., 2019). MnO_2 nanosheets (NSs) have obtained high-level interest as a brand new type of two-dimensional (2D) nanomaterial (Chen et al., 2019). MnO_2 nanosheet is a kind of graphene-like nanomaterial, which can be used as a DNA nanocarrier to construct ratiometric fluorescence biosensors to detect miRNA and living cell imaging (Wang et al., 2019a). Due to its large particular sensing area, high chemical durability and inherent oxidative enzyme mimic activity, MnO_2 NSs are widely utilized in biosensors. The strong oxidation ability of MnO_2 NSs makes it great potential to constitute a colorimetric strategy for practical applications. Also, MnO_2 has excellent ion exchange and redox capabilities that can be widely used in supercapacitors, batteries and catalysis. It has been identified as the most promising electrode material for electrochemical energy storage systems, depending on its high density, high purity and sufficient electrochemical activity (Guo et al., 2019). some MnO_2 NSs based material has been synthesized for photoelectrochemical detection of Cu^{2+} (Hammami et al., 2021), electrochemiluminescence detection of glutathione (Gao et al., 2016), fluorescence detection of Fe^{2+} (Jiang et al., 2022), ascorbic acid (Xu et al., 2017), and glutathione (Wang et al., 2016), colorimetric detect of glutathione (Ge et al., 2019), acetylcholinesterase (Yan et al., 2017) and chlorothalonil (Sheng et al., 2020). Nevertheless, the colorimetric assays based on MnO_2 NSs for Cu^{2+} detection are very rare.

Herein, based on the catalytic oxidation activity of MnO_2 NSs, an easy, speedy and economic colorimetric assay is established for the sensitive determination of Cu^{2+}. TMB can be quickly oxidized by MnO_2 NSs to form blue oxTMB without the need for H_2O_2. After interaction with reduced glutathione (GSH), the MnO_2 NSs are dissolved, which reduce the formation amount of blue oxTMB, so the mixture remains colorless. When Cu^{2+} ions are introduced into the reaction mixture, Cu^{2+} catalyzes the formation of GSSG (oxidized glutathione) from GSH and thus inhibits the decomposition of MnO_2 NSs. As a result, the color of the mixture changes from colorless to blue. According to these results, a simple colorimetric method for Cu^{2+} was established. Moreover, this method has high sensitivity and selectivity for the determination of Cu^{2+}. The applicability of the assay in practical samples was also investigated.

METHODS AND MATERIALS

Materials and Reagents

Tetramethylammonium hydroxide (TMAOH), cysteine (Cys), ascorbic acid (AA), uric acid (UA) were purchased from Aladdin Reagent Co., Ltd (Shanghai, China). Bovine serum albumin (BSA) and L-glutathione (GSH) were received from Sigma-Aldrich (St. Louis, Missouri, United States). Manganese chloride tetrahydrate ($MnCl_2.4H_2O$), hydrogen peroxide (H_2O_2, 30 wt%), sodium hydroxide (NaOH), copper sulfate ($CuSO_4.5H_2O$), acetic acid (HAc), and ethanol were obtained from Sinopharm Chemical Reagent Co. (Shanghai, China). TMB substrate solution was obtained from Beyotime Biotechnology (Shanghai, China). All of the reagents used were analytical grades and were used directly (without further treatment). All the solutions were prepared from ultrapure water produced by a Milli-Q system.

Apparatus and Instrumentation

UV-Vis absorption spectra had been measured on the Cary-300 UV-Vis spectrophotometer (Agilent, United States). X-ray photoelectron spectroscopy (XPS) spectra were measured on the ESCALAB MKⅡX-ray photoelectron spectrometer (Thermo Fisher Scientific, United States). Morphology of MnO_2 NSs was analyzed by Nova NanoSEM 230 field-emission scanning electron microscopy (FEI, United States). Transmission electron microscope (TEM) photographs of MnO_2 NSs were obtained on the JEM-2100 transmission electron microscope (JEOL, Japan). The level of metal ions in practical water samples was evaluated by an X SERIES II inductively coupled plasma mass spectroscopy (ICP-MS) (Thermo Fisher Scientific, United States).

Synthesis of MnO_2 NSs

MnO_2 NSs were prepared according to the previous literature (Liu et al., 2017). Briefly, the mixture composed of 4.4 mL (25 wt

%) TMAOH, 2 mL (3 wt%) H_2O_2 and 15 mL ultrapure water was quickly added into 10 mL $MnCl_2.4H_2O$ solution (0.3 M) within 15 s. Then, the resulting dark brown suspension was stirred vigorously overnight at room temperature. After that, the prepared bulk manganese dioxide was centrifuged at 8,000 rpm for 10 min and washed three times with a large amount of distilled water and alcohol. The washed precipitate and 20 mg of BSA were dispersed in 20 mL ultrapure water and then treated with ultrasound for 10 h. The suspension was then centrifuged at 4,000 rpm for 15 min to remove the undispersed pellet. The supernatant was placed in the dark at 4°C for further use.

Colorimetric Detection of Cu^{2+}

Copper sulfate was dissolved in ultrapure water to prepare various concentrations of Cu^{2+} solutions. At first, 14 μL of 0.5 mM GSH solution was mixed with 40 μL different concentrations of Cu^{2+} solutions and reacted for 5 min. Then, 15 μL MnO_2 NSs (1.3 mg/mL) and 200 μL citric acid buffer (0.01 M, pH = 5.0) were added to the mixture and maintained 10 min at 45°C to ensure complete reaction. Subsequently, 100 μL of TMB substrate solution was introduced into each tube for another 10 min. Finally, the absorbance of the reaction solution in the wavelength range of 500–800 nm was determined. All reactions were carried out at 45°C.

Selectivity Investigation of Cu^{2+} Assay

In order to study whether other ions might interfere with the detection of Cu^{2+}, some other metal ions were applied to the system with ten times concentrations of that of Cu^{2+}. These ions including Fe^{3+}, Ni^{2+}, Ca^{2+}, Mg^{2+}, K^+, Zn^{2+}, Mn^{2+}, Pb^{2+}, Na^+, Hg^{2+}, and Ag^+. 1.0 μM Cu^{2+} was used for the test and the concentration of other metal ions was 10 μM.

Detection of Cu^{2+} in Actual Samples

To investigate the application ability of the colorimetric method in the practical samples, the collected tap water and waste water were naturally settled overnight for experiments. The supernatant obtained was treated with the 0.45 μm filtration membrane to take away particulate impurity. Then different concentrations of Cu^{2+} were introduced to the filtrate for further detection. The procedure described above was used for Cu^{2+} detection in the tap water and waste water samples.

RESULTS AND DISCUSSION

The Principle of Colorimetric Determination of Cu^{2+}

The strategy of Cu^{2+} colorimetric assay based on MnO_2 NSs is described in **Scheme 1**. Due to its intrinsic oxidase-like activity, the synthesized MnO_2 NSs can catalyze the formation of blue oxidation product (oxTMB) from colorless substrate TMB, which possesses an absorption peak at 650 nm. No additional H_2O_2 is added during this process. As an antioxidant, GSH can react with MnO_2 NSs in the way shown in **Eq. 1**, resulting in the reduction and decomposition of MnO_2 NSs. The released Mn^{2+} loses the catalytic ability, thus the chromogenic reaction of TMB is inhibited. In the presence of Cu^{2+}, Cu^{2+} can catalyze GSH to GSSG (Tang et al., 2016), resulting in less decomposition of MnO_2 NSs and more generation of oxTMB. As a result, the color of the solution turns blue. Cu^{2+} concentration is linearly related to the absorption value of TMB oxidation products. Thus, a sensitive "turn on" Cu^{2+} detection scheme is established.

$$MnO_2 + 2GSH + 2H^+ \rightarrow Mn^{2+} + GSSG + 2H_2O \qquad (1)$$

Feasibility of the Cu^{2+} Colorimetric Assay

Some control experiments were performed to confirm the feasibility of the colorimetric assay. As shown in **Figure 1A**, the characteristic peak (380 nm) of MnO_2 NSs gradually decreased with the increasing GSH concentration, indicating that MnO_2 NSs have been decomposed by GSH. Without GSH, the TMB oxidation process can be promoted by MnO_2 NSs, generating colored solution and significant absorption signal (**Figure 1B**, curve a). After interaction with GSH, the MnO_2 NSs was decomposed, and TMB oxidization was inhibited, which resulted in colorless solution and a great decrease of absorption signal (**Figure 1B**, curve b). Through the catalysis of Cu^{2+}, GSH was oxidized to GSSG, which inhibited MnO_2 NSs dissociation. Thus the absorption signal was enhanced (**Figure 1B**, curve c). According to these results, we concluded that Cu^{2+} could be quantified by measuring the absorption values of TMB oxidation products at 650 nm.

Characterization of MnO_2 NSs

After interaction with TMAOH, Mn^{2+} was oxidized to Mn^{4+} by H_2O_2 to form bulk MnO_2. By treating it with BSA under ultrasonication, MnO_2 NSs with good dispersibility, biocompatibility and high peroxidase activity were obtained, as previously described (Liu et al., 2012). The morphology of MnO_2 NSs was analyzed by scanning electron microscopy (SEM). As displayed in **Supplementary Figure S1**, the obtained MnO_2 NSs presented an obvious sheet-like morphology and well dispersed in water. As the TEM image (**Figure 2A**) shown, the obtained MnO_2 NSs exhibit characteristic 2-D layered architecture with partial folds/wrinkles, which contribute to the large specific surface area and good dispersibility.

The UV-Vis absorption spectra in **Figure 2B** shows that MnO_2 NSs have a wide absorption spectra in the 250–500 nm range with a maximum absorption band at 380 nm, which can be ascribed to a d-d jump of Mn^{4+}. This is in agreement with the optical properties of MnO_2 NSs reported previously (Liu et al., 2012). Furthermore, with the increase of MnO_2 NSs, the absorption intensity at 380 nm increased.

Chemical and elemental compositions of MnO_2 NSs were analyzed by XPS. The wide scan spectrum results are represented in **Figure 2C**. Four main peaks centered at 647.2, 528.7, 401.6 and 284.7 eV can be ascribed to Mn 2p, O 1s, N 1s and C 1s (Liu et al., 2012; Asif et al., 2019b). **Figure 3** shows the high-resolution XPS spectra of Mn 2p and O 1s. From **Figure 3A**, two strong characteristic peaks located at 652.9 and 641.2 eV emerge in the Mn $2p_{1/2}$ and Mn $2p_{3/2}$ core-level spectra, corresponding to the presence of Mn^{4+} moieties (Iftikhar et al., 2021). In **Figure 3B**, the peak at 528.7 eV is caused by O 1s. The O 1 s

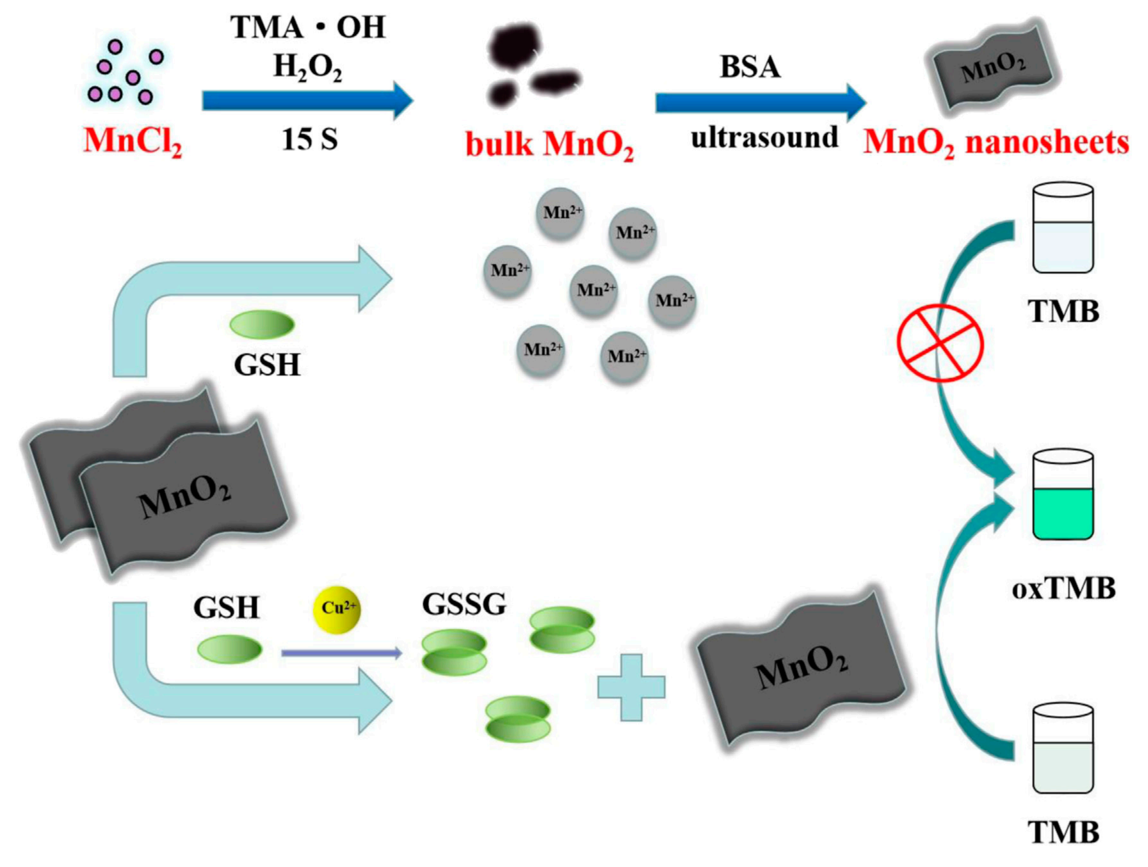

SCHEME 1 | Schematic diagram of colorimetric determination of Cu^{2+} based on MnO_2 NSs.

spectrum contains two sub energy states in **Figure 3B** and these peaks can be assigned to Mn–O–Mn and Mn–O–H (Liu et al., 2012; Asif et al., 2022; Aziz et al., 2022).This indicate that the acquisition of pure MnO_2 and the oxidation valence of Mn is +4 (Saha and Pal, 2014). These results indicate the successful synthesis of MnO_2 NSs.

Optimization of the Experimental Conditions

In order to improve the sensitivity of the Cu^{2+} detection system, we further optimized some important experimental conditions, including pH, reaction temperature, the dosage of TMB substrate solution and GSH concentration. At first, the optimal pH of the reaction system was studied. HAc-NaAc buffer solutions with different pH were added to the reaction system. **Supplementary Figure S2** shows the absorption values at different pH in the presence and absence of Cu^{2+}. In the presence of 250 nM Cu^{2+}, the absorption increment increases sharply in the pH range of 3.5–5.0. While the pH reaches 5.5, the increment of absorption decreases instead. As continues to raise the pH, the absorption increment returns to a slow upward trend. It is determined that the absorption increment is maximal when the pH value is 5.0. Therefore, the pH was selected at 5.0 for further test.

We also studied the influence of temperature on Cu^{2+} sensing systems. The absorption values at different temperatures in the presence and absence of Cu^{2+} are shown in **Supplementary Figure S3**. In the range of 25–45°C, the increase of temperature is beneficial to the reaction, and the absorbance difference of the final solution presents a steady rise trend. When the temperature reaches 45°C, the absorbance difference reached the maximum. Once the temperature is above 45°C, the temperature has a negative impact on this system. In order to obtain good experimental results, the colorimetric Cu^{2+} detection was carried out at the temperature of 45°C.

Subsequently, it was found that the amount of TMB substrate solution was related to the absorption intensity of the reaction solution at 650 nm. As **Supplementary Figure S4** shown, the absorption value increases gradually with the increase of TMB substrate solution and remains stable when the amount of TMB is more than 100 μL. Therefore, the dosage of TMB substrate solution was selected as 100 μL.

The concentration of GSH used to decompose MnO_2 NSs is critical. In order to achieve higher detection sensitivity, it was also optimized. As shown in **Supplementary Figure S5A**, the absorption value of the solution gradually decreases with the increase of GSH concentration in the reaction system. The solution color also changes from blue to colorless. These results indicated that MnO_2 NSs were decomposed into Mn^{2+} by GSH, which inhibited the production of blue oxTMB. Meanwhile, there was a good linear relationship between the absorbance and the concentration of GSH from 0 to 18.75 μM (**Supplementary Figure S5B**). Considering the sensitivity and

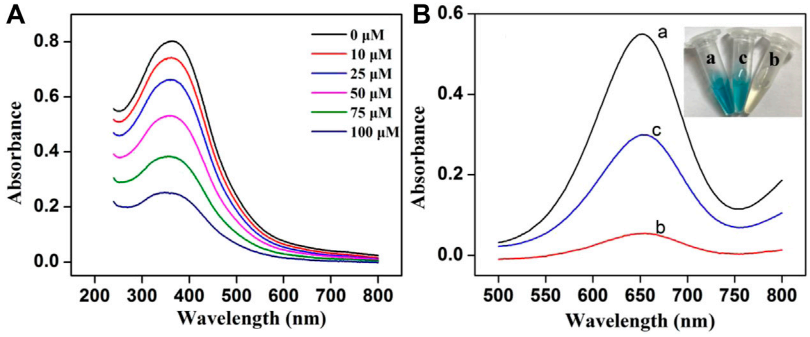

FIGURE 1 | (A) The UV-vis absorption spectra of MnO_2 NSs (162.5 μg/mL) with different concentrations of GSH **(B)** Absorption spectra of the system under different conditions: (a) MnO_2 + TMB, (b) MnO_2 + GSH + TMB and (c) MnO_2 + Cu^{2+} + GSH + TMB (Inset: the photograph of the solution color).

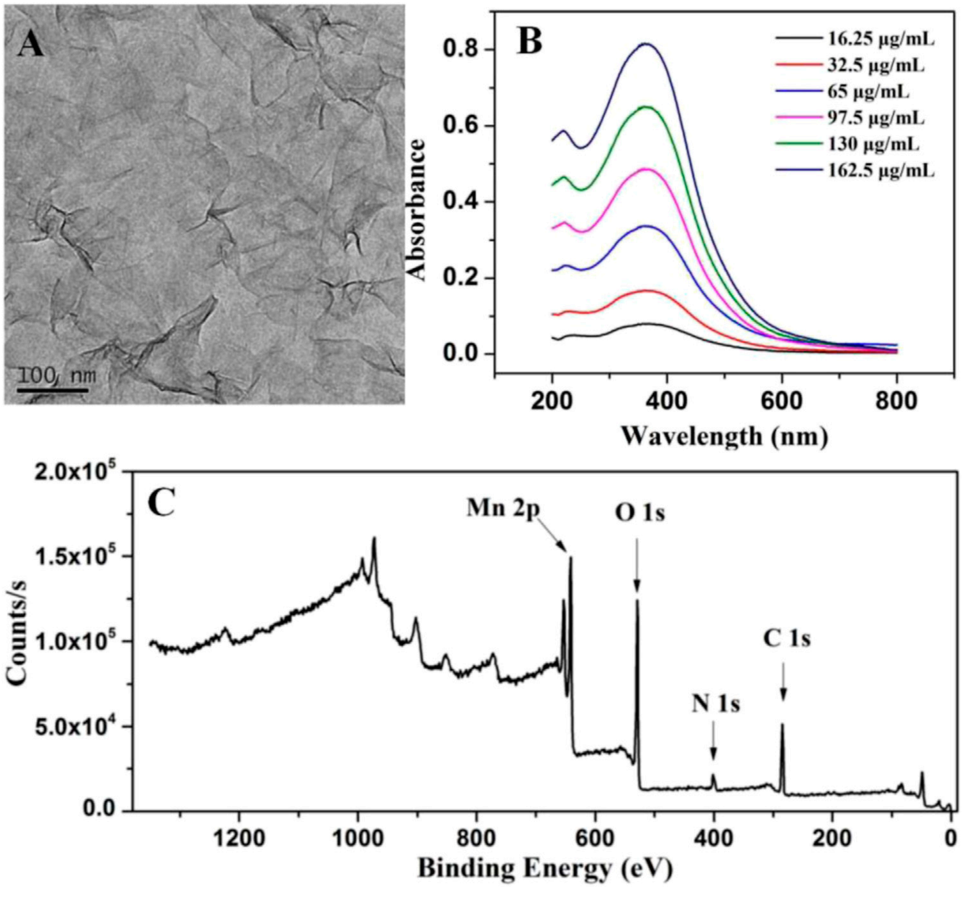

FIGURE 2 | (A) TEM photograph of MnO_2 NSs **(B)** Absorption spectra of different concentrations of MnO_2 NSs **(C)** XPS characterization of MnO_2 NSs.

practical conditions of the system, the colorimetric assay was performed by selecting 17.5 μM GSH.

Sensitivity, Reproducibility and Stability Investigation of Cu^{2+} Assay

The sensitivity of the colorimetric assay was verified by adding different concentrations of Cu^{2+} to the solution at the optimal conditions. The recorded UV-vis absorption spectra of the system and the calibration curve established by absorption values of different concentrations of Cu^{2+} at 650 nm are presented in **Figure 4**. The results showed that with the increase of Cu^{2+} concentration, absorption value exhibited a rising trend and the color of the solution became deeper (**Figure 4A**). The absorption value has a good linear relationship with Cu^{2+} concentration from 10 to 300 nM, and

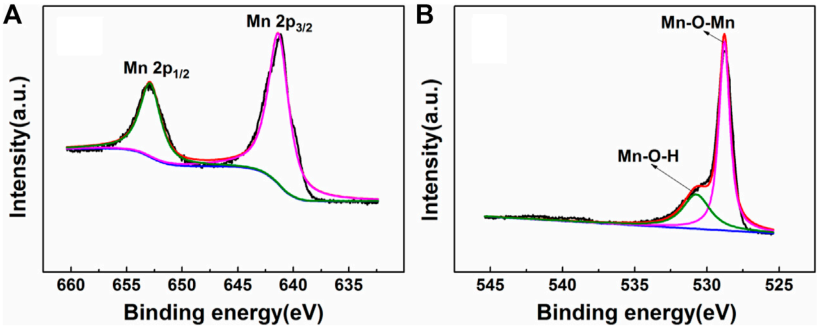

FIGURE 3 | The XPS spectra of **(A)** Mn 2p and **(B)** O 1 s.

the correlation coefficient is 0.997 (**Figure 4B**). Cu^{2+} detection limit (LOD) was estimated to about 6.9 nM (3σ). Because of the hazardous effects of high levels of Cu^{2+}, the US Environmental Protection Agency stipulates that the maximum level of Cu^{2+} allowed in drinking water was about 20 μM (U.S.E.P. Agency, 2012). Thus, this colorimetric assay is suitable for the detection of low concentration Cu^{2+} in the environment.

Compared with other reported methods in **Table 1**, this strategy could achieve a lower detection limit and a wider detection range. Besides, the characteristic of the novel colorimetric assay, such as simple operation (no additional H_2O_2 was required), low toxicity, and low cost (without the need of precious metal or nucleic acid), makes it great potential in high sensitivity and rapid test of Cu^{2+} in drinking water and environment.

The reproducibility of the colorimetric sensor was evaluated by intra-assay. Five parallel measurements have been performed to detect 100 nM Cu^{2+} at the same conditions. The obtained relative standard deviation (RSD) was calculated to be 2.9%. The long-term stability of the colorimetric sensor was also investigated. The MnO_2 NSs were stored in dark under 4 °C when it is not used. After stored for more than 1 month, the Cu^{2+} induced absorption response could retain 96% of its original value. These results indicate that the colorimetric sensor shows good repeatability and stability.

Interference Study

To investigate the specificity of colorimetric determination of Cu^{2+}, series interference experiments were also carried out. Various metal ions including Fe^{3+}, Ni^{2+}, Ca^{2+}, Mg^{2+}, K^+, Zn^{2+}, Mn^{2+}, Pb^{2+}, Na^+, Hg^{2+}, Ag^+ and common compounds with redox properties were studied. Under the same conditions, 1.0 μM Cu^{2+} or other metal ions with ten times the concentration of Cu^{2+} were added to the system to collect the absorption signal. Although Ag^+ and Hg^{2+} could give rise to measurable absorbance signals (**Supplementary Figure S6**) in the concentration of 10 μM, the interference is small when they are at the same concentration as Cu^{2+} (1.0 μM) (**Supplementary Figure S7**), and they will not significantly affect the detection of Cu^{2+} at this concentration in the environmental system. In addition, KBr (1.25 mM) and KCl (12.5 mM) were used as masking agents to eliminate the interference of Hg^{2+} and Ag^+. It could be seen in **Figure 5** that with the coexistence of KBr and KCl, the colorimetric assay showed high specificity for Cu^{2+}. At the same time, other metal ions with concentration ten times of Cu^{2+} made no difference in the sensitivity of Cu^{2+} analysis. Common redox substances, such as 100 μM of Cys, AA, UA and 1.0 mg/mL of BSA had no significant effect on the detection of Cu^{2+} (**Supplementary Figure S7**). It is worth noting that the selectivity can be observed with the naked eye. Hence, the specific detection of Cu^{2+} can be achieved by the established colorimetric assay.

Detection of Cu^{2+} in Real Samples

To verify the applicability of this method in practical samples and complex sample matrix, Cu^{2+} spiked tap water (collected from the laboratory) and waste water (collected from a point source suspected to discharge metal ions by Longyan Rare Earths LTD.) were prepared for the test. The practical samples were settled overnight at room temperature, and then the impurities were removed by filtration with a 0.45 μm filter membrane. For comparison, ICP-MS was also used to evaluate the Cu^{2+} level in these samples. The initial concentration of Cu^{2+} detected by ICP-MS in tap water and waste water is 3.5 and 235.2 nM, respectively. The analytical performances of the proposed colorimetric assay for the detection of Cu^{2+} from waste water is in good agreement with the results obtained by ICP-MS with RSD value of 1.74% (**Supplementary Table S1**). This result indicated the good accuracy of the proposed colorimetric assay for the analysis of Cu^{2+} in real samples. After dilution, series of Cu^{2+} with different concentrations were added into the pretreated water samples and detected by this colorimetric method. The detection results are listed in **Supplementary Table S1**. The recovery of standard Cu^{2+} spiked samples is between 95.2 and 105.7%, with RSD< 3.24% (n = 3). The results illustrate that this colorimetric method is promising for applying efficient quantitative detection of Cu^{2+} in actual samples with high sensitivity.

CONCLUSION

To summarize, we developed a novel colorimetric method to detect Cu^{2+} rapidly and effectively. The basic principle of the

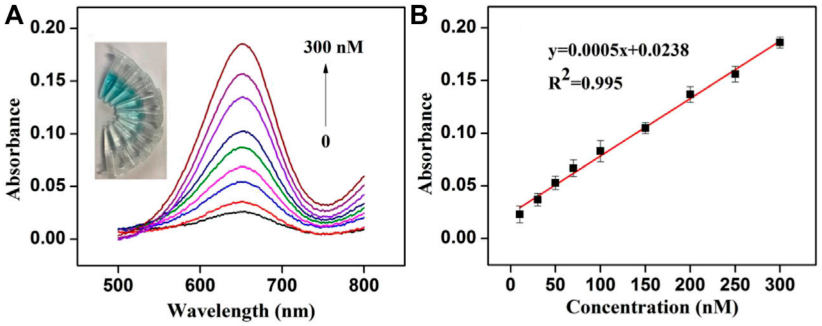

FIGURE 4 | (A) Absorption spectra obtained for colorimetric detection of Cu^{2+} (Inset: the photograph of the color change of the solution) **(B)** Linear relationship between Cu^{2+}concentration (10–300 nM) and the absorption value.

TABLE 1 | The list comparison of this work with other previously published works.

Method	Material	Analytical ranges	LOD	Ref
Fluorescence	Upconversion nanoparticles	0.125–3.125 μM	100 nM	Su et al. (2021)
Fluorescence	Ag_2S quantum dots	25 nM~10 μM	27.6 nM	Jiang et al. (2019)
Fluorescence	HP-GO[a]	0–3.93 μM	54 nM	Awad et al. (2020)
Fluorescence	CdTe quantum dot	0–1,000 nM	1.45 nM	Ye et al. (2020)
Colorimetric	$MMoO_4$[b]	0.1–24 μM	24 nM	Luo et al. (2020)
Colorimetric	Au@Pt nanocatalysts	20–300 nM	3.7 nM	Wang et al. (2017)
Colorimetric	ZnO-Co_3O_4 nanocages protein-based nanoprobe	2–100 nM	1.08 nM	Lv et al. (2021)
Colorimetric	protein-based nanoprobe	0–8 μM	160 nM	Hu et al. (2021)
Electrochemistry	Au Nanoparticles	2.5–25 μg/L	0.9 μg/L	Wang et al. (2019b)
Electrochemistry	IIP-film[c]	0.95–244 nM	2.7 nM	Di Masi et al. (2020)
Colorimetric	GSH/MnO_2 NSs	10–300 nM	6.9 nM	This work

[a] *Hematoporphyrin modified graphene oxide.*
[b] *M = co, Ni.*
[c] *Ion imprinted polymeric film.*

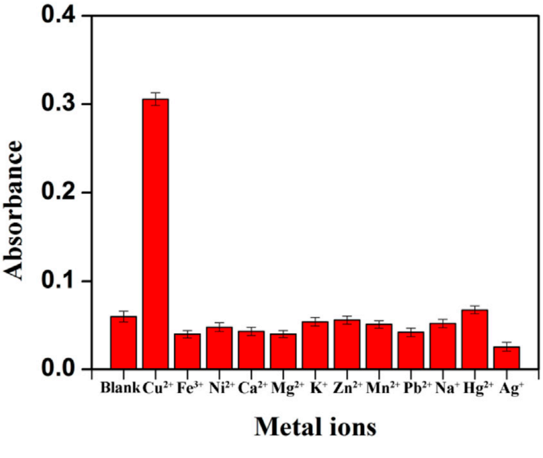

FIGURE 5 | Study on the selectivity of the established Cu^{2+} assay after the addition of masking agents (The concentration of Cu^{2+} was 1.0 μM, other metal ions concentration was ten-fold of Cu^{2+}).

method is that Cu^{2+} can catalyze GSH to GSSG, thus inhibiting the decomposition of the single-layer MnO_2 NSs into Mn^{2+} by GSH to achieve Cu^{2+} detection. Under the optimal experimental conditions, the colorimetric system exhibits highly sensitive, broad linear range, low detection limit and rapid analysis. In addition, the experimental results showed that this method is expected to be used for the determination of Cu^{2+} in practical conditions. Compared to natural enzymes, the layered nanostructures of 2D MnO_2 NSs makes themselves possess higher chemical and thermal stability. It should be noted that the TMB can be quickly oxidized by MnO_2 NSs with high oxidase-like activity within 10 min. Importantly, the colorimetric assay does not require any expensive reagents, additional H_2O_2 or complicated modification processes and can complete the detection under mild conditions in a short time, which is expected to be applied to the detection of Cu^{2+} in other practical situations. It is worth mentioning that combining with Cu-contained nanomaterials, this colorimetric method can provide a novel general sensing strategy for the indirect detection of a variety of analytes.

DATA AVAILABILITY STATEMENT

The original contributions presented in the study are included in the article/**Supplementary Material**, further inquiries can be directed to the corresponding authors.

AUTHOR CONTRIBUTIONS

ST and YW designed this study. QL carried out the experiment, data acquisition, and data analysis. JH provided assistance for data acquisition and manuscript editing. ST and QL drafted the manuscript. WC provided contribution suggestions of the manuscript. FA, HX, HS, and WY helped to revise the manuscript. All authors contributed to the manuscript and approved the final version.

FUNDING

This work was supported by the National Natural Science Foundation of China (21874019, 21605019) and the Natural Science Foundation of Fujian Province (2020J01635, 2019J05046).

ACKNOWLEDGMENTS

We thank all members of laboratory for their technical support and academic discussions.

SUPPLEMENTARY MATERIAL

The Supplementary Material for this article can be found online at: https://www.frontiersin.org/articles/10.3389/fchem.2021.812503/full#supplementary-material

REFERENCES

Asif, M., Aziz, A., Ashraf, G., Iftikhar, T., Sun, Y., Xiao, F., et al. (2022). Unveiling Microbiologically Influenced Corrosion Engineering to Transfigure Damages into Benefits: A Textile Sensor for H_2O_2 Detection in Clinical Cancer Tissues. *Chem. Eng. J.* 427, 131398. doi:10.1016/j.cej.2021.131398

Asif, M., Aziz, A., Ashraf, G., Wang, Z., Wang, J., Azeem, M., et al. (2018). Facet-Inspired Core-Shell Gold Nanoislands on Metal Oxide Octadecahedral Heterostructures: High Sensing Performance toward Sulfide in Biotic Fluids. *ACS Appl. Mater. Inter.* 10, 36675–36685. doi:10.1021/acsami.8b12186

Asif, M., Aziz, A., Wang, H., Wang, Z., Wang, W., Ajmal, M., et al. (2019a). Superlattice Stacking by Hybridizing Layered Double Hydroxide Nanosheets with Layers of Reduced Graphene Oxide for Electrochemical Simultaneous Determination of Dopamine, Uric Acid and Ascorbic Acid. *Microchim. Acta* 186 (2), 61. doi:10.1007/s00604-018-3158-y

Asif, M., Aziz, A., Wang, Z., Ashraf, G., Wang, J., Luo, H., et al. (2019b). Hierarchical CNTs@CuMn Layered Double Hydroxide Nanohybrid with Enhanced Electrochemical Performance in H_2S Detection from Live Cells. *Anal. Chem.* 91 (6), 3912–3920. doi:10.1021/acs.analchem.8b04685

Asif, M., Haitao, W., Shuang, D., Aziz, A., Zhang, G., Xiao, F., et al. (2017b). Metal Oxide Intercalated Layered Double Hydroxide Nanosphere: With Enhanced Electrocatalyic Activity towards H_2O_2 for Biological Applications. *Sensors Actuators B: Chem.* 239, 243–252. doi:10.1016/j.snb.2016.08.010

Asif, M., Liu, H., Aziz, A., Wang, H., Wang, Z., Ajmal, M., et al. (2017a). Core-shell Iron Oxide-Layered Double Hydroxide: High Electrochemical Sensing Performance of H_2O_2 Biomarker in Live Cancer Cells with Plasma Therapeutics. *Biosens. Bioelectron.* 97, 352–359. doi:10.1016/j.bios.2017.05.057

Awad, F. S., AbouZied, K. M., Bakry, A. M., Abou El-Maaty, W. M., El-Wakil, A. M., and El-Shall, M. S. (2020). Highly Fluorescent Hematoporphyrin Modified Graphene Oxide for Selective Detection of Copper Ions in Aqueous Solutions. *Analytica Chim. Acta* 1140, 111–121. doi:10.1016/j.aca.2020.10.016

Aziz, A., Asif, M., Ashraf, G., Iftikhar, T., Hu, J., Xiao, F., et al. (2022). Boosting Electrocatalytic Activity of Carbon Fiber@Fusiform-like Copper-Nickel LDHs: Sensing of Nitrate as Biomarker for NOB Detection. *J. Hazard. Mater.* 422, 126907. doi:10.1016/j.jhazmat.2021.126907

Aziz, A., Asif, M., Azeem, M., Ashraf, G., Wang, Z., Xiao, F., et al. (2019). Self-Stacking of Exfoliated Charged Nanosheets of LDHs and Graphene as Biosensor with Real-Time Tracking of Dopamine from Live Cells. *Analytica Chim. Acta* 1047, 197–207. doi:10.1016/j.aca.2018.10.008

Chen, J., Meng, H., Tian, Y., Yang, R., Du, D., Li, Z., et al. (2019). Recent Advances in Functionalized MnO_2 Nanosheets for Biosensing and Biomedicine Applications. *Nanoscale Horiz.* 4 (2), 321–338. doi:10.1039/c8nh00274f

Chowdhury, S., Rooj, B., Dutta, A., and Mandal, U. (2018). Review on Recent Advances in Metal Ions Sensing Using Different Fluorescent Probes. *J. Fluoresc.* 28 (4), 999–1021. doi:10.1007/s10895-018-2263-y

Dai, B., Cao, M., Fang, G., Liu, B., Dong, X., Pan, M., et al. (2012). Schiff Base-Chitosan Grafted Multiwalled Carbon Nanotubes as a Novel Solid-phase Extraction Adsorbent for Determination of Heavy Metal by ICP-MS. *J. Hazard. Mater.* 219-220, 103–110. doi:10.1016/j.jhazmat.2012.03.065

Deng, J., Jiang, Q., Wang, Y., Yang, L., Yu, P., and Mao, L. (2013). Real-Time Colorimetric Assay of Inorganic Pyrophosphatase Activity Based on Reversibly Competitive Coordination of Cu^{2+} between Cysteine and Pyrophosphate Ion. *Anal. Chem.* 85 (19), 9409–9415. doi:10.1021/ac402524e

Di Masi, S., Pennetta, A., Guerreiro, A., Canfarotta, F., De Benedetto, G. E., and Malitesta, C. (2020). Sensor Based on Electrosynthesised Imprinted Polymeric Film for Rapid and Trace Detection of Copper(II) Ions. *Sensors Actuators B: Chem.* 307, 127648. doi:10.1016/j.snb.2019.127648

Du, Y., Lim, B. J., Li, B., Jiang, Y. S., Sessler, J. L., and Ellington, A. D. (2014). Reagentless, Ratiometric Electrochemical DNA Sensors with Improved Robustness and Reproducibility. *Anal. Chem.* 86, 8010–8016. doi:10.1021/ac5025254

Flavel, B. S., Nambiar, M., and Shapter, J. G. (2011). Electrochemical Detection of Copper Using a Gly-Gly-His Modified Carbon Nanotube Biosensor. *Silicon* 3 (4), 163–171. doi:10.1007/s12633-011-9080-0

Gao, W., Liu, Z., Qi, L., Lai, J., Kitte, S. A., and Xu, G. (2016). Ultrasensitive Glutathione Detection Based on Lucigenin Cathodic Electrochemiluminescence in the Presence of MnO_2 Nanosheets. *Anal. Chem.* 88 (15), 7654–7659. doi:10.1021/acs.analchem.6b01491

Ge, J., Cai, R., Chen, X., Wu, Q., Zhang, L., Jiang, Y., et al. (2019). Facile Approach to Prepare HSA-Templated MnO_2 Nanosheets as Oxidase Mimic for Colorimetric Detection of Glutathione. *Talanta* 195, 40–45. doi:10.1016/j.talanta.2018.11.024

Guo, C., Liu, H., Li, J., Hou, Z., Liang, J., Zhou, J., et al. (2019). Ultrathin δ-MnO_2 Nanosheets as Cathode for Aqueous Rechargeable Zinc Ion Battery. *Electrochimica Acta* 304, 370–377. doi:10.1016/j.electacta.2019.03.008

Hammami, A., Assaker, I. B., and Chtourou, R. (2021). Regenerative, Low-Cost and Switchable Photoelectrochemical Sensor for Detection of Cu^{2+} Using MnO_2-GO Heterojunction. *J. Solid State. Electrochem.* doi:10.1007/s10008-021-05092-9

Hormozi Jangi, S. R., Akhond, M., and Absalan, G. (2020). A Novel Selective and Sensitive Multinanozyme Colorimetric Method for Glutathione Detection by Using an Indamine Polymer. *Analytica Chim. Acta* 1127, 1–8. doi:10.1016/j.aca.2020.06.012

Hu, J., Wang, L., Zhang, X., Yu, W., Gao, H.-W., Solin, N., et al. (2021). Selective Colorimetric Detection of Copper (II) by a Protein-Based Nanoprobe. *Spectrochimica Acta A: Mol. Biomol. Spectrosc.* 252, 119462. doi:10.1016/j.saa.2021.119462

Iftikhar, T., Xu, Y., Aziz, A., Ashraf, G., Li, G., Asif, M., et al. (2021). Tuning Electrocatalytic Aptitude by Incorporating α-MnO_2 Nanorods in Cu-MOF/rGO/CuO Hybrids: Electrochemical Sensing of Resorcinol for Practical Applications. *ACS Appl. Mater. Inter.* 13 (27), 31462–31473. doi:10.1021/acsami.1c07067

Jiang, M., Xu, S., Yu, Y., Gao, Y., Yin, Z., Li, J., et al. (2022). Turn-on Fluorescence Ferrous Ions Detection Based on MnO_2 Nanosheets Modified Upconverion Nanoparticles. *Spectrochimica Acta Part A: Mol. Biomol. Spectrosc.* 264, 120275. doi:10.1016/j.saa.2021.120275

Jiang, P., Li, S., Han, M., Liu, Y., and Chen, Z. (2019). Biocompatible Ag_2S Quantum Dots for Highly Sensitive Detection of Copper Ions. *Analyst* 144 (8), 2604–2610. doi:10.1039/c9an00096h

Khan, N., Jeong, I. S., Hwang, I. M., Kim, J. S., Choi, S. H., Nho, E. Y., et al. (2014). Analysis of Minor and Trace Elements in Milk and Yogurts by Inductively Coupled Plasma-Mass Spectrometry (ICP-MS). *Food Chem.* 147, 220–224. doi:10.1016/j.foodchem.2013.09.147

Kuo, C.-C., Lan, W.-J., and Chen, C.-H. (2014). Redox Preparation of Mixed-Valence Cobalt Manganese Oxide Nanostructured Materials: Highly Efficient Noble Metal-free Electrocatalysts for Sensing Hydrogen Peroxide. *Nanoscale* 6, 334–341. doi:10.1039/c3nr03791f

Lan, G.-Y., Huang, C.-C., and Chang, H.-T. (2010). Silver Nanoclusters as Fluorescent Probes for Selective and Sensitive Detection of Copper Ions. *Chem. Commun.* 46 (8), 1257–1259. doi:10.1039/b920783j

Lee, S., Barin, G., Ackerman, C. M., Muchenditsi, A., Xu, J., Reimer, J. A., et al. (2016). Copper Capture in a Thioether-Functionalized Porous Polymer Applied to the Detection of Wilson's Disease. *J. Am. Chem. Soc.* 138, 7603–7609. doi:10.1021/jacs.6b02515

Li, L., Yuan, Z., Peng, X., Li, L., He, J., and Zhang, Y. (2014). Highly Selective Colorimetric Detection of Copper Ions Using Cysteamine Functionalized Gold Nanoparticles. *J. Chin. Chem. Soc* 61 (12), 1371–1376. doi:10.1002/jccs.201400188

Lima, G. F., Ohara, M. O., Clausen, D. N., Nascimento, D. R., Ribeiro, E. S., Segatelli, M. G., et al. (2012). Flow Injection On-Line Minicolumn Preconcentration and Determination of Trace Copper Ions Using an Alumina/Titanium Oxide Grafted Silica Matrix and FAAS. *Microchim. Acta* 178 (1-2), 61–70. doi:10.1007/s00604-012-0807-4

Lin, Y., Zhao, M., Guo, Y., Ma, X., Luo, F., Guo, L., et al. (2016). Multicolor Colormetric Biosensor for the Determination of Glucose Based on the Etching of Gold Nanorods. *Sci. Rep.* 6 (1), 37879. doi:10.1038/srep37879

Liu, J., Meng, L., Fei, Z., Dyson, P. J., Jing, X., and Liu, X. (2017). MnO_2 Nanosheets as an Artificial Enzyme to Mimic Oxidase for Rapid and Sensitive Detection of Glutathione. *Biosens. Bioelectron.* 90, 69–74. doi:10.1016/j.bios.2016.11.046

Liu, X., Wang, Q., Zhao, H., Zhang, L., Su, Y., and Lv, Y. (2012). BSA-templated MnO_2 Nanoparticles as Both Peroxidase and Oxidase Mimics. *Analyst* 137 (19), 4552–4558. doi:10.1039/c2an35700c

Luo, L., Su, Z., Zhuo, J., Huang, L., Nian, Y., Su, L., et al. (2020). Copper-Sensitized "Turn on" Peroxidase-like Activity of $MMoO_4$ (M = Co, Ni) Flowers for Selective Detection of Aquatic Copper Ions. *ACS Sust. Chem. Eng.* 8 (33), 12568–12576. doi:10.1021/acssuschemeng.0c03822

Lv, J., Zhang, C., Wang, S., Li, M., and Guo, W. (2021). MOF-derived Porous ZnO-Co_3O_4 Nanocages as Peroxidase Mimics for Colorimetric Detection of Copper(ii) Ions in Serum. *Analyst* 146 (2), 605–611. doi:10.1039/d0an01383h

Ma, Y.-r., Niu, H.-y., Zhang, X.-l., and Cai, Y.-q. (2011). Colorimetric Detection of Copper Ions in Tap Water during the Synthesis of Silver/Dopamine Nanoparticles. *Chem. Commun.* 47 (47), 12643–12645. doi:10.1039/c1cc15048k

Saha, S., and Pal, A. (2014). Microporous Assembly of MnO_2 Nanosheets for Malachite green Degradation. *Sep. Purif. Tech.* 134, 26–36. doi:10.1016/j.seppur.2014.07.021

Scheiber, I., Dringen, R., and Mercer, J. F. B. (2013). Copper: Effects of Deficiency and Overload. *Met. Ions Life* 13, 359–387. doi:10.1007/978-94-007-7500-8_11

Sheng, E., Lu, Y., Tan, Y., Xiao, Y., Li, Z., and Dai, Z. (2020). Oxidase-mimicking Activity of Ultrathin MnO2 Nanosheets in a Colorimetric Assay of Chlorothalonil in Food Samples. *Food Chem.* 331, 127090. doi:10.1016/j.foodchem.2020.127090

Su, S., Mo, Z., Tan, G., Wen, H., Chen, X., and Hakeem, D. A. (2021). PAA Modified Upconversion Nanoparticles for Highly Selective and Sensitive Detection of Cu^{2+} Ions. *Front. Chem.* 8, 619764. doi:10.3389/fchem.2020.619764

Tang, S., Wang, M., Li, Z., Tong, P., Chen, Q., Li, G., et al. (2017). A Novel Sensitive Colorimetric Sensor for Cu^{2+} Based on *In Situ* Formation of Fluorescent Quantum Dots with Photocatalytic Activity. *Biosens. Bioelectron.* 89, 866–870. doi:10.1016/j.bios.2016.09.105

U.S.E.P. Agency (2012). *Edition of the Drinking Water Standards and Health Advisories*.

Wang, H.-B., Chen, Y., Li, Y., and Liu, Y.-M. (2016). A Sensitive Fluorescence Sensor for Glutathione Detection Based on MnO_2 Nanosheets-Copper Nanoclusters Composites. *RSC Adv.* 6 (83), 79526–79532. doi:10.1039/c6ra17850b

Wang, S., Wang, L., Xu, X., Li, X., and Jiang, W. (2019a). MnO_2 Nanosheet-Mediated Ratiometric Fluorescence Biosensor for MicroRNA Detection and Imaging in Living Cells. *Analytica Chim. Acta* 1063, 152–158. doi:10.1016/j.aca.2019.02.049

Wang, X., Feng, S., He, D., and Jiang, P. (2020). Porous Manganese-Cobalt Oxide Microspheres with Tunable Oxidase Mimicking Activity for Sulfide Ion Colorimetric Detection. *Chem. Commun.* 56 (90), 14098–14101. doi:10.1039/d0cc06209j

Wang, X., Liu, G., Qi, Y., Yuan, Y., Gao, J., Luo, X., et al. (2019b). Embedded Au Nanoparticles-Based Ratiometric Electrochemical Sensing Strategy for Sensitive and Reliable Detection of Copper Ions. *Anal. Chem.* 91 (18), 12006–12013. doi:10.1021/acs.analchem.9b02945

Wang, Y.-F., Pan, N., and Peng, C.-F. (2017). A Highly Sensitive Colorimetric Method for Copper Ions Detection Based on Controlling the Peroxidase-like Activity of Au@Pt Nanocatalysts. *Anal. Sci.* 33 (3), 321–325. doi:10.2116/analsci.33.321

Weng, Z., Wang, H., Vongsvivut, J., Li, R., Glushenkov, A. M., He, J., et al. (2013). Self-Assembly of Core-Satellite Gold Nanoparticles for Colorimetric Detection of Copper Ions. *Analytica Chim. Acta* 803, 128–134. doi:10.1016/j.aca.2013.09.036

Xia, Y., Chen, T., Zhang, L., Zhang, X., Shi, W., Chen, G., et al. (2021). Colorimetric Detection of Exosomal MicroRNA through Switching the Visible-Light-Induced Oxidase Mimic Activity of Acridone Derivate. *Biosens. Bioelectron.* 173, 112834. doi:10.1016/j.bios.2020.112834

Xu, Y.-L., Niu, X.-Y., Chen, H.-L., Zhao, S.-G., and Chen, X.-G. (2017). Switch-on Fluorescence Sensor for Ascorbic Acid Detection Based on MoS_2 Quantum Dots-MnO_2 Nanosheets System and its Application in Fruit Samples. *Chin. Chem. Lett.* 28 (2), 338–344. doi:10.1016/j.cclet.2016.10.003

Yan, X., Song, Y., Wu, X., Zhu, C., Su, X., Du, D., et al. (2017). Oxidase-mimicking Activity of Ultrathin MnO_2 nanosheets in Colorimetric Assay of Acetylcholinesterase Activity. *Nanoscale* 9 (6), 2317–2323. doi:10.1039/c6nr08473g

Ye, Z., Li, L., Zhao, F., Yang, Q., Wang, Y., Bohinc, K., et al. (2020). Dual-Emission Fluorescent Probe Templated by Spherical Polyelectrolyte Brush for Ratiometric Detection of Copper Ions. *J. Mater. Sci.* 55, 10168–10184. doi:10.1007/s10853-020-04757-6

Yin, K., Li, B., Wang, X., Zhang, W., and Chen, L. (2015). Ultrasensitive Colorimetric Detection of Cu^{2+} Ion Based on Catalytic Oxidation of L-Cysteine. *Biosens. Bioelectron.* 64, 81–87. doi:10.1016/j.bios.2014.08.058

Zhang, J., Chen, M.-Y., Bai, C.-B., Qiao, R., Wei, B., Zhang, L., et al. (2020). A Coumarin-Based Fluorescent Probe for Ratiometric Detection of Cu^{2+} and its Application in Bioimaging. *Front. Chem.* 8, 800. doi:10.3389/fchem.2020.00800

Zhang, S., Yu, T., Sun, M., Yu, H., Zhang, Z., Wang, S., et al. (2014). Highly Sensitive and Selective Fluorescence Detection of Copper (II) Ion Based on Multi-Ligand Metal Chelation. *Talanta* 126, 185–190. doi:10.1016/j.talanta.2014.03.076

Zhou, X., Wu, X., He, H., Liang, H., Yang, X., Nie, J., et al. (2020). Contrast-Enhancing Fluorescence Detection of Copper Ions by Functional Fluorescent Microgels. *Sensors Actuators B: Chem.* 320, 128328. doi:10.1016/j.snb.2020.128328

Zhu, R., Zhou, G., Tang, F., Tong, C., Wang, Y., and Wang, J. (2017). Detection of Cu^{2+} in Water Based on Histidine-Gold Labeled Multiwalled Carbon Nanotube Electrochemical Sensor. *Int. J. Anal. Chem.* 2017, 1–8. doi:10.1155/2017/1727126

Conflict of Interest: The authors declare that the research was conducted in the absence of any commercial or financial relationships that could be construed as a potential conflict of interest.

frontiers in Chemistry

ORIGINAL RESEARCH
published: 25 January 2022
doi: 10.3389/fchem.2021.805205

Fluorescent Copper Nanomaterials for Sensing NO_2^- and Temperature

Ning Wang[1], Lu Ga[2], Jun Ai[1] and Yong Wang[3]*

[1]Inner Mongolian Key Laboratory of Environmental Chemistry, College of Chemistry and Environmental Science, Inner Mongolia Normal University, Hohhot, China, [2]School of Pharmacy, Inner Mongolia Medical University, Hohhot, China, [3]College of Geographical Science, Inner Mongolia Normal University, Hohhot, China

In this work, highly fluorescent copper nanomaterials were synthesized by using ascorbic acid as a ligand. The excitation wavelength of copper nanomaterials is 367 nm, and the emission wavelength is 420 nm. The size range is 5–6 nm. Nitrite can selectively quench the fluorescence of copper nanomaterials. Therefore, copper nanomaterials can be used to selectively detect nitrite ions. The linear equation is $F = -32.94\ c\ (NO_2^-) + 8{,}455$, and the correlation coefficient is 0.9435. At the same time, we found that the fluorescence intensity of copper nanomaterials has a good correlation with temperature (20–60°C), which shows that they have great potential in the application of nanothermometers.

Keywords: CuNPs, nitrite, temperature detection, nanomaterial, fluorescence

INTRODUCTION

Nitrite, as a food additive and soil raw material, widely exists in food and environment. But excessive nitrite in actual water will cause serious harm to public health and environment (Davis and Compton, 2000; Kroupova et al., 2008; Wang et al., 2009; Zhao and Li, 2020; Jahan et al., 2021). When the concentration of nitrite is higher than 4.5 mg/ml (Iii and Finke, 1999), it will damage the nervous system, spleen, and kidney of human beings and even leads to a high risk of cancer. Therefore, accurate detection of nitrite in drinking water sources, wastewater treatment systems, the food industry, and environment is of great significance.

In recent years, copper nanoparticles with high fluorescence have been widely used in biomedicine (Zhang et al., 2018), bioimaging (Satyvaldiev et al., 2018), environmental detection (Zhong et al., 2015; Li et al., 2018), catalysis (Wang et al., 2019), and other fields due to their excellent photoelectric properties, great biocompatibility, good stability, and low toxicity. Wang's group reported that copper nanoclusters were synthesized using glutathione as stabilizer and ascorbic acid as reductant, and they detected nitrite ions by utilizing the quenching fluorescence effect (Zhou et al., 2017). The method has been successfully applied to the detection of nitrite ions in actual water samples. Li's group reported that copper nanomaterials were synthesized using cysteine (Li et al., 2015; Ashraf et al., 2019; Aziz et al., 2019; Ashraf et al., 2020; Ashraf et al., 2021; Iftikhar et al., 2021). Based on the aggregation induction (AIE) of copper nanoclusters induced by sulfur ions, they established a fluorescence analysis method for the determination of hydrogen sulfide. It was applied to the detection of practical samples. Current analytical challenges faced by researchers in carrying out nitrite detection and temperature sensing are that the methods used are not suitable for online monitoring and in-site detection as they require fine instruments and complicated sample pretreatment. Therefore, fluorescence sensing has emerged as a tempting analytical method, as it does not require expensive instruments and involves a simple pretreatment procedure. Herein, copper nanomaterials were selected because the synthesis cost of copper nanomaterials is low and the fluorescence signal is good.

Edited by:
Muhammad Asif,
Wuhan Institute of Technology, China

Reviewed by:
Ayesha Aziz,
Huazhong University of Science and Technology, China
Muhammad Wajid Ullah,
Jiangsu University, China

***Correspondence:**
Jun Ai
imacaj01@163.com

Specialty section:
This article was submitted to Analytical Chemistry, a section of the journal Frontiers in Chemistry

Received: 30 October 2021
Accepted: 16 December 2021
Published: 25 January 2022

Citation:
Wang N, Ga L, Ai J and Wang Y (2022) Fluorescent Copper Nanomaterials for Sensing NO_2^- and Temperature. Front. Chem. 9:805205. doi: 10.3389/fchem.2021.805205

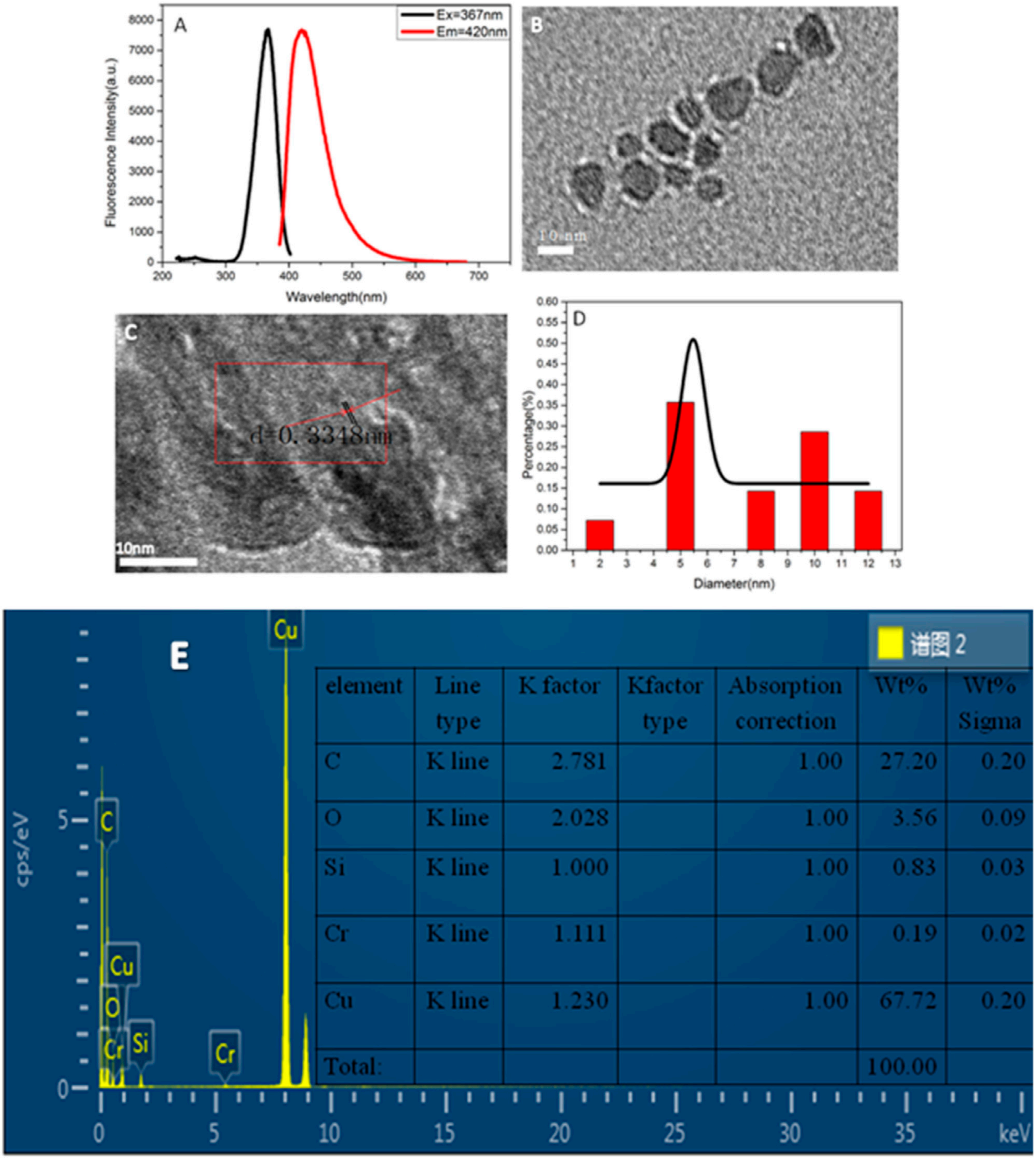

element	Line type	K factor	Kfactor type	Absorption correction	Wt%	Wt% Sigma
C	K line	2.781		1.00	27.20	0.20
O	K line	2.028		1.00	3.56	0.09
Si	K line	1.000		1.00	0.83	0.03
Cr	K line	1.111		1.00	0.19	0.02
Cu	K line	1.230		1.00	67.72	0.20
Total:					100.00	

FIGURE 1 | (A) Fluorescence spectra of copper nanomaterials; **(B)** TEM image of copper nanomaterials; **(C)** HRTEM image of copper nanomaterials; **(D)** size distribution histogram of copper nanomaterials; **(E)** ED image of CuNPs.

In this study, highly fluorescent copper nanomaterials were synthesized with ascorbic acid as a protective and reducing agent. Nitrite ions can effectively quench the fluorescence of copper nanomaterials and realize the detection of nitrite ions. As the synthesized copper nanomaterials have good temperature sensitivity, they can also be used as temperature sensors. The fluorescence intensity of copper nanomaterials is linear at different temperatures. Therefore, the synthesized copper nanomaterials have great potential in ion sensing, detection, and drug delivery.

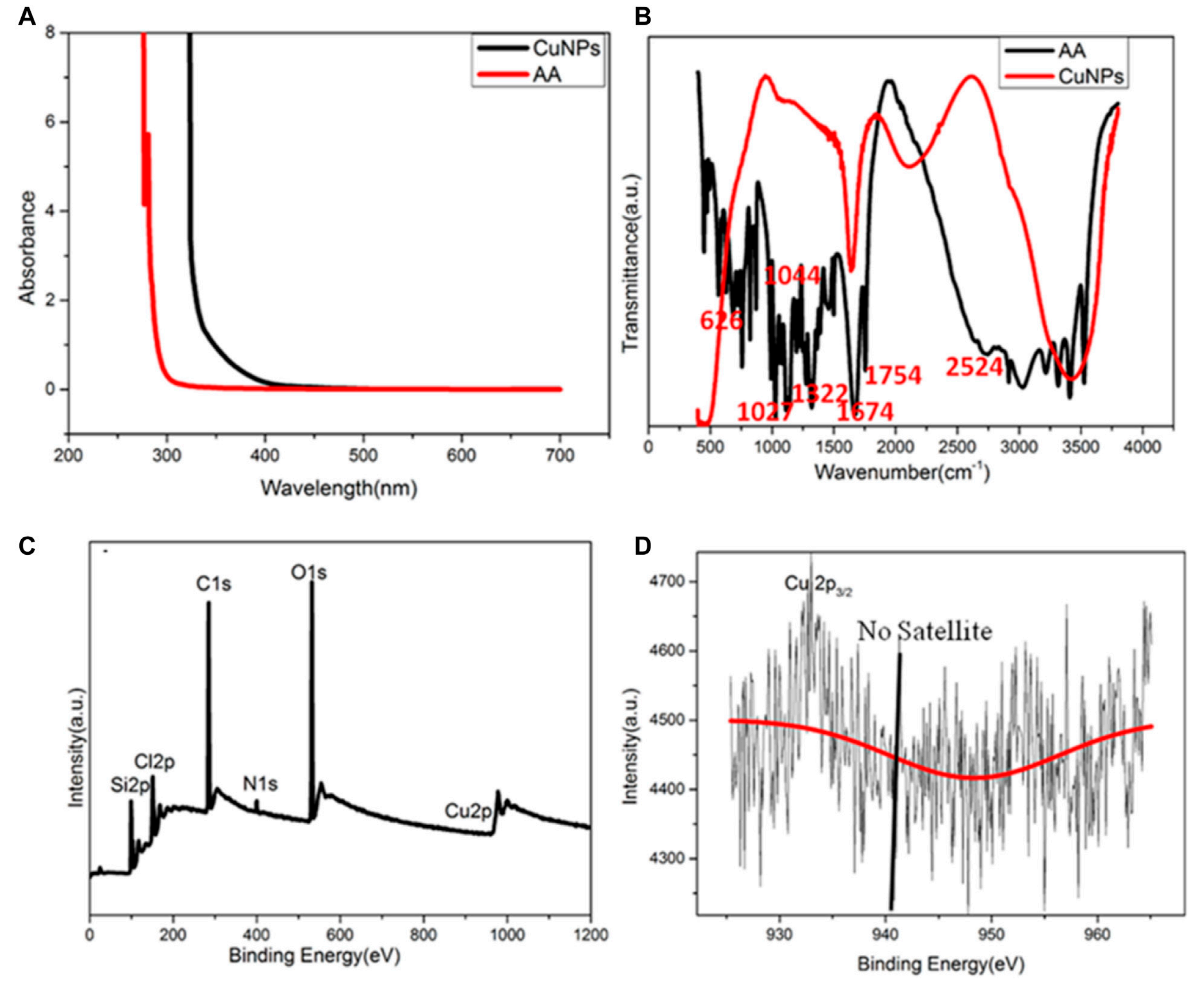

FIGURE 2 | (A) UV–vis spectra of CuNPs and AA; **(B)** FT-IR spectra of CuNPs and AA; **(C)** XPS of CuNPs thus obtained; **(D)** amplified XPS of Cu 2p electrons.

INSTRUMENT, REAGENT, AND EXPERIMENTAL SECTION

Instrumentation

Fluorescence spectrogram was obtained by using an F-4600 fluorescence spectrophotometer (Hitachi High Tech. Company). Transmission electron microscope (TEM) signals were obtained by a JEOL-2100F transmission electron microscope (Japan) operating at a voltage of 200 kV. TEM sample characterization was carried out by dropping the sample in a carbon-coated copper mesh dispersion solution and drying at room temperature. An ESCALAB-250-XI X-ray photoelectron spectroscopy (XPS) analyzer was used (Thermo Fischer Scientific).

Chemical Reagent

Ascorbic acid ($C_6H_8O_6$); $Cu(NO_3)_2{\cdot}3H_2O$; $ZnSO_4{\cdot}7H_2O$; $Pb(NO_3)_2$ (analytically pure, Tianjin Wind Ship Chemical Reagent Technology Co., Ltd.); $Bi(NO_3)_3{\cdot}3H_2O$; $AgNO_3$ (analytically pure, Beijing Fuchen Chemical Reagents Co., Ltd.); $FeCl_2{\cdot}4H_2O$ (analytically pure, Beijing Shle Chemical Plant); $MnSO_4{\cdot}H_2O$ (analytically pure, Beijing Chaoyang District Chemical Four Plant); $Ni(NO_3)_2{\cdot}6H_2O$ (analytically pure, Beijing 5671 Chemical Plant); $Al(NO_3)_3{\cdot}9H_2O$ (analytically pure, Tian Jin Bo Di Chemical Co., Ltd.); sodium citrate (analytically pure, Tian Jin Public and Private Joint Chemical Reagent First Plant); $Cd(NO_3)_2$ (analytically pure, Beijing Chemical Co., Ltd.); $CoCl_2{\bullet}6H_2O$ (analytically pure, Shang Hai Public and Private Joint Venture Factory); NaF (Beijing Public and Private Chemical Plant); NaCl, $Na_2S_2O_3{\cdot}5H_2O$, and KCl (Tian Jin North Union Fine Chemicals Development Co., Ltd.); $AgNO_3$ (Beijing Fuzhou Chemical Reagents Co., Ltd.); $NaNO_2$ (Tianjin Public and Private Chemical Reagents First Plant); NaBr and NH_4Cl (Tian Jin People Chemical Plant); $Na_2SiO_3.9H_2O$ (Beijing Yizhuang Middle School Chemical Plant); and water used in all experiments is ultra-pure water with a resistance of 18.25 MΩ.

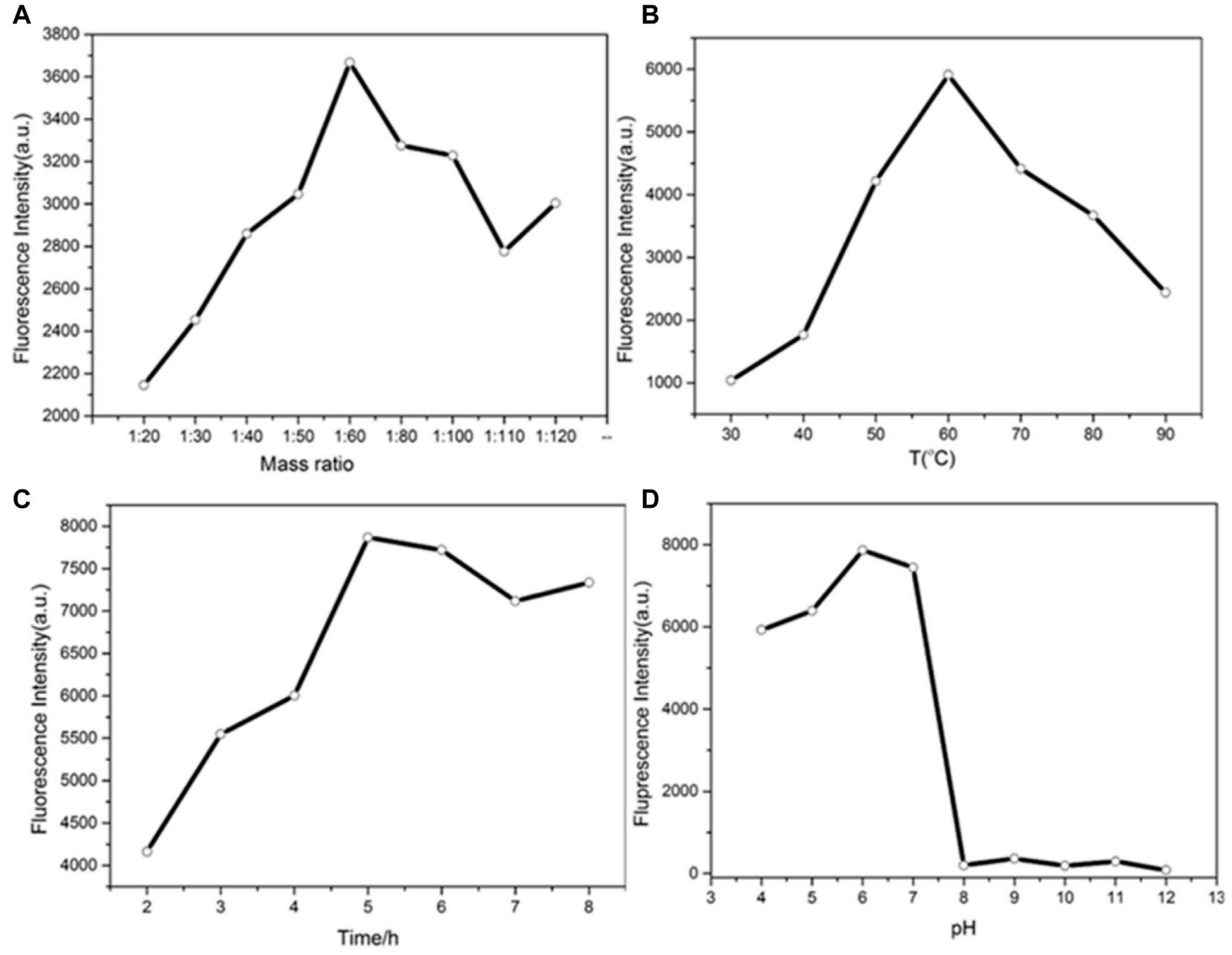

FIGURE 3 | (A) Determination of the mass ratio of the synthesized CuNPs; **(B)** temperature of the synthesized CuNPs; **(C)** time of CuNP synthesis; **(D)** pH of CuNP synthesis.

Synthesis of CuNPs

The specific method for synthesizing copper nanomaterials is as follows: first, 0.5 ml of 1 mmol/L copper nitrate solution and 3 ml of 10 mmol/L ascorbic acid solution were mixed and stirred for 20 min. Then 10 mmol/L sodium hydroxide solution was used to adjust the pH of the mixed solution to 6. After that, the solution was transferred to a 60°C constant temperature water bath for 5 h. Finally, after centrifugation, the supernatant of copper nanomaterials was preserved at 4°C for later use.

Detection of NO_2^-

Of the prepared copper nanoparticles, 450 ml was placed in 1.5-ml centrifuge tubes, and then 50 ml of nitrite solution was added at different concentrations to the centrifuge tubes. The fluorescence intensity was measured at 365 nm after 40 min reaction at room temperature.

Copper Nanomaterials for Temperature Sensing

The copper nanomaterial solution was placed in 1.5-ml centrifuge tubes. The tubes were heated at different temperatures for 20 min, and then the fluorescence intensities of the solutions were measured with a fluorescence spectrophotometer.

RESULTS AND DISCUSSION

Characterization of Copper Nanomaterials

Figure 1A shows the excitation and emission spectra of copper nanomaterials. It demonstrates that the synthesized copper nanomaterials have a strong fluorescence signal, and the maximum emission wavelength is 420 nm. The copper nanomaterials were dropped on the nickel mesh of the carbon support. The samples were dried and tested by TEM and energy dispersive spectroscopy (EDS). The morphology of the prepared copper nanomaterials was characterized by TEM (**Figure 1B**). As shown in **Figure 1B**, the copper nanomaterials are uniformly dispersed and have a smaller particle size. **Figure 1C** presents a high-resolution transmission electron microscopy (HRTEM) image. The crystal lattice of d = 0.3348 nm corresponding to the face-centered cubic structure (110) of copper can be clearly seen. **Figure 1D** indicates that the particle size distribution of the

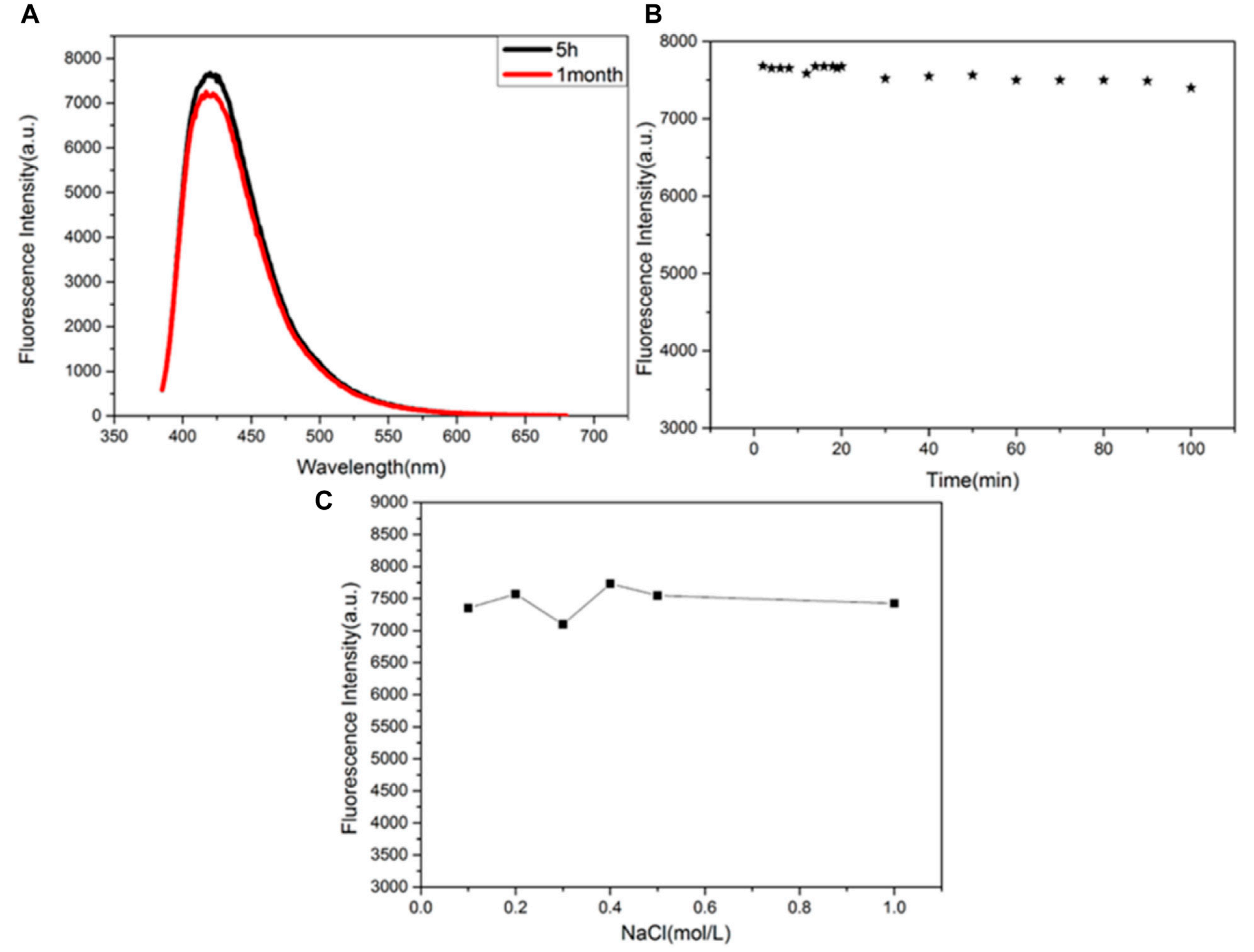

FIGURE 4 | (A) Storage time; **(B)** irradiation time; **(C)** effects of the concentration of NaCl solution on the fluorescence intensity of the CuNPs.

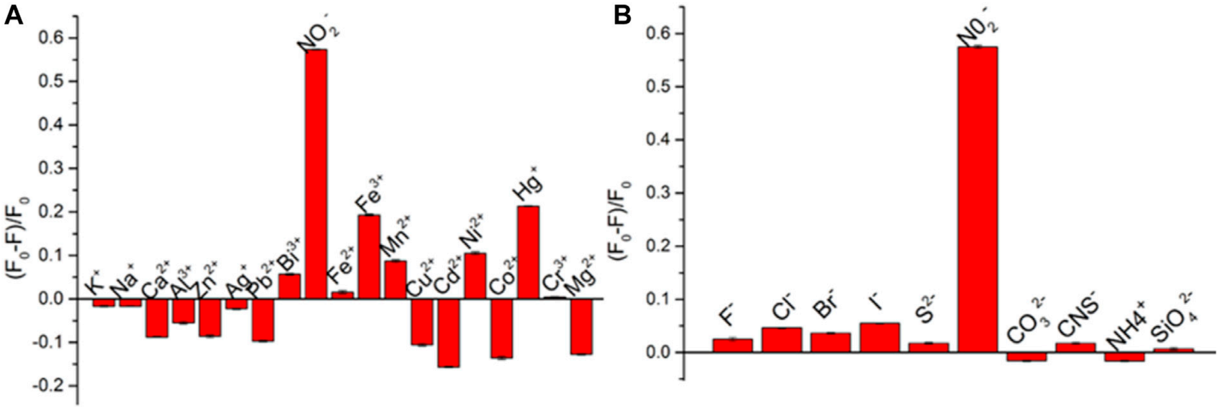

FIGURE 5 | Selectivity of CuNPs toward I^- sensing over other common metal ions **(A)** and anions **(B)**. The concentration of all metal ions is 100 μmol/L.

copper nanomaterials is uniform, and the average diameter of the copper nanomaterials is in the range of 5.0 ± 0.1 nm. The EDS image and the elemental contents in the copper nanomaterials are presented in **Figure 1E**. The percentage of copper was 67.72%. The results indicated that the synthesized copper nanomaterials have the characteristics of good fluorescence, uniform dispersion, and

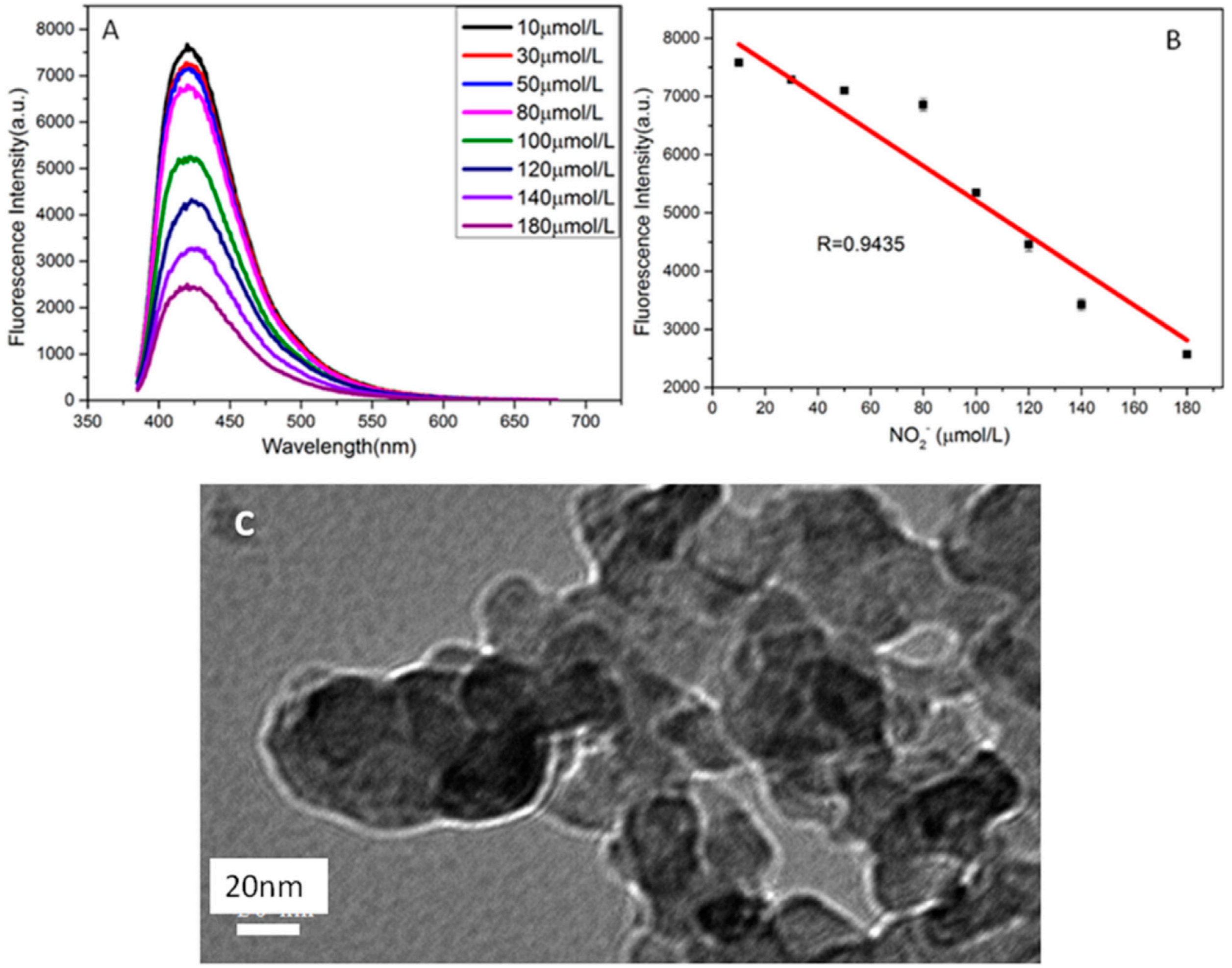

FIGURE 6 | (A) Fluorescence spectra of CuNPs obtained with different concentrations of NO_2^- (from top to bottom: 10, 30, 50, 80, 100, 120, 1,400, and 180 μmol/L, respectively); **(B)** relationship between F and the concentration of NO_2^-; **(C)** TEM of copper nanomaterials after adding NO_2^-.

small particle size, which indicates that highlyfluorescent copper nanomaterials have been successfully synthesized.

The chemical and surface properties of the copper nanoparticles were analyzed by ultraviolet-visible (UV) spectroscopy and Fourier transform infrared (FT-IR) spectroscopy. **Figure 2A** shows the ultraviolet absorption spectra of CuNPs and ascorbic acid. There is no obvious absorption peak of ascorbic acid but a small ultraviolet absorption peak of CuNPs near 340 nm, which corresponds to the fluorescence excitation wavelength of copper nanomaterials. **Figure 2B** exhibits the infrared spectra of the copper nanomaterials and ascorbic acid, which can broaden the characteristic peaks of CuNPs. The shrinkage vibration peak of 2,524 cm^{-1} belonging to -OH has disappeared in the copper nanomaterials, which proves that glutathione molecules bond to the surface of copper nanomaterials through Cu-O. The characteristic peaks of ascorbic acid did not appear, which proves that the ligand exchange was complete.

XPS was used to characterize the valence state of copper in CuNPs. The full spectrum indicated that CuNPs consist of C, O, N, Si, and Cu (**Figure 2C**). **Figure 2D** shows that no satellite peaks appear, which means that no Cu^{2+} exists. The strong peak of 932.3 eV belongs to zero-valent copper's 2p3/2, and this is consistent with previous literature reports (Koski et al., 2012). However, it should be noted that the binding energy of 2p3/2 of Cu(0) is similar to that of Cu(I). Due to the charge transfer of the Cu-O bond, the valence state of Cu nanomaterials may be between 0 and +1.

Optimization of Experimental Synthesis Conditions

The synthesis time, temperature, molar ratio, and pH were optimized. By adjusting the molar ratio of copper nitrate to ascorbic acid, the appropriate drug dosage for the synthesis of copper nanomaterials was determined. As shown in **Figure 3A**, when the molar ratio of copper nitrate to ascorbic acid is 1:60, the fluorescence intensity of copper nanomaterials is higher. Therefore, the best molar ratio is 1:60. **Figure 3B** shows the effect of synthesis temperature on fluorescence intensities. When the temperature was changed from 30 to 90°C, the fluorescence intensities of CuNPs first increased and then decreased. The fluorescence intensity of

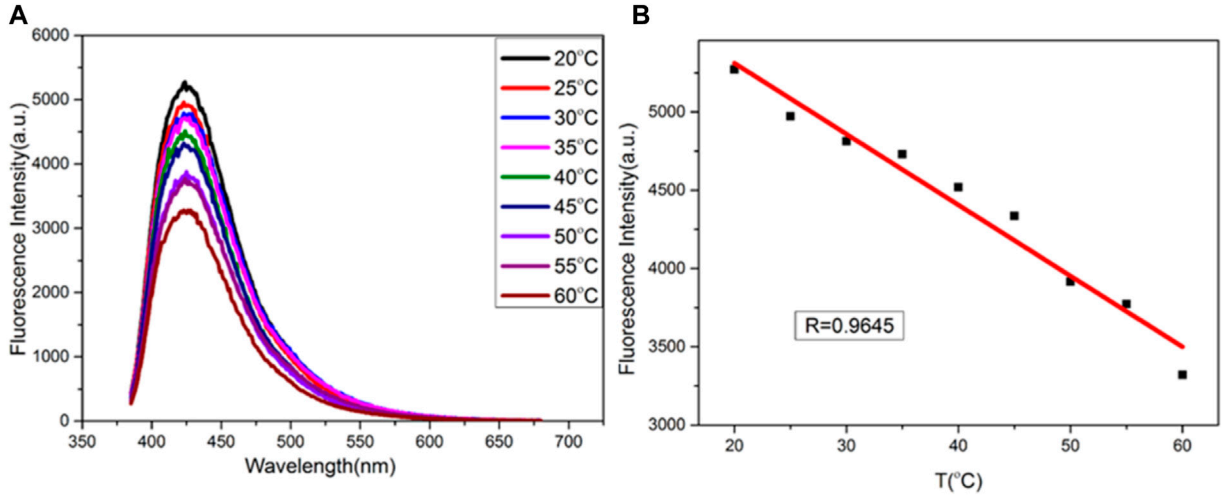

FIGURE 7 | (A) Fluorescence spectra of CuNPs obtained at different temperatures (from top to bottom: 20, 25, 30, 35, 40, 45, 50, 55, and 60°C, respectively); **(B)** relationship between F and temperature.

CuNPs was the highest at 60°C. Therefore, the optimal synthesis temperature of copper nanomaterials is 60°C. **Figures 3C,D** show the optimum time and pH data for the synthesis of copper nanomaterials. With the increase in time, the fluorescence intensity of copper nanomaterials increases. When the synthesis time is set to 5 h, the fluorescence intensity is the highest (**Figure 3C**). Therefore, the optimal synthesis time of copper nanomaterials is 5 h. As shown in **Figure 3D**, the fluorescence intensity of copper nanomaterials is the highest at pH 6. Therefore, we chose pH 6 as the best condition. Here, we synthesized CuNPs under the above optimum conditions.

Stability of CuNPs

The stability of the synthesized CuNPs was evaluated by comparing the fluorescence intensities of CuNPs stored for different periods and at different conditions (**Figure 4**). **Figure 4A** shows that the fluorescence intensity of the synthesized CuNPs measured at 5 h and 1 month after storage remains basically unchanged. It is concluded that CuNPs can be preserved for 1 month at 4°C. The fluorescence intensities of CuNPs were almost unchanged when the CuNPs were exposed to a xenon lamp for 100 min (**Figure 4B**). **Figure 4C** depicts the effect of different concentrations of NaCl solutions on the stability of CuNPs. It was found that the fluorescence intensity of copper nanomaterials was independent of the concentration of NaCl solution (up to 1 mol/L). These results indicate that the nanomaterials have good storage and fluorescence stability.

Selectivity

To further investigate the selectivity of this method, contrast experiments were performed using 18 metal cations (K^+, Na^+, Ca^{2+}, Hg^+, Cr^{3+}, Fe^{3+}, Pb^{2+}, and Bi^{3+}) and 10 inorganic anions (F^-, Cl^-, Br^-, I^-, S^{2-}, and NO_2^-) as the interference for detection of nitrite ions at the concentration of interference are 100 μmol/L. As shown in **Figure 5**, only nitrite ions show a strong quenching effect on the fluorescence of CuNPs. While Cd^{2+}, Fe^{3+}, and Hg^+ have little effect on the fluorescence of CuNPs, other ions have no obvious effect on it. All these results indicate that this method possesses good selectivity for nitrite ion detection.

Detection of NO_2^-

Based on the quenching effect of nitrite ions on the fluorescence of CuNPs, we established a fluorescence quenching sensor for accurate detection of nitrite ions. **Figure 6A** indicates that the fluorescence intensities of copper nanomaterials decrease with the increasing concentration of nitrite ions. **Figure 6B** shows a good linear relationship between the quenching fluorescence intensities of CuNPs and nitrite concentration in the range of 10 μ M–180 μ M. The linear equation is F = −32.94 c (NO_2^-) + 8,455, and the correlation coefficient is 0.9435. **Figure 6C** shows the TEM image of CuNPs after adding NO_2^-. It demonstrates that the fluorescence quenching is caused by the aggregation of nanomaterials because of the interaction between the surface ligand (ascorbic acid) of CuNPs and NO_2^-. The results are basically consistent with previous reports. Nitrite is a kind of food additive and is used for its coloring and antiseptic properties. It is widely used in cooked meat and canned animal food and is also used as an enema agent. Nitrite is not only a carcinogen but can also cause food poisoning when ingested at 0.2–0.5 g and can cause death at 3 g. Accurate detection of the nitrite content in food online is a key problem.

Temperature Sensing

A temperature-sensitive sensor based on copper nanomaterials was studied. As shown in **Figure 7A**, the fluorescence intensity of copper nanomaterials varies with temperature, from 20°C to 60°C. There is a good linear relationship between fluorescence intensity and temperature. The calibration equation is F = − 42.62T + 7,200, and the correlation coefficient is 0.9645 (as shown in **Figure 7B**). Therefore, the synthesized copper nanomaterial shows great potential in the application of nanothermometers.

CONCLUSION

In summary, we synthesized a new kind of copper nanomaterial using ascorbic acid as both protectant and reductant. Nitrite ions can selectively quench the fluorescence of copper nanomaterials. Based on the fluorescence quenching mechanism, a sensor for detecting nitrite ions was established. We also found that there is a linear relationship between fluorescence signal and temperature in the temperature range of 20–60°C. Therefore, our new copper nanomaterials show great potential in the application of nanothermometers.

DATA AVAILABILITY STATEMENT

The original contributions presented in the study are included in the article/Supplementary Material; further inquiries can be directed to the corresponding author.

AUTHOR CONTRIBUTIONS

NW: synthesis; LG: characterization; and JA: drafting and writing the manuscript.

FUNDING

This work was supported by the National Natural Science Foundation of China (Grant Nos 21864020 and 51503106); the Natural Science Foundation of Inner Mongolia (Grant No. 2018MS02012); the Collaborative Innovation Center for Water Environmental Security of Inner Mongolia Autonomous Region, China (Grant No. XTCX003); and the Inner Mongolia Innovation Guide Project and Research Project of Higher School, Department of Education of Inner Mongolia Autonomous Region (Grant No. NJZC16047).

REFERENCES

Ashraf, G., Asif, M., Aziz, A., Dao, A. Q., Zhang, T., Iftikhar, T., et al. (2020). Facet-energy Inspired Metal Oxide Extended Hexapods Decorated with Graphene Quantum Dots: Sensitive Detection of Bisphenol A in Live Cells. *Nanoscale* 12 (16), 9014–9023. doi:10.1039/c9nr10944g

Ashraf, G., Asif, M., Aziz, A., Iftikhar, T., and Liu, H. (2021). Rice-Spikelet-like Copper Oxide Decorated with Platinum Stranded in the CNT Network for Electrochemical *In Vitro* Detection of Serotonin. *ACS Appl. Mater. Inter.* 13 (5), 6023–6033. doi:10.1021/acsami.0c20645

Ashraf, G., Asif, M., Aziz, A., Wang, Z., Qiu, X., Huang, Q., et al. (2019). Nanocomposites Consisting of Copper and Copper Oxide Incorporated into MoS4 Nanostructures for Sensitive Voltammetric Determination of Bisphenol A. *Microchim Acta* 186 (6), 337. doi:10.1007/s00604-019-3406-9

Aziz, A., Asif, M., Ashraf, G., Azeem, M., Majeed, I., Ajmal, M., et al. (2019). Advancements in Electrochemical Sensing of Hydrogen Peroxide, Glucose and Dopamine by Using 2D Nanoarchitectures of Layered Double Hydroxides or Metal Dichalcogenides. A Review. *Microchim Acta* 186 (10), 671. doi:10.1007/s00604-019-3776-z

Davis, J., and Compton, R. G. (2000). Sonoelectrochemically Enhanced Nitrite Detection. *Analytica Chim. Acta* 404, 241–247. doi:10.1016/s0003-2670(99)00724-2

Iftikhar, T., Xu, Y., Aziz, A., Ashraf, G., Li, G., Asif, M., et al. (2021). Tuning Electrocatalytic Aptitude by Incorporating α-MnO2 Nanorods in Cu-MOF/rGO/CuO Hybrids: Electrochemical Sensing of Resorcinol for Practical Applications. *ACS Appl. Mater. Inter.* 13 (27), 31462–31473. doi:10.1021/acsami.1c07067

Iii, J. D. A., and Finke, R. G. (1999). A Review of Modern Transition-Metal Nanoclusters: Their Synthesis, Characterization, and Applications in Catalysis. *J. Mole. Catal. Chem.* 145, 1–44. doi:10.1016/S1381-1169(99)00098-9

Jahan, I., Erci, F., and Isildak, I. (2021). Facile Microwave-Mediated green Synthesis of Non-toxic Copper Nanoparticles Using Citrus Sinensis Aqueous Fruit Extract and Their Antibacterial Potentials. *J. Drug Deliv. Sci. Technol.* 61, 102172. doi:10.1016/j.jddst.2020.102172

Koski, K. J., Cha, J. J., Reed, B. W., Wessells, C. D., Kong, D., and Cui, Y. (2012). High-Density Chemical Intercalation of Zero-Valent Copper into Bi2Se3 Nanoribbons. *J. Am. Chem. Soc.* 134, 7584–7587. doi:10.1021/ja300368x

Kroupova, H., Machova, J., Piackova, V., Blahova, J., Dobsikova, R., Novotny, L., et al. (2008). Effects of Subchronic Nitrite Exposure on Rainbow trout (*Oncorhynchus mykiss*). *Ecotoxicology Environ. Saf.* 71, 813–820. doi:10.1016/j.ecoenv.2008.01.015

Li, S., Tang, T., Chai, F., Qu, F., Wei, T., Wang, C., et al. (2018). Facile Synthesis of Bimetallic Ag-Cu Nanoparticles for Colorimetric Detection of Mercury Ion and Catalysis. *Sens. Actua. Chem.* 325, 255–260. doi:10.1016/j.snb.2017.08.159

Li, Z., Guo, S., and Lu, C. (2015). A Highly Selective Fluorescent Probe for Sulfide Ions Based on Aggregation of Cu Nanocluster Induced Emission Enhancement. *Analyst* 140, 2719–2725. doi:10.1039/c5an00017c

Satyvaldiev, A. S., Zhasnakunov, Z. K., Omurzak, E., Doolotkeldieva, T. D., Bobusheva, S. T., Orozmatova, G. T., et al. (2018). Copper Nanoparticles: Synthesis and Biological Activity. *IOP Conf. Ser. Mater. Sci. Eng.* 302, 012075. doi:10.1088/1757-899x/302/1/012075

Wang, N., Ga, L., and Ai, J. (2019). Synthesis of Novel Fluorescent Copper Nanomaterials and Their Application in Detection of Iodide Ions and Catalysis. *Anal. Methods* 11, 44–48. doi:10.1039/c8ay01871e

Wang, P., Mai, Z., Dai, Z., Li, Y., and Zou, X. (2009). Construction of Au Nanoparticles on Choline Chloride Modified Glassy Carbon Electrode for Sensitive Detection of Nitrite. *Biosens. Bioelectron.* 24, 3242–3247. doi:10.1016/j.bios.2009.04.006

Zhang, D., Hu, J., Yang, X.-y., Wu, Y., Su, W., and Zhang, C.-Y. (2018). Target-initiated Synthesis of Fluorescent Copper Nanoparticles for the Sensitive and Label-free Detection of Bleomycin. *Nanoscale* 10, 11134–11142. doi:10.1039/c8nr02780c

Zhao, Z., and Li, Y. (2020). Developing Fluorescent Copper Nanoclusters: Synthesis, Properties, and Applications. *Colloids Surf. B-Biointerfaces* 195, 111244. doi:10.1016/j.colsurfb.2020.111244

Zhong, Y., Wang, Q., He, Y., Ge, Y., and Song, G. (2015). A Novel Fluorescence and Naked Eye Sensor for Iodide in Urine Based on the Iodide Induced Oxidative Etching and Aggregation of Cu Nanoclusters. *Sensors Actuators B: Chem.* 209, 147–153. doi:10.1016/j.snb.2014.11.060

Zhou, D.-L., Huang, H., and Wang, Y. (2017). Sensitive and Selective Detection of Nitrite Ions with Highly Fluorescent Glutathione-Stabilized Copper Nanoclusters. *Anal. Methods* 9, 5668–5673. doi:10.1039/c7ay02035j

Conflict of Interest: The authors declare that the research was conducted in the absence of any commercial or financial relationships that could be construed as a potential conflict of interest.

frontiers in Chemistry

ORIGINAL RESEARCH
published: 10 February 2022
doi: 10.3389/fchem.2022.843859

Boosting the Electrochemical Performance of PI-5-CA/C-SWCNT Nanohybrid for Sensitive Detection of *E. coli* O157:H7 From the Real Sample

Huan Wang [1†], ***Yanmiao Fan*** [2†], ***Qiaoli Yang*** [1], ***Xiaoyu Sun*** [1], ***Hao Liu*** [1], ***Wei Chen*** [1], ***Ayesha Aziz*** [1]* ***and Shenqi Wang*** [1]*

[1]Advanced Biomaterials and Tissue Engineering Center, College of Life Science and Technology, Huazhong University of Life Science and Technology, Wuhan, China, [2]School of Chemical Science and Engineering Fiber and Polymer Technology, KTH Royal Institute of Technology, Stockholm, Sweden

Edited by:
Muhammad Asif,
Wuhan Institute of Technology, China

Reviewed by:
Muhammad Ajmal,
Xiamen University, China
Hongwei Liu,
Sun Yat-sen University, China

***Correspondence:**
Ayesha Aziz
anaa_meraal@yahoo.com
Shenqi Wang
shenqiwang131@hust.edu.cn

†These authors have contributed equally to this work

Specialty section:
This article was submitted to Analytical Chemistry, a section of the journal Frontiers in Chemistry

Received: *27 December 2021*
Accepted: *17 January 2022*
Published: *10 February 2022*

Citation:
Wang H, Fan Y, Yang Q, Sun X, Liu H, Chen W, Aziz A and Wang S (2022) Boosting the Electrochemical Performance of PI-5-CA/C-SWCNT Nanohybrid for Sensitive Detection of E. coli *O157:H7 From the Real Sample. Front. Chem. 10:843859. doi: 10.3389/fchem.2022.843859*

Redox activity is an important indicator for evaluating electrochemical biosensors. In this work, we have successfully polymerized indole-5-carboxylic acid into poly-5-carboxyindole nanomaterials (PI-5-CA), using its superior redox activity, and introduced carboxylated single-walled carbon nanotubes (C-SWCNTs) to synthesize a composite material. Finally, a synthesized composite material was used for the modification of the glass carbon electrode to fabricate the PI-5-CA/C-SWCNTs/GCE-based immunosensor and was successfully applied for the sensitive detection of *E. coli* O157:H7. The fabricated immunosensor exhibited an outstanding electrocatalytic activity toward the detection of *E. coli* O157:H7 with a remarkably lowest limit of detection (2.5 CFU/ml, $LOD = 3\,SD/k$, $n = 3$) and has a wide linear range from 2.98×10^1 to 2.98×10^7 CFU/ml. Inspired from the excellent results, the fabricated electrode was applied for the detection of bacteria from real samples (water samples) with a good recovery rate (98.13–107.69%) as well as an excellent stability and specificity. Owing to its simple preparation, excellent performance, and detection time within 30 min, our proposed immunosensor will open a new horizon in different fields for the sensitive detection of bacteria from real samples.

Keywords: poly-5-carboxyindole, carboxylated single-walled carbon nanotubes, *E. coli* O157:H7, electrochemical immunosensor, indole-5-carboxylic acid, plate counting method

HIGHLIGHTS

- PI-5-CA/C-SWCNT nanohybrids are synthesized by facile methods
- The PI-5-CA/C-SWCNT nanohybrid-modified GCE was further incubated with the *E. coli* antibody to complete the antigen–antibody reaction to fabricate the Ab/PI-5-CA/C-SWCNTs/GCE immunosensor
- Ab/PI-5-CA/C-SWCNTs/GCE shows an excellent electrochemical activity for *E. coli* O157 detection
- Real-time *in vitro* detection of *E. coli* O157 from real samples and compared results obtained from the actual samples

1 INTRODUCTION

To date, the most important topic of concern for food industries is the alarming increase of food- and waterborne diseases (Law et al., 2015; Patra and Baek, 2016). According to statistics from the World Health Organization (WHO), up to 30% of the world's population suffers from foodborne diseases every year (Jia and Jukes, 2013). Factors that cause foodborne diseases include bacteria, parasites, viruses, chemicals, and toxins (Aziz et al., 2021; Rad et al., 2021). Among these factors, bacterial contamination is an alarming threat to human health (Chen et al., 2017; Sai-Anand et al., 2019). Bacteria are ubiquitous in nature, and bacterial contamination may occur in any food chain (Odeyemi et al., 2020). If food chains once get infected with these pathogens, it can seriously threaten human health and can cause economic losses, if not treated timely (Asif et al., 2018). In 2011, there was an outbreak in the United States due to the contamination of cantaloupe instigated by *Listeria monocytogenes*, which infected 147 with 33 deaths (Ghosh et al., 2019). In the same year, Germany also experienced a massive outbreak of hemolytic uremic syndrome, which was initiated by *E. coli* O104:H4 infection (Stockman, 2013). Above all, every year, the number of infections caused by *Salmonella* crossed one million, leading to severe illness and sometimes death (Jarvis et al., 2016). In 2016, 13 cases of diarrhea occurred in nine U.S. states due to the consumption of flour infected with *E. coli* O157:H7 (Sperber and North American Millers' Association Microbiology Working Group, 2007). Therefore, fast and reliable detection of pathogens is essential to prevent and control the outbreaks of foodborne diseases.

Among the common pathogens in daily life, *E. coli* O157:H7 is one of the most hazardous foodborne pathogens because of its virulence and pathogenicity (Buchanan and Doyle, 1997; Zhao et al., 2021). Diseases caused by *E. coli* O157:H7 include diarrhea, fever, and vomiting (Pandey et al., 2017). At present, quite a lot of attention has been devoted to the research for the rapid detection of *E. coli* O157:H7 (Park et al., 2020) The conventionally used plate counting method is reliable to some extent but inevitably limited owing to the time-consumption (Sieuwerts et al., 2008; Zhao et al., 2014). Technological advances introduced and proposed new methods and techniques, such as polymerase chain reaction (PCR) (Amagliani et al., 2004; Zhou et al., 2022) and enzyme-linked immunosorbent assay (ELISA) (Di Febo et al., 2019; Hu Y. et al., 2021), but the requirement of high precision and accuracy as well as the need of highly professional trainers limited their use to some extent. To address all these issues related to conventional and advanced techniques, biosensors have been developed (Aziz et al., 2022). The development of biosensors can solve the abovementioned problems (Asif et al., 2019; Aziz et al., 2019b), such as colorimetry (Yao et al., 2020), fluorescence (Shi et al., 2015), and electrochemistry (Li et al., 2021). Among them, the electrochemical method has received widespread attention because of the low cost, easy handling, and portability (Asif et al., 2022).

Many electrochemical redox active materials have been used as electronic media for the development of electrochemical biosensors, such as ferrocene (Hu L. et al., 2021), graphene oxide (GO) (Aziz et al., 2019a), and Prussian blue (22). However, most of these materials suffer low conductivity and poor stability, so their effects in the field of electrochemical detection are not satisfactory (Kang et al., 2016). As a conductive polymer, poly (indole-5-carboxylic acid) (PI-5-CA) exhibits good electrochemical behavior, good thermal stability, and superior redox activity due to its abundant functional groups and specific surface area (Asif et al., 2015; Yang et al., 2019). At the same time, the introduction of carboxylated single-walled carbon nanotubes (C-SWCNTs) can further improve the specific surface area and the electrical conductivity of PI-5-CA. Due to its tubular hollow structure, carbon nanotubes have unique electrical conductivity, high strength, flexibility, stable chemical properties, and excellent specific surface area (Kumar and Sundramoorthy, 2019; Li et al., 2021). Through chemical synthesis, PI-5-CA and C-SWCNTs are synthesized into a composite material to syndicate the electrochemical advantages of the two, and using their abundant carboxyl functional groups to combine with various biological recognition molecules (Yang et al., 2019).

Therefore, we use the superior electrical conductivity of C-SWCNTs and the ultrahigh redox activity of PI-5-CA to construct an electrochemical sensing platform (Joshi and Prakash, 2013; Yang et al., 2019). At the same time, we use the characteristic of antigen-antibody-specific binding to propose an electrochemical immunosensor to detect *E. coli* O157:H7. First, the PI-5-CA/C-SWCNT composite material was synthesized for the modification of glassy carbon electrode (GCE), and the redox characteristics of the material were explored using the classic three-electrode system. By activating the carboxyl group on the surface of the material and binding with the amino group of the antibody, the anti-*E. coli* antibody is connected to the surface of the modified GCE for *E. coli* O157:H7 detection as represented by **Figure 1**. In this research work, PI-5-CA was used to provide a stable redox signal to improve the detection sensitivity (Joshi and Prakash, 2013), while C-SWCNT coupling was used to further improve stability and conductivity (Joshi and Prakash, 2013), as well as provide abundant binding sites for antibodies, which in turn ensure the detection specificity. By detecting the change of PI-5-CA redox current, the rapid and sensitive detection effect of *E. coli* O157:H7 is realized (Yang et al., 2021). We used this constructed biosensor to successfully detect *E. coli* in domestic water, and compared the results with the traditional culture method to determine the sensitivity and reliability of the fabricated sensor.

2 EXPERIMENTAL SECTIONS

2.1 Chemicals and Reagents

Indole-5-carboxylic acid (I-5-CA) was purchased from Shanghai Vita Chemical Regent Co., Ltd. (Shanghai, China). Carboxylated single-walled carbon nanotubes (C-SWCNTs) were purchased from Nanjing Xian Feng Nanomaterials Technology Co., Ltd. (Nanjing, China). N-hydroxysuccinimide (NHS) and N-(3-dimethylaminopropyl)-N′-ethylcarbodiimide hydrochloride

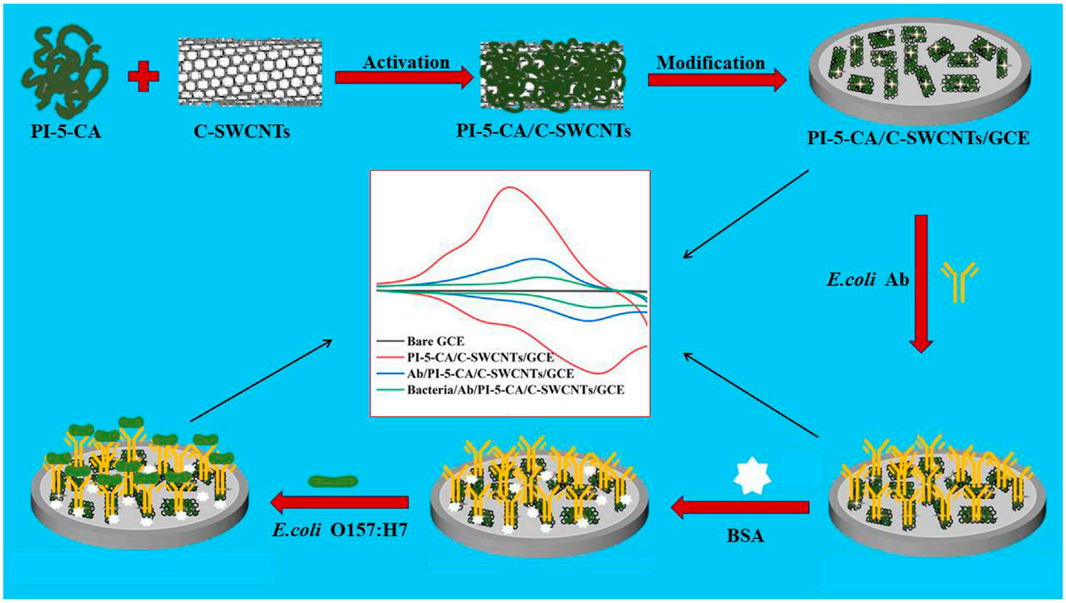

FIGURE 1 | Schematic illustration of the step-by-step preparation of PI-5-CA/C-SWCNTs/GCE and its modification with antibodies and BSA for the sensitive detection of *E. coli* O157:H7.

TABLE 1 | Information of the strains used in this work.

Bacteria	Strain number
E. coli O157:H7	CCTCC AB 200051
Staphylococcus aureus	CCTCC AB 2013186
Salmonella typhimurium	CCTCC AB 204062
Pseudomonas aeruginosa	ATCC27853

(EDC) were purchased from Aladdin Chemistry Co., Ltd. (Shanghai, China). Bovine serum albumin (BSA) and 2-morpholinoethanesulfonic acid (MES) were purchased from Sigma-Aldrich (United States). The anti-*E. coli* O157:H7 antibody was purchased from Thermo (United States). Ethanol, ammonium persulfate (APS), disodium hydrogen phosphate (Na_2HPO_4), sodium dihydrogen phosphate (NaH_2PO_4), and H_2SO_4 were purchased from Sinopharm Chemical Co., Ltd. (Shanghai, China). All the chemicals and reagents were used as it is, without further purification. The four different strains were used in this research as shown in **Table 1.**

2.2 Synthesis of PI-5-CA/C-SWCNTs

The PI-5-CA/C-SWCNT nanocomposite was synthesized by the chemical method. First, 100 mg of In-5-COOH monomer and 2 mg of carboxylated single-walled carbon nanotubes (C-SWCNTs) were dissolved in 2.5 ml of absolute ethanol, Next, 100 mg ammonium persulfate (APS) was dissolved in 10.0 ml of H_2SO_4 (pH = 1). Under constant temperature stirring, the mixed solution of 100 mg ammonium persulfate (APS) dissolved in 10 ml H_2SO_4 (pH = 1) was added gradually, and the mixture was left to react at 30°C for 6 h. After the reaction was completed, the product was filtered and washed with ultrapure water and absolute ethanol several times in sequence. Finally, we used this solid product to prepare 1 mg/ml solution in ultrapure water for further use.

2.3 Fabrication of the Electrochemical Immunosensor

Before each experiment, the glassy carbon electrode (3 mm in diameter) was polished to a mirror surface with 0.05 μM alumina powder and ultrasonically treated with ultrapure water and absolute ethanol, respectively. Finally, the cleaned electrode was dried with high-purity nitrogen for the next modification.

For the modification of electrode, 10 μL of 1 mg/ml solution of PI-5-CA/C-SWCNTs was injected onto the surface of the GCE and dried in air naturally. To activate the carboxyl group on the composite material, first, the modified electrode was immersed in a mixed solution (containing 40 mM NHS, 100 mM EDC and 100 mM MES), and then incubated at 37°C for 30 min accompanied by the subsequent deposition of 10 μL of Ab solution (5 μg/ml). After that the prepared Ab/PI-5-CA/C-SWCNTs/GCE was further incubated at 37°C for 2 h to ensure that the antibodies bind to the electrode surface. Next, 10 μL of BSA (1 mg/ml) was added dropwise onto the electrode surface and incubated at 37°C for 30 min to block the residual active sites. Finally, the prepared immunosensor was successfully used against bacterial detection and repeated the same procedure after each experiment. It is noted that after each modification, the electrode should be gently washed with PBS (pH = 6) to remove physical adsorption (26).

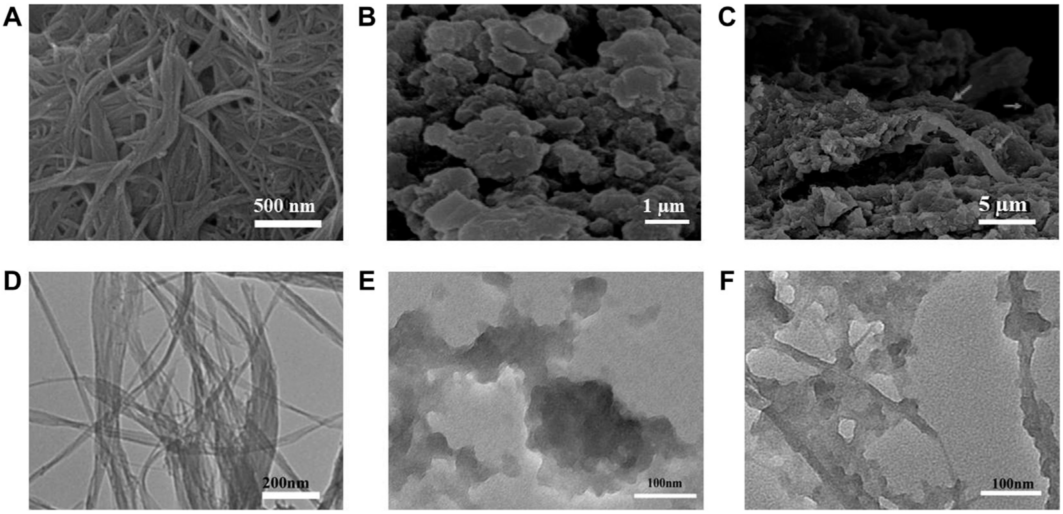

FIGURE 2 | (A–C) SEM images of C-SWCNTs, PI-5-CA, and PI-5-CA/C-SWCNTs at different magnifications, and TEM images of **(D)** C-SWCNTs, **(E)** PI-5-CA, and **(F)** PI-5-CA/C-SWCNTs.

2.4 Preparation of Samples

In order to obtain satisfactory results, pretreatment of the bacterial culture medium is necessary. The bacterial strains used in the research were inoculated into the 5 ml LB medium and cultured at 37°C and 200 rpm for 6 h to their logarithmic growth phase. After that, the freshly cultivated bacterial liquids were centrifuged and immersed in PBS to further dilute into appropriate concentrations. The sample preparation process for actual testing is as follows: first, the tap water was filtered three times with a 0.22 μM filter membrane, and then freshly cultured *E. coli* O157:H7 was added to obtain a natural sample.

2.5 Analytical Performance of the Immunosensor

First, 10 μL of the above bacterial liquid was injected to the surface of the immunosensor electrode, and it was incubated at 37°C for 2 h to complete the antigen–antibody reaction. After that, the electrode was gently washed with PBS (pH = 6) to remove the physical absorption. All electrochemical experiments were performed on a CHI660A electrochemical workstation. Throughout the electrochemical experimentation, a three-electrode system (Ag/AgCl as the reference electrode, platinum plate as the counter electrode, and modified electrode as the working electrode) was used to perform cyclic voltammetry (CV) under −0.2–0.8 V at a scanning speed of 100 mV/s to evaluate the electrode surface behavior. Throughout the experimentations, PBS (pH = 6) was used.

3 CHARACTERIZATION OF THE PI-5-CA/C-SWCNTS COMPOSITE

The surface morphologies of PI-5-CA and C-SWCNTs were initially characterized by using the transmission electron microscope (TEM) and scanning electron microscope (SEM) to observe the morphology of the three-dimensional structure of PI-5-CA/C-SWCNTs. The SEM images of PI-5-CA/C-SWCNT nanocomposite at different magnifications showed in **Figures 2A–C** formed a three-dimensional layered porous structure, which can facilitate the combination of various biorecognition molecules and improve the analytical performance of the electrochemical sensor based on PI-5-CA/C-SWCNTs. PI-5-CA exhibited a distinct aggregated morphology that was further combined with SWCNTs to form a distinct three-dimensional structure. SWCNT rods covered with aggregated PI-5-CA as rough surfaces greatly enhance the surface area to provide more active sites to complete the catalytic reaction. SWCNTs support completely burying inside PI-5-CA enhances the catalytic efficiency of the fabricated material being conductive materials. The SEM image results are also consistent with the TEM results taken at different magnification as shown in **Figures 2D–F**.

The polymerization mechanism of PI-5-CA was studied by Fourier transform infrared spectroscopy (FT-IR), and the result is shown in **Figure 3A**. The spectral absorption peak intensity of PI-5-CA is significantly wider than that of I-5-CA monomer, which may be attributable to the wide conjugated chain length distribution of polymers (Liu et al., 2016; Yang et al., 2021). Among them, in the spectrum of monomer I-5-CA and polymer PI-5-CA, the fluctuation of absorption peak in the range of 700–820 cm^{-1} is caused by the deformation vibration of three C-H on the benzene ring, which indicates that the polymerization of monomer occurs on the pyrrole ring (Sivakkumar et al., 2005). The = CH-N stretching vibration of the monomer near 890 cm^{-1} disappeared in the polymer spectrum. The peaks near 1,478–1,838 cm^{-1} showed the presence of carboxyl groups in the monomer I-5-CA and the polymer PI-5-CA (Narang et al., 2013). Compared with the FT-IR spectra of PI-5-CA, the FT-IR spectra of PI-5-CA/C-SWCNT nanocomposites showed a one-point positive shift in the C=C bond, which should be attributed to

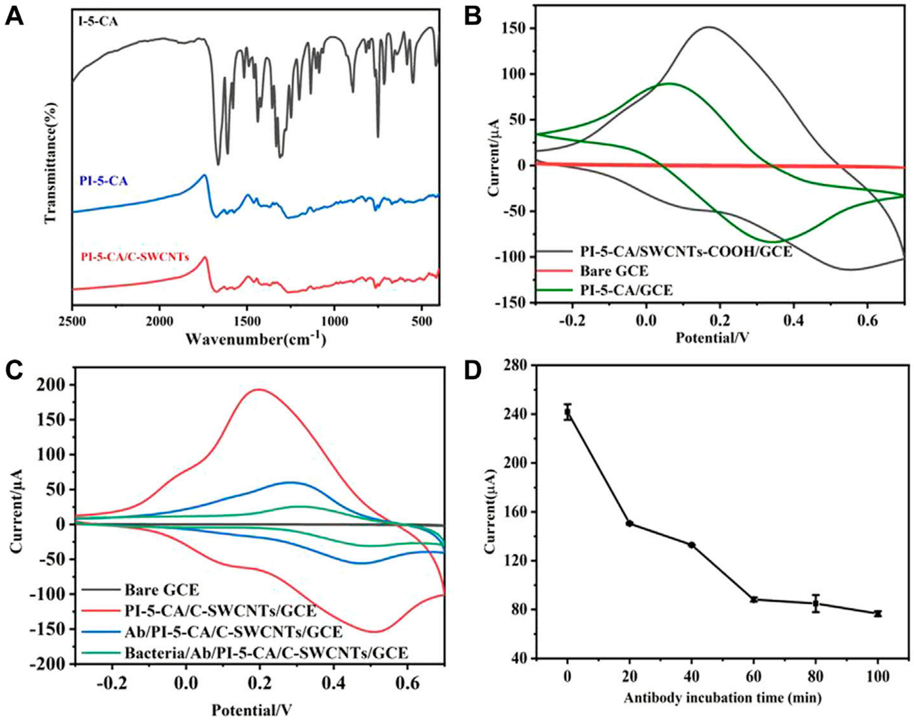

FIGURE 3 | (A) FT-IR characterization results of I-5-CA, PI-5-CA, and PI-5-CA/C-SWCNTs. **(B)** CV of electrodes modified with PI-5-CA/C-SWCNTs, bare GC, and PI-5-CA in 0.1 M PBS (pH = 6). **(C)** CV representation of the electrode in 0.1 M PBS (pH = 6) after each step of modification, and **(D)** the current changes of the immunosensor under different antibody incubation times in 0.1 M PBS (pH = 6).

the π–π interaction between PI-5-CA and C-SWCNTs (Yang et al., 2019).

4 RESULTS AND DISCUSSION

4.1 Electrochemical Performance of PI-5-CA/C-SWCNTs/GCE

Compared with the bare GCE, both PI-5-CA/C-SWCNTs and PI-5-CA-modified electrodes can promote electron transfer and generate redox current. It can be seen from **Figure 3B** that the redox current peak value of PI-5-CA/C-SWCNTs/GCE is significantly higher than that of PI-5-CA/GCE, which may be attributed to the tubular structure of C-SWCNTs promoting the electron transfer of PI-5-CA. **Figure 3C** shows the electron transfer behavior of the electrode surface after each modification. Because PI-5-CA/C-SWCNTs have higher redox activity and conductivity, a higher redox current peak can be clearly seen. In that case, when antibodies bound to the carboxyl groups present on the surface of PI-5-CA/C-SWCNTs, a reduction in the peak redox current can be clearly observed. This is due to the fact that the antibody protein is a non-conductive substance, which causes hindrance during the electron transfer on the electrode surface that resultantly causes a decrease in redox current. After incubating with *E. coli* O157:H7 bacterial solution, the peak redox current further decreased, which just proved that the bacterial solution successfully combined with the antibody on the electrode surface. This reduction was due to the increased steric effect of antigen–antibody immune complexes during electron transfer. The current change on the surface of the glassy carbon electrode indicates the successful preparation of the immunosensor, which can be further used as a potential platform for detecting bacteria.

4.2 Optimization of Experimental Parameters

4.2.1 Optimization of Antibody Incubation Time

When the PI-5-CA/C-SWCNT composite material was deposited on the surface of the electrode, the carboxyl group can be activated with a mixed solution containing EDC, NHS, and MES. Then, 10 μL of antibody solution was dropped onto the surface of the electrode, which helps antibodies to get attached to the surface of the GCE through the amino-carboxyl reaction in a 37°C water bath. In order to make sure the -COOH group of the PI-5-CA/C-SWCNT composite material can bind to more and more antibodies, the incubation time was optimized within 100 min.

It can be seen from **Figure 3D** that as the incubation time increases, the peak value of the redox current on the electrode surface gradually decreases. This is due to the gradual increase in the amount of antibodies bound to the electrode surface, which increases the impedance of electron transfer. As shown in **Figure 3D**, after about 60 min of reaction, the current peak

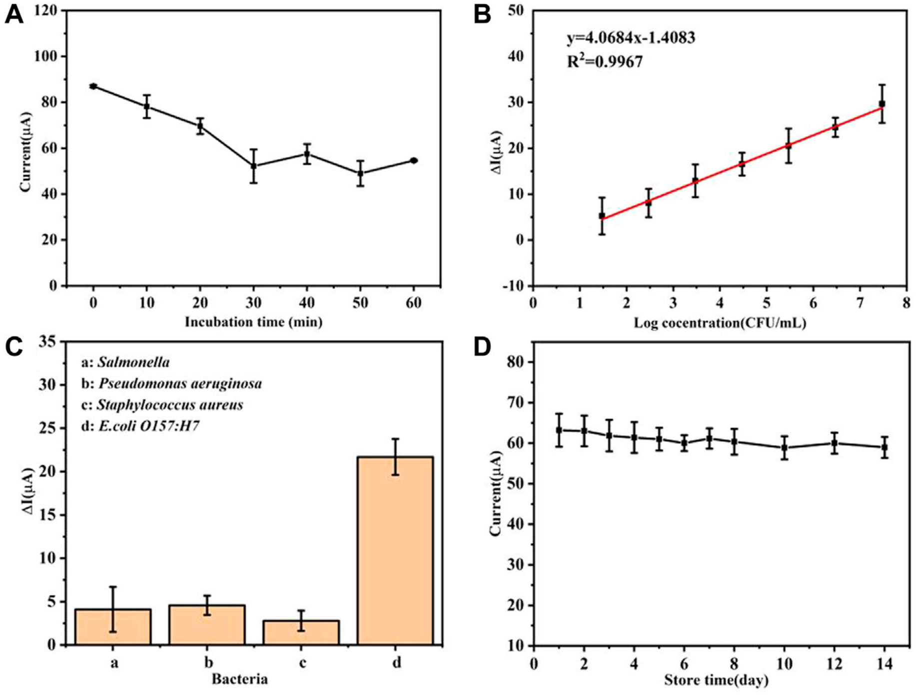

FIGURE 4 | (A) Current changes of the immunosensor under different bacterial incubation times, **(B)** linear relationship between the current change value and the logarithm of the bacterial concentration, **(C)** detection specificity of the immunosensor, and **(D)** performance of the electrochemical immunosensors at various storage periods.

gradually stabilized. It can be concluded that the antibodies bound to the electrode surface reach a relatively saturated state after 60 min of incubation. Later studies also chose 60 min as the antibody incubation time.

4.2.2 Optimization of Incubation Time for *E. coli* O157:H7

In order to ensure the binding of sufficient amount of bacteria on the electrode to achieve a sensitive detection effect, the incubation time of the bacteria solution was further optimized. The freshly cultured *E. coli* O157:H7 bacterial solution was immersed in PBS after centrifugation, and then was diluted to different concentrations. In total, 10 μL of 4×10^6 CFU/mL *E. coli* O157:H7 bacterial liquid was added dropwise to the prepared immunosensing electrode and incubated at 37°C for different times.

As the incubation time increases, the oxidation peak current gradually decreases and the current value tends to stabilize at about 30 min as depicted by **Figure 4A**. In the subsequent incubation time, the fluctuation of the current value may be attributed to the reversibility of the antigen–antibody immune binding reaction (Ghosh, 2006). In summary, 30 min was selected as the reaction time for the combination of bacteria and immunosensor.

4.3 Analytical Performance of the Immunosensor

Under the optimal experimental conditions, the analytical performance of the prepared immunosensor was studied. The *E. coli* O157:H7 monoclonal colony was picked into the LB liquid medium and cultivated to a logarithmic phase at 37°C with 200 rpm shaking. Later, the freshly cultured bacterial solution was centrifuged and immersed in PBS. Finally, the bacterial liquid was diluted to a series of concentration gradient from 2.98×10^1 to 2.98×10^7 CFU/ml, and 10 μL of the abovementioned diluted bacterial solution was dropped onto the electrode surface and incubated for 30 min in a 37°C water bath. After that, the current changes on the electrode surface were recorded.

It can be seen from **Figure 4B** that there is a good linear relationship between the current change value (ΔI) (before and after the immunosensor is combined with the bacterial solution) and the logarithmic value of the bacterial solution concentration [Log(CFU/ml)]. After fitting, within the linear range, the linear relationship between ΔI and the concentration of *E. coli* O157:H7 is $\Delta I = 4.0684\ \mathrm{Log(CFU/mL)}-1.4083$ ($R^2 = 0.9976$) with a low limit of detection of 2.5 CFU/ml ($LOD = 3\ SD/\mathrm{k}$, $n = 3$). It can be concluded that the prepared immunosensor platform has great potential for the rapid detection of *E. coli* O157:H7, which can provide a basis for the next step of detection in natural samples.

4.4 Analytical Specificity of the Immunosensor

In order to explore specificity of the biosensing system for *E. coli* O157:H7 detection, different types of strains such as *Salmonella*, *Pseudomonas aeruginosa*, *Staphylococcus aureus*, and *E. coli* O157:H7 have been detected by repeating the same detection procedure. In

TABLE 2 | Assay results of the actual sample using the proposed and plate counting method.

Added (CFU/mL)	Detected (CFU/mL)		Recovery (%)	
	Biosensor	Plate count	Biosensor	Plate count
1.04×10^2	1.12×10^2	1.08×10^2	107.69	103.85
3.2 × 102	3.21 × 102	3.43 × 102	100.31	107.19
3.2×10^4	3.14×10^4	3.16×10^4	98.13	98.75
3.2×10^6	3.32×10^6	3.19×10^6	103.75	99.69

total, 10 μL of 10^6 CFU/ml of the aforementioned various fresh bacterial liquids were injected onto the prepared immune-electrode surface, respectively, for the sensitive strain detection.

In comparison to the *E. coli* O157:H7 modified immunosensor, the other immunosensors modified with *Salmonella*, *Pseudomonas aeruginosa*, and *Staphylococcus aureus* exhibited up to 20% less response toward the target strain as shown in **Figure 4C**. It can be seen that the specificity of the developed electrochemical immunosensor is acceptable.

4.5 Stability of the Immunosensor

The storage performance of this sensor also was studied. The prepared antibody sensor was stored at 4°C and the peak value of the redox current on the electrodes was detected every other day. It can be seen from **Figure 4D** that the prepared immunosensor has good storage stability. After 1 week, it can still maintain 96.78% of the original current value. After 2 weeks of storage, the current value was about 93.30% of the original value, which further shows that the sensor has good stability and practical applications potential.

4.6 Detection and Analysis of Real Samples

Benefitted from the excellent electrochemical performance, we applied our modified electrode for the detection of *E. coli* O157:H7 from the real samples and compared the results obtained from the actual samples with the plate counting method in **Table 2**.

Recovery (%) is expressed as the ratio of the number of detected/number of spiked. As shown in **Table 2**, the recovery rate of the prepared biosensor is 98.13–107.69%, indicating that the proposed immunosensor for *E. coli* O157:H7 detection has good accuracy. In other words, this electrochemical immunosensor provides a potential application prospect for the analysis of *E. coli* O157:H7 in natural samples.

5 CONCLUSION

In summary, we have successfully proposed a PI-5-CA/C-SWCNT-based electrochemical immunosensor for the rapid detection of *E. coli* O157:H7. First, we prepared PI-5-CA/C-SWCNT composites with a three-dimensional porous structure through a simple chemical oxidation polymerization method. The PI-5-CA/C-SWCNT material has a stable redox activity, good conductivity, large specific surface area, and abundant functional groups. By taking the advantage of these superb characteristics, we used antibodies as biorecognition molecules to construct Ab/PI-5-CA/C-SWCNTs/GCE immunosensing electrodes for the sensitive detection of *E. coli* O157:H7. Compared with previous reported works (Xue et al., 2020; Yang et al., 2020; Qaanei et al., 2021), our fabricated biosensor can detect bacteria as low as 29.8 CFU/ml within 30 min, which greatly shorten the detection time. At the same time, the immunosensor shows good sensitivity, specificity, reproducibility, and stability toward the detection of *E. coli* O157:H7. We believe that the bacteria detection method proposed in this article has good application prospects, which can not only be used for the sensitive and selective detection of *E. coli* O157:H7 but also pave a way for the simple and fast detection of different bacterial strains as well as other substances.

DATA AVAILABILITY STATEMENT

The original contributions presented in the study are included in the article/Supplementary Material; further inquiries can be directed to the corresponding authors.

AUTHOR CONTRIBUTIONS

HW conceived the idea, carried out the whole experimental work, and wrote the manuscript. YF contributed in conceiving the idea and helped in revising the manuscript. QY helped in revision. XS helped in experiments. HL contributed in arranging bacteria. WC helped in experiments and removed typo mistakes. AA helped in visualization, writing—original draft, and revision. SW helped in different aspects, funding acquisition, conceptualization, visualization, writing—original draft, and revision.

FUNDING

This research work was funded by the National Key Research and Development Program of China under Grant 2017YFC1104402, the China Postdoctoral Science Foundation (2016M602291), the initial research fund from Chinese Scholarship Council (CSC), and 3551 Project, Optics Valley of China.

REFERENCES

Amagliani, G., Brandi, G., Omiccioli, E., Casiere, A., Bruce, I. J., and Magnani, M. (2004). Direct Detection of Listeria Monocytogenes from Milk by Magnetic Based DNA Isolation and PCR. *Food Microbiol.* 21 (5), 597–603. doi:10.1016/j.fm.2003.10.008

Asif, M., Aziz, A., Dao, A. Q., Hakeem, A., Wang, H., Dong, S., et al. (2015). Real-Time Tracking of Hydrogen Peroxide Secreted by Live Cells Using MnO2 Nanoparticles Intercalated Layered Doubled Hydroxide Nanohybrids. *Analytica Chim. Acta* 898, 34–41. doi:10.1016/j.aca.2015.09.053

Asif, M., Aziz, A., Azeem, M., Wang, Z., Ashraf, G., Xiao, F., et al. (2018). A Review on Electrochemical Biosensing Platform Based on Layered Double Hydroxides for Small Molecule Biomarkers Determination. *Adv. Colloid Interf. Sci.* 262, 21–38. doi:10.1016/j.cis.2018.11.001

Asif, M., Aziz, A., Wang, H., Wang, Z., Wang, W., Ajmal, M., et al. (2019). Superlattice Stacking by Hybridizing Layered Double Hydroxide Nanosheets with Layers of Reduced Graphene Oxide for Electrochemical Simultaneous Determination of Dopamine, Uric Acid and Ascorbic Acid. *Microchim Acta* 186 (2), 61. doi:10.1007/s00604-018-3158-y

Asif, M., Aziz, A., Ashraf, G., Iftikhar, T., Sun, Y., Xiao, F., et al. (2022). Unveiling Microbiologically Influenced Corrosion Engineering to Transfigure Damages into Benefits: A Textile Sensor for H2O2 Detection in Clinical Cancer Tissues. *Chem. Eng. J.* 427, 131398. doi:10.1016/j.cej.2021.131398

Aziz, A., Asif, M., Ashraf, G., Azeem, M., Majeed, I., Ajmal, M., et al. (2019a). Advancements in Electrochemical Sensing of Hydrogen Peroxide, Glucose and Dopamine by Using 2D Nanoarchitectures of Layered Double Hydroxides or Metal Dichalcogenides. A Review. *Microchim Acta* 186 (10), 671. doi:10.1007/s00604-019-3776-z

Aziz, A., Asif, M., Azeem, M., Ashraf, G., Wang, Z., Xiao, F., et al. (2019b). Self-Stacking of Exfoliated Charged Nanosheets of LDHs and Graphene as Biosensor with Real-Time Tracking of Dopamine from Live Cells. *Analytica Chim. Acta* 1047, 197–207. doi:10.1016/j.aca.2018.10.008

Aziz, A., Asif, M., Ashraf, G., Farooq, U., Yang, Q., and Wang, S. (2021). Trends in Biosensing Platforms for SARS-CoV-2 Detection: A Critical Appraisal against Standard Detection Tools. *Curr. Opin. Colloid Interf. Sci* 52, 101418. doi:10.1016/j.cocis.2021.101418

Aziz, A., Asif, M., Ashraf, G., Iftikhar, T., Hu, J., Xiao, F., et al. (2022). Boosting Electrocatalytic Activity of Carbon Fiber@fusiform-Like Copper-Nickel LDHs: Sensing of Nitrate as Biomarker for NOB Detection. *J. Hazard. Mater.* 422, 126907. doi:10.1016/j.jhazmat.2021.126907

Buchanan, R. L., and Doyle, M. P. (1997). Foodborne Disease Significance of *Escherichia C* O157: H7 and Other Enterohemorrhagic *E. C. Food Technol. (Chicago)* 51 (10), 69–76.

Chen, J., Andler, S. M., Goddard, J. M., Nugen, S. R., and Rotello, V. M. (2017). Integrating Recognition Elements with Nanomaterials for Bacteria Sensing. *Chem. Soc. Rev.* 46 (5), 1272–1283. doi:10.1039/c6cs00313c

Di Febo, T., Schirone, M., Visciano, P., Portanti, O., Armillotta, G., Persiani, T., et al. (2019). Development of a Capture ELISA for Rapid Detection of *Salmonella E* in Food Samples. *Food Anal. Methods* 12 (2), 322–330. doi:10.1007/s12161-018-1363-2

Ghosh, P., Zhou, Y., Richardson, Q., and Higgins, D. E. (2019). Characterization of the Pathogenesis and Immune Response to Listeria Monocytogenes Strains Isolated from a Sustained National Outbreak. *Sci. Rep.* 9 (1), 19587. doi:10.1038/s41598-019-56028-3

Ghosh, R. (2006). Membrane Chromatographic Immunoassay Method for Rapid Quantitative Analysis of Specific Serum Antibodies. *Biotechnol. Bioeng.* 93 (2), 280–285. doi:10.1002/bit.20707

Hu, L., Gong, B., Jiang, N., Li, Y., and Wu, Y. (2021a). Electrochemical Biosensor for Cytokinins Based on the CHASE Domain of Arabidopsis Histidine Kinases 4. *Bioelectrochemistry* 141, 107872. doi:10.1016/j.bioelechem.2021.107872

Hu, Y., Sun, Y., Gu, J., Yang, F., Wu, S., Zhang, C., et al. (2021b). Selection of Specific Nanobodies to Develop an Immuno-Assay Detecting *Staphylococcus A* in Milk. *Food Chem.* 353, 129481. doi:10.1016/j.foodchem.2021.129481

Jarvis, N. A., O'Bryan, C. A., Dawoud, T. M., Park, S. H., Kwon, Y. M., Crandall, P. G., et al. (2016). An Overview of Salmonella Thermal Destruction during Food Processing and Preparation. *Food Control* 68, 280–290. doi:10.1016/j.foodcont.2016.04.006

Jia, C., and Jukes, D. (2013). The National Food Safety Control System of China - A Systematic Review. *Food control* 32 (1), 236–245. doi:10.1016/j.foodcont.2012.11.042

Joshi, L., and Prakash, R. (2013). Synthesis of Conducting Poly(5-Carboxyindole)/Au Nanocomposite: Investigation of Structural and Nanoscale Electrical Properties. *Thin solid films* 534, 120–125. doi:10.1016/j.tsf.2013.02.025

Kang, D., Ricci, F., White, R. J., and Plaxco, K. W. (2016). Survey of Redox-Active Moieties for Application in Multiplexed Electrochemical Biosensors. *Anal. Chem.* 88 (21), 10452–10458. doi:10.1021/acs.analchem.6b02376

Kumar, T. H. V., and Sundramoorthy, A. K. (2019). Electrochemical Biosensor for Methyl Parathion Based on Single-Walled Carbon Nanotube/Glutaraldehyde Crosslinked Acetylcholinesterase-Wrapped Bovine Serum Albumin Nanocomposites. *Analytica Chim. Acta* 1074, 131–141. doi:10.1016/j.aca.2019.05.011

Law, J. W.-F., Ab Mutalib, N.-S., Chan, K.-G., and Lee, L.-H. (2015). Rapid Methods for the Detection of Foodborne Bacterial Pathogens: Principles, Applications, Advantages and Limitations. *Front. Microbiol.* 5, 770. doi:10.3389/fmicb.2014.00770

Li, J., Wang, W., Liu, J., Li, H., Zhang, N., Yang, F., et al. (2021). Human-Like Performance Umami Electrochemical Biosensor by Utilizing Co-Electrodeposition of Ligand Binding Domain T1R1-VFT and Prussian Blue. *Biosens. Bioelectron.* 193, 113627. doi:10.1016/j.bios.2021.113627

Liu, H., Zhen, S., Ming, S., Lin, K., Gu, H., Zhao, Y., et al. (2016). Furan and Pyridinechalcogenodiazole-Based π-Conjugated Systems via a Donor-Acceptor Approach. *J. Solid State. Electrochem.* 20 (8), 2337–2349. doi:10.1007/s10008-016-3253-0

Narang, J., Chauhan, N., Rani, P., and Pundir, C. S. (2013). Construction of an Amperometric TG Biosensor Based on AuPPy Nanocomposite and Poly (Indole-5-Carboxylic Acid) Modified Au Electrode. *Bioproc. Biosyst Eng* 36 (4), 425–432. doi:10.1007/s00449-012-0799-9

Odeyemi, O. A., Alegbeleye, O. O., Strateva, M., and Stratev, D. (2020). Understanding Spoilage Microbial Community and Spoilage Mechanisms in Foods of Animal Origin. *Compr. Rev. Food Sci. Food Saf.* 19 (2), 311–331. doi:10.1111/1541-4337.12526

Pandey, A., Gurbuz, Y., Ozguz, V., Niazi, J. H., and Qureshi, A. (2017). Graphene-Interfaced Electrical Biosensor for Label-Free and Sensitive Detection of Foodborne Pathogenic *E. C* O157:H7. *Biosens. Bioelectron.* 91, 225–231. doi:10.1016/j.bios.2016.12.041

Park, J. Y., Park, K., Ok, G., Chang, H.-J., Park, T. J., Choi, S.-W., et al. (2020). Detection of *Escherichia C* O157:H7 Using Automated Immunomagnetic Separation and Enzyme-Based Colorimetric Assay. *Sensors* 20 (5), 1395. doi:10.3390/s20051395

Patra, J., and Baek, K.-H. (2016). Antibacterial Activity and Action Mechanism of the Essential Oil from Enteromorpha Linza L. Against Foodborne Pathogenic Bacteria. *Molecules* 21 (3), 388. doi:10.3390/molecules21030388

Qaanei, M., Taheri, R. A., and Eskandari, K. (2021). Electrochemical Aptasensor for *Escherichia C* O157: H7 Bacteria Detection Using a Nanocomposite of Reduced Graphene Oxide, Gold Nanoparticles and Polyvinyl Alcohol. *Anal. Methods* 13, 3101–3109. doi:10.1039/d1ay00563d

Rad, A. H., Aghebati-Maleki, L., Kafil, H. S., Gilani, N., Abbasi, A., and Khani, N. (2021). Postbiotics, as Dynamic Biomolecules, and Their Promising Role in Promoting Food Safety. *Biointerface Res. Appl. Chem.* 11 (6), 14529–14544. doi:10.33263/briac116.1452914544

Sai-Anand, G., Sivanesan, A., Benzigar, M. R., Singh, G., Gopalan, A.-I., Baskar, A. V., et al. (2019). Recent Progress on the Sensing of Pathogenic Bacteria Using Advanced Nanostructures. *Bull. Chem. Soc. Jpn.* 92 (1), 216–244. doi:10.1246/bcsj.20180280

Shi, J., Chan, C., Pang, Y., Ye, W., Tian, F., Lyu, J., et al. (2015). A Fluorescence Resonance Energy Transfer (FRET) Biosensor Based on Graphene Quantum Dots (GQDs) and Gold Nanoparticles (AuNPs) for the Detection of mecA Gene Sequence of *Staphylococcus A. Biosens. Bioelectron.* 67, 595–600. doi:10.1016/j.bios.2014.09.059

Sieuwerts, S., De Bok, F. A. M., Mols, E., De Vos, W. M., and van Hylckama Vlieg, J. E. T. (2008). A Simple and Fast Method for Determining Colony Forming Units. *Lett. Appl. Microbiol.* 47 (4), 275–278. doi:10.1111/j.1472-765x.2008.02417.x

Sivakkumar, S. R., Angulakshmi, N., and Saraswathi, R. (2005). Characterization of Poly(indole-5-Carboxylic Acid) in Aqueous Rechargeable Cells. *J. Appl. Polym. Sci.* 98 (2), 917–922. doi:10.1002/app.22202

Sperber, W. H., North American Millers' Association Microbiology Working Group (2007). Role of Microbiological Guidelines in the Production and Commercial Use of Milled Cereal Grains: a Practical Approach for the 21st century. *J. Food Prot.* 70 (4), 1041–1053. doi:10.4315/0362-028x-70.4.1041

Stockman, J. A. (2013). German Outbreak of *Escherichia Coli* O104:H4 Associated with Sprouts. *Yearb. Pediatr.* 2013, 287–289. doi:10.1016/j.yped.2011.12.017

Xue, L., Huang, F., Hao, L., Cai, G., Zheng, L., Li, Y., et al. (2020). A Sensitive Immunoassay for Simultaneous Detection of Foodborne Pathogens Using MnO2 Nanoflowers-Assisted Loading and Release of Quantum Dots. *Food Chem.* 322, 126719. doi:10.1016/j.foodchem.2020.126719

Yang, T., Ren, X., Yang, M., Li, X., He, K., Rao, A., et al. (2019). A Highly Sensitive Label-Free Electrochemical Immunosensor Based on Poly(Indole-5-Carboxylicacid) with Ultra-High Redox Stability. *Biosens. Bioelectron.* 141, 111406. doi:10.1016/j.bios.2019.111406

Yang, T., Yang, X., Guo, X., Fu, S., Zheng, J., Chen, S., et al. (2020). A Novel Fluorometric Aptasensor Based on Carbon Nanocomposite for Sensitive Detection of *Escherichia C* O157:H7 in Milk. *J. Dairy Sci.* 103 (9), 7879–7889. doi:10.3168/jds.2020-18344

Yang, Q., Deng, S., Xu, J., Farooq, U., Yang, T., Chen, W., et al. (2021). Poly (Indole-5-Carboxylic Acid)/Reduced Graphene Oxide/gold Nanoparticles/ Phage-Based Electrochemical Biosensor for Highly Specific Detection of Yersinia Pseudotuberculosis. *Microchimica Acta* 188 (4), 1–13. doi:10.1007/ s00604-020-04676-y

Yao, L., Zheng, L., Cai, G., Wang, S., Wang, L., and Lin, J. (2020). A Rapid and Sensitive Salmonella Biosensor Based on Viscoelastic Inertial Microfluidics. *Sensors* 20 (9), 2738. doi:10.3390/s20092738

Zhao, X., Lin, C.-W., Wang, J., and Oh, D. H. (2014). Advances in Rapid Detection Methods for Foodborne Pathogens. *J. Microbiol. Biotechnol.* 24 (3), 297–312. doi:10.4014/jmb.1310.10013

Zhao, L., Guo, J., Li, S., and Wang, J. (2021). The Development of Thermal Immunosensing for the Detection of Food-Borne Pathogens *E. coli* O157: H7 Based on the Novel Substoichiometric Photothermal Conversion Materials MoO3-X NPs. *Sensors Actuators B: Chem.* 344, 130306. doi:10.1016/j.snb.2021.130306

Zhou, B., Ye, Q., Chen, M., Li, F., Xiang, X., Shang, Y., et al. (2022). Novel Species-Specific Targets for Real-Time PCR Detection of Four Common Pathogenic Staphylococcus Spp. *Food Control* 131, 108478. doi:10.1016/j.foodcont.2021. 108478

Conflict of Interest: The authors declare that the research was conducted in the absence of any commercial or financial relationships that could be construed as a potential conflict of interest.

frontiers in Chemistry

ORIGINAL RESEARCH
published: 22 March 2022
doi: 10.3389/fchem.2022.873187

Functionalized Graphene Fiber Modified With MOF-Derived Rime-Like Hierarchical Nanozyme for Electrochemical Biosensing of H_2O_2 in Cancer Cells

Wei Huang*[1,2], *Yun Xu*[2] and *Yimin Sun*[1]

[1]Hubei Key Laboratory of Plasma Chemistry and Advanced Materials, School of Materials Science and Engineering, Wuhan Institute of Technology, Wuhan, China, [2]Key Laboratory of Material Chemistry for Energy Conversion and Storage, Ministry of Education, School of Chemistry and Chemical Engineering, Huazhong University of Science & Technology, Wuhan, China

Edited by:
Muhammad Asif,
Wuhan Institute of Technology, China

Reviewed by:
Shenqi Wang,
Huazhong University of Science and Technology, China
Zhao Anshun,
The First Affiliated Hospital of Henan University of Science and Technology, China
Umamaheswari Rajaji,
National Taipei University of Technology, Taiwan

****Correspondence:***
Yimin Sun
ymsun@wit.edu.cn

Specialty section:
This article was submitted to Analytical Chemistry, a section of the journal Frontiers in Chemistry

Received: *10 February 2022*
Accepted: *17 February 2022*
Published: *22 March 2022*

Citation:
Huang W, Xu Y and Sun Y (2022) Functionalized Graphene Fiber Modified With MOF-Derived Rime-Like Hierarchical Nanozyme for Electrochemical Biosensing of H_2O_2 in Cancer Cells.
Front. Chem. 10:873187.
doi: 10.3389/fchem.2022.873187

The rational design and construction of high-performance flexible electrochemical sensors based on hierarchical nanostructure functionalized microelectrode systems are of vital importance for sensitive *in situ* and real-time detection of biomolecules released from living cells. Herein, we report a novel and facile strategy to synthesize a new kind of high-performance microelectrode functionalized by dual nanozyme composed of rime-like $Cu_2(OH)_3NO_3$ wrapped ZnO nanorods assembly [$Cu_2(OH)_3NO_3$@ZnO], and explore its practical application in electrochemical detection of hydrogen peroxide (H_2O_2) released from living cells. Benefiting from the merits of the unique hierarchical nanohybrid structure and high catalytic activities, the resultant $Cu_2(OH)_3NO_3$@ZnO-modified AGF microelectrode shows remarkable electrochemical sensing performance towards H_2O_2 with a low detection limit of 1 μM and a high sensitivity of 272 μA cm^{-2} mM^{-1}, as well as good anti-interference capability, long-term stability, and reproducibility. These properties enabled the proposed microelectrode-based electrochemical platform to be applied for *in situ* amperometric tracking of H_2O_2 released from different types of human colon cells, thus demonstrating its great prospect as a sensitive cancer cell detection probe for the early diagnosis and management of various cancer diseases.

Keywords: graphene fibers, hierarchical structure, flexible microelectrode, nanozymatic electrochemical sensor, *in situ* cancer cell detection

INTRODUCTION

Since cancer is the second leading cause of death globally, there has always been an increasing research interest in developing efficient techniques for early cancer diagnosis and treatment to circumvent the challenges being faced in clinical practices (Labib et al., 2016; Lin et al., 2016; Asif et al., 2018b). Hydrogen peroxide (H_2O_2), one of the most common reactive oxygen species, performs as a critical component within biological systems (Lippert et al., 2011; Aziz et al., 2019a). The level of H_2O_2 in human body can be regarded as a versatile biomarker for early diagnosis of various diseases such as cancer (Xiao et al., 2016). For effective and accurate monitoring of the versatile biomarkers associated with cancer, electrochemical biosensors have comprehensive advantages of fast response, low detection limit, high sensitivity, good reproducibility, easy operation, and the ability to be miniaturized for online, and *in vivo* analysis (Sun et al., 2015; Sun et al., 2016; Zhao et al., 2021). Moreover, the development of wearable and implantable electrochemical sensing systems for continuous monitoring of the H_2O_2concentration in the human body has shown greater prospects in clinical diagnosis (Wang L. et al., 2018; Asif et al., 2022). Therefore, it is of great significance to construct structural rigidity, high mechanical strength functionalized microelectrodes, which can be integrated into wearable flexible electrochemical sensors to achieve fast, real-time, and high-sensitivity detection (Aziz et al., 2021b).

The development of advanced electrochemical sensors necessitates the design and construction of freestanding electrode system with good mechanical strength and high flexibility (Aziz et al., 2021a), which can be rolled up for use as well as good sensing performance in cancer cell detection. In this regard, graphene fiber (GF), a new type of carbon fiber assembled from graphene nanosheets, possesses one-dimensional microstructure with good flexibility, mechanical strength, high electronic conductivity, and excellent electrochemical stability (Xin et al., 2015; Huang et al., 2018; Xin et al., 2019). The prepared GF integrates the high electrical conductivity of graphene nanosheets and the unique mechanical properties of its macroscopic fiber structure, which has broad application prospects in flexible energy storage/conversion devices, wearable devices, artificial intelligence, etc. (Zhang et al., 2016; Huang et al., 2018). In particular, the intrinsic advantages GF microelectrode, such as adjustable active sites, high signal-to-noise ratio, and good biological compatibility, as well as immobilization of enzyme, enable its application in electrochemical sensing fields (Ding et al., 2016; Chen et al., 2019; Zeng et al., 2019). However, among different kinds of electrochemical sensors, GF microelectrode-based electrochemical biosensor is still in its infancy, so rational design of nanohybrid GF with active components is important for improving the comprehensive performance of electrochemical sensors for the detection of biomolecules. Nanozyme is a class of nanomaterials with enzyme-like characteristics (Wang H. et al., 2018; Wu et al., 2019). With the recent advance of nanotechnology with biology, a variety of nanozymes, such as carbon-based nanomaterials (Ji et al., 2021; Li et al., 2021), transition metal dichalcogenides/peroxides/oxides nanosheets (Asif et al., 2018a; Asif et al., 2019; Huang et al., 2019), noble metal nanoparticles (NPs) (Shen et al., 2015; Xu et al., 2018), and their hybrids (Zhang et al., 2019), have been discovered to possess unique enzyme-mimic catalytic activities and used in the biomedicine or bioanalysis by virtue of their reasonable stability, low cost, mass production, and long-term storage properties that are superior to nature enzymes. In the past few years, tremendous research efforts have been devoted to developing nanozyme-modified GF microelectrodes, which have been used in electrochemical detection of versatile biomarkers, such as adrenaline (Zeng et al., 2019), glucose (Chen et al., 2019), dopamine (Cai et al., 2016; Aziz et al., 2019b), and H_2O_2 (Peng et al., 2018; Zhao et al., 2020; Guo et al., 2021). Although considerable progress has been made in this field, it is still a challenge for the development of high-performance functionalized GF-based microelectrodes with optimized microstructural configurations by judiciously selecting electroactive species and rationally designing the composition and structure of nanozyme for continuous detection of biological samples.

In this work, we have developed an activated graphene fiber (AGF) modified with MOF-mediated rime-like hierarchical nanozyme as flexible and biocompatible microelectrode for *in situ* electrochemical detection of H_2O_2 in human colon cells. As far as we know, this has never been reported previously. As shown in **Figure 1**, the freestanding and flexible AGF is synthesized by wet-spinning using graphene oxide as the structural units and ionic liquid (IL) as coagulation bath to introduce heteroatoms (Cheng et al., 2015). The introduction of heteroatoms into the graphene materials not only possesses superior charge mobility to deliver high electrochemical activity, but also provides abundant active sites for the accessibility of substrate molecules and anchoring extrinsic functional species. To improve its catalytic activity, a metal-organic framework (MOF)-mediated rime-like hierarchical nanozyme [i.e., $Cu_2(OH)_3NO_3$@ZnO] is assembled on heteroatom-doped GF (Cui et al., 2016). Specifically, ZnO nanorods are grown on AGF *via* a typical solvothermal method. ZIF-8 is then *in situ* grown on ZnO nanorods by the impregnation method to obtain ZIF-8@ZnO/AGF. The $Cu_2(OH)_2(NO_3)$ is bonded to ZnO/AGF by chemical etching of ZIF-8, named, $Cu_2(OH)_3NO_3$@ZnO/AGF. Benefitting from the synergistic contributions of dual nanozymatic activity of rime-like hierarchical $Cu_2(OH)_3NO_3$@ZnO as well as unique structural and electrical properties, the resultant rime-like hierarchical $Cu_2(OH)_3NO_3$@ZnO-decorated heteroatom-doped GF [$Cu_2(OH)_3NO_3$@ZnO/AGF] microelectrode demonstrated significantly improved sensing performances to H_2O_2 detection, with a low detection limit (LOD) of 1 μM (S/N = 3) and a sensitivity of 272 $\mu A\ cm^{-2}\ mM^{-1}$. These characteristics combined with its favorable anti-interference ability, high reducibility, and long-term stability, as well as good biocompatibility, enable a $Cu_2(OH)_3NO_3$@ZnO/AGF microelectrode-based electrochemical biosensor to be used for real-time tracking of H_2O_2 released from different live human colon cells, which can act as a sensitive probe to distinguish colon cancer cells and normal colon epithelial cells. Thus, our strategy for the development of high-performance electrochemical biosensor coupled with recent advance in GF microelectrode and nanozyme opens up a new avenue for facile and efficient detection of possible disease-related clinical specimens, which is of great significance for the early diagnosis of various diseases in clinic practice.

EXPERIMENTAL SECTION

Chemicals and Materials

Sulfuric acid (H_2SO_4, 98%), hydrochloric acid (HCl, 37%), potassium nitrate (KNO_3), potassium permanganate ($KMnO_4$), hydrogen peroxide (H_2O_2, 30%), ethanol, zinc nitrate hexahydrate ($Zn(NO_3)_2{\cdot}6H_2O$), zinc acetate dihydrate ($Zn(CH_3COO)_2){\cdot}2H_2O$, hexamethylenetetramine ($C_6H_{12}N_4$),

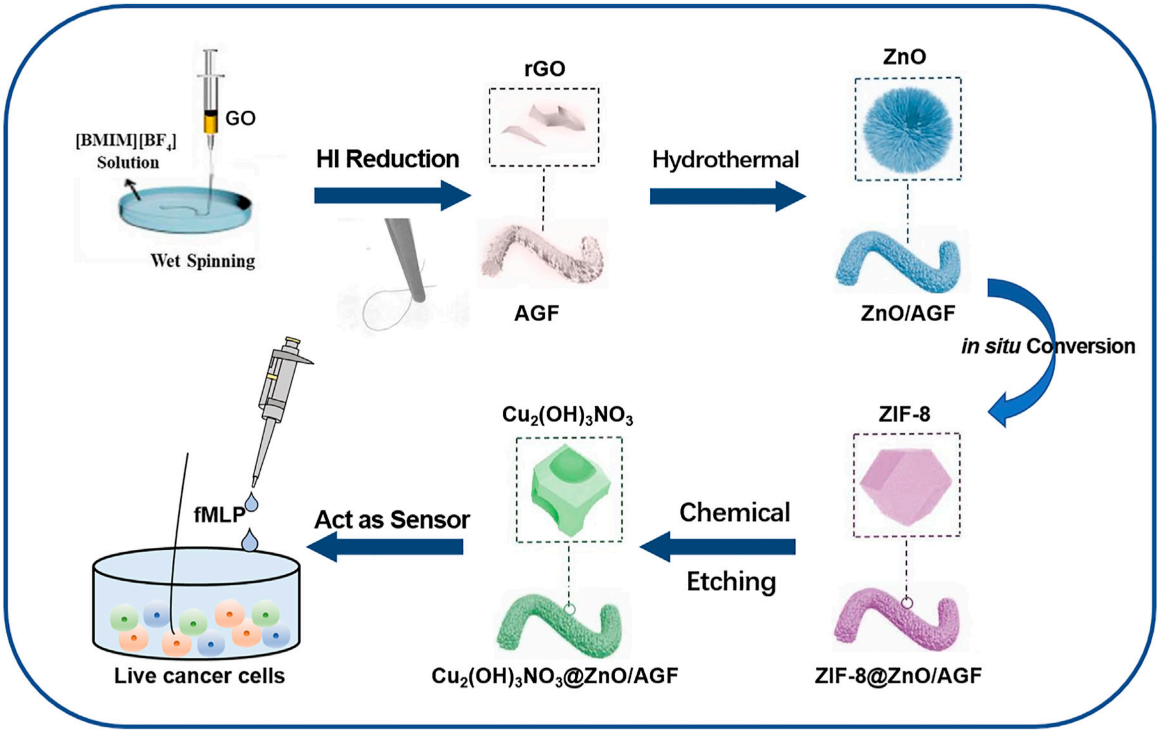

FIGURE 1 | Fabrication procedure of a rime-like $Cu_2(OH)_3NO_3$@ZnO/AGF microelectrode for live cancer cell detection.

and copper nitrate trihydrate ($Cu(NO_3)_2{\cdot}3H_2O$) were purchased from the Sinopharm Chemical Reagent Co., Ltd. 1-Butyl-3-methylimidazolium tetrafluoroborate ([BMIM][BF_4]), hydroiodic acid (HI, 48%), and worm-like expanded graphite powder (50 mesh number) were purchased from Shanghai Aladdin Biochemical Technology Co. Ltd. Guanine (G), adenine (A), cytosine (C), uracil (U), ascorbic acid (AA), D(+)-glucose (Glu), uric acid (UA), and dopamine (DA) were purchased from the Macklin Co. Ltd. N-formylmethionyl-leucyl-phenyl-alanine (fMLP, ≥99.5%) was obtained from Sigma-Aldrich (United States). All chemicals and reagents are of analytical grade and used without any further purification.

Instruments

SEM images were acquired on Nova NanoSEM 450 (10 kV). TEM images were examined by Tecnai G2-F20 (200 kV). X-ray photoelectron spectroscopy (XPS) measurements were carried out on a Perkin-Elmer model PHI 5600 XPS system; all peaks were standardized to C 1s line at 284.6 eV correction. Powder x-ray diffraction (PXRD) was performed on a Rigaku D/max-IIIA diffractometer (Cu Kα, $\lambda = 1.54056$ Å) at room temperature. Electrochemical experiments were conducted on a CHI 760E electrochemical workstation (Shanghai CH Instruments Co., China).

Synthesis of GF

Graphene oxide (GO) was first synthesized from worm-like expanded graphite powder based on a modified Hummer's method (Xu et al., 2016). The as-obtained GO suspension was centrifuged twice at 14,000 rpm for 30 min to obtain concentrated GO suspension with a mass concentration of 20 mg ml^{-1}. For wet spinning of GO fiber, the concentrated GO suspension was transferred into a 5-ml syringe connected by polyetheretherketone tube with a glass capillary (inner diameter of 500 μm) at the other end (**Supplementary Figure S1**). It was pumped into [BMIM][BF_4] IL coagulation bath solution at a rate of 450 μl min^{-1}. Subsequently, GO fibers were immersed into 30 ml of HI solution and kept at 80°C for 12 h to be reduced. Finally, they were washed successively with water and methanol to remove the HI and the iodine and dried at 60°C for 12 h.

Synthesis of $Cu_2(OH)_3NO_3$@ZnO/AGF Microelectrode

Reduced GF was placed in 30 ml of 30% H_2O_2 solutions at 70°C for 30 min and then washed with ultrapure water to obtain AGF. For the synthesis of ZnO nanorod-modified graphene fibers (ZnO/AGF), $Zn(NO_3)_2$ $6H_2O$ (59.50 mg) and hexamethylenetetramine (28.04 mg) were dissolved in 40 ml of deionized water and stirred for 10 min. AGF was placed in a PTFE autoclave containing the above solution for 12 h at 90°C. Then, the obtained fibers were placed into a high-temperature tube furnace, and heated to 400°C at a heating rate of 5°C min^{-1} for 40 min to obtain ZnO/AGF. The as-synthesized ZnO/AGF was incubated into 2-methylimidazole solution (1.5 M, 30 ml) for

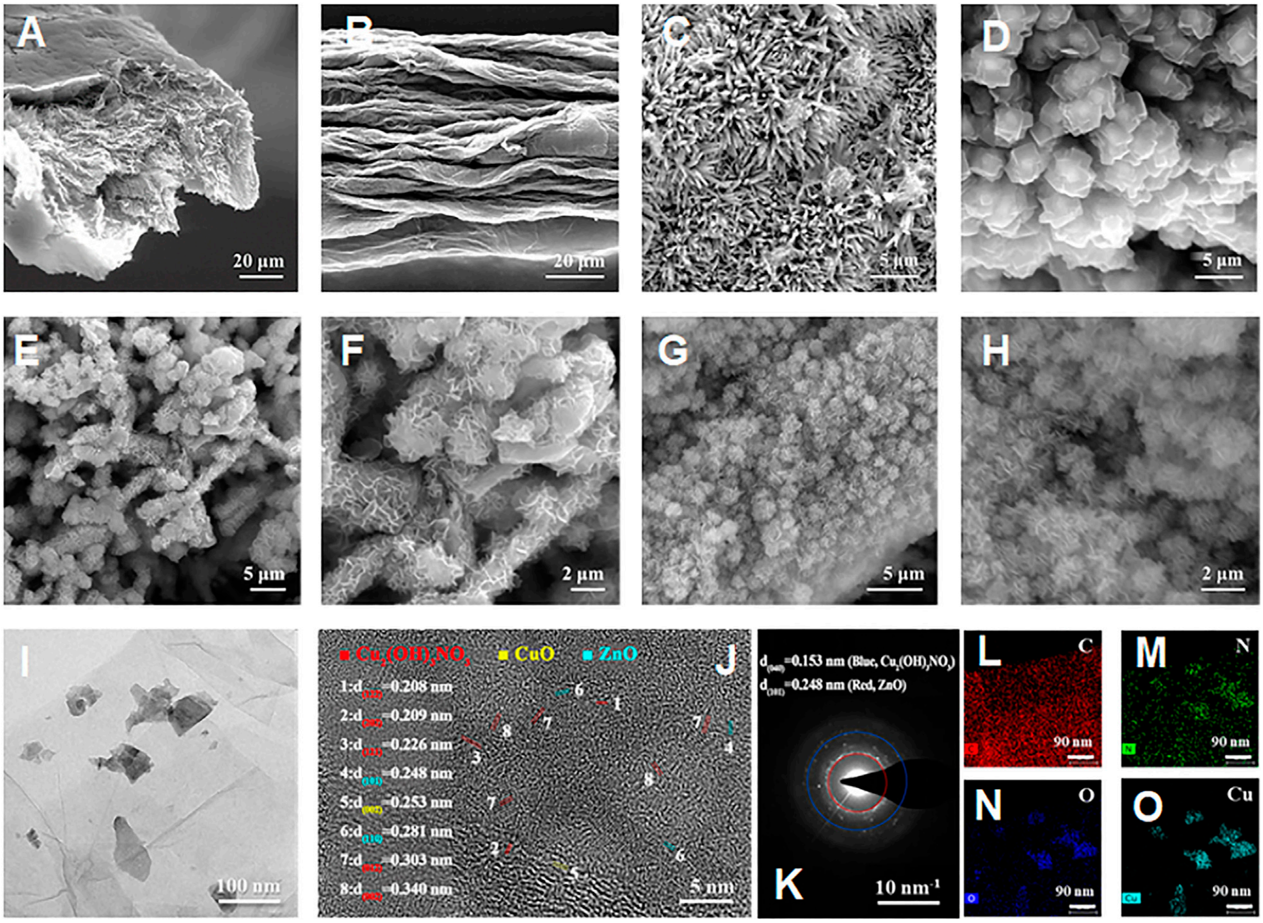

FIGURE 2 | SEM images of **(A)** cross-sectional view and **(B)** front view of the AGF; SEM images of **(C)** ZnO/AGF and **(D)** ZIF-8@ZnO/AGF; SEM images of **(E–H)** $Cu_2(OH)_3NO_3$@ZnO/AGF at different magnifications; TEM image of **(I)** $Cu_2(OH)_3NO_3$@ZnO/AGF; **(J)** HRTEM image and corresponding **(K)** SAED pattern of $Cu_2(OH)_3NO_3$@ZnO/AGF; **(L–O)** EDS mappings of C, Cu, N, O, and Zn elements in $Cu_2(OH)_3NO_3$@ZnO/AGF.

24 h for the *in situ* growth of ZIF-8 (ZIF-8@ZnO/AGF). Then, the ZIF-8@ZnO/AGF was soaked in $Cu(NO_3)_2$ solution (0.5 M) for 5–10 min to obtain $Cu_2(OH)_3NO_3$@ZnO/AGF.

Cell Culture

Human colon cells SW-48, NCM-460, and HCT-116 were obtained from the American Type Culture Collection (ATCC, Manassas, VA, United States). Cells were seeded in a 6-well plate for 24 h, and grown in Dulbecco's modified eagle medium containing 10% fetal bovine serum supplemented with 100 units ml^{-1} penicillin and 100 mg ml^{-1} streptomycin in an incubator at 37°C with 5% CO_2. The incubation solution was removed after growing to 90% confluence, then washed with PBS for three times to collect cells. The number of cells was counted by a hemocytometer. For real-time measurements of H_2O_2 in live cells, a three-electrode system was located on the plate containing 3 ml of PBS with the cell density of 5×10^6 cells ml^{-1}, and the amperometric responses of different live cells were recorded.

Cell Detection

Nikon Ti-U microscope was used to record the color changes of fluorescent dichlorofluorescein. The microscope was equipped with a CSU-X1 spinning-disk confocal unit (Yokogawa) and an EM-charge-coupled device camera (iXon+; Andor). The chronoamperometry (*i-t*) measurement was performed at an applied potential of −0.8 V vs. Ag/AgCl. After the baseline was stable, 10 µl of fMLP (1 mg ml^{-1}) was injected into wells (1 ml) of different types of colon cell, and then the responding currents were recorded to monitor the concentration of H_2O_2.

RESULTS AND DISCUSSION

Morphological and Structural Characterization

For the preparation of hierarchical nanohybrid microelectrode, the flexible GF has been used as the freestanding electrode substrate. As shown in **Figures 2A,B**, it can be observed that GF consists of stacked graphene nanosheets neatly aligned along the axis to form a layered structure with a uniform diameter of

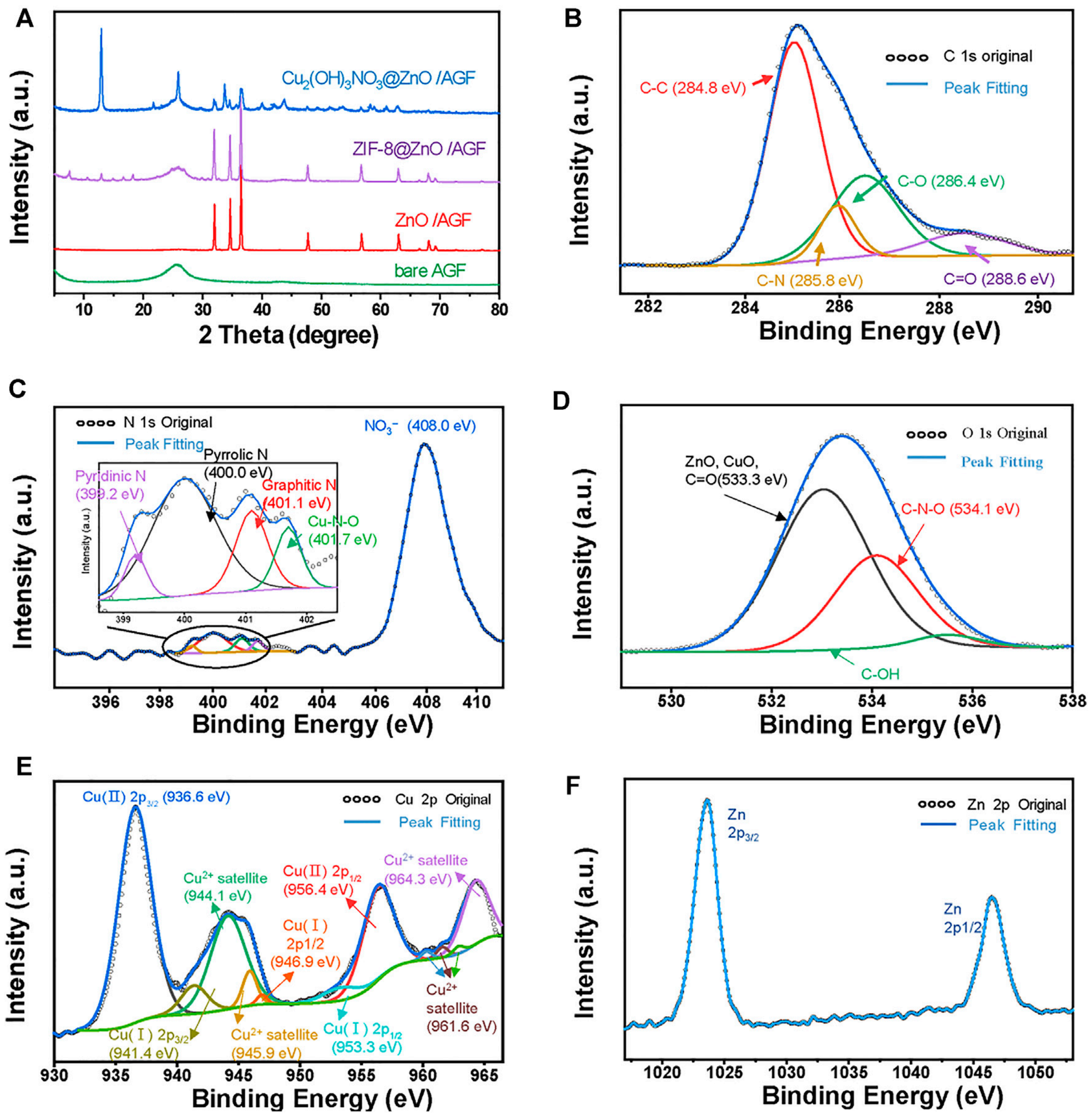

FIGURE 3 | (A) PXRD patterns of AGF, ZnO/AGF, ZIF-8@ZnO/AGF, and $Cu_2(OH)_3NO_3$@ZnO/AGF. High-resolution XPS spectra of **(B)** C 1s, **(C)** N 1s, **(D)** O 1s, **(E)** Cu 2p, and **(F)** Zn 2p regions in $Cu_2(OH)_3NO_3$@ZnO/AGF.

~50 μm and wrinkled structure (**Figure 2B**). The wrinkled structure endows the GF with a typical porous microstructure, which provides a larger specific surface area. For the subsequent growth of nanohybrids, the pristine GF is oxidized by chemical methods to introduce the desired functional groups on its surface to enhance its hydrophilicity. The ZnO is synthesized by a hydrothermal method with a rod-like morphology (**Figure 2C**), endowing ZnO/AGF with a larger surface area than bare AGF, which is conducive to easier loading of other active materials in subsequent derivatization steps. After the coordination of 2-methylimidazole with zinc ions, the ZnO nanorods are *in situ* converted to ZIF-8 with rhombic dodecahedron morphology. The average particle size of ZIF-8 is about 3 μm with smooth and uniform surface (**Figure 2D**). Then, ZIF-8 is used as a mediator to facilitate the growth of $Cu_2(OH)_3NO_3$ nanozyme on ZnO nanorods. As shown in **Figures 2E–H**, ZIF-8 with rhombic dodecahedron is etched into irregular particles, while the inner part of the particles still has a rod-shaped ZnO skeleton. The morphology of $Cu_2(OH)_3NO_3$@ZnO/AGF resembles rime in natural landscape (**Supplementary Figure S2**). The nanostructure of $Cu_2(OH)_3NO_3$@ZnO/AGF has also been investigated by transmission electron microscopy (TEM). **Figure 2I** reveals that $Cu_2(OH)_3NO_3$@ZnO/AGF possesses ultrathin nanosheet morphology. The ultrathin nanosheet morphology further endows the microelectrode with more exposed active sites and high electrocatalytic activity towards H_2O_2. High-resolution TEM (HRTEM) image shows that the lattice fringe with a crystal spacing of 0.248 and 0.153 nm matches well with the crystal plane ZnO (101) and $Cu_2(OH)_3NO_3$ (040), respectively (**Figure 2J**). The corresponding selected area electron diffraction (SAED) pattern presents some clear bright spots, further confirming the composition of $Cu_2(OH)_3NO_3$@ZnO/AGF (**Figure 2K**). The HAADF-STEM and the corresponding energy-dispersive spectroscopy (EDS) mappings demonstrate the distribution of C, N, O, Cu, and Zn in $Cu_2(OH)_3NO_3$@ZnO/AGF (**Figures 2L–O**), further confirming the successful synthesis of $Cu_2(OH)_3NO_3$@ZnO/AGF.

The composition of hierarchical nanohybrids has been investigated by powder x-ray diffraction (PXRD) analysis. **Figure 3A** shows that the PXRD patterns of AGF exhibit a broad peak at 26.4°, corresponding to the crystallographic planes of C (002). After decorating with ZnO, four distinct characteristic diffraction peaks are observed at 31.7°, 34.4°, 36.2°, and 47.4°, corresponding to the (100), (002), (101), and (102) planes of ZnO (PDF#36-1451) (Anila et al., 2021). A series of peaks with weak intensity appeared at 5°–20° in the ZIF-8@ZnO/AGF pattern, which can be attributed to the diffraction peaks of ZIF-8. The PXRD pattern of $Cu_2(OH)_3NO_3$@ZnO/AGF exhibits new peaks at 12.8°, 25.7°, 33.6°, 35.3°, 36.4°, 39.8°, 43.5°, and 49.2°, corresponding to the crystallographic planes of (001), (002), (−201), (−121), (121), (−202), (122), and (−131) of $Cu_2(OH)_3NO_3$ (PDF#15-0014) (**Supplementary Figure S3**), which are well consistent with the HRTEM characterization (Munyemana et al., 2020). Thermogravimetric analysis (TGA) under N_2 atmosphere provides stability information of $Cu_2(OH)_3NO_3$@ZnO/AGF, which shows a two-step weight loss (**Supplementary Figure S4**). TG curve shows a sharp weight loss beyond 225°C associated with the decomposition of $Cu_2(OH)_3NO_3$, followed by a long plateau until 700°C. The mass loss at 700°C corresponds to the reduction of ZnO by carbon at high temperature to generate carbon dioxide or carbon monoxide. These results demonstrate the successful synthesis of hierarchical nanohybrids on AGF.

The surface chemical states of different elements in $Cu_2(OH)_3NO_3$@ZnO/AGF have further been verified by x-ray photoelectron spectroscopy (XPS) analysis. The survey spectrum exhibits five predominant peaks at 285, 400, 533, 930, and 1,030 eV, assigned to C 1s, N 1s, O 1s, Cu 2p, and Zn 2p, respectively (**Supplementary Figure S5**). The surface atomic ratio of C:N:O:Cu:Zn is 29.87:8.42:44.46:10.59:6.65. The corresponding fitting curves of these elements are depicted in **Figures 3B–F**. The C 1s spectra can be deconvoluted into four components corresponding to different functional groups. The peaks at 284.8, 285.8, 286.4, and 288.6 eV are designated as C-C, C-N, C-O, and C=O, respectively. The high-resolution spectrum of N 1s shows a strong intensity of peak at 408.0 eV and a smaller intensity of peak in the range of 399–402 eV. The strong intensity of peak is assigned to NO_3^- and the smaller intensity of peak region is deconvoluted into four peaks at 399.2, 400.0, 401.1, and 401.7 eV, which are further assigned to pyridinic N, pyrrolic N, graphitic N, and N-oxide/Cu, respectively (Zhuang et al., 2014). The O 1s spectrum of $Cu_2(OH)_3NO_3$@ZnO/AGF can be deconvoluted into three spin-orbit doublets, the fitting peaks at a binding energy of 533.3, 534.1, and 535.0 eV corresponding well with C=O, C-N-O, and C-O respectively. The Cu 2p core level XPS spectrum exhibits the Cu^{2+} $2p_{3/2}$ peak at 936.6 eV and the Cu^{2+} $2p_{1/2}$ peaks at 956.4 eV, with an energy gap of 19.8 eV, indicating that Cu exhibits only one oxidation valence of +2. The Zn 2p core level XPS spectrum exhibits the Zn $2p_{3/2}$ peak at 1,023 eV and the Zn $2p_{1/2}$ peaks at 1,047 eV, with an energy gap of 24 eV. All XPS results indicated that the successful synthesis of hierarchical dual nanozyme $Cu_2(OH)_3NO_3$@ZnO on AGF.

Electrochemical Characterization of Microelectrodes

The electrochemical properties of the stepwise fabrication process of nanohybrid microelectrodes, such as current responses (I_{pa}) and peak-to-peak separation (ΔE_p), are studied by CV in 0.1 M KCl solution containing 5.0 mM $[Fe(CN)_6]^{3-/4-}$. The voltammetric curves for ZIF-8@ZnO/AGF and $Cu_2(OH)_3NO_3$@ZnO/AGF exhibit a pair of well-defined quasi-reversible peaks (**Figure 4A**), which signify the oxidation/reduction process by outer-sphere electrode reaction of the redox couple. However, ZnO/AGF does not show a pair of well-defined quasi-reversible peaks, which is due to the insulator characteristics of ZnO. The current response is sequentially improved by modification with ZIF-8@ZnO and $Cu_2(OH)_3NO_3$@ZnO nanohybrids, respectively. The oxidation and reduction peak currents of $Cu_2(OH)_3NO_3$@ZnO/AGF are approximately 24 times higher than that of ZnO/AGF. However, the peak separation is increased after modification, which should be attributed to the non-porous structure of $Cu_2(OH)_3NO_3$. Furthermore, CVs of the stepwise fabrication process of nanohybrid microelectrodes in contact with 0.1 M KCl solution containing 5.0 mM $[Fe(CN)_6]^{3-/4-}$ at different scan rates from 0.01 to 0.09 V s^{-1} are recorded. **Figures 4B,C** and **Supplementary Figure S6** show that the current response increases with the increase in scan rate. As seen in **Figures 4B,C** inset and **Supplementary Figure S6** inset, plots of anodic (I_{pa}) peak currents against square root of scan rate show the great linearity, suggesting that the reaction mechanism is diffusion-controlled. Based on the Randles-Sevick equation, the electroactive surface area of the modified electrodes is calculated to be 0.0091, 0.0351, and 0.2995 cm^2 for ZnO/AGF, ZIF-8@ZnO/AGF, and $Cu_2(OH)_3NO_3$@ZnO/AGF, respectively. Compared to ZnO/AGF, the peak current densities of the modified electrodes are drastically increased in the order of ZnO/GF < ZIF-8@ZnO/GF < $Cu_2(OH)_3NO_3$@ZnO/AGF, indicating that decorating $Cu_2(OH)_3NO_3$@ZnO on the surface of AGF-based microelectrodes remarkably improves the electroactive surface area and increases the rate of electron transfer between active sites and the redox species in solution.

To investigate the charge transport mechanisms of various fabricated microelectrodes, electrochemical impedance spectroscopy (EIS) measurements are conducted using $[Fe(CN)_6]^{3-/4-}$ as redox probes, where the Nyquist plots can be fitted by an equivalent circuit (**Supplementary Figure S7**). Typically, the semicircular part of the Nyquist plot in the EIS coincides with the electron transfer-dependent process, where the diameter represents the interfacial charge transfer resistance (R_{ct}), and the low frequency of the linear part is attributed to the

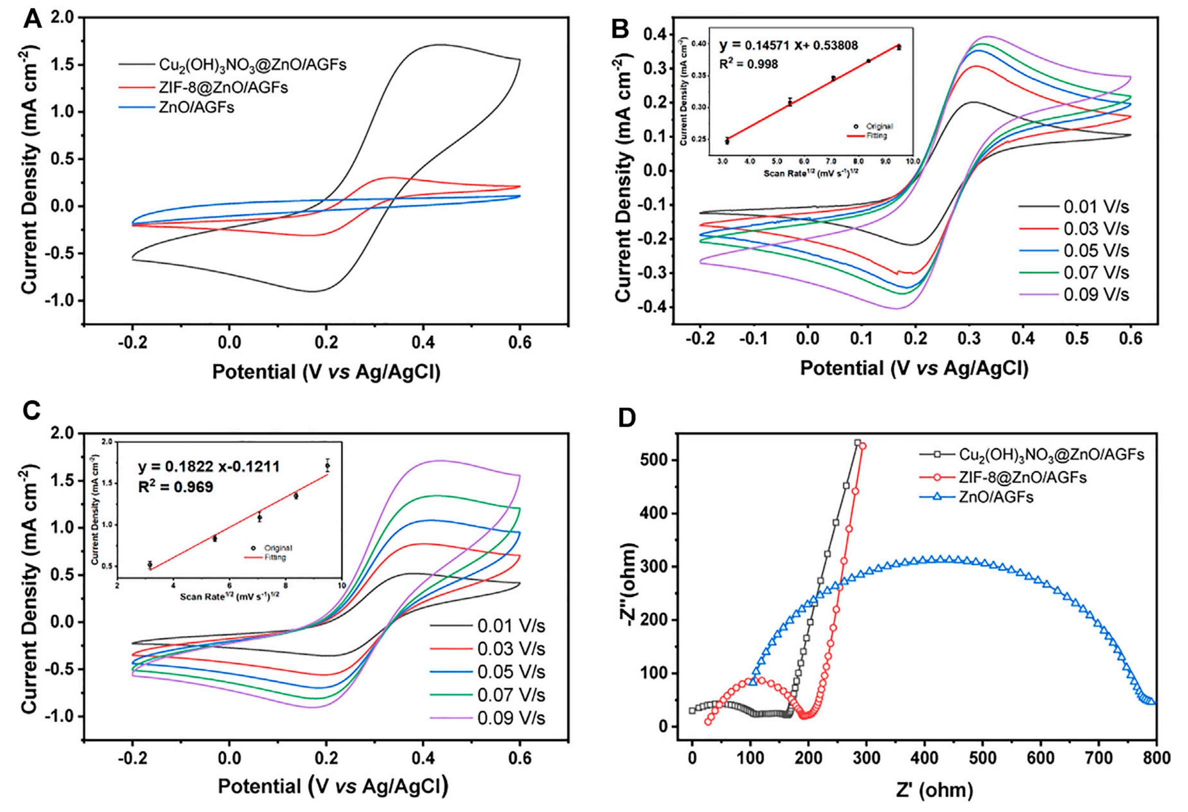

FIGURE 4 | (A) CV curves of different microelectrodes in 0.1 M KCl solution containing 5.0 mM $[Fe(CN)_6]^{3-/4-}$. Scan rate: 0.09 V s^{-1}. CV measurements of **(B)** ZIF-8@ZnO/AGF and **(C)** $Cu_2(OH)_3NO_3$@ZnO/AGF are performed with $[Fe(CN)_6]^{3-/4-}$ as the redox probe at different scan rates from 0.01 to 0.09 V s^{-1}. **(D)** Nyquist plots of ZnO/AGF, ZIF-8@ZnO/AGF, and $Cu_2(OH)_3NO_3$@ZnO/AGF in 5 mM $[Fe(CN)_6]^{3-/4-}$ solution. Frequency range: 0.01–10^6 Hz.

diffusion-dependent process (Ciucci 2019). As shown in **Figure 4D**, there are larger R_{ct} values of 504.4 Ω for ZnO/AGF. The R_{ct} decreases to 141.4 Ω after ZIF-8 *in situ* grown on ZnO/AGF, which should be attributed to the porosity of ZIF-8 facilitating charge transport to GF by ions in solution. When the $Cu_2(OH)_3NO_3$ is bonded to ZnO/AGF by chemical etching of ZIF-8, the R_{ct} value is further decreased to 52.8 Ω, which is due to the positive charge of $[Cu_2(OH)_3]^+$ (the electrostatic attraction between positively charged`` $[Cu_2(OH)_3]^+$ and negatively charged $[Fe(CN)_6]^{3-/4-}$ facilitates the charge transfer of $[Fe(CN)_6]^{3-/4-}$ on the electrode surface). All the above EIS results indicate that the electrochemical sensing platforms for H_2O_2 are fabricated successfully as expected.

Electrochemical Sensing Performance of the $Cu_2(OH)_3NO_3$@ZnO/AGF Microelectrode

Considering the unique hierarchical structure of $Cu_2(OH)_3NO_3$@ZnO/AGF, the electrocatalytic performance of different microelectrodes towards H_2O_2 has been investigated by CV measurements in 0.1 M PBS (pH 7.4) solution containing 5 mM H_2O_2. As shown in **Figure 5A**, the CV curve of $Cu_2(OH)_3NO_3$@ZnO/AGF shows a clear reduction peak at −0.8 V, and the peak current density is much higher than that of ZnO/AGF and ZIF-8@ZnO/AGF. With the addition of H_2O_2, the reduction current increases linearly, indicating that $Cu_2(OH)_3NO_3$@ZnO/AGF possesses high electrocatalytic activity towards H_2O_2 (**Figure 5B**). However, CV curves of ZIF-8@ZnO/AGF and ZnO/AGF show relatively low activity towards H_2O_2 (**Supplementary Figure S8**). This result can be explained in the following two aspects: (I) From a structure point of view, after *in situ* conversion of ZnO nanorods to ZIF-8, ZIF-8@ZnO/AGF possesses a larger surface area and adsorption capacity due to the unique porous structure of the metal-organic framework, benefiting the catalytic activity of ZIF-8@ZnO/AGF towards H_2O_2. In addition, a redox couple of Cu^{2+}/Cu^+ is introduced by the metal salt impregnation method to etch ZIF-8 into rime-like $Cu_2(OH)_3NO_3$, which greatly improves the catalytic activity of $Cu_2(OH)_3NO_3$@ZnO/AGF. (II) From an electrochemical perspective, the charge transfer from $Cu_2(OH)_3NO_3$@ZnO to AGF microelectrode leads to a slight change in the electronic structure of $Cu_2(OH)_3NO_3$, which further improves their electrocatalytic performance. In terms of the catalytic mechanisms, the exposure of Cu^{2+}/Cu^+ sites can act as a facilitating center to promote H_2O_2 activation. For the reaction process on $Cu_2(OH)_3NO_3$, $Cu_2\ (OH)_3NO_3$ is partially reduced *in situ* into $Cu_2(OH)NO_3$ during electrochemical treatment (Yi et al., 2020). Then, the

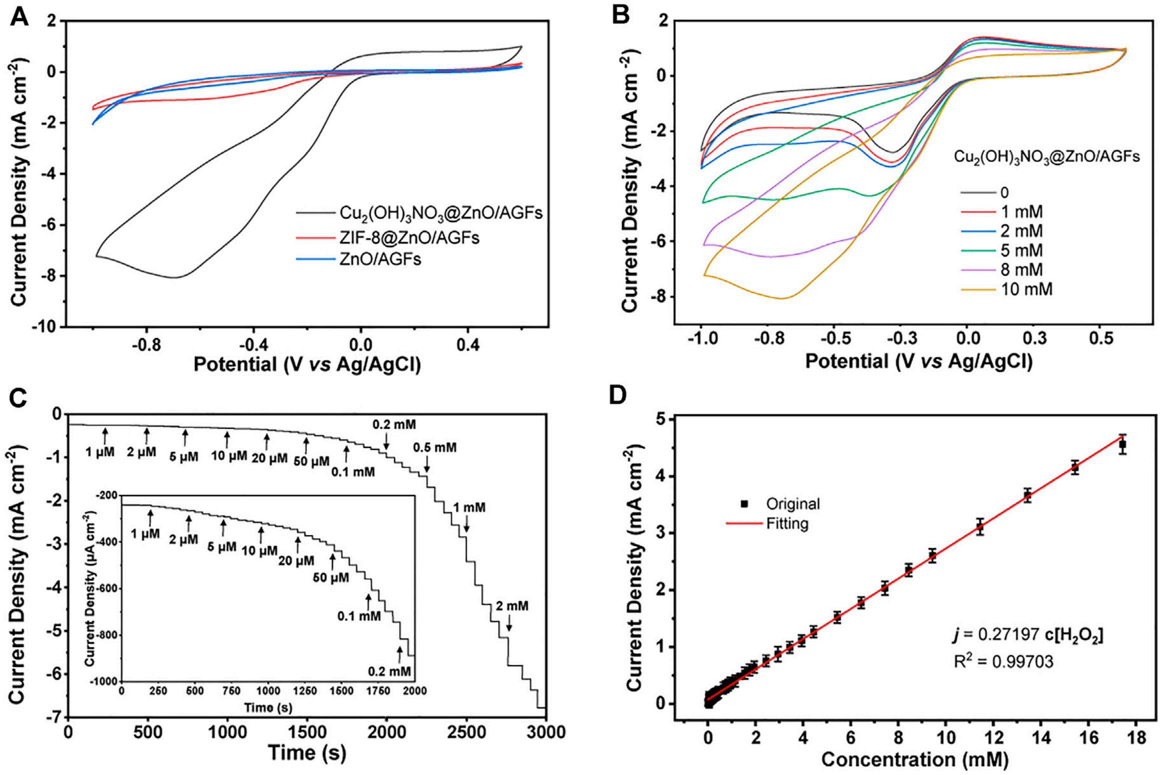

FIGURE 5 | (A) CV curves of ZnO/AGF, ZIF-8@ZnO/AGF, and $Cu_2(OH)_3NO_3$@ZnO/AGF in 0.1 M PBS solution (pH 7.4) containing 5 mM H_2O_2. **(B)** CV curves of $Cu_2(OH)_3NO_3$@ZnO/AGF in 0.1 M PBS solution (pH 7.4) containing different concentrations of H_2O_2. Scan rate: 50 mV s^{-1}. **(C)** Amperometric current responses of $Cu_2(OH)_3NO_3$@ZnO/AGF upon stepwise addition of different concentrations gradients of H_2O_2 in stirred 0.1 M PBS solution (pH 7.4). Inset: Amperometric current responses of $Cu_2(OH)_3NO_3$@ZnO/AGF at low concentrations. Applied potential: −0.8 V. **(D)** Linear relationship between the corresponding current and H_2O_2 concentration.

generated $Cu_2(OH)NO_3$ are oxidized again to $Cu_2(OH)_3NO_3$ in the presence of H_2O_2. The mechanism process of $Cu_2(OH)_3NO_3$@ZnO/AGF to catalyze the decomposition of H_2O_2 can be presented as follows (Ling et al., 2020):

$$Cu_2(OH)_3NO_3 + 2e^- \rightarrow Cu(OH)NO_3 + 2OH^- \quad (1)$$

$$Cu_2(OH)NO_3 + H_2O_2 \rightarrow Cu_2(OH)_3NO_3 \quad (2)$$

Furthermore, the amperometric measurements are applied to evaluate the sensitivity of $Cu_2(OH)_3NO_3$@ZnO/AGF upon stepwise addition of different concentrations of H_2O_2 in 0.1 M PBS solution with stirring (pH 7.4), where an optimal applied potential of −0.8 V is selected for testing. As shown in **Figure 5C**, a fast response signal can be observed with the addition from 1 μM to 2 mM H_2O_2, reaching 95% of the steady-state current within 3 s. The significant drop of the reduction current can be attributed to the rapid diffusion and activation of H_2O_2 on the active sites of the rime-like $Cu_2(OH)_3NO_3$ with high specific surface, which could facilitate the fast electron transfer kinetics. **Figure 5D** shows that the proposed electrochemical sensor displays a wide linear range of the reduction current versus H_2O_2 concentration in the range of 1 μM–17.4 mM with a sensitivity value of 272 μA cm^{-2} mM^{-1}. The calculated LOD is as low as 1 μM (S/N = 3). These results are better than or comparable with those of most H_2O_2 sensors reported in the recently published literature (**Supplementary Table S1**).

Anti-interference is another essential parameter of H_2O_2 sensors. In this work, the injection of 1.0 mM interfering species, i.e., K^+, Na^+, H_2S, UA, AA, Glu, DA, GSH, DA, U, A, C, and G almost does not cause distinctive amperometric current density changes compared with 0.2 mM H_2O_2 under the negative applied potential of −0.8 V, demonstrating the preferential selectivity of $Cu_2(OH)_3NO_3$@ZnO/AGF towards the detection of H_2O_2 (**Figure 6A**). The reproducibility of the proposed flexible electrode is also evaluated by successive monitoring of 0.2 mM H_2O_2 with six modified electrodes prepared under the same procedure. The relative standard derivation value of their amperometric current responses is measured to be only 5% (**Figure 6B** inset). In addition, the current response maintains 90% of its initial current value after 4 weeks by periodically recording the current response to 0.2 mM H_2O_2, indicative of its good long-term stability (**Figure 6B**).

Monitoring of H_2O_2 in Live Cells

Colon cancer is a clinically common human gastrointestinal malignancy with the third highest incidence worldwide and the fifth highest mortality rate among all malignancies in China, and the only way to improve survival rate as well as to

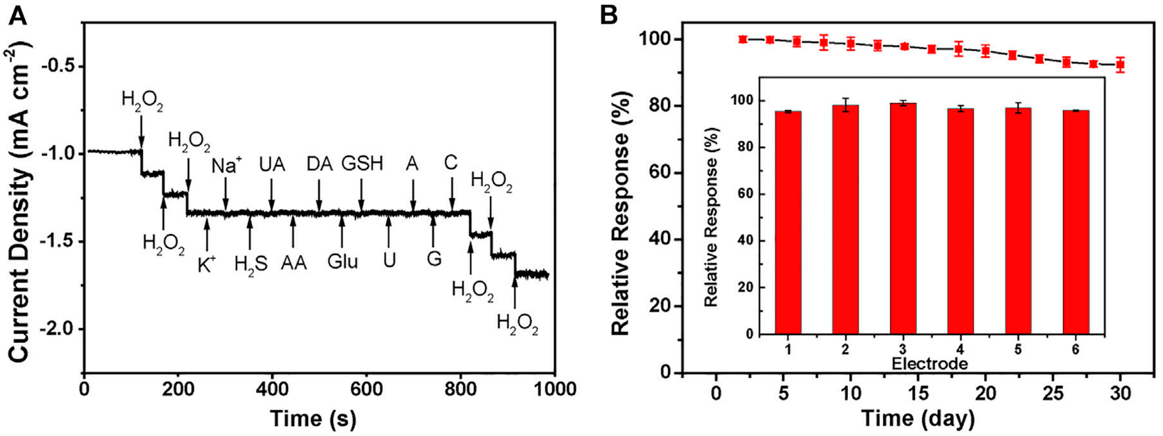

FIGURE 6 | (A) Amperometric current response curves of $Cu_2(OH)_3NO_3$@ZnO/AGF to 0.2 mM H_2O_2, KCl, NaCl, H_2S, UA, AA, Glu, DA, GSH, DA, U, A, C, and G. Applied potential: −0.8 V. **(B)** Current responses of six different $Cu_2(OH)_3NO_3$@ZnO/AGF to 0.2 mM H_2O_2. Inset: Current responses of $Cu_2(OH)_3NO_3$@ZnO/AGF to 0.2 mM H_2O_2 for 4 weeks.

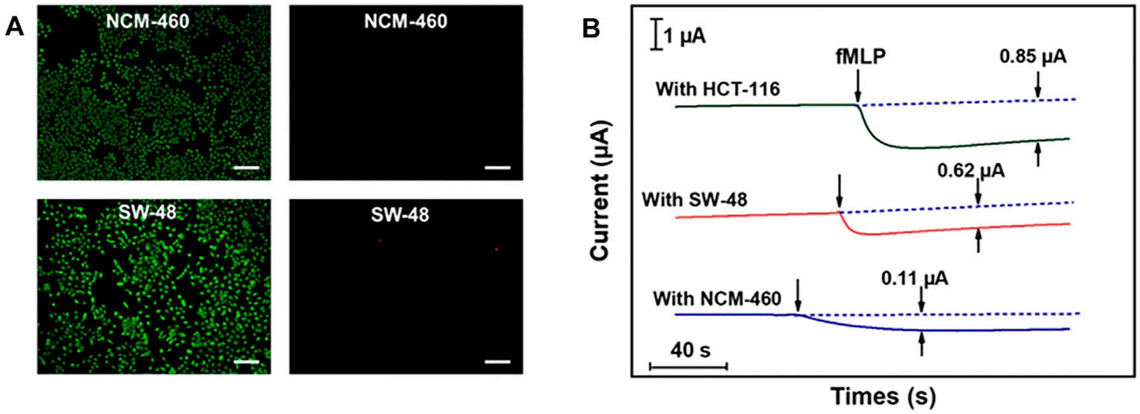

FIGURE 7 | (A) Live and dead body fluorescence images of SW-48 and NCM-460 cells, detected by Calcein-AM/PI, with Calcein-AM staining surviving cells green and PI staining dead cells red. Scale bar, 100 µm. **(B)** Amperometric current responses of $Cu_2(OH)_3NO_3$@ZnO/AGF to the addition of 10 µM fMLP in test solution containing 5.0 × 10^6 NCM-460, SW-48, and HCT-116 cells.

escape from these deadly attacks is through early diagnosis (Wang et al., 2021). Therefore, the practical application of the proposed $Cu_2(OH)_3NO_3$@ZnO/AGF microelectrode has been explored for tracking intracellular H_2O_2 fluctuations in different human colon cells, i.e., colon cancer cells (SW-48 and HCT-116), and epithelial cell lines from normal colon (NCM-460). Cytotoxicity tests show that $Cu_2(OH)_3NO_3$@ZnO/AGF microelectrode does not induce cell death (apoptosis and necrosis) in SW-48 and NCM-460 cells (**Figure 7A**). fMLP is a kind of chemotactic peptide, used as a stimulator to initiate the release of H_2O_2 from living cells. The amperometric curves will exhibit an obvious reduced current density after injecting an amount of fMLP in the test cell containing different human body cells. Afterwards, the released H_2O_2 is quantified by electrochemical measurement using $Cu_2(OH)_3NO_3$@ZnO/AGF as probe. **Figure 7B** shows the amperometric current responses to the addition of 10 µM fMLP in test solution containing 5.0 × 10^6 cells. The amperometric current values increase by 0.11, 0.62, and 0.85 µA for NCM-460, SW-48, and HCT-116, respectively. These results indicate that human colon cancer cells produce more extracellular H_2O_2 than normal cells, which is consistent with the titration measurement observation (**Supplementary Table S2**). Thus, the $Cu_2(OH)_3NO_3$@ZnO/AGF-based electrochemical sensor can be applied to effectively differentiate normal and tumor cells for cancer cell detection.

CONCLUSION

In summary, we have developed a new type of high-performance flexible microelectrode based on MOF-mediated hierarchical nanohybrid-modified AGF, and used it in the electrochemical sensing system. Our results show that due to the synergistic effects of dual nanozymatic activity of rime-like hierarchical $Cu_2(OH)_3NO_3$@ZnO as well as their unique structural and electrical properties, excellent sensitivity, selectivity, long-term stability, reproducibility, and practicality, the $Cu_2(OH)_3NO_3$@ZnO/AGF microelectrode shows remarkable electrochemical sensing performance towards H_2O_2. The resultant electrochemical sensing platforms can be used for real-time tracking of H_2O_2 released from different kinds of live colon cells, which provides an effective strategy to distinguish cancer cells from the normal one for clinical diagnosis. An extension to more complex systems can be foreseen, upon conducting process/device engineering with this system. We envision that this work will open up a new pathway for the design of an assisting technology for cancer diagnosis and treatments in the future to hold great potential in the development of advanced implantable and wearable smartsensor for clinical practices.

DATA AVAILABILITY STATEMENT

The original contributions presented in the study are included in the article/**Supplementary Material**, further inquiries can be directed to the corresponding author.

AUTHOR CONTRIBUTIONS

WH: Conceptualization, Methodology, Investigation, and Writing—original draft. YX: Methodology, Validation, Investigation, Data curation, and Formal analysis. YS: Conceptualization, Writing—review and editing, Supervision, Project administration, and Funding acquisition.

FUNDING

This work is supported by National Natural Science Foundation of China (Project No. 51772110 and 82102513).

ACKNOWLEDGMENTS

We thank all members of the laboratory for their technical support and academic discussions.

SUPPLEMENTARY MATERIAL

The Supplementary Material for this article can be found online at: https://www.frontiersin.org/articles/10.3389/fchem.2022.873187/full#supplementary-material

REFERENCES

Asif, M., Aziz, A., Ashraf, G., Iftikhar, T., Sun, Y., Xiao, F., et al. (2022). Unveiling Microbiologically Influenced Corrosion Engineering to Transfigure Damages into Benefits: A Textile Sensor for H2O2 Detection in Clinical Cancer Tissues. *Chem. Eng. J.* 427, 131398. doi:10.1016/j.cej.2021.131398

Asif, M., Aziz, A., Ashraf, G., Wang, Z., Wang, J., Azeem, M., et al. (2018a). Facet-Inspired Core-Shell Gold Nanoislands on Metal Oxide Octadecahedral Heterostructures: High Sensing Performance toward Sulfide in Biotic Fluids. *ACS Appl. Mater. Inter.* 10, 36675–36685. doi:10.1021/acsami.8b12186

Asif, M., Aziz, A., Azeem, M., Wang, Z., Ashraf, G., Xiao, F., et al. (2018b). A Review on Electrochemical Biosensing Platform Based on Layered Double Hydroxides for Small Molecule Biomarkers Determination. *Adv. Colloid Interf. Sci.* 262, 21–38. doi:10.1016/j.cis.2018.11.001

Asif, M., Aziz, A., Wang, Z., Ashraf, G., Wang, J., Luo, H., et al. (2019). Hierarchical CNTs@CuMn Layered Double Hydroxide Nanohybrid with Enhanced Electrochemical Performance in H2S Detection from Live Cells. *Anal. Chem.* 91, 3912–3920. doi:10.1021/acs.analchem.8b04685

Aziz, A., Asif, M., Ashraf, G., Azeem, M., Majeed, I., Ajmal, M., et al. (2019a). Advancements in Electrochemical Sensing of Hydrogen Peroxide, Glucose and Dopamine by Using 2D Nanoarchitectures of Layered Double Hydroxides or Metal Dichalcogenides. A Review. *Microchim Acta* 186, 671. doi:10.1007/s00604-019-3776-z

Aziz, A., Asif, M., Ashraf, G., Farooq, U., Yang, Q., and Wang, S. (2021a). Trends in Biosensing Platforms for SARS-CoV-2 Detection: A Critical Appraisal against Standard Detection Tools. *Curr. Opin. Colloid Interf. Sci.* 52, 101418. doi:10.1016/j.cocis.2021.101418

Aziz, A., Asif, M., Ashraf, G., Iftikhar, T., Hu, J., Xiao, F., et al. (2021b). Boosting Electrocatalytic Activity of Carbon Fiber@fusiform-like Copper-Nickel LDHs: Sensing of Nitrate as Biomarker for NOB Detection Copper-Nickel LDHs: Sensing of Nitrate as Biomarker for NOB Detection. *J. Hazard. Mater.* 422, 126907. doi:10.1016/j.jhazmat.2021.126907

Aziz, A., Asif, M., Azeem, M., Ashraf, G., Wang, Z., Xiao, F., et al. (2019b). Self-stacking of Exfoliated Charged Nanosheets of LDHs and Graphene as Biosensor with Real-Time Tracking of Dopamine from Live Cells. *Analytica Chim. Acta* 1047, 197–207. doi:10.1016/j.aca.2018.10.008

Cai, W., Lai, J., Lai, T., Xie, H., and Ye, J. (2016). Controlled Functionalization of Flexible Graphene Fibers for the Simultaneous Determination of Ascorbic Acid, Dopamine and Uric Acid. *Sensors Actuators B: Chem.* 224, 225–232. doi:10.1016/j.snb.2015.09.079

Chen, L., Ding, X., Zeng, J., Jiao, L., Wu, C., Wang, Y., et al. (2019). A Three-Dimensional Hollow Graphene Fiber Microelectrode with Shrink-Effect-Enabled Enzyme Immobilization for Sensor Applications. *Sci. Bull.* 64, 718–722. doi:10.1016/j.scib.2019.04.031

Cheng, Y., Wang, R., Sun, J., and Gao, L. (2015). A Stretchable and Highly Sensitive Graphene-Based Fiber for Sensing Tensile Strain, Bending, and Torsion. *Adv. Mater.* 27, 7365–7371. doi:10.1002/adma.201503558

Ciucci, F. (2019). Modeling Electrochemical Impedance Spectroscopy. *Curr. Opin. Electrochemistry* 13, 132–139. doi:10.1016/j.coelec.2018.12.003

Cui, Y., Li, B., He, H., Zhou, W., Chen, B., and Qian, G. (2016). Metal-Organic Frameworks as Platforms for Functional Materials. *Acc. Chem. Res.* 49, 483–493. doi:10.1021/acs.accounts.5b00530

Ding, X., Bai, J., Xu, T., Li, C., Zhang, H.-M., and Qu, L. (2016). A Novel Nitrogen-Doped Graphene Fiber Microelectrode with Ultrahigh Sensitivity for the Detection of Dopamine. *Electrochemistry Commun.* 72, 122–125. doi:10.1016/j.elecom.2016.09.021

Guo, X., Lin, C., Zhang, M., Duan, X., Dong, X., Sun, D., et al. (2021). 2D/3D Copper-Based Metal-Organic Frameworks for Electrochemical Detection of Hydrogen Peroxide. *Front. Chem.* 9, 743637. doi:10.3389/fchem.2021.743637

Huang, L., Niu, Y., Li, R., Liu, H., Wang, Y., Xu, G., et al. (2019). VOx Quantum Dots with Multienzyme-Mimic Activities and the Application in Constructing a Three-Dimensional (3D) Coordinate System for Accurate Discrimination of the Hydrogen Peroxide over a Broad Concentration Range. *Anal. Chem.* 91, 5753–5761. doi:10.1021/acs.analchem.8b05923

Huang, L., Santiago, D., Loyselle, P., and Dai, L. (2018). Graphene-Based Nanomaterials for Flexible and Wearable Supercapacitors. *Small* 14, 1800879. doi:10.1002/smll.201800879

Ji, S., Jiang, B., Hao, H., Chen, Y., Dong, J., Mao, Y., et al. (2021). Matching the Kinetics of Natural Enzymes with a Single-Atom Iron Nanozyme. *Nat. Catal.* 4, 407–417. doi:10.1038/s41929-021-00609-x

Labib, M., Sargent, E. H., and Kelley, S. O. (2016). Electrochemical Methods for the Analysis of Clinically Relevant Biomolecules. *Chem. Rev.* 116, 9001–9090. doi:10.1021/acs.chemrev.6b00220

Li, P., Sun, X.-Y., and Shen, J.-S. (2021). A Multi-Catalytic Sensing for Hydrogen Peroxide, Glucose, and Organophosphorus Pesticides Based on Carbon Dots. *Front. Chem.* 9, 713104. doi:10.3389/fchem.2021.713104

Lin, M., Song, P., Zhou, G., Zuo, X., Aldalbahi, A., Lou, X., et al. (2016). Electrochemical Detection of Nucleic Acids, Proteins, Small Molecules and Cells Using a DNA-Nanostructure-Based Universal Biosensing Platform. *Nat. Protoc.* 11, 1244–1263. doi:10.1038/nprot.2016.071

Ling, P., Cheng, S., Chen, N., Qian, C., and Gao, F. (2020). Nanozyme-Modified Metal-Organic Frameworks with Multienzymes Activity as Biomimetic Catalysts and Electrocatalytic Interfaces. *ACS Appl. Mater. Inter.* 12, 17185–17192. doi:10.1021/acsami.9b23147

Lippert, A. R., Van de Bittner, G. C., and Chang, C. J. (2011). Boronate Oxidation as a Bioorthogonal Reaction Approach for Studying the Chemistry of Hydrogen Peroxide in Living Systems. *Acc. Chem. Res.* 44, 793–804. doi:10.1021/ar200126t

Munyemana, J. C., Chen, J., Wei, X., Ali, M. C., Han, Y., and Qiu, H. (2020). Deep Eutectic Solvent-Assisted Facile Synthesis of Copper Hydroxide Nitrate Nanosheets as Recyclable Enzyme-Mimicking Colorimetric Sensor of Biothiols. *Anal. Bioanal. Chem.* 412, 4629–4638. doi:10.1007/s00216-020-02712-7

Peng, Y., Lin, D., Justin Gooding, J., Xue, Y., and Dai, L. (2018). Flexible Fiber-Shaped Non-enzymatic Sensors with a Graphene-Metal Heterostructure Based on Graphene Fibres Decorated with Gold Nanosheets. *Carbon* 136, 329–336. doi:10.1016/j.carbon.2018.05.004

Sajjad, A., Bhatti, S. H., Ali, Z., Jaffari, G. H., Khan, N. A., Rizvi, Z. F., et al. (2021). Photoinduced Fabrication of Zinc Oxide Nanoparticles: Transformation of Morphological and Biological Response on Light Irradiance. *ACS Omega* 6, 11783–11793. doi:10.1021/acsomega.1c01512

Shen, X., Liu, W., Gao, X., Lu, Z., Wu, X., and Gao, X. (2015). Mechanisms of Oxidase and Superoxide Dismutation-like Activities of Gold, Silver, Platinum, and Palladium, and Their Alloys: A General Way to the Activation of Molecular Oxygen. *J. Am. Chem. Soc.* 137, 15882–15891. doi:10.1021/jacs.5b10346

Sun, Y., He, K., Zhang, Z., Zhou, A., and Duan, H. (2015). Real-Time Electrochemical Detection of Hydrogen Peroxide Secretion in Live Cells by Pt Nanoparticles Decorated Graphene-Carbon Nanotube Hybrid Paper Electrode. *Biosens. Bioelectron.* 68, 358–364. doi:10.1016/j.bios.2015.01.017

Sun, Y., Zheng, H., Wang, C., Yang, M., Zhou, A., and Duan, H. (2016). Ultrasonic-Electrodeposition of PtPd Alloy Nanoparticles on Ionic Liquid-Functionalized Graphene Paper: Towards a Flexible and Versatile Nanohybrid Electrode. *Nanoscale* 8, 1523–1534. doi:10.1039/C5NR06912B

Wang, H., Wan, K., and Shi, X. (2018). Recent Advances in Nanozyme Research. *Adv. Mater.* 31, 1805368. doi:10.1002/adma.201805368

Wang, J., Liu, L., Cai, Y., Gao, Y., Guo, Z., Yu, F., et al. (2021). Trends in the Age-Related Incidence of colon and Rectal Cancers in China, 2005-2015. *Dig. Liver Dis.* 53, 908–914. doi:10.1016/j.dld.2021.01.009

Wang, L., Wang, L., Zhang, Y., Pan, J., Li, S., Sun, X., et al. (2018). Weaving Sensing Fibers into Electrochemical Fabric for Real-Time Health Monitoring. *Adv. Funct. Mater.* 28, 1804456. doi:10.1002/adfm.201804456

Wu, J., Wang, X., Wang, Q., Lou, Z., Li, S., Zhu, Y., et al. (2019). Nanomaterials with Enzyme-like Characteristics (Nanozymes): Next-Generation Artificial Enzymes (II). *Chem. Soc. Rev.* 48, 1004–1076. doi:10.1039/C8CS00457A

Xiao, F., Wang, L., and Duan, H. (2016). Nanomaterial Based Electrochemical Sensors for *In Vitro* Detection of Small Molecule Metabolites. *Biotechnol. Adv.* 34, 234–249. doi:10.1016/j.biotechadv.2016.01.006

Xin, G., Yao, T., Sun, H., Scott, S. M., Shao, D., Wang, G., et al. (2015). Highly Thermally Conductive and Mechanically Strong Graphene Fibers. *Science* 349, 1083–1087. doi:10.1126/science.aaa6502

Xin, G., Zhu, W., Deng, Y., Cheng, J., Zhang, L. T., Chung, A. J., et al. (2019). Microfluidics-Enabled Orientation and Microstructure Control of Macroscopic Graphene Fibres. *Nat. Nanotech* 14, 168–175. doi:10.1038/s41565-018-0330-9

Xu, Q., Yuan, H., Dong, X., Zhang, Y., Asif, M., Dong, Z., et al. (2018). Dual Nanoenzyme Modified Microelectrode Based on Carbon Fiber Coated with AuPd Alloy Nanoparticles Decorated Graphene Quantum Dots Assembly for Electrochemical Detection in Clinic Cancer Samples. *Biosens. Bioelectron.* 107, 153–162. doi:10.1016/j.bios.2018.02.026

Xu, Z., Peng, L., Liu, Y., Liu, Z., Sun, H., Gao, W., et al. (2016). Experimental Guidance to Graphene Macroscopic Wet-Spun Fibers, Continuous Papers, and Ultralightweight Aerogels. *Chem. Mater.* 29, 319–330. doi:10.1021/acs.chemmater.6b02882

Yi, J. D., Xie, R., Xie, Z. L., Chai, G. L., Liu, T. F., Chen, R. P., et al. (2020). Highly Selective CO 2 Electroreduction to CH 4 by *In Situ* Generated Cu 2 O Single-Type Sites on a Conductive MOF: Stabilizing Key Intermediates with Hydrogen Bonding. *Angew. Chem. Int. Ed.* 59, 23641–23648. doi:10.1002/anie.202010601

Zeng, J., Xu, R., Jiao, L., Wang, Y., Chen, L., Windle, C. D., et al. (2019). A 3D-Graphene Fiber Electrode Embedded with Nitrogen-Rich-Carbon-Coated ZIF-67 for the Ultrasensitive Detection of Adrenaline. *J. Mater. Chem. B* 7, 5291–5295. doi:10.1039/C9TB01223K

Zhang, T., Xing, Y., Song, Y., Gu, Y., Yan, X., Lu, N., et al. (2019). AuPt/MOF-Graphene: A Synergistic Catalyst with Surprisingly High Peroxidase-like Activity and its Application for H2O2 Detection. *Anal. Chem.* 91, 10589–10595. doi:10.1021/acs.analchem.9b01715

Zhang, Y., Li, Y., Ming, P., Zhang, Q., Liu, T., Jiang, L., et al. (2016). Ultrastrong Bioinspired Graphene-Based Fibers via Synergistic Toughening. *Adv. Mater.* 28, 2834–2839. doi:10.1002/adma.201506074

Zhao, A., She, J., Manoj, D., Wang, T., Sun, Y., Zhang, Y., et al. (2020). Functionalized Graphene Fiber Modified by Dual Nanoenzyme: Towards High-Performance Flexible Nanohybrid Microelectrode for Electrochemical Sensing in Live Cancer Cells. *Sensors Actuators B: Chem.* 310, 127861. doi:10.1016/j.snb.2020.127861

Zhao, A., She, J., Xiao, C., Xi, J., Xu, Y., Manoj, D., et al. (2021). Green and Controllable Synthesis of Multi-Heteroatoms Co-doped Graphene Fiber as Flexible and Biocompatible Microelectrode for *In Situ* Electrochemical Detection of Biological Samples. *Sensors Actuators B: Chem.* 335, 129683. doi:10.1016/j.snb.2021.129683

Zhuang, X., Zhang, F., Wu, D., and Feng, X. (2014). Graphene Coupled Schiff-Base Porous Polymers: Towards Nitrogen-Enriched Porous Carbon Nanosheets with Ultrahigh Electrochemical Capacity. *Adv. Mater.* 26, 3081–3086. doi:10.1002/adma.201305040

Conflict of Interest: The authors declare that the research was conducted in the absence of any commercial or financial relationships that could be construed as a potential conflict of interest.

The reviewer SW declared a shared affiliation with the authors HW and YX to the handling editor at the time of the review.

frontiers in Chemistry

REVIEW
published: 31 March 2022
doi: 10.3389/fchem.2022.881172

Advanced Metal–Organic Frameworks-Based Catalysts in Electrochemical Sensors

Yana Chen[1], Zhiquan Yang[1], Huilin Hu[1], Xinchen Zhou[1], Feng You[1], Chu Yao[1], Fang Jun Liu[1], Peng Yu[1], Dan Wu[1], Junlong Yao[1], Ruofei Hu[2]*, Xueliang Jiang[1]* and Huan Yang[1]*

[1]Hubei Key Laboratory of Plasma Chemistry and Advanced Materials, School of Materials Science and Engineering, Wuhan Institute of Technology, Wuhan, China, [2]Department of Food Science and Chemical Engineering, Hubei University of Arts and Science, Xiangyang, China

Developing efficient catalysts is vital for the application of electrochemical sensors. Metal–organic frameworks (MOFs), with high porosity, large specific surface area, good conductivity, and biocompatibility, have been widely used in catalysis, adsorption, separation, and energy storage applications. In this invited review, the recent advances of a novel MOF-based catalysts in electrochemical sensors are summarized. Based on the structure–activity–performance relationship of MOF-based catalysts, their mechanism as electrochemical sensor, including metal cations, synthetic ligands, and structure, are introduced. Then, the MOF-based composites are successively divided into metal-based, carbon-based, and other MOF-based composites. Furthermore, their application in environmental monitoring, food safety control, and clinical diagnosis is discussed. The perspective and challenges for advanced MOF-based composites are proposed at the end of this contribution.

Keywords: metal–organic frameworks (MOFs), electrochemical sensors, composites, sensitivity, stability

Edited by:
Fei Xiao,
Huazhong University of Science and Technology, China

Reviewed by:
Xinlong Tian,
Hainan University, China
Bokai Liao,
Guangzhou University, China

Correspondence:
Ruofei Hu
rhuvip@hbuas.edu.cn
Xueliang Jiang
jiangxl@wit.edu.cn
Huan Yang
yangh@wit.edu.cn

Specialty section:
This article was submitted to Nanoscience,
a section of the journal Frontiers in Chemistry

Received: 22 February 2022
Accepted: 08 March 2022
Published: 31 March 2022

Citation:
Chen Y, Yang Z, Hu H, Zhou X, You F, Yao C, Liu FJ, Yu P, Wu D, Yao J, Hu R, Jiang X and Yang H (2022) Advanced Metal–Organic Frameworks-Based Catalysts in Electrochemical Sensors.
Front. Chem. 10:881172.
doi: 10.3389/fchem.2022.881172

INTRODUCTION

With the development of science and technology, the demand for substance detection is becoming more selective (Sharma and Mutharasan, 2013). Sensors can effectively respond to an electrical, optical, or other signal in the presence of the analyte, and then, it will convert the physical parameters to complete the detection of the substance (Justino et al., 2015). The sensor system includes an identification element, a sensor, and a detector, which can be divided into several sensors (Chiu et al., 2017; Gogotsi et al., 2017; Zhou et al., 2017; Li S. et al., 2018; Shankar et al., 2018; Liu et al., 2021; Lin et al., 2022; Lu et al., 2022; Zamzami et al., 2022). Among them, electrochemical sensors, with simplicity, strong selectivity, and high sensitivity, have attracted wide attention (Yang S et al., 2021). Recently, nanomaterials with the advantages of high specific surface area, excellent catalytic performance, conductivity, and biocompatibility, can help the electrochemical sensors amplify signals and improve the sensitivity of the sensors as well as reduce the detection range (Yang Q et al., 2017). An efficient electrochemical sensor requires two requirements: high specificity of the signal tag and an electrode with superior sensitivity and stability (Yang ZH et al., 2017; Yang et al., 2022).

Metal–organic frameworks (MOFs) are known as coordination polymer networks or porous coordination polymers (Rosi, 2003; Zhang and Lin, 2014). The structure of different target molecules can be designed by selecting metal coordination nodes and organic junctions. Importantly, a metal-center (e.g., electrical, catalytic, or magnetic), an organic ligand (e.g., luminescent, fluorescent, or chiral), or a combination of both may produce a universal framework function that exceeds the accessible porosity (Liu et al., 2018). However, the slow mass transfer, low conductivity, and instable structure of MOF as catalysts limit their practical application (Ma and Zhu, 2020). MOF-based composites present higher surface area and richer active sites and exhibit highly ordered pore-like arrangement, which can expose active sites to a greater extent and make them have higher catalytic activity (Qin et al., 2018; Ma et al., 2020a; Ma et al., 2020b).

Recently, different effective strategies have been proposed to modify MOFs for improved electrocatalytic behavior, mechanical properties, and stability. Generally, metal nanoparticles, with the advantages of superior conductivity and high surface area, can be used to increase the electron transfer rate (Samadi-Maybodi et al., 2015; Da Silva et al., 2016). Thus, MOF–metal nanocomposites present versatility, high stability, and dispersibility. As a result, MOF composite with metal particles is an effective route to design the superior electrochemical sensors (Meng et al., 2018). MOFs composited with noble metals, transition metals, and two different metal cations are regarded as effective strategies to prepare sensing materials with higher stability and catalytic efficiency (Nan et al., 2020; Yang et al., 2020). Furthermore, MOFs show low electronic conductivity, electrical reactivity, and stability in aqueous media, which limit their applications in electrochemical sensors. Assembling MOFs with conductive materials, such as graphene, carbon nanotubes, carbon blocks, and carbon nanofibers, is an effective strategy (Wang et al., 2017; Lai et al., 2019; Li L et al., 2019; Zhou Y. et al., 2020). In addition, doping graphene with heteroatom can further improve the catalytic activity of MOF-based carbon materials (Deng et al., 2020a). Similar to carbon nanomaterials, conductive polymers present excellent electrical conductivity, low cost, and ease of polymerization that are ideal materials to overcome poor electrical conductivity of MOFs (Liu et al., 2020). The introduced nonnatural polymers, such as new functional groups, can significantly improve the structure and properties of MOFs. Moreover, by integrating heme into MOFs, the dimerization and oxidative self-destruction of heme are improved, contributing to their optimum detection performance and stability (Zhang et al., 2015).

In this review, advances of MOF-based catalysts in electrochemical sensors are comprehensively summarized. Based on the structure–activity–performance relationship of MOF-based catalysts, we introduce the mechanism of MOF-based catalysts as electrochemical sensors, including metal cations, synthetic ligands, and structure. Then, the MOF-based composites are successively divided into metal-based, carbon-based, and other MOF-based composites. Furthermore, their application in environmental monitoring, food safety control, and clinical diagnosis is discussed. The perspective and challenges for advanced MOF-based composites are proposed at the end of this contribution.

MECHANISM OF METAL–ORGANIC FRAMEWORKS-BASED CATALYSTS IN ELECTROCHEMICAL SENSOR

MOFs, with high porosity, biocompatibility, and superior specific surface area, have been widely applied in catalysis, adsorption, separation, and energy storage (Jiawen et al., 2019). The mechanism of MOFs in electrochemical sensors is as follows: 1) Signal amplification: loading different functional materials and signal molecules on MOFs is beneficial to the electrochemical detection (Yi et al., 2016; Liu et al., 2020). 2) Catalysts and signal probes: MOFs present periodic porous structure by coordination of metal cations and organic ligands, which can induce rich catalytic activity and redox activity centers, attributing to superior electrochemical properties (Liu et al., 2018). 3) Size selection: the macroporous structure of MOFs is helpful to easily introduce the guest materials and perform the size selection of substance molecules (Zhu and Xu, 2014; Zhang et al., 2019). 4) MOFs can generate interaction forces with analytes (including Van der Waals force, covalent bond, and p–p interaction), resulting in the improved selectivity for electrochemical detection (Carrasco, 2018).

In this review, the mechanism of MOFs in catalysts and signal probes, including the effects of catalytic active centers and redox active centers on electrochemical sensors, is mainly discussed (Liu et al., 2018). MOF materials with metal cations and ligands can provide the desired active sites, which deserve high catalytic activity for various detection molecules. In the electrochemical sensors, metal ions can be used as charge carriers. The interaction between the sensing material and target analyte is beneficial to enhance its selectivity at room temperature (Li et al., 2021). Furthermore, the active metal ions in MOF-based nanomaterials can be used as the catalysts, which can improve the activity of the oxidation–reduction reaction, resulting in the amplified electrochemical signals and the improved sensitivity (Liu et al., 2018). Furthermore, the metal cations in MOFs also act as coordination centers to form an infinite crystal network. For example, common active metal nodes, such as Co, Cu, Zn, and Cr, and their redox activity can enhance the catalytic ability of MOFs (Liu et al., 2020). In addition, organic ligands with redox activity are also attributed to the catalytic active sites of MOFs (Yang et al., 2022). In general, the organic ligands for MOFs can be divided into chemical ligands and biological ligands (Smaldone et al., 2010). For instance, porphyrin, heme, and amino acids are common organic ligands, which present affinity to metal cations and combine well with them.

The superior structure of MOFs also plays an important effect on the boosted electrochemical activity. Their flexible and highly porous structure can be helpful to the easy diffusion of analyte molecules, facilitating the interaction between the host and analyte (Liao et al., 2018; Yang et al., 2022). Furthermore, MOFs, with a porous structure and superior specific surface area, act as a good carrier to form composite materials, resulting in the improved electrochemical activity (Kitagawa et al., 2004; Cui et al., 2013; Wang C et al., 2018; Li D et al., 2019; Wang Y et al., 2020). Therefore, regulating the structure of MOFs is an effective route to adjust its composition and structure, leading to larger surface area, higher porosity, and better electrochemical activity (He et al., 2021).

METAL–ORGANIC FRAMEWORK-BASED COMPOSITES

MOFs, with the merits of diverse chemical combinations, rich metal active sites, and adjustable structure, have attracted wide attention (Li et al., 2020). However, the slow mass transfer, low conductivity, and instable structure of MOFs as catalysts limit their practical application (Ma and Zhu, 2020). Various strategies are adopted to improve the electrocatalytic behavior, mechanical properties, and stability of MOFs. Designing MOF–metal, MOF–carbon, and other MOF-based nanocomposites is an effective strategy to induce MOFs with high porosity and ordered crystal pores (Bradshaw et al., 2012; Moon et al., 2013; Qiang et al., 2013; Falcaro et al., 2014; Li et al., 2016).

Metal–Organic Framework–Metal Nanocomposites

Due to the limited pore size of MOFs, the size of synthesized particles will be confined to nanoscale. Metal nanoparticles, with the advantages of superior conductivity and high surface area, can be used to increase the electron transfer rate (Ghaffari et al., 2015; Da Silva et al., 2016). Generally, MOF–metal nanocomposites present versatility, high stability, and dispersibility. Therefore, MOF composite with metal particles is an effective route to design the superior electrochemical sensors (Meng et al., 2018).

The size and morphology of noble metal nanoparticles can reduce the overpotential of oxidation and reduction, which can effectively regulate the electrocatalytic properties (Azad and Ganesan, 2010; Gupta and Ganesan, 2015; Sonkar and Ganesan, 2015). Recently, grafting noble metal nanoparticles on MOFs is widely applied as new electrode materials for various electrochemical and biochemical sensors (Turner et al., 2008; Sabo et al., 2007; Zhu et al., 2017; Mosleh et al., 2017). For instance, a porous rhombic dodecahedron structure of Ag@ zeolitic imidazolate framework-67 is synthesized, which presents a strong electrocatalytic activity and low detection limit toward H_2O_2 reduction (Dong et al., 2019). Interestingly, combined with photocatalytic technology and electrochemical sensing, a novel synthetic method of Ag/MIL-160 hybrid is developed to detect p-nitrophenol (**Figure 1A**) (Liu Q. et al., 2019). The generated charge carrier in the Ag/MIL-160 organic molecule initiates its photocatalytic functionality (**Figure 1B**), the high sensitivity for pollutant reduction is dictated by the photocatalytic activity of Ag nanoparticles, and selective electron migration on the electrode interface (**Figure 1C**). In another example, Ag/MIL-101 composite-modified GCE is reported to be useful for monitoring tryptophan (Peng et al., 2016). The existed p–p accumulation between the ligands of MOF and tryptophan increases the diffusion of analyte molecules. Furthermore, the electromagnetic field generated by the noble metal nanoparticles promotes the accumulation of tryptophan molecules on the surface of MIL-101 (Yang J et al., 2015).

Transition metals, such as Cu, Fe, Co, Ni, Zn, and Mg, present the merits of low price and high efficiency; they have been widely introduced to composites with MOF (Li et al., 2019; Hosseini et al., 2016). For instance, Cu(II)-anchored MOFs are constructed as signal probes (**Figure 1D**) (Zhang et al., 2020). This prepared composite presents an excellent glucose oxidation activity and amplified electrochemical signal, which can be ascribed to the oxidation of glucose by the generated Cu(III) from the oxidation of Cu(II) (**Figure 1E**). Furthermore, ionic conductive metal–organic framework sensor arrays act as charge carriers, which can directly and selectively interact with analytes (Lu et al., 2020). For example, a series of IC-MOF sensor arrays are constructed by modulating various metal nodes (Cu, Co, Ni, Zn, and Mg) and organic ligands (H_2TCPP, H_2THPP, and H_4BTEC) (**Figure 1F**) (Li et al., 2021). Due to the strong interaction between H_2S and Cu^{2+}, the synthesized material can generate CuS during the detection process, resulting in an irreversible reaction, which can be adopted to detect volatile sulfide (**Figures 1G,H**).

The bonding between two different metal cations can increase electrical conductivity and improve the electrocatalytic efficiency, which is ascribed to different oxidation potentials and associated electron configurations (Yang et al., 2018). Therefore, a unique synergistic effect between two different metal elements is helpful in obtaining higher stability and efficiency (Wen et al., 2015; Jiang et al., 2018). Recently, bimetallic nanoparticles, including Fe, Co, Ni, or Cu, with a cooperative effect have been developed to optimize the performance of MOFs (Tang et al., 2016; Wang Z. et al., 2018). For instance, Au@Cu MOF nanomaterials with unique structures can effectively increase the number of binding sites on the polymer network, obtaining a more sensitive electrochemical sensor (Hatamluyi et al., 2020). The advanced core–shell heterostructure is introduced to fabricate composites by encapsulating metal oxides or metal nanoparticles as a core and MOFs as a shell (Paolo et al., 2016; Wengert et al., 2017; Yang Q. et al., 2017). The metal oxides or metal nanoparticle cores (e.g., magnetic, electrical, and catalytic properties, etc.) act as a catalyst, and MOFs shells (e.g., multiple coordination sites, ordered crystalline pores, structural adaptability advantages, and flexibility, etc.) act as a recognition agent for analog molecular sieves, may be combined. These advanced structures can greatly improve their anti-aggregation stability and avoid undesirable dissolution or corrosion in the photocatalytic process, resulting in boosted catalytic and adsorption properties (Liu and Tang, 2013; Kempahanumakkagari et al., 2018). For instance, Fe-MOF@ Fe_3O_4@C core–shell nanostructured composite is composed of iron-based MOF and mesoporous Fe_3O_4@C (Zhang et al., 2017). Specific aptamer metal ions (e.g., Pb^{2+} and As^{3+}) are attached to the constructed nanocomposites by supramolecular stacking and hydrogen bond interactions, exhibiting good anti-interference characteristics and detection of Pb^{2+} and As^{3+} ions in spiked river water.

Metal–Organic Framework–Carbon Nanomaterial Composites

The weak electronic conductivity, electrical reactivity, and low stability in aqueous media of MOFs limit their applications in electrochemical sensors. To overcome these technical shortcomings, they can be assembled with conductive materials, such as graphene, carbon nanotubes, carbon blocks, and carbon nanofibers, which are introduced to be assembled with MOFs (Wang et al., 2017; Lai et al., 2019; Li Y et al., 2019;

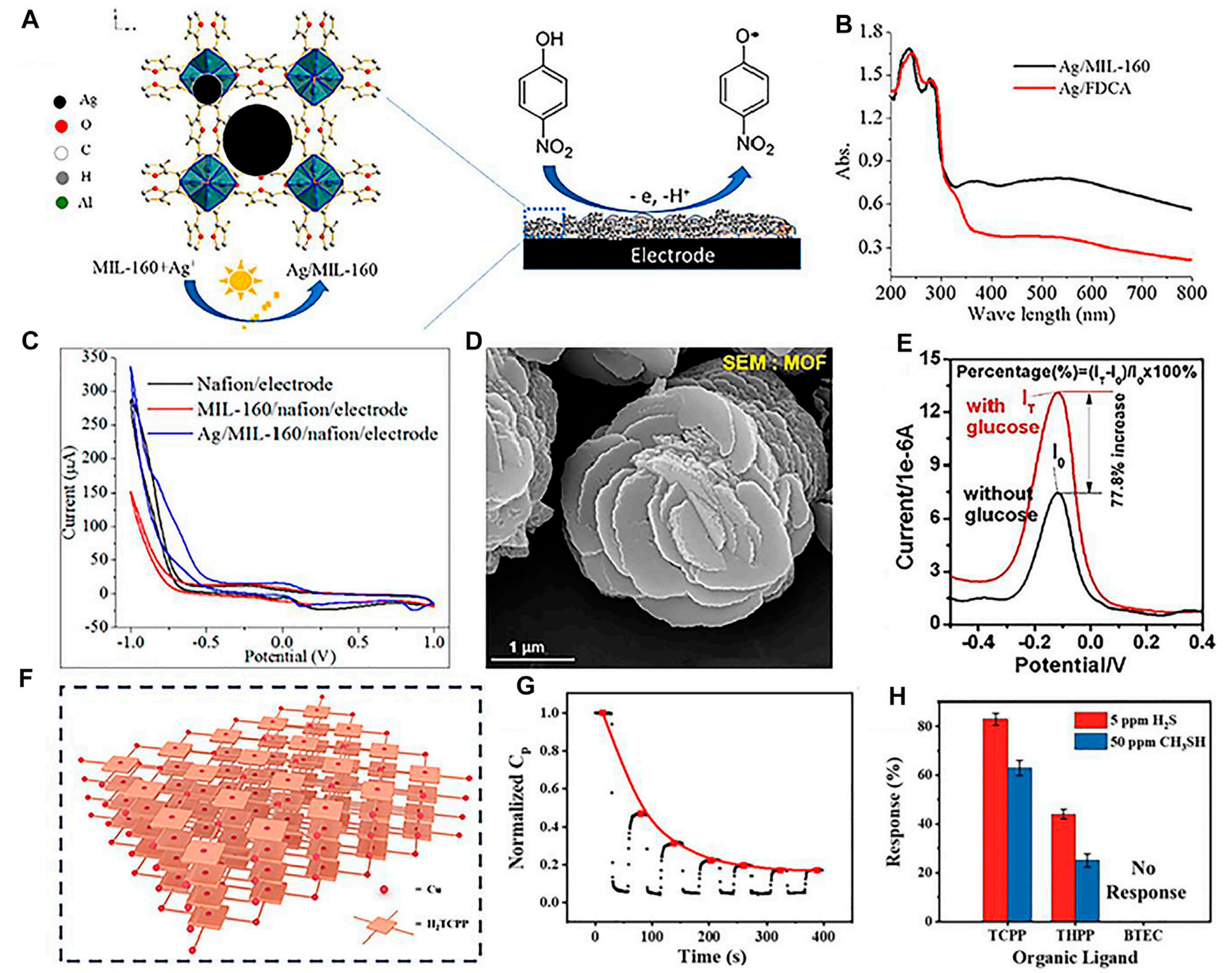

FIGURE 1 | (A) Synthetic process of Ag/MIL-160; **(B)** UV–vis diffuse reflectance spectra of prepared composites; **(C)** CV curves of different electrodes at a scan rate of 50 mV s^{-1} in an electrolyte with *p*-NP. Reproduced with permission (Liu et al., 2019). Copyright 2019, ACS. Scanning electron microscope (SEM) image **(D)** and DPV responses without and with 4 mM glucose **(E)** of Cu(II)-anchored MOFs. Reproduced with permission (Zhang et al., 2020). Copyright 2020, Elsevier. Scheme **(F)**, normalized capacitance response **(G)** of the Cu-TCPP IC-MOF sensor and **(H)** Cu-X IC-MOF sensors to 5 ppm H_2S and 50 ppm CH_3SH. Reproduced with permission (Li et al., 2021). Copyright 2020, Wiley.

Zhou et al., 2020). Among which, graphene oxide/reduced graphene oxides/carbon nanotubes as unique conductive additives can improve the electrical conductivity and mechanical strength of MOFs (Zhang et al., 2014; Liu et al., 2016).

The simplest way to improve the conductivity of MOF materials is to mix them with highly conductive carbon paste electrodes (Yang et al., 2014; Wang et al., 2013). The pore structure of carbon paste electrode-modified MOFs composite can allow the analyte to be pre-concentrated from the bulk solution onto the electrode surface, which helps to improve the selectivity of the analyte (Doménech et al., 2007). For instance, Co-based metal–organic coordination polymer-modified carbon paste electrodes are developed to analyze the electrocatalytic performance of redox glutathione (**Figure 2A**) (Yuan et al., 2014). This constructed composite exhibits excellent electrocatalytic oxidation–reduction and high selectivity of glutathione (**Figures 2B,C**). Furthermore, carbon paste electrodes modified with MOFs can be used for the electrocatalytic oxidation and detection of nitrite (Zhou et al., 2014). The modified material demonstrates improved sensitivity and selectivity. However, high background currents and continuous use of the electrode material will lack stability and reproducibility. Carbon nanotubes, with the advantages of the high aspect ratio, large specific surface area, and good mechanical properties and electrical properties, are widely used as electrode materials (Chen and Dai, 2013). Single-walled carbon nanotubes (SWCNTs) are covalently functionalized with benzoic acid and transition metal ions, which can form a 3D porous inorganic–organic hybrid framework, resulting in good electrochemical performance and reproducibility. Therefore,

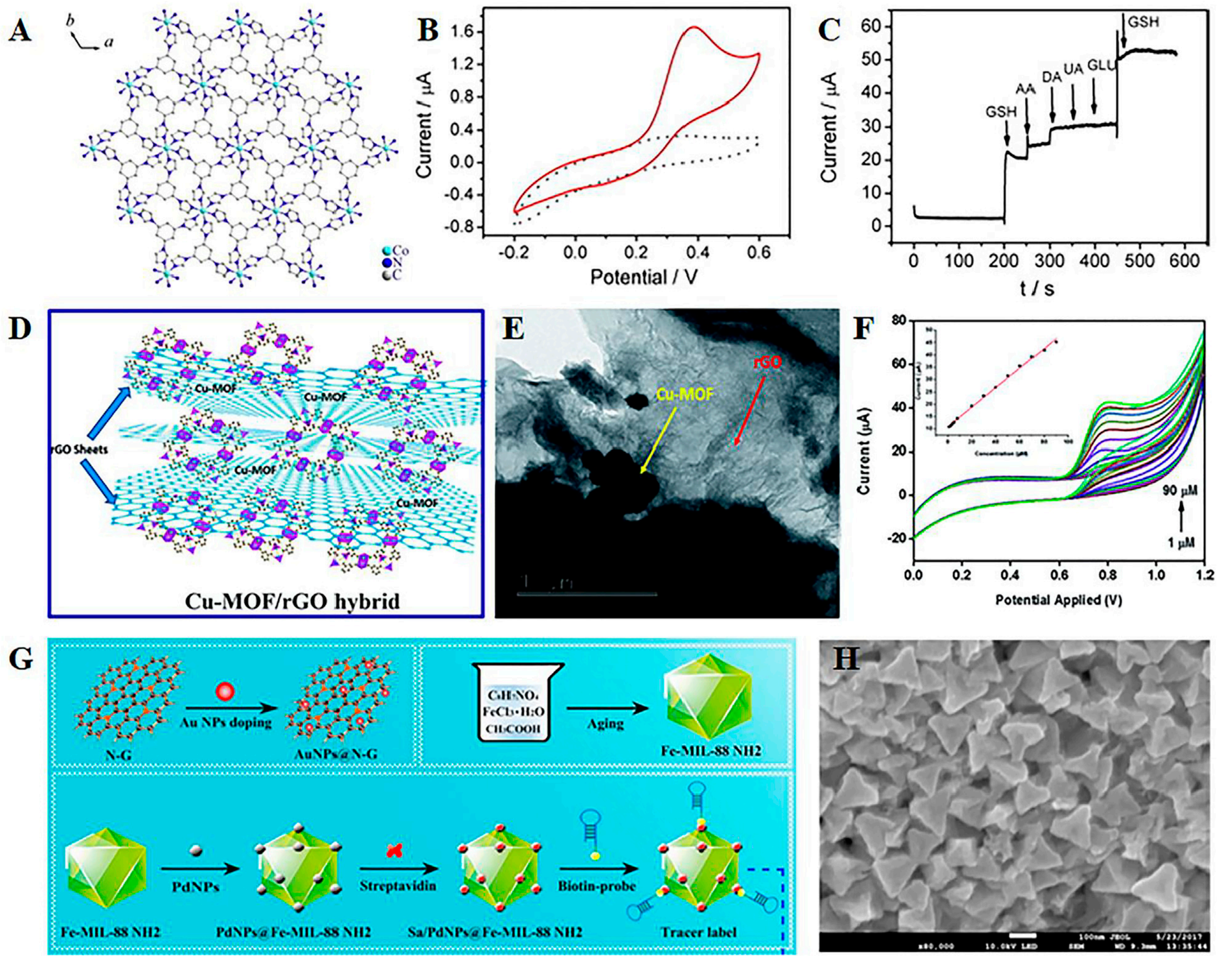

FIGURE 2 | (A) Illustration of the structure of metal–organic coordination polymers with 1,3,5-tris (1-imidazolyl) benzene and transition element Co^{2+} (Co-MOCP), CVs **(B)**, and interference test **(C)** of the Co-MOCP/carbon paste electrode in the different solution. Reproduced with permission (Yuan et al., 2014). Copyright 2014, Elsevier. Schematic structure **(D)**, transmission electron microscope (TEM) images **(E)**, and CV curves at different nitrite concentrations **(F)** of the Cu-MOF/rGO hybrid. Reproduced with permission (Saraf et al., 2016). Copyright 2016, RSC. **(G)** Synthetic route of different composites; **(H)** field emission scanning electron microscope image of PdNPs@Fe-MOFs. Reproduced with permission (Li et al., 2018). Copyright 2018, Elsevier.

SWCNT–MOF composite is an effective electrochemical sensor material for organophosphorus pesticides.

Similarly, graphene is a well-known advanced two-dimensional nanomaterial with advantages of large specific surface area and ultrafast carrier mobility (Chen et al., 2013). Therefore, MOF/graphene (or graphene oxide) composites have been developed in various electrochemical sensing applications. A copper-based MOF is proposed by combining with graphene for electrochemical sensing of H_2O_2 and ascorbic acid (Yang T et al., 2015). Due to the hydrogen bond between Cu-MOF and graphene, p-p stacking, and Cu-O coordination, the synthesized nanocomposites exhibit high stability and good anti-interference properties detect H_2O_2 and ascorbic acid in various carbohydrates. Furthermore, rGO can be introduced to the composite with MOF for detection of nitrite 1 (**Figure 2D**) (Saraf et al., 2016). rGO can greatly improve the conductivity of MOF in the composite. The positive synergistic effects exist between Cu-MOF crystals and rGO nanosheets (**Figure 2E**), and these can be attributed to the improved electrocatalytic performance of the prepared electrochemical sensor electrode (**Figure 2F**).

In general, nitrogen-doped graphene can present more defect sites and lower aggregation of graphene sheets, which is beneficial to increase the biocompatibility of graphene sheets and functionalize easily with noble metal nanoparticles (Chen et al., 2016). A signal amplification strategy is developed to construct AuNPs-functionalized nitrogen-doped graphene as capture probes, and PdNPs@Fe-MOFs as nanocarriers (**Figures 2G,H**) (Li et al., 2018). This assembled structure can initiate the next reaction process, which induces numerous tracer indicators anchored onto the sensing interfaces, contributing to the superior specificity and recovery in spiked serum samples. In

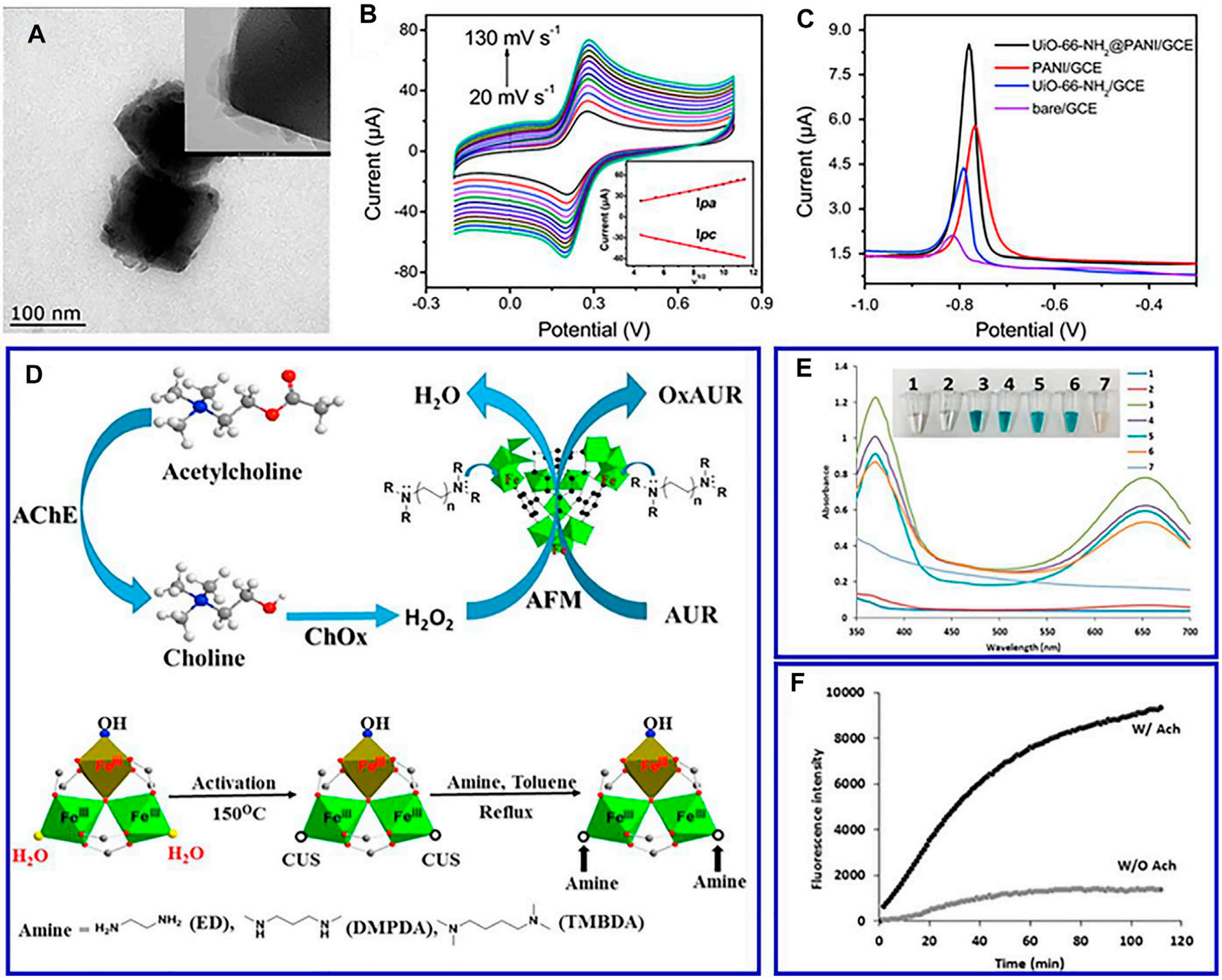

FIGURE 3 | TEM images **(A)**, CV in 0.1 mol L^{-1} KCl solution with 1 mmol L^{-1} $Fe(CN)_6^{3-/4-}$ at different scan rates **(B)**, and differential pulse voltammograms of 100 μg L^{-1} Cd(ii) **(C)** of prepared UiO-66-NH_2@PANI. Reproduced with permission (Wang et al., 2017). Copyright 2017, RSC. **(D)** Schematic representation of the route and coordinatively unsaturated grafted MIL-100(Fe); **(E)** comparison of the peroxidase-mimic activity of different samples; **(F)** time-dependent fluorescence intensities. Reproduced with permission (Valekar et al., 2018). Copyright 2018, Elsevier.

addition, black phosphorus can bind with antibodies and enhance electron transfer; thus, the black phosphorus electrochemical sensor based on magnetic covalent organic frameworks is developed to detect prostate-specific antigens, which can be widely applied in detecting biomarkers of cancer (Pandey et al., 2021).

Other Metal–Organic Framework-Based Composites

Similar to carbon nanomaterials, conductive polymers present excellent electrical conductivity, low cost, and ease of polymerization that are ideal materials to overcome poor electrical conductivity of MOFs (Liu et al., 2020; Deng et al., 2020b). For instance, MOF–polyaniline composite (UiO-66-NH_2@PANI) was synthesized by polymerizing a conductive PANI in the presence of pre-synthesized UiO-66-NH_2 (Wang et al., 2017). The composite exhibited excellent electrochemical redox performance of Cd^{2+} ions, which is related to the synergistic effect between UiO-66-NH_2 and PANI (**Figures 3A–C**). Furthermore, the large surface area and the existing chelating groups in MOF increase the number of conduction paths and increase the electron transfer rate between the solution and the composite electrode surface. The introduced nonnatural polymers, such as new functional groups, can significantly improve the structure and properties of MOFs. MIL-53(Fe), a flexible material consisting of iron oxides and phthalate, is functionalized by polymethyl methacrylate and can be used to make electrochemical sensor materials for detecting melamine in milk samples (Yang Z et al., 2021). In addition, MOFs have the merits of abundant pores, large surface area, and good biocompatibility, which can effectively prevent the aggregation and leakage of enzymes and improve the biological activity and stability of enzymes (Liu et al., 2020). Therefore, MOFs are usually used to immobilize enzyme and other biomacromolecules.

Heme is a famous natural metalloporphyrin, which acts as the active center of hemoglobin. Due to the reversible conversion of Fe(III)/Fe(II), heme presents significant peroxidase-like catalytic activity (Reuillard et al., 2017). However, its catalytic life is limited due to dimerization and oxidative self-destruction in the aqueous medium (Li et al., 2018). Anchoring hemin on a suitable carrier material is an effective strategy to remedy these shortcomings (Wang et al., 2016). MOFs with a regular porous structure are ideal candidates for hemin fixation (Zhang et al., 2015). By integrating heme into MOFs, the dimerization and oxidative self-destruction of heme are improved, contributing to the optimum catalytic performance and chemical stability of MOFs. For instance, a novel amine-grafted MOFs is designed as a promising alternative to peroxidase enzyme (**Figure 3D**) (Valekar et al., 2018). The synergetic effect of the enhanced negative potential and tuned molecular size of the grafted diamine are attributed to the improved fluorescent assay of choline and acetylcholine, which effectively detect choline and acetylcholine levels in real samples of milk and serum (**Figures 3E,F**).

APPLICATION OF METAL–ORGANIC FRAMEWORK-BASED CATALYSTS IN ELECTROCHEMICAL SENSORS

Environmental Monitoring

With rapid urbanization and industrialization, the ecological environment is suffering from serious damage (He et al., 2021). Developing satisfactory electrochemical sensors is an effective route to detect harmful chemicals, especially the detection of toxic gases with low concentrations and heavy metal ions in water (Dorda et al., 2003; Aslam et al., 2014; Zhang et al., 2017). MOF-based composites can be used to transform harmful chemicals in air and water into electrochemistry as fine-sensing materials. However, the formation of MOF inorganic clusters is highly dependent on the geometry, length, and connectivity of building organic linkers (Bai et al., 2016; Cho et al., 2019). Therefore, expanding the diversity and properties of MOFs is critical to their applications in environmental monitoring.

For instance, a layered porous Cu–benzene-1,3,5-tricarboxylic acid MOF is constructed for the glyphosate detection (Cao et al., 2019). The response current of the synthetic material is significantly increased, which can be ascribed to the strong affinity between chelate groups on the glyphosate with Cu^{2+}. In another example, gold-modified MoS_2/rGO and AuPd@Fe-MOFs are constructed as an electrochemical adapter sensor for detecting Pb^{2+} (Wang Z et al., 2020). The combination of catalytic chain and base complementary is contributed to the improved detection performance. Interestingly, the hinge-like organic ligand is obtained by the desymmetrization strategy (Feng et al., 2019). MOF materials are modified at the molecular level, which can realize the coexistence of acidic sites and alkaline sites in the material. This synthetic mesoporous composite with a functional structure is beneficial to the transformation of cascade catalytic, achieving high activity of a two-step efficient series catalytic reaction (**Figure 4A**).

MOF-based composites with the merits of excellent gas adsorption/separation capability can be adopted as electrically transduced gas sensors (Yao et al., 2021). Integrating MOFs onto capacitive sensors based on interdigitated electrode chips is an effective route to improve their detection performance. For example, an *in situ* growth strategy is adopted to synthesize fumarate-based fcu-MOF thin film on an interdigitated electrode (**Figure 4B**). This constructed sensor presents a remarkable detection sensitivity (down to 100 ppb) and lower detection limit (around 5 ppb) for H_2S (**Figure 4C**). Furthermore, the Langmuir–Blodgett method is used to deposit MIL-96(Al) MOF thin films on the interdigitated electrode chips (**Figure 4D**) (Andrés et al., 2020). These prepared films achieve superior selective and short response/recovery for water and methanol (**Figure 4E**), which can be also extended to the detection of methanol, toluene, and chloroform, etc.

Food Safety Control

Electrochemical (biological) sensors are one of the most sensitive, simple, and selective chemical sensors, which have been widely used in rapid and reliable food safety control (Otles and Yalcin, 2012). MOFs, with the merits of uniform structures, ultrahigh porosity, and tunable composition, act as the promising sensor for food safety control. Nevertheless, the reuse and long-term storage of electrochemical sensor materials fabricated from MOFs in complex sample matrices remain a challenge. Inexpensive microbial sensors are designed for single use to avoid degradation of biosensor elements in complex matrices (Semih Otles, 2012).

In a recent study, Pt nanoparticles were decorated on a glassy carbon electrodes-modified Fe-based MOFs, and this designed MOF-based composites acted as a sensitive label-free electrochemical aptasensor to detect aflatoxin M1 (**Figure 5A**) (Jahangiri-Dehaghani et al., 2020). The fabricated aptasensor was successfully applied to measure AFM1 concentration in powder and pasteurized milk samples. Furthermore, molecularly imprinted mMOFs was synthesized by layer–layer modification to detect turtotomycin (Li et al., 2021). The magnetic pole in molecularly imprinted mMOFs is beneficial to form an electrochemical sensing interface, and its imprinted cavity can serve as electronic channels for probes for label-free detection of over-the-counter drugs.

In general, when food with packaging is stored for a long time, foodborne pathogen infection will occur, resulting in many health-related problems (Jahangiri-Dehaghani et al., 2020). This MOF-based luminescent sensor can be adopted to detect these foodborne pathogens. For instance, a fluorescent MOF [NH_2-MIL-53(Fe)] with a target-specific bacteriophage was synthesized for the detection of *Staphylococcus aureus* (**Figure 5B**) (Bhardwaj et al., 2017). The advanced structure of MOF can offer a precise control on particle size distribution (**Figures 5C,D**), which is helpful to construct a better structural compatibility with bacteriophages, contributing to the high

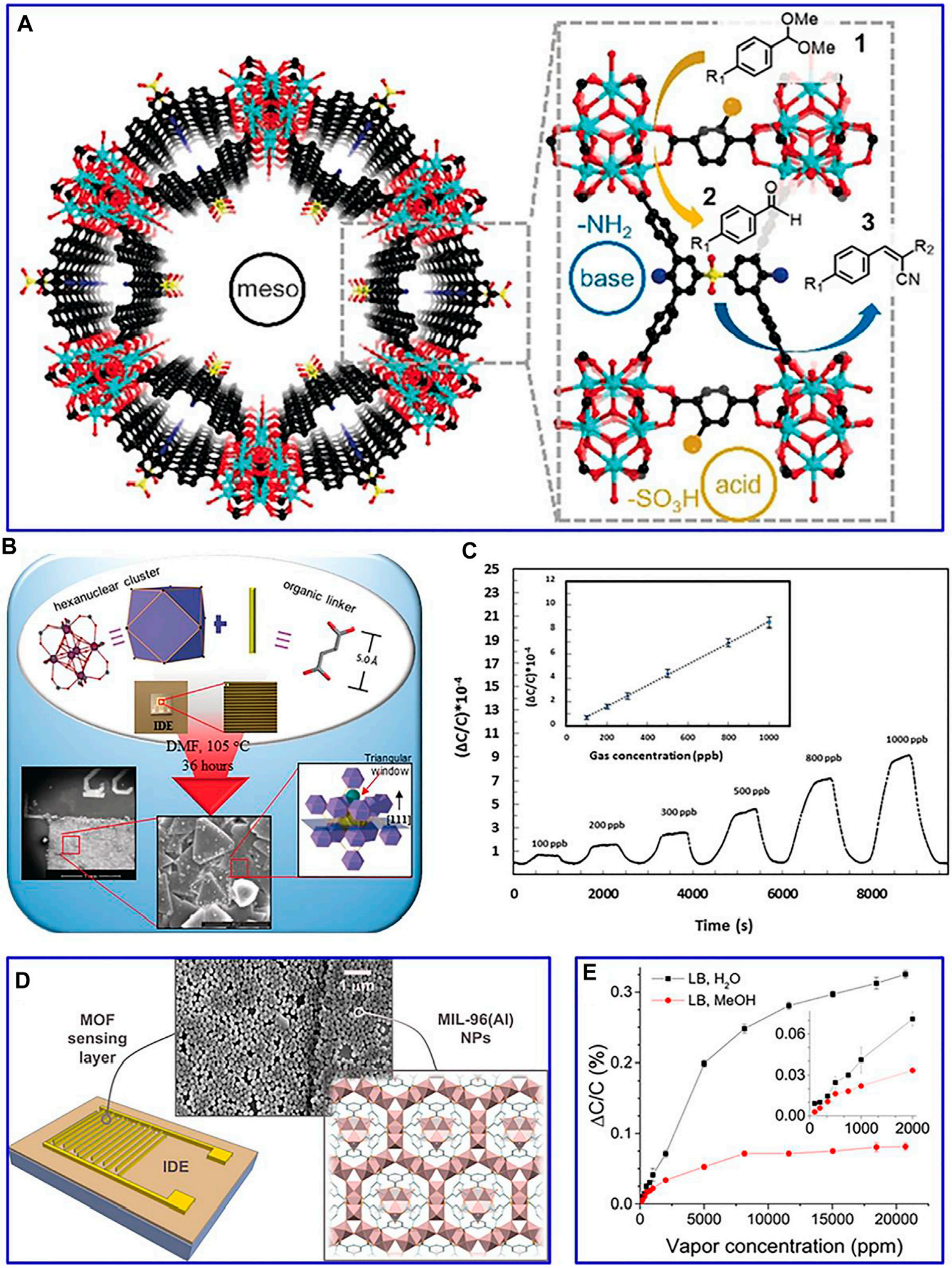

FIGURE 4 | (A) One-pot tandem reaction of benzaldehyde dimethylacetal and malononitrile by bifunctional mesoporous catalyst. Reproduced with permission (Feng et al., 2019). Copyright 2019, Wiley. **(B)** Schematic of the prepared approach of the fumarate-based fcu-MOF; **(C)** detection of H_2S with concentrations of 1–100 ppm. Reproduced with permission (Yassine et al., 2016). Copyright 2016, Wiley. **(D)** Illustration of the structure of the used IDEs showing the MOF LB film characterization by SEM; **(E)** normalized capacitive response of IDEs to water and methanol. Reproduced with permission (Andrés et al., 2020). Copyright 2020, ACS.

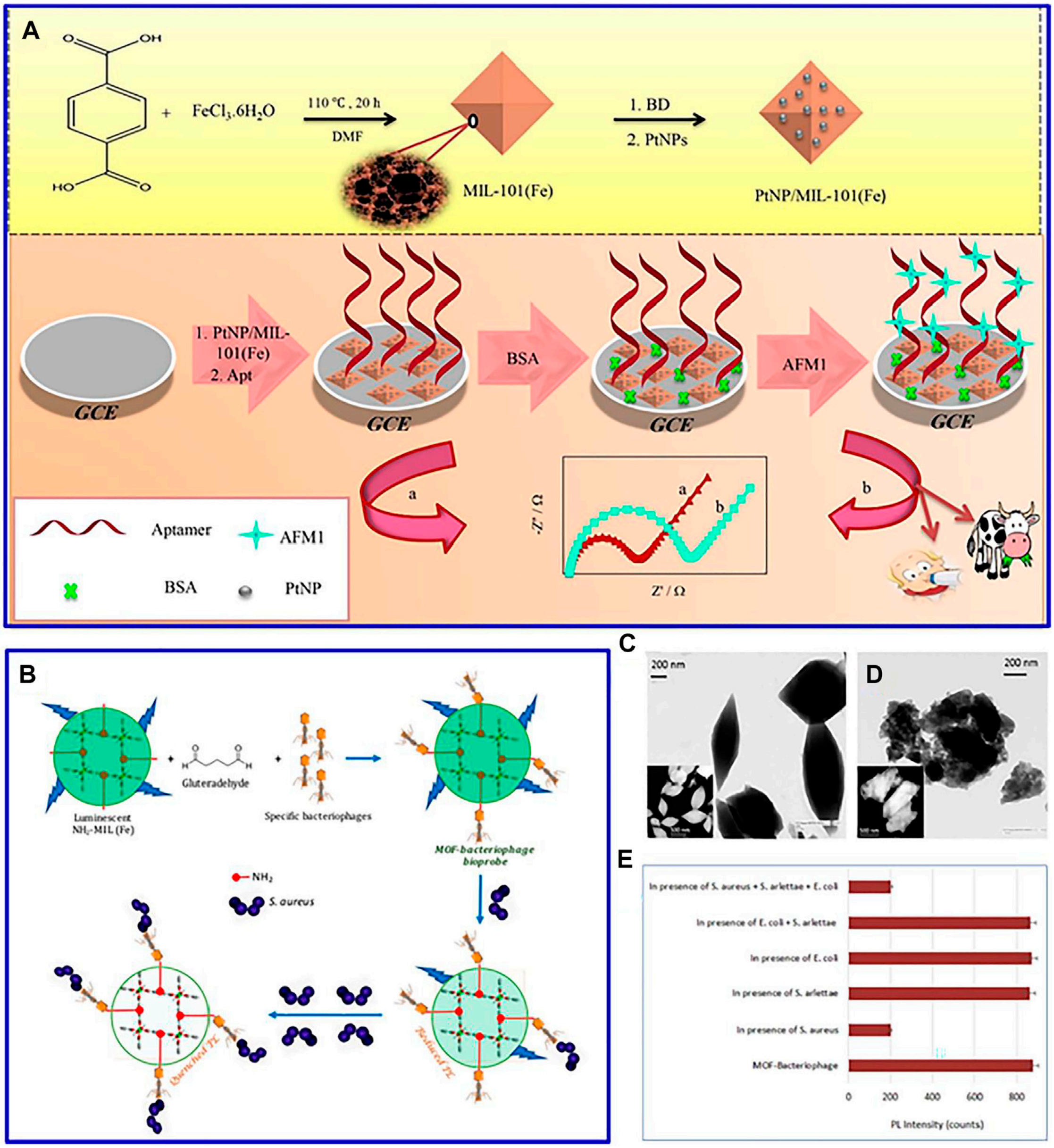

FIGURE 5 | (A) Schematic diagram for the preparation schematic diagram and electrochemical test of PtNP/MIL-101(Fe). Reproduced with permission (Jahangiri-Dehaghani et al., 2020). Copyright 2020, Elsevier. **(B)** Schematic of NH_2-MIL53(Fe)-bacteriophage biosensor; TEM image of **(C)** NH_2-MIL-53 MOF and **(D)** bacteriophage-loaded NH_2-MIL-53 MOF; **(E)** specificity of the proposed biosensor. Reproduced with permission (Bhardwaj et al., 2017). Copyright 2017, ACS.

stability, specificity, reusability, and wider linear range of the bacteriophage sensor (**Figure 5E**). In addition, CeO_2/CuO_x@MC nanocomposite is introduced as a carrier to detect the microtobramycin in milk (Cheng et al., 2021). The combination of different materials presents a strong biological affinity for the adaptor chain, contributing to a wide linear range and low detection limit of tobramycin.

Clinical Diagnosis

MOF materials, with the advantages of selective composition, adjustable pore size, and large surface area are widely used as electrochemical sensor materials in biomedical fields, including cancer diagnosis (e.g., cancer markers, microRNA, and live cancer cells) and glucose detection (Chen et al., 2013; Qin et al., 2016; Xie et al., 2018; Petrosillo et al., 2020). Nevertheless, it is difficult to construct the nanoparticles and active biomolecules in the same MOF-based structure. Recently, many strategies, such as functional MOFs and combination with bionic enzyme, as well as utilization of biosensing and molecular recognition technology, have been developed to improve the photoelectric and catalytic properties of MOF materials (Liao et al., 2017; Shen et al., 2018).

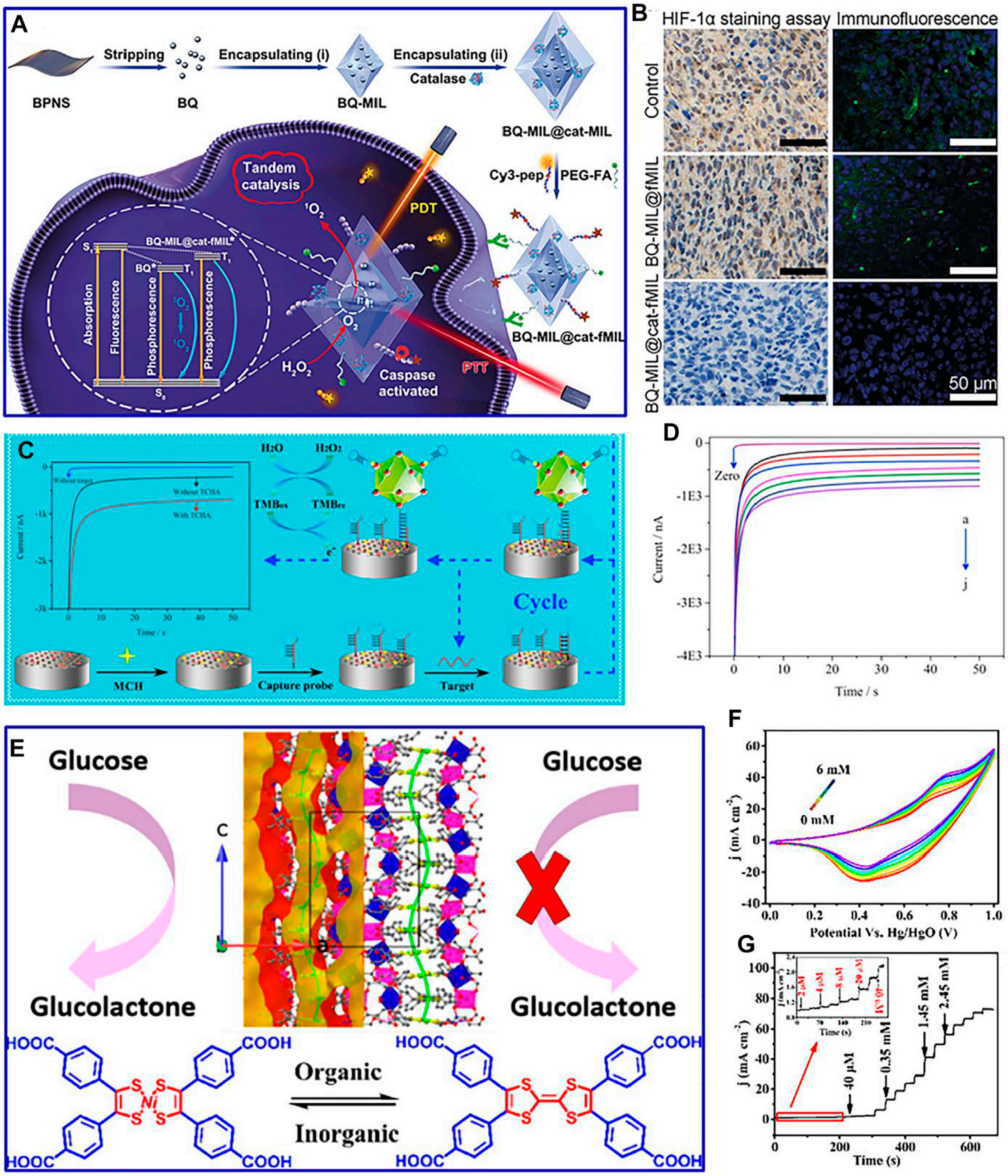

FIGURE 6 | (A) Assemble process of synthetic material and its mechanism against hypoxic tumor cells; **(B)** immunohistochemistry and immunofluorescence staining of HIF-1α in tumor slices of different composites. Reproduced with permission (Liu et al., 2019). Copyright 2019, Wiley. **(C)** Fabrication process of the biosensor and the target-catalyzed hairpin assembly for target recycle; amperometric curves **(D)** of the proposed biosensor incubated with different concentrations of miR-122 containing 1 mM 3,3′,5,5′-tetramethylbenzidine and 20 μM H_2O_2. Reproduced with permission (Li et al., 2018). Copyright 2018, Elsevier. **(E)** Structures of the constructed material; CV curves **(F)** and amperometric response **(G)** of the constructed material with varied glucose concentrations. Reproduced with permission (Zhou et al., 2020). Copyright 2020, ACS.

For instance, a multifunctional homologous MOF hybrid material is designed with enhanced therapeutic effect on hypoxic tumor cells by the *in situ* growth method (Liu et al., 2019). Black phosphorus quantum dots and catalase were precisely assembled into the inner and outer layers of a layered MOF to form a multifunctional MOF heterostructure (**Figure 6A**). This advanced heterostructure converts excess H_2O_2 into O_2 by catalase wrapped in its outer shell, improving the hypoxic microenvironment of tumor cells (**Figure 6B**). An innovative MOF-on-MOF method is adopted to construct Zn-MOF-on-Zr-MOF composite for detecting protein tyrosine kinase-7 (Nan et al., 2019). The synthetic Zn-MOF-on-Zr-

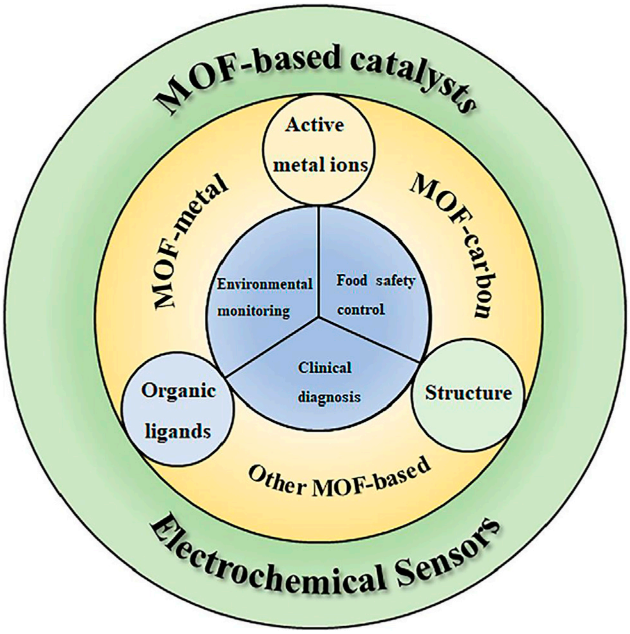

FIGURE 7 | Mechanism and application of MOF-based catalysts as electrochemical sensors.

MOF composite presents hierarchical cross leaves and multilayer nanosheet structures, which demonstrate excellent sensing capabilities for the detection of protein tyrosine kinase-7. This improved performance is mainly ascribed to the presence of Zr-MOF, which significantly facilitates aptamer fixation and stabilizes the formed G-tetrexes, providing a new avenue for the application of bimetallic MOFs in the early cancer diagnosis. Interestingly, multifunctional iron-based MOFs, with the advantages of superior peroxidase-like activity, are developed as a sandwich-type biosensor (**Figure 6C**) (Li et al., 2018). The biosensor demonstrates a low detection limit (0.003 fM) and wide detection range (0.01 fM to 10 p.m.) for detecting miR-122 in human serum (**Figure 6D**). This strategy can be adopted to detect drug-induced liver injury at an early stage.

Recently, commercial glucose sensors are mainly based on glucose oxidase-assisted electrooxidation. In order to avoid low reproducibility, complex immobilized enzyme process, and decreased enzyme activity of commercial glucose sensors, based on the direct electrocatalysis of electrode materials, the application of MOFs in nonenzymatic sensors has been designed and developed (Burke and Gorodetsky, 2012). Nevertheless, the existing small detection range, low sensitivity, and poor stability of MOFs in nonenzymatic glucose electrochemical sensors limit their commercial application (Al-Zoubi et al., 2020). Therefore, it is vital to develop MOF-based composites with good stability and high activity for glucose detection. For example, the Au/Cu MOFs coupled with a capture probe and a convertase form a bioconjugate (Liu et al., 2020). This modified electrode is incubated in sucrose solution, which can effectively detect glucose. Furthermore, coordinating metals with the functional tetrathiafulvalene core is an insightful route to modulate the catalytic performance of MOF-based composites. For instance, nickel bis(dithiolene-dibenzoic acid) as a redox-active linker is constructed for functional MOFs (**Figure 6E**) (Zhou et al., 2020). This synthetic composite presents high sensitivity, wide detection range, and low detection limit for the detection of glucose (**Figures 6F,G**), which is ascribed to the oxidation of glucolactone by several reversible and stable oxidation states of nickel bis(dithiolene) compounds.

PERSPECTIVE AND PROSPECT

Developing efficient catalysts is vital for the application of electrochemical sensors. MOFs, with high porosity, large specific surface area, good conductivity, and biocompatibility, have been widely used in catalysis, adsorption, separation, and energy storage applications. In this review, based on the structure–activity–performance relationship of MOF-based catalysts, the mechanism of MOF-based catalysts as electrochemical sensors, including metal cations, synthetic ligands, and structure, is introduced. Then, the MOF-based composites are successively divided into metal-based, carbon-based, and other MOF-based composites. Furthermore, their application in environmental monitoring, food safety control, and clinical diagnosis is discussed (**Figure 7**). Recently, many efforts have been devoted to constructing high efficiency MOF-based catalysts. However, there still exist some challenges to achieve superior MOF-based catalysts for electrochemical sensors.

First, MOF materials with an excellent redox and catalytic activity in electrochemical sensors are still an urgent need. Due to the large surface area of MOFs, the nonspecific adsorption of coexisting substances will occur in the complex matrix, which will negatively affect the sensing performance. The fine regulation of the pore structure of MOFs can provide precision for the selective adsorption of the target. Furthermore, most MOFs with weak mechanical properties are unstable in water. Surface modification can be adopted to hydrophobic materials or introduce surface functional groups, which is a good method to improve the stability of MOFs in water.

Second, MOF-based catalysts for peroxidase-like enzymes have much lower catalytic activity than natural enzymes. Construction of MOF-based catalysts with higher surface area and richer active sites can alleviate this problem. Furthermore, the catalytic activity of MOFs can also be improved by reasonable selection of multivalent ligands and metal nodes. The weak binding force between the target analyte and MOFs affects the detection sensitivity. Surface functional group modification is an effective strategy to provide stronger binding sites for the adsorption of the target analyte. In addition to carbonizing MOFs and introducing highly conductive species to the host MOFs, *in situ* or posttreatment of doped conductive impurities to MOFs is an alternative to improve their conductivity, resulting in the improved performance.

In addition, during the synthetic and detection process, developing advanced observation techniques will be helpful to understand the structure–activity–performance relationship of

MOF-based catalysts for electrochemical sensors. Moreover, the electrochemical sensors based on MOF catalysts still have limitations under laboratory conditions. Further research on MOF-based catalysts is needed to improve their electrochemical properties and pave the way for further application. With the development of nanoscience and biotechnology, it is believed that MOF-based electrochemical sensors will bring a broader development prospect in environmental, food safety, and clinical aspects.

AUTHOR CONTRIBUTIONS

HY conceived and guided the project. YC, ZY, HH, and XZ performed the manuscript parts. FY, CY, FL, PY, DW, and JY discussed the work and revised the manuscript. RH, XJ, and HY discussed, wrote, and revised the manuscript. All of the authors have commented on the manuscript.

ACKNOWLEDGMENTS

We acknowledge the support of the National Natural Science Foundation of China (22102125), the Scientific Research Foundation of Wuhan Institute of Technology (K2021040), the Graduate Education Innovation Fund of Wuhan Institute of Technology (CX2021168), and the Innovation Foundation of Key Laboratory of Green Chemical Engineering Process of Ministry of Education (GCX202108).

REFERENCES

Al-Zoubi, T., Zhou, Y., Yin, X., Janicek, B., Sun, C., Schulz, C. E., et al. (2020). Preparation of Nonprecious Metal Electrocatalysts for the Reduction of Oxygen Using a Low-Temperature Sacrificial Metal. *J. Am. Chem. Soc.* 142, 5477–5481. doi:10.1021/jacs.9b11061

Andrés, M. A., Vijjapu, M. T., Surya, S. G., Shekhah, O., Salama, K. N., Serre, C., et al. (2020). Methanol and Humidity Capacitive Sensors Based on Thin Films of MOF Nanoparticles. *ACS Appl. Mater. Inter.* 12, 4155–4162. doi:10.1021/acsami.9b20763

Aslam, M., Ismail, I. M. I., Almeelbi, T., Salah, N., Chandrasekaran, S., and Hameed, A. (2014). Enhanced Photocatalytic Activity of V_2O_5 -ZnO Composites for the Mineralization of Nitrophenols. *Chemosphere* 117, 115–123. doi:10.1016/j.chemosphere.2014.05.076

Azad, U. P., and Ganesan, V. (2010). Influence of Metal Nanoparticles on the Electrocatalytic Oxidation of Glucose by poly(NiIIteta) Modified Electrodes. *Electroanalysis* 22, 575–583. doi:10.1002/elan.200900435

Bai, Y., Dou, Y., Xie, L.-H., Rutledge, W., Li, J.-R., and Zhou, H.-C. (2016). Zr-based Metal-Organic Frameworks: Design, Synthesis, Structure, and Applications. *Chem. Soc. Rev.* 45, 2327–2367. doi:10.1039/C5CS00837A

Bhardwaj, N., Bhardwaj, S. K., Mehta, J., Kim, K.-H., and Deep, A. (2017). MOF-bacteriophage Biosensor for Highly Sensitive and Specific Detection of staphylococcus Aureus. *ACS Appl. Mater. Inter.* 9, 33589–33598. doi:10.1021/acsami.7b07818

Blöcher, C., Dorda, J., Mavrov, V., Chmiel, H., Lazaridis, N. K., and Matis, K. A. (2003). Hybrid Flotation-Mmembrane Filtration Process for the Removal of Heavy Metal Ions from Wastewater. *Water Res.* 37, 4018–4026. doi:10.1016/S0043-1354(03)00314-2

Bradshaw, D., Garai, A., and Huo, J. (2012). Metal-organic Framework Growth at Functional Interfaces: Thin Films and Composites for Diverse Applications. *Chem. Soc. Rev.* 41, 2344–2381. doi:10.1039/c1cs15276a

Burke, A. M., and Gorodetsky, A. A. (2012). Taking Charge of Detection. *Nat. Chem* 4, 595–597. doi:10.1038/nchem.1418

Cao, Y., Wang, L., Shen, C., Wang, C., Hu, X., and Wang, G. (2019). An Electrochemical Sensor on the Hierarchically Porous Cu-BTC MOF Platform for Glyphosate Determination. *Sensors Actuators B: Chem.* 283, 487–494. doi:10.1016/j.snb.2018.12.064

Carrasco, S. (2018). Metal-organic Frameworks for the Development of Biosensors: a Current Overview. *Biosensors* 8, 92. doi:10.3390/bios8040092

Chen, L., Zheng, H., Zhu, X., Lin, Z., Guo, L., Qiu, B., et al. (2013). Metal-organic Frameworks-Based Biosensor for Sequence-specific Recognition of Double-Stranded DNA. *Analyst* 138, 3490–3493. doi:10.1039/c3an00426k

Chen, M., Hou, C., Huo, D., Bao, J., Fa, H., and Shen, C. (2016). An Electrochemical DNA Biosensor Based on Nitrogen-Doped graphene/Au Nanoparticles for Human Multidrug Resistance Gene Detection. *Biosens. Bioelectron.* 85, 684–691. doi:10.1016/j.bios.2016.05.051

Chen, Q., SongChang, W.-C., Song, H., Song, H.-B., Hu, T.-L., and Bu, X.-H. (2013). A Controllable Gate Effect in Cobalt(II) Organic Frameworks by Reversible Structure Transformations. *Angew. Chem. Int. Ed.* 52, 11550–11553. doi:10.1002/anie.201306304

Chen, T., and Dai, L. (2013). Carbon Nanomaterials for High-Performance Supercapacitors. *Mater. Today* 16, 272–280. doi:10.1016/j.mattod.2013.07.002

Cheng, W., Tang, X., Zhang, Y., Wu, D., and Yang, W. (2021). Applications of Metal-Organic Framework (MOF)-based Sensors for Food Safety: Enhancing Mechanisms and Recent Advances. *Trends Food Sci. Technol.* 112, 268–282. doi:10.1016/j.tifs.2021.04.004

Chiu, N.-F., Fan, S.-Y., Yang, C.-D., and Huang, T.-Y. (2017). Carboxyl-functionalized Graphene Oxide Composites as SPR Biosensors with Enhanced Sensitivity for Immunoaffinity Detection. *Biosens. Bioelectron.* 89, 370–376. doi:10.1016/j.bios.2016.06.073

Cho, H. S., Yang, J., Gong, X., Zhang, Y.-B., Momma, K., Weckhuysen, B. M., et al. (2019). Isotherms of Individual Pores by Gas Adsorption Crystallography. *Nat. Chem.* 11, 562–570. doi:10.1038/s41557-019-0257-2

Cui, J., Li, Y., Guo, Z., and Zheng, H. (2013). A Porous Metal-Organic Framework Based on Zn_6O_2 clusters: Chemical Stability, Gas Adsorption Properties and Solvatochromic Behavior. *Chem. Commun.* 49, 555–557. doi:10.1039/c2cc36713k

Da Silva, C. T. P., Veregue, F. R., Aguiar, L. W., Meneguin, J. G., Moisés, M. P., Fávaro, S. L., et al. (2016). AuNp@MOF Composite as Electrochemical Material for Determination of Bisphenol A and its Oxidation Behavior Study. *New J. Chem.* 40, 8872–8877. doi:10.1039/C6NJ00936K

Deng, Y., Tian, X., Chi, B., Wang, Q., Ni, W., Gao, Y., et al. (2020a). Hierarchically Open-Porous Carbon Networks Enriched with Exclusive Fe-Nx Active Sites as Efficient Oxygen Reduction Catalysts towards Acidic H2-O2 PEM Fuel Cell and Alkaline Zn-Air Battery. *Chem. Eng. J.* 390, 124479. doi:10.1016/j.cej.2020.124479

Deng, Y., Tian, X., Shen, G., Gao, Y., Lin, C., Ling, L., et al. (2020b). Coupling Hollow Fe3O4 Nanoparticles with Oxygen Vacancy on Mesoporous Carbon as a High-Efficiency ORR Electrocatalyst for Zn-Air Battery. *J. Colloid Interf. Sci.* 567, 410–418. doi:10.1016/j.jcis.2020.02.013

Doménech, A., García, H., Doménech-Carbó, M. T., and Llabrés-i-Xamena, F. (2007). Electrochemistry of Metal-Organic Frameworks: A Description from the Voltammetry of Microparticles Approach. *J. Phys. Chem. C* 111, 13701–13711. doi:10.1021/jp073458x

Dong, Y., Duan, C., Sheng, Q., and Zheng, J. (2019). Preparation of Ag@zeolitic Imidazolate Framework-67 at Room Temperature for Electrochemical Sensing of Hydrogen Peroxide. *Analyst* 144, 521–529. doi:10.1039/C8AN01641K

Falcaro, P., Ricco, R., Doherty, C. M., Liang, K., Hill, A. J., and Styles, M. J. (2014). MOF Positioning Technology and Device Fabrication. *Chem. Soc. Rev.* 43, 5513–5560. doi:10.1039/C4CS00089G

Falcaro, P., Ricco, R., Yazdi, A., Imaz, I., Furukawa, S., Maspoch, D., et al. (2016). Application of Metal and Metal Oxide nanoparticles@MOFs. *Coord. Chem. Rev.* 307, 237–254. doi:10.1016/j.ccr.2015.08.002

Feng, L., Wang, Y., Zhang, K., Wang, K. Y., Fan, W., Wang, X., et al. (2019). Molecular Pivot-Hinge Installation to Evolve Topology in Rare-Earth Metal-Organic Frameworks. *Angew. Chem. Int. Ed.* 58, 16682–16690. doi:10.1002/anie.201910717

Gupta, R., and Ganesan, V. (2015). Gold Nanoparticles Impregnated Mesoporous Silica Spheres for Simultaneous and Selective Determination of Uric Acid and Ascorbic Acid. *Sensors Actuators B: Chem.* 219, 139–145. doi:10.1016/j.snb.2015.05.018

Hatamluyi, B., Rezayi, M., Beheshti, H. R., and Boroushaki, M. T. (2020). Ultrasensitive Molecularly Imprinted Electrochemical Sensor for Patulin Detection Based on a Novel Assembling Strategy Using Au@Cu-Mof/n-GQDs. *Sensors Actuators B: Chem.* 318, 128219. doi:10.1016/j.snb.2020.128219

He, Y., Wang, Z., Wang, H., Wang, Z., Zeng, G., Xu, P., et al. (2021). Metal-organic Framework-Derived Nanomaterials in Environment Related fields: Fundamentals, Properties and Applications. *Coord. Chem. Rev.* 429, 213618. doi:10.1016/j.ccr.2020.213618

Hosseini, M. S., Zeinali, S., and Sheikhi, M. H. (2016). Fabrication of Capacitive Sensor Based on Cu-BTC (MOF-199) Nanoporous Film for Detection of Ethanol and Methanol Vapors. *Sensors Actuators B: Chem.* 230, 9–16. doi:10.1016/j.snb.2016.02.008

Jahangiri–Dehaghani, F., Zare, H. R., and Shekari, Z. (2020). Measurement of Aflatoxin M1 in Powder and Pasteurized Milk Samples by Using a Label-free Electrochemical Aptasensor Based on Platinum Nanoparticles Loaded on Fe-Based Metal-Organic Frameworks. *Food Chem.* 310, 125820. doi:10.1016/j.foodchem.2019.125820

Jiang, D., Xu, P., Wang, H., Zeng, G., Huang, D., Chen, M., et al. (2018). Strategies to Improve Metal Organic Frameworks Photocatalyst's Performance for Degradation of Organic Pollutants. *Coord. Chem. Rev.* 376, 449–466. doi:10.1016/j.ccr.2018.08.005

Justino, C. I. L., Freitas, A. C., Pereira, R., Duarte, A. C., and Rocha Santos, T. A. P. (2015). Recent Developments in Recognition Elements for Chemical Sensors and Biosensors. *Trac Trends Anal. Chem.* 68, 2–17. doi:10.1016/j.trac.2015.03.006

Kempahanumakkagari, S., Vellingiri, K., Deep, A., Kwon, E. E., Bolan, N., and Kim, K.-H. (2018). Metal-Organic Framework Composites as Electrocatalysts for Electrochemical Sensing Applications. *Coord. Chem. Rev.* 357, 105–129. doi:10.1016/j.ccr.2017.11.028

Kitagawa, S., Kitaura, R., and Noro, S.-i. (2004). Functional Porous Coordination Polymers. *Angew. Chem. Int. Ed.* 43, 2334–2375. doi:10.1002/anie.200300610

Lai, C., Huang, F., Zeng, G., Huang, D., Qin, L., Cheng, M., et al. (2019). Fabrication of Novel Magnetic MnFe2O4/bio-Char Composite and Heterogeneous Photo-Fenton Degradation of Tetracycline in Near Neutral pH. *Chemosphere* 224, 910–921. doi:10.1016/j.chemosphere.2019.02.193

Li, B., Wen, H.-M., Cui, Y., Zhou, W., Qian, G., and Chen, B. (2016). Emerging Multifunctional Metal-Organic Framework Materials. *Adv. Mater.* 28, 8819–8860. doi:10.1002/adma.201601133

Li, D., Xu, H.-Q., Jiao, L., and Jiang, H.-L. (2019). Metal-organic Frameworks for Catalysis: State of the Art, Challenges, and Opportunities. *EnergyChem* 1, 100005. doi:10.1016/j.enchem.2019.100005

Li, H.-Y., Zhao, S.-N., Zang, S.-Q., and Li, J. (2020). Functional Metal-Organic Frameworks as Effective Sensors of Gases and Volatile Compounds. *Chem. Soc. Rev.* 49, 6364–6401. doi:10.1039/C9CS00778D

Li, L., Lai, C., Huang, F., Cheng, M., Zeng, G., Huang, D., et al. (2019). Degradation of Naphthalene with Magnetic Bio-Char Activate Hydrogen Peroxide: Synergism of Bio-Char and Fe-Mn Binary Oxides. *Water Res.* 160, 238–248. doi:10.1016/j.watres.2019.05.081

Li, L., Zhang, S., Lu, Y., Zhang, J., Zhang, X., Wang, R., et al. (2021). Highly Selective and Sensitive Detection of Volatile Sulfur Compounds by Ionically Conductive Metal-Organic Frameworks. *Adv. Mater.* 33, 2104120. doi:10.1002/adma.202104120

Li, P.-P., Liu, X.-P., Mao, C.-J., Jin, B.-K., and Zhu, J.-J. (2019). Photoelectrochemical DNA Biosensor Based on G-C3N4/MoS2 2D/2D Heterojunction Electrode Matrix and Co-sensitization Amplification with CdSe QDs for the Sensitive Detection of ssDNA. *Analytica Chim. Acta* 1048, 42–49. doi:10.1016/j.aca.2018.09.063

Li, S., Liu, X., Chai, H., and Huang, Y. (2018). Recent Advances in the Construction and Analytical Applications of Metal-Organic Frameworks-Based Nanozymes. *Trac Trends Anal. Chem.* 105, 391–403. doi:10.1016/j.trac.2018.06.001

Li, Y., Xie, M., Zhang, X., Liu, Q., Lin, D., Xu, C., et al. (2019). Co-MOF Nanosheet Array: A High-Performance Electrochemical Sensor for Non-enzymatic Glucose Detection. *Sensors Actuators B: Chem.* 278, 126–132. doi:10.1016/j.snb.2018.09.076

Li, Y., Yu, C., Yang, B., Liu, Z., Xia, P., and Wang, Q. (2018). Target-catalyzed Hairpin Assembly and Metal-Organic Frameworks Mediated Nonenzymatic Co-reaction for Multiple Signal Amplification Detection of miR-122 in Human Serum. *Biosens. Bioelectron.* 102, 307–315. doi:10.1016/j.bios.2017.11.047

Liao, F.-S., Lo, W.-S., Hsu, Y.-S., Wu, C.-C., Wang, S.-C., Shieh, F.-K., et al. (2017). Shielding against Unfolding by Embedding Enzymes in Metal-Organic Frameworks via a De Novo Approach. *J. Am. Chem. Soc.* 139, 6530–6533. doi:10.1021/jacs.7b01794

Liao, J., Jin, B., Zhao, Y., and Liang, Z. (2019). Highly Efficient and Durable Metal-Organic Framework Material Derived Ca-Based Solid Sorbents for CO_2 Capture. *Chem. Eng. J.* 372, 1028–1037. doi:10.1016/j.cej.2019.04.212

Liao, P.-Q., Shen, J.-Q., and Zhang, J.-P. (2018). Metal-organic Frameworks for Electrocatalysis. *Coord. Chem. Rev.* 373, 22–48. doi:10.1016/j.ccr.2017.09.001

Lin, H., Wang, F., Duan, Y., Kang, W., Chen, Q., and Xue, Z. (2022). Early Detection of Wheat Aspergillus Infection Based on Nanocomposite Colorimetric Sensor and Multivariable Models. *Sensors Actuators B: Chem.* 351, 130910. doi:10.1016/j.snb.2021.130910

Liu, J., Liu, T., Du, P., Zhang, L., and Lei, J. (2019). Metal-organic Framework (MOF) Hybrid as a Tandem Catalyst for Enhanced Therapy against Hypoxic Tumor Cells. *Angew. Chem. Int. Ed.* 58, 7808–7812. doi:10.1002/anie.201903475

Liu, L., Zhou, Y., Liu, S., and Xu, M. (2018). The Applications of Metal-Organic Frameworks in Electrochemical Sensors. *ChemElectroChem* 5, 6–19. doi:10.1002/celc.201700931

Liu, Q., Dordick, J. S., and Dinu, C. Z. (2019). Metal-organic Framework-Based Composite for Photocatalytic Detection of Prevalent Pollutant. *ACS Appl. Mater. Inter.* 11, 31049–31059. doi:10.1021/acsami.9b10438

Liu, S., Lai, C., Liu, X., Li, B., Zhang, C., Qin, L., et al. (2020). Metal-organic Frameworks and Their Derivatives as Signal Amplification Elements for Electrochemical Sensing. *Coord. Chem. Rev.* 424, 213520. doi:10.1016/j.ccr.2020.213520

Liu, X.-W., Sun, T.-J., Hu, J.-L., and Wang, S.-D. (2016). Composites of Metal-Organic Frameworks and Carbon-Based Materials: Preparations, Functionalities and Applications. *J. Mater. Chem. A.* 4, 3584–3616. doi:10.1039/C5TA09924B

Liu, Y., and Tang, Z. (2013). Multifunctional Nanoparticle@MOF Core-Shell Nanostructures. *Adv. Mater.* 25, 5819–5825. doi:10.1002/adma.201302781

Liu, Y., Zhong, L., Zhang, S., Wang, J., and Liu, Z. (2022). An Ultrasensitive and Wearable Photoelectrochemical Sensor for Unbiased and Accurate Monitoring of Sweat Glucose. *Sensors Actuators B: Chem.* 354, 131204. doi:10.1016/j.snb.2021.131204

Lu, Y., Zhang, S., Dai, S., Liu, D., Wang, X., Tang, W., et al. (2020). Ultrasensitive Detection of Electrolyte Leakage from Lithium-Ion Batteries by Ionically Conductive Metal-Organic Frameworks. *Matter* 3, 904–919. doi:10.1016/j.matt.2020.05.021

Lu, Z., Zhong, Y., Li, G., and Hu, Y. (2022). Rapid Analysis of Quinoxalines in Feeds by a Fluorescence Sensor Based on Tetraphenylmethane Porous Organic Framework Membrane. *Sensors Actuators B: Chem.* 356, 131350. doi:10.1016/j.snb.2021.131350

Ma, D.-D., and Zhu, Q.-L. (2020). MOF-based Atomically Dispersed Metal Catalysts: Recent Progress towards Novel Atomic Configurations and Electrocatalytic Applications. *Coord. Chem. Rev.* 422, 213483. doi:10.1016/j.ccr.2020.213483

Ma, J., Chen, G., Bai, W., and Zheng, J. (2020a). Amplified Electrochemical Hydrogen Peroxide Sensing Based on Cu-Porphyrin Metal-Organic Framework Nanofilm and G-Quadruplex-Hemin DNAzyme. *ACS Appl. Mater. Inter.* 12, 58105–58112. doi:10.1021/acsami.0c09254

Ma, J., Zhang, X., Zhang, Y., Li, H., Wei, C., Yang, J., et al. (2020b). A New Watermelon Cultivar-'ShanNong No.4'. *Acta Hortic.* 58, 389–392. doi:10.17660/ActaHortic.2020.1282.58

Meng, W., Wen, Y., Dai, L., He, Z., and Wang, L. (2018). A Novel Electrochemical Sensor for Glucose Detection Based on Ag@ZIF-67 Nanocomposite. *Sensors Actuators B: Chem.* 260, 852–860. doi:10.1016/j.snb.2018.01.109

Moon, H. R., Lim, D.-W., and Suh, M. P. (2013). Fabrication of Metal Nanoparticles in Metal-Organic Frameworks. *Chem. Soc. Rev.* 42, 1807–1824. doi:10.1039/C2CS35320B

Mosleh, S., RahimiGhaedi, M. R., Ghaedi, M., Dashtian, K., Hajati, S., and Wang, S. (2017). Ag_3PO_4/AgBr/Ag-HKUST-1-MOF Composites as Novel Blue LED

Light Active Photocatalyst for Enhanced Degradation of Ternary Mixture of Dyes in a Rotating Packed Bed Reactor. *Chem. Eng. Process. Process Intensification* 114, 24–38. doi:10.1016/j.cep.2017.01.009

Nan, H., Su, Y.-Q., Tang, C., Cao, R., Li, D., Yu, J., et al. (2020). Engineering the Electronic and Strained Interface for High Activity of PdMcore@Ptmonolayer Electrocatalysts for Oxygen Reduction Reaction. *Sci. Bull.* 65, 1396–1404. doi:10.1016/j.scib.2020.04.015

Nan, Z. A., Fs, B., Cg, B., Lh, B., Zj, A., Mw, B., et al. (2019). Two-dimensional Oriented Growth of Zn-MOF-On-Zr-MOF Architecture: A Highly Sensitive and Selective Platform for Detecting Cancer Markers-ScienceDirect. *Biosens.Bioelectron* 123, 51–58. doi:10.1016/j.bios.2018.09.079

Otles, S., and Yalcin, B. (2012). Review on the Application of Nanobiosensors in Food Analysis. *Acta Sci. Pol. Technol. Aliment.* 11, 7–18. doi:10.1007/s11783-011-0280-z

Otles, S., and Yalcin, B. (2012). Review on the Application of Nanobiosensors in Food Analysis. *Acta Sci. Pol. Technol. Aliment.* 11, 7–18. doi:10.1007/s11783-011-0280-z

Pandey, A., Nikam, A. N., Padya, B. S., Kulkarni, S., Fernandes, G., Shreya, A. B., et al. (2021). Surface Architectured Black Phosphorous Nanoconstructs Based Smart and Versatile Platform for Cancer Theranostics. *Coord. Chem. Rev.* 435, 213826. doi:10.1016/j.ccr.2021.2138210.1016/j.ccr.2021.213826

Peng, Z., Jiang, Z., and Li, Y. (2016). A Novel Electrochemical Sensor of Tryptophan Based on Silver Nanoparticles/metal-Organic Framework Composite Modified Glassy Carbon Electrode. *RSC Adv.* 6, 13742–13748. doi:10.1039/C5RA25251B

Petrosillo, N., Viceconte, G., Ergonul, O., Ippolito, G., and Petersen, E. (2020). COVID-19, SARS and MERS: Are They Closely Related? *Clin. Microbiol. Infect.* 26, 729–734. doi:10.1016/j.cmi.2020.03.026

Qin, L., Lin, L.-X., Fang, Z.-P., Yang, S.-P., Qiu, G.-H., Chen, J.-X., et al. (2016). A Water-Stable Metal-Organic Framework of a Zwitterionic Carboxylate with Dysprosium: a Sensing Platform for Ebolavirus RNA Sequences. *Chem. Commun.* 52, 132–135. doi:10.1039/C5CC06697B

Qin, L., Wang, X., Liu, Y., and Wei, H. (2018). 2D-metal-organic-framework-nanozyme Sensor Arrays for Probing Phosphates and Their Enzymatic Hydrolysis. *Anal. Chem.* 90, 9983–9989. doi:10.1021/acs.analchem.8b02428

Reuillard, B., Carrière, S., Le Goff, A., and Cosnier, S. (2017). Biomimetic versus Enzymatic High-Potential Electrocatalytic Reduction of Hydrogen Peroxide on a Functionalized Carbon Nanotube Electrode. *Chem. Sci.* 6, 5139–5143. doi:10.1039/C5SC01473E

Rosi, N. L., Eckert, J., Eddaoudi, M., Vodak, D. T., Kim, J., O'Keeffe, M., et al. (2003). Hydrogen Storage in Microporous Metal-Organic Frameworks. *Science* 300, 1127–1129. doi:10.1126/science.1083440

Sabo, M., Henschel, A., Fröde, H., Klemm, E., and Kaskel, S. (2007). Solution Infiltration of Palladium into MOF-5: Synthesis, Physisorption and Catalytic Properties. *J. Mater. Chem.* 17, 3827–3832. doi:10.1039/B706432B

Samadi-Maybodi, A., Ghasemi, S., and Ghaffari-Rad, H. (2015). A Novel Sensor Based on Ag-Loaded Zeolitic Imidazolate Framework-8 Nanocrystals for Efficient Electrocatalytic Oxidation and Trace Level Detection of Hydrazine. *Sensors Actuators B: Chem.* 220, 627–633. doi:10.1016/j.snb.2015.05.127

Saraf, M., Rajak, R., and Mobin, S. M. (2016). A Fascinating Multitasking Cu-MOF/rGO Hybrid for High Performance Supercapacitors and Highly Sensitive and Selective Electrochemical Nitrite Sensors. *J. Mater. Chem. A.* 4, 16432–16445. doi:10.1039/C6TA06470A

Sarycheva, A., Makaryan, T., Maleski, K., Satheeshkumar, E., Melikyan, A., Minassian, H., et al. (2017). Two-dimensional Titanium Carbide (MXene) as Surface-Enhanced Raman Scattering Substrate. *J. Phys. Chem. C* 121, 19983–19988. doi:10.1021/acs.jpcc.7b08180

Sharma, H., and Mutharasan, R. (2013). Review of Biosensors for Foodborne Pathogens and Toxins. *Sensors Actuators B: Chem.* 183, 535–549. doi:10.1016/j.snb.2013.03.137

Shen, H., Liu, J., Lei, J., and Ju, H. (2018). A Core-Shell Nanoparticle-Peptide@metal-Organic Framework as pH and Enzyme Dual-Recognition Switch for Stepwise-Responsive Imaging in Living Cells. *Chem. Commun.* 54, 9155–9158. doi:10.1039/C8CC04621B

Singha, S. S., Mondal, S., BhattacharyaShankar, T. S., Das, L., Sen, K., Satpati, B., et al. (2018). Au Nanoparticles Functionalized 3D-MoS_2 Nanoflower: An Efficient SERS Matrix for Biomolecule Sensing. *Biosens. Bioelectron.* 119, 10–17. doi:10.1016/j.bios.2018.07.061

Smaldone, R. A., Forgan, R. S., Furukawa, H., Gassensmith, J. J., Slawin, M. Z., Yaghi, O. M., et al. (2010). Metal-organic Frameworks from Edible Natural Products. *Angew. Chem.* 122, 8812–8816. doi:10.1002/anie.20100234310.1002/ange.201002343

Sonkar, P. K., and Ganesan, V. (2015). Synthesis and Characterization of Silver Nanoparticle-Anchored Amine-Functionalized Mesoporous Silica for Electrocatalytic Determination of Nitrite. *J. Solid State. Electrochem.* 19, 2107–2115. doi:10.1007/s10008-014-2725-3

Tang, H., Cai, S., Xie, S., Wang, Z., Tong, Y., Pan, M., et al. (2016). Metal-Organic-Framework-Derived Dual Metal- and Nitrogen-Doped Carbon as Efficient and Robust Oxygen Reduction Reaction Catalysts for Microbial Fuel Cells. *Adv. Sci.* 3, 1500265. doi:10.1002/advs.201500265

Turner, S., Lebedev, O. I., Schröder, F., Esken, D., Fischer, R. A., and Tendeloo, G. V. (2008). Direct Imaging of Loaded Metal-Organic Framework Materials (Metal@MOF-5). *Chem. Mater.* 20, 5622–5627. doi:10.1021/cm801165s

Valekar, A. H., Batule, B. S., Kim, M. I., Cho, K.-H., Hong, D.-Y., Lee, U.-H., et al. (2018). Novel Amine-Functionalized Iron Trimesates with Enhanced Peroxidase-like Activity and Their Applications for the Fluorescent Assay of Choline and Acetylcholine. *Biosens. Bioelectron.* 100, 161–168. doi:10.1016/j.bios.2017.08.056

Wang, C., Langrock, C., Marandi, A., Jankowski, M., Zhang, M., Desiatov, B., et al. (2018). Ultrahigh-efficiency Wavelength Conversion in Nanophotonic Periodically Poled Lithium Niobate Waveguides. *Optica* 5, 1438–1441. doi:10.1364/OPTICA.5.001438

Wang, L., Teng, Q., Sun, X., Chen, Y., Wang, Y., Wang, H., et al. (2018). Facile Synthesis of Metal-Organic Frameworks/ordered Mesoporous Carbon Composites with Enhanced Electrocatalytic Ability for Hydrazine. *J. Colloid Interf. Sci.* 512, 127–133. doi:10.1016/j.jcis.2017.10.050

Wang, L., Yang, H., He, J., Zhang, Y., Yu, J., and Song, Y. (2016). Cu-hemin Metal-Organic-Frameworks/chitosan-Reduced Graphene Oxide Nanocomposites with Peroxidase-like Bioactivity for Electrochemical Sensing. *Electrochimica Acta* 213, 691–697. doi:10.1016/j.electacta.2016.07.162

Wang, Y., Wang, L., Huang, W., Zhang, T., Hu, X., Perman, J. A., et al. (2017). A Metal-Organic Framework and Conducting Polymer Based Electrochemical Sensor for High Performance Cadmium Ion Detection. *J. Mater. Chem. A.* 5, 8385–8393. doi:10.1039/C7TA01066D

Wang, Y., Wu, Y., Xie, J., and Hu, X. (2013). Metal-organic Framework Modified Carbon Paste Electrode for lead Sensor. *Sensors Actuators B: Chem.* 177, 1161–1166. doi:10.1016/j.snb.2012.12.048

Wang, Y., Zhao, G., Zhang, G., Zhang, Y., Wang, H., Cao, W., et al. (2020). An Electrochemical Aptasensor Based on Gold-Modified MoS_2/rGO Nanocomposite and Gold-Palladium-Modified Fe-MOFs for Sensitive Detection of lead Ions. *Sensors Actuators B: Chem.* 319, 128313. doi:10.1016/j.snb.2020.128313

Wang, Z., Jin, H., Meng, T., Liao, K., Meng, W., Yang, J., et al. (2018). Fe, Cu-Coordinated ZIF-Derived Carbon Framework for Efficient Oxygen Reduction Reaction and Zinc-Air Batteries. *Adv. Funct. Mater.* 28, 1802596. doi:10.1002/adfm.201802596

Wang, Z., Wang, H., Zeng, Z., Zeng, G., Xu, P., Xiao, R., et al. (2020). Metal-organic Frameworks Derived $Bi_2O_2CO_3$/porous Carbon Nitride: A Nanosized Z-Scheme Systems with Enhanced Photocatalytic Activity. *Appl. Catal. B: Environ.* 267, 118700. doi:10.1016/j.apcatb.2020.118700

Wen, J., Li, X., Liu, W., Fang, Y., Xie, J., and Xu, Y. (2015). Photocatalysis Fundamentals and Surface Modification of TiO_2 Nanomaterials. *Chin. J. Catal.* 36, 2049–2070. doi:10.1016/S1872-2067(15)60999-8

Wengert, S., Albrecht, J., Ruoss, S., Stahl, C., Schütz, G., and Schäfer, R. (2017). Smooth and Rapid Microwave Synthesis of MIL-53(Fe) Including Superparamagnetic γ-Fe_2O_3 Nanoparticles. *J. Magnetism Magn. Mater.* 444, 168–172. doi:10.1016/j.jmmm.2017.08.013

Xie, B.-P., Qiu, G.-H., Hu, P.-P., Liang, Z., Liang, Y.-M., Sun, B., et al. (2018). Simultaneous Detection of Dengue and Zika Virus RNA Sequences with a Three-Dimensional Cu-Based Zwitterionic Metal-Organic Framework, Comparison of Single and Synchronous Fluorescence Analysis. *Sensors Actuators B: Chem.* 254, 1133–1140. doi:10.1016/j.snb.2017.06.085

Yang, H., Han, X., Douka, A. I., Huang, L., Gong, L., Xia, C., et al. (2020). Advanced Oxygen Electrocatalysis in Energy Conversion and Storage. *Adv. Funct. Mater.* 31, 2007602. doi:10.1002/adfm.202007602

Yang, H. M., Song, X. L., Yang, T. L., Liang, Z. H., Fan, C. M., and Hao, X. G. (2014). Electrochemical Synthesis of Flower Shaped Morphology MOFs in an Ionic Liquid System and Their Electrocatalytic Application to the Hydrogen Evolution Reaction. *RSC Adv.* 4, 15720–15726. doi:10.1039/C3RA47744D

Yang, J., Zhao, F., and Zeng, B. (2015). One-step Synthesis of a Copper-Based Metal-Organic Framework-Graphene Nanocomposite with Enhanced Electrocatalytic Activity. *RSC Adv.* 5, 22060–22065. doi:10.1039/c4ra16950f

Yang, Q., Xu, Q., and Jiang, H.-L. (2017). Metal-organic Frameworks Meet Metal Nanoparticles: Synergistic Effect for Enhanced Catalysis. *Chem. Soc. Rev.* 46, 4774–4808. doi:10.1039/C6CS00724D

Yang, S., Karve, V. V., Justin, A., Kochetygov, I., Espín, J., Asgari, M., et al. (2021). Enhancing MOF Performance through the Introduction of Polymer Guests. *Coord. Chem. Rev.* 427, 213525. doi:10.1016/j.ccr.2020.213525

Yang, T., Yang, H., Zhen, S. J., and Huang, C. Z. (2015). Hydrogen-bond-mediated In Situ Fabrication of AgNPs/Agar/PAN Electrospun Nanofibers as Reproducible SERS Substrates. *ACS Appl. Mater. Inter.* 7, 1586–1594. doi:10.1126/science.108344010.1021/am507010q

Yang, Y., Zeng, Z., Zhang, C., Huang, D., Zeng, G., Xiao, R., et al. (2018). Construction of Iodine Vacancy-Rich BiOI/Ag@AgI Z-Scheme Heterojunction Photocatalysts for Visible-Light-Driven Tetracycline Degradation: Transformation Pathways and Mechanism Insight. *Chem. Eng. J.* 349, 808–821. doi:10.1016/j.cej.2018.05.093

Yang, Z.-H., Ren, S., Zhuo, Y., Yuan, R., and Chai, Y.-Q. (2017). Cu/Mn Double-Doped CeO_2 Nanocomposites as Signal Tags and Signal Amplifiers for Sensitive Electrochemical Detection of Procalcitonin. *Anal. Chem.* 89, 13349–13356. doi:10.1021/acs.analchem.7b03502

Yang, Z., Zhang, W., Yin, Y., Fang, W., and Xue, H. (2022). Metal-organic Framework-Based Sensors for the Detection of Toxins and Foodborne Pathogens. *Food Control* 133, 108684. doi:10.1016/j.foodcont.2021.108684

Yang, Z., Zhou, X., Yin, Y., and Fang, W. (2021). Determination of Nitrite by noble Metal Nanomaterial-Based Electrochemical Sensors: A Minireview. *Anal. Lett.* 54, 2826–2850. doi:10.1080/00032719.2021.1897134

Yao, M.-S., Li, W.-H., and Xu, G. (2021). Metal-organic Frameworks and Their Derivatives for Electrically-Transduced Gas Sensors. *Coord. Chem. Rev.* 426, 213479. doi:10.1016/j.ccr.2020.213479

Yassine, O., Shekhah, O., Assen, A. H., Belmabkhout, Y., Salama, K. N., and Eddaoudi, M. (2016). H_2S Sensors: Fumarate-Based Fcu-MOF Thin Film Grown on a Capacitive Interdigitated Electrode. *Angew. Chem. Int. Ed.* 55, 15879–15883. doi:10.1002/anie.201608780

Yi, F.-Y., Chen, D., Wu, M.-K., Han, L., and Jiang, H.-L. (2016). Chemical Sensors Based on Metal-Organic Frameworks. *ChemPlusChem* 81, 675–690. doi:10.1002/cplu.201600137

Yuan, B., Zhang, R., Jiao, X., Li, J., Shi, H., and Zhang, D. (2014). Amperometric Determination of Reduced Glutathione with a New Co-based Metal-Organic Coordination Polymer Modified Electrode. *Electrochemistry Commun.* 40, 92–95. doi:10.1016/j.elecom.2014.01.006

Zamzami, M. A., Rabbani, G., Ahmad, A., Basalah, A. A., Al-Sabban, W. H., Nate Ahn, S., et al. (2022). Carbon Nanotube Field-Effect Transistor (CNT-FET)-based Biosensor for Rapid Detection of SARS-CoV-2 (COVID-19) Surface Spike Protein S1. *Bioelectrochemistry* 143, 107982. doi:10.1016/j.bioelechem.2021.107982

Zhang, M., Gu, Z.-Y., Bosch, M., Perry, Z., and Zhou, H.-C. (2015). Biomimicry in Metal-Organic Materials. *Coord. Chem. Rev.* 293-294, 327–356. doi:10.1016/j.ccr.2014.05.031

Zhang, T., and Lin, W. (2014). Metal-organic Frameworks for Artificial Photosynthesis and Photocatalysis. *Chem. Soc. Rev.* 43, 5982–5993. doi:10.1039/c4cs00103f

Zhang, X., Jiang, Y., Zhu, M., Xu, Y., Guo, Z., Shi, J., et al. (2020). Electrochemical DNA Sensor for Inorganic Mercury(II) Ion at Attomolar Level in Dairy Product Using Cu(II)-anchored Metal-Organic Framework as Mimetic Catalyst. *Chem. Eng. J.* 383, 123182. doi:10.1016/j.cej.2019.123182

Zhang, X., Li, G., Wu, D., Li, X., Hu, N., Chen, J., et al. (2019). Recent Progress in the Design Fabrication of Metal-Organic Frameworks-Based Nanozymes and Their Applications to Sensing and Cancer Therapy. *Biosens. Bioelectron.* 137, 178–198. doi:10.1016/j.bios.2019.04.061

Zhang, Y., Brooks, W. A., Goswami, D., Rahman, M., Luby, S. P., and Erdman, D. D. (2014). A Duplex Recombinant Viral Nucleoprotein Microbead Immunoassay for Simultaneous Detection of Seroresponses to Human Respiratory Syncytial Virus and Metapneumovirus Infections. *J. Virol. Methods* 206, 55–62. doi:10.1016/j.jviromet.2014.05.008

Zhang, Z., Ji, H., Song, Y., Zhang, S., Wang, M., Jia, C., et al. (2017). Fe(III)-based Metal-Organic Framework-Derived Core-Shell Nanostructure: Sensitive Electrochemical Platform for High Trace Determination of Heavy Metal Ions. *Biosens. Bioelectron.* 94, 358–364. doi:10.1016/j.bios.2017.03.014

Zhou, B., Liang, L.-M., and Yao, J. (2014). Effects of Isomorphous Substitution of a Coordination Polymer on the Properties and its Application in Electrochemical Sensing. *J. Solid State. Chem.* 215, 109–113. doi:10.1016/j.jssc.2014.03.028

Zhou, Q., Lin, Y., Zhang, K., Li, M., and Tang, D. (2018). Reduced Graphene oxide/BiFeO3 Nanohybrids-Based Signal-On Photoelectrochemical Sensing System for Prostate-specific Antigen Detection Coupling with Magnetic Microfluidic Device. *Biosens. Bioelectron.* 101, 146–152. doi:10.1016/j.bios.2017.10.027

Zhou, X., Zeng, Z., Zeng, G., Lai, C., Xiao, R., Liu, S., et al. (2020). Persulfate Activation by Swine Bone Char-Derived Hierarchical Porous Carbon: Multiple Mechanism System for Organic Pollutant Degradation in Aqueous media. *Chem. Eng. J.* 383, 123091. doi:10.1016/j.cej.2019.123091

Zhou, Y., Hu, Q., Yu, F., Ran, G.-Y., Wang, H.-Y., Shepherd, N. D., et al. (2020). A Metal-Organic Framework Based on a Nickel Bis(dithiolene) Connector: Synthesis, crystal Structure, and Application as an Electrochemical Glucose Sensor. *J. Am. Chem. Soc.* 142, 20313–20317. doi:10.1021/jacs.0c09009

Zhu, N.-N., Liu, X.-H., Li, T., Ma, J.-G., Cheng, P., and Yang, G.-M. (2017). Composite System of Ag Nanoparticles and Metal-Organic Frameworks for the Capture and Conversion of Carbon Dioxide under Mild Conditions. *Inorg. Chem.* 56, 3414–3420. doi:10.1021/acs.inorgchem.6b02855

Zhu, Q.-L., and Xu, Q. (2014). Metal-organic Framework Composites. *Chem. Soc. Rev.* 43, 5468–5512. doi:10.1039/C3CS60472A

Conflict of Interest: The authors declare that the research was conducted in the absence of any commercial or financial relationships that could be construed as a potential conflict of interest.

frontiers | Frontiers in Chemistry

ORIGINAL RESEARCH
published: 29 April 2022
doi: 10.3389/fchem.2022.874965

A Multicomponent Polymer-Metal-Enzyme System as Electrochemical Biosensor for H_2O_2 Detection

Pengfei Tong[1], *Muhammad Asif*[2], *Muhammad Ajmal*[3], *Ayesha Aziz*[2] *and Yimin Sun*[4]*

[1]Henan Institute of Microsurgery, The First Affiliated Hospital, College of Clinical Medicine of Henan University of Science and Technology, Luoyang, China, [2]School of Chemistry and Chemical Engineering, Huazhong University of Science and Technology, Wuhan, China, [3]Department of Chemistry, College of Chemistry and Chemical Engineering, Xiamen University, Xiamen, China, [4]Hubei Key Laboratory of Plasma Chemistry and Advanced Materials, School of Materials Science and Engineering, Wuhan Institute of Technology, Wuhan, China

Herein, an Au nanoparticles-polydopamine-poly acrylic acid-graphene (Au NPs-PDA-PAA-graphene) multicomponent nanohybrid is fabricated by surface functionalization of graphene alongside extensive *in-situ* growth of Au nanoparticles. The as-obtained nanocomposite possesses good hydrophilicity, excellent biocompatibility and high biomolecules loading capacity, which acts as an ideal platform for enzyme modification. Considering this fact, Horseradish peroxidase is expressively immobilized upon Au NPs-PDA-PAA-graphene surface, in order to lay the foundations of a biosensor that is majorly based on enzymatic activity. The biosensor exhibits higher sensitivity towards the determination of H_2O_2 with linearity ranging from 0.1 μm upto 20 mm, and the limit of detection going down to 0.02 μm. Encouraged by its acceptable electrocatalytic performance, this multicomponent system can also be easily employed for carrying out the real-time tracking of H_2O_2 coming out of Macrophage cells. Therefore, this work designs an extraordinarily updated platform for biosensing related applications, and also presents a reliable platform for the direct detection of H_2O_2 *in vivo* and *in vitro*, which show great potential in bioelectroanalytical chemistry, cellular biology, and pathophysiology.

Keywords: graphene, multicomponent nanohybrid, electrochemical biosensor, H_2O_2 detection, multicomponenet polymer

Edited by:
Mani Govindasamy,
National Taipei University of Technology, Taiwan

Reviewed by:
Zheng Fang,
Wuhan Textile University, China
Qiying Lv,
Huazhong University of Science and Technology, China

***Correspondence:**
Yimin Sun
ymsun@wit.edu.edu

Specialty section:
This article was submitted to Analytical Chemistry, a section of the journal Frontiers in Chemistry

Received: *13 February 2022*
Accepted: *29 March 2022*
Published: *29 April 2022*

Citation:
Tong P, Asif M, Ajmal M, Aziz A and Sun Y (2022) A Multicomponent Polymer-Metal-Enzyme System as Electrochemical Biosensor for H_2O_2 Detection. Front. Chem. 10:874965. doi: 10.3389/fchem.2022.874965

INTRODUCTION

The structural shape of graphene based nanocomposites incorporated with polymers as well as metallic nanoparticles, and other species to harvest synergetic effects and integrated properties of the individuals, has claimed great interest due to their wide range of scientific as well as industrial implications (Badhulika et al., 2015; Sun et al., 2016; Liao et al., 2018; White et al., 2019; Gao et al., 2021). Graphene has, for a long time, been an attractive choice as the building block for nanocomposites owing to its extraordinary mechanical, electronic, and thermal characteristics, as well as the large surface area (Sun et al., 2015; Zeng et al., 2019; Zhao et al., 2020). Graphene nanocomposites with well-designed nanostructures have been extensively fabricated in order to produce diverse materials with desired performance (Aziz et al., 2019a; Asif et al., 2019; Ibrahim et al., 2021). In particular, graphene and metal based nanoparticle composites have been an area of immense significance from the present day research perspective taking advantage of their unmatched implications in the area of sensors, fuel cells, and energy conversions (Nan et al., 2018; Darabdhara et al., 2019). So far, huge progress is reported to have been undertaken for the improved synthesis as well as manufacturing of graphene and metal based nanoparticle composites (Huang et al., 2011; Mangadlao et al., 2017; Ashraf et al., 2020). Among them, graphene-gold nanoparticles (Au NPs) are the ones being investigated the most, and many systematic approaches are reported to prepare Au NPs with various sizes (Asif et al., 2018a; Li et al., 2021). However, some challenges still remain in those methods, such as how to prevent the aggregation and restack of graphene sheet to get higher specific surface areas; how to ensure improved biocompatibility; and how to keep in check the spatial distribution as well as size for the nanoparticles on the surface of graphene. To address those problems, a surface modification strategy of graphene is proposed to fabricate an efficient substrate for the development and growth of gold NPs.

Covalent binding of polymers with graphene through interfacial interactions represents an effective approach for the development of special functional graphene composite (Sun et al., 2020; Perumal et al., 2021). When incorporated with polymer, the aggregation of graphene nanosheets will be effectively inhibited, thus providing the large surface area (Sun et al., 2017). In this paper, covalently functionalized graphene sheets are prepared through grafting poly acrylic acid (PAA) chains on its surface. PAA is a water soluble polymer with many advantages, such as good biocompatibility, non-toxicity, and easy chemical modification (Kausar, 2020). Both hydrophilicity and biocompatibility of graphene could be realized by functionalization of graphene with PAA. Because of plethora carbonyl groups on PAA, dopamine (DA) can be covalently bonded to PAA chain to form PDA-PAA-graphene. Dopamine, a naturally occurring neurotransmitter, found in a variety of animals, is generally regarded as a unique component that can mimick the proteins which are adhesive in nature (Li et al., 2015). Moreover, DA is also used as a reducing agent and stabilizer which is commonly used for the synthesis of metal-nanoparticles (Au, Ag, Pt et al.) by directly reducing the salt of metal precursor (Zhang et al., 2013; Ren et al., 2016; Wen et al., 2018). By using the *in situ* reducing method, Au NPs could easily be distributed upon the surface of the graphene nanosheets in a homogeneous way. The resulting Au NPs-PDA-PAA-graphene nanocomposites work an ideal platform for the modification of biomolecules. Horseradish peroxidase (HRP), with this unique ability of catalyzing the oxidation for an ample amount of substrates *via* hydrogen peroxide or any other closely related components, is hailed as a mainstream tool metalloenzyme for establishing the electrochemical biosensors (Sellami et al., 2022). As a potential application, by further linking peroxidase, an amplified biosensing toward H_2O_2 at such Au NPs-PDA-PAA-graphene nanocomposites is constructed.

H_2O_2 is reckoned as an extremely stable reactive oxygen species, which serves as a transporter in a variety of ongoing cellular activities, which holds a pivotal contribution in the case of dealing with unwanted oxidative stress, slowing down the aging process, as well as combating the pathological processes, like cancer, neurological disarray, and cardiovascular issues (Xiao et al., 2012; Asif et al., 2017; Zhang et al., 2017; Asif et al., 2018b; Aziz et al., 2019b; Zhao et al., 2021). Therefore, the quantitative determination of intracellular and extracellular H_2O_2 is known to offer more comprehensive illustration of the clinical aspects of the rise in H_2O_2 concentrations, alongside its assistance in studies put forward to elaborate the biological implications of H_2O_2 in cells (Xi et al., 2018; Ma et al., 2020; Yuan et al., 2020; Zhang et al., 2020; Wang et al., 2021; Zong et al., 2021).

In this paper, a novel Au NPs-PDA-PAA-graphene composite film is designed, which offers superior results both in loading and in the activity of immobilized enzymes. Apart from this, the mentioned film also presents improved electrocatalysis/nano-enhancement activity for H_2O_2 biosensing. PAA as a "friendly" and "soft" linker, DA as a coupling and reducing agent for $HAuCl_4$, Au NPs as a catalyst for electrode reaction, and HRP as an enzyme, are mixed to yield graphene-based bionanocomposites. The proposed material showcases impressive biocompatibility, superbly uniform distribution of the nanoparticles, and a much higher loading/activity of the immobilized enzymes. This nanohybrid system shows immensely bettered amperometric biosensing activity in contrast to those based on traditional methods and techniques, e.g., a higher detection sensitivity or a sub-micromolar level detection limit, which makes H_2O_2 extremely useful for both *in vivo* and *in vitro detections.* This graphene-based bionanocomposites enzyme electrode shows great potential application in the second-generation style of biosensing.

MATERIALS AND METHODS

Preparation of Au NPs-PDA-PAA-Graphene

The preparation of PAA-graphene: The synthesis of PAA-graphene was performed by hydrolyzing poly tert-butylacrylate (PtBA). The synthetic procedure of PtBA-graphene was described in our previously published paper (Sun et al., 2018). Brifly, 200 mg graphene-PtBA was distributed into 20 ml CH_2Cl_2, and 1 ml trifluoroacetic acid (TFA) was added. Later, the prepared mixture was stirred at 40°C for 36 h. Then, CH_2Cl_2 was removed by centrifugation, and sediment was washed thoroughly by acetone and water to get pure PAA-graphene.

The synthesis of PDA-PAA-graphene: PAA-graphene (200 mg) was dissolved in 10 ml of deionized water, Na_2CO_3 solution was poured to adjust the pH to 8.5. After sonication for 0.5 h, the solution became homogeneous. This solution was then transferred to an ice-bath, and followed by the addition of N-Hydroxysuccinimide (NHS, 50 mg) and 1-(3-Dimethylaminopropyl)-3-ethylcarbodiimide hydrochloride (EDCHCl, 200 mg), the mixture solution (denoted as solution A) was made to stir under N_2 for about 15 min. Meanwhile, Na_2CO_3 (55 mg) was dissolved in 10 ml of deionized water in order to prepare solution B. This solution was also made to stir under N_2 for about 15 min, and then dopamine HCl (240 mg) was poured in with yet another degassing for about 15 min. Later, solution B was mixed with solution A and was again stirred for about 30 min inside an iced-water bath for about 12 h at around 35°C. During this process, dopamine is easy to polymerize to form polydopamine in alkaline conditions. Eventually, the reaction mixture was made to centrifuge and was also washed thoroughly using deionized water to achieve PDA-PAA-graphene.

The preparation of Au NPs-PDA-PAA-graphene: PDA-PAA-graphene (10.0 mg) was put inside a reaction vessel, and was poured with 10 ml of $HAuCl_4$ solution (50 mm). The reaction was allowed to continue overnight at the expected room temperature. At the end of the reaction, the Au NPs deposited PDA-PAA-graphene was removed from the suspension *via* centrifugation process and were frequently washed with water.

The Preparation of Enzyme Electrode

The enzyme based electrode was designed by immersing Au NPs-PDA-PAA-graphene electrodes into phosphate buffer solution (PBS) with 0.2 mg ml^{-1} HRP for overnight reaction, followed by washing with Milli-Q water and then drying at 4°C.

Characterization

A Kratos-Axis spectrometer having monochromatic Al KR of (1,486.71 eV), an X-ray radiation of (15 kV and 10 mA) and a strong hemispherical electron energy analyzer, was used to carry out X-ray photoelectron spectroscopy (XPS) determinations. Casa XPS software was employed to accomplish curve fitting and background suppression. Fourier-transformed infrared spectrum (FT-IR) was observed on Perkin Elmer FTIR. Thermogravimetric Analysis (TGA) was achieved with the help of TA Instruments TGA/DSC. 1H NMR measurement was performed on a Bruker AVANCE NEO 400 M equipment with D_2O as solvent. UV-vis spectra were observed on a Schimadu UV-2550 spectrometer. Scanning electron microscopy images were acquired by using FESEM instrument (JSM-6700F, Japan). CV and chronoamperometric analysis were undertaken by a CHI 660 D electrochemical workstation (CH Instrument Company). For this purpose, a traditional three-electrode system was selected. HRP/Au NPs-PDA-PAA-graphene electrode was used as a working electrode. The auxiliary and reference electrodes were Pt wire and Ag/AgCl, respectively. All the measurements were conducted at room temperature.

Cell Culture

ATCC (United States) supplied the macrophages and the cells containing Bovine Brain Extract (BBE) supplement were stored in Endothelial Cell Growth Medium (EGM). EGM® is a modified MCDB 131 formulation and is supplemented with 10 µg/ml hEGF (human recombinant Epidermal Growth Factor), 1.0 mg/ml Hydrocortisone, 50 mg/ml Gentamicin, 50 µg/ml Amphotericin B, 3 mg/ml Bovine Brain Extract (2 ml), 2% v/v Fetal Bovine Serum (FBS) and stored at 37°C in humid conditions with 5% CO_2. 24-well plate was used to seed macrophages where they gained 80% confluency before experiments. Calcein-AM was used for living cell staining. Macrophages cells were incubated at 37°C for 15 min before imaging.

RESULTS AND DISCUSSION

The detailed process employed for carrying out the preparation of the Au NPs-PDA-PAA-graphene composite is illustrated in **Figure 1**. The synthetic procedure of PAA-graphene was reported previously (Sun et al., 2018), then DA is covalent linked to PAA *via* the condensation reaction between the NH_2 group in DA and the carboxyl group in PAA, meanwhile, DA will polymerize to form polydopamine (PDA) in alkaline conditions. Next, Au NPs are immobilized onto PDA-PAA-graphene by *in situ* reducing of $HAuCl_4$ by dopamine. Au NPs-PDA-PAA-graphene was coated on the glassy carbon electrode to build a platform for enzyme loading. Finally, HRP was absorbed on the electrode to construct an enzyme electrode.

X-ray photoelectron spectroscopy (XPS) is first applied to trace the synthesis process. The condensation reaction between dopamine and PAA-graphene can be verified by noticing a new absorbance peak at 400.8 eV linked to the binding energy of N1s in an XPS spectrum of PDA-PAA-graphene (**Figure 2A**). After introducing Au NPs to PDA-PAA-graphene, the representing peaks of Au $4f_{7/2}$ and Au $4f_{5/2}$ show up at the binding energies of 83.9 and 87.7 eV respectively (**Figure 2B**), suggesting the successful immobilization of Au NPs upon the PDA-PAA-graphene surface. FT-IR measurement provides further evidences of the above chemical changes as the carboxylate peak in PAA is no longer present, and amine and aromatic rings peaks appear at 1,670, 1,620, and 1,550 cm^{-1}, individually (**Figure 2C**) (Wu et al., 2011).

The condensation reaction can also be identified by 1H NMR spectrum (**Figure 2D**). Comparing with that of PAA-graphene, new peaks appear at *d* 6.83–6.40 and 2.5–3.0 at the 1H NMR spectrum of PDA-PAA-graphene, which directly corresponds to the chemical shift of protons in aromatic rings and alkyl of DA. f = A/A_0 is used to determine the dopamine content (mol%) in PDA-PAA-graphene. Where, A stands for the integral part of the peaks at *d* 6.83–6.40 representing the quantity of H in the aromatic rings of the given catechol moieties, while A_0 corresponds to the integral part of the peaks at *d* 2.2–1.2 showcasing the quantity of H in the PAA backbone. The dopamine ratio found in the resultant polymer is nearly 25% as per the given method. This result is a little lower than that calculated by thermogravimetric analysis (31%) (**Supplementary Figure S1**).

The as-prepared Au NPs-PDA-PAA-graphene composite is also confirmed by UV-vis absorption spectrum as displayed in **Figure 2E**. The spectrum of PAA-graphene presents a maximum absorption at 263 nm, which signifies π-π* transitions between the aromatic C=C bonds (He et al., 2011). After reacting with DA, a shoulder peak at 275 nm, a characteristic absorption for catechol, is detected (Bui et al., 2021). After reduction of $HAuCl_4$, a relatively new peak at 556 nm appears and the solution becomes violet black in color. This newly appearing peak can well be stemming from the surface plasmon resonance (SPR) absorptive band for Au NPs, highlighting the reducibility of $AuCl_4^{-1}$ to Au NPs in a successful way (Mawlud et al., 2017). In contrast to the as-prepared Au colloids present in aqueous solution (Song et al., 2011), the obtained absorption maxima is found to be red-shifted, which in turn can consequently be attributed to the altering refractive index and to some extent partial aggregation of the seed particles inside the growth solution. These results further go on to prove that as far as *in*

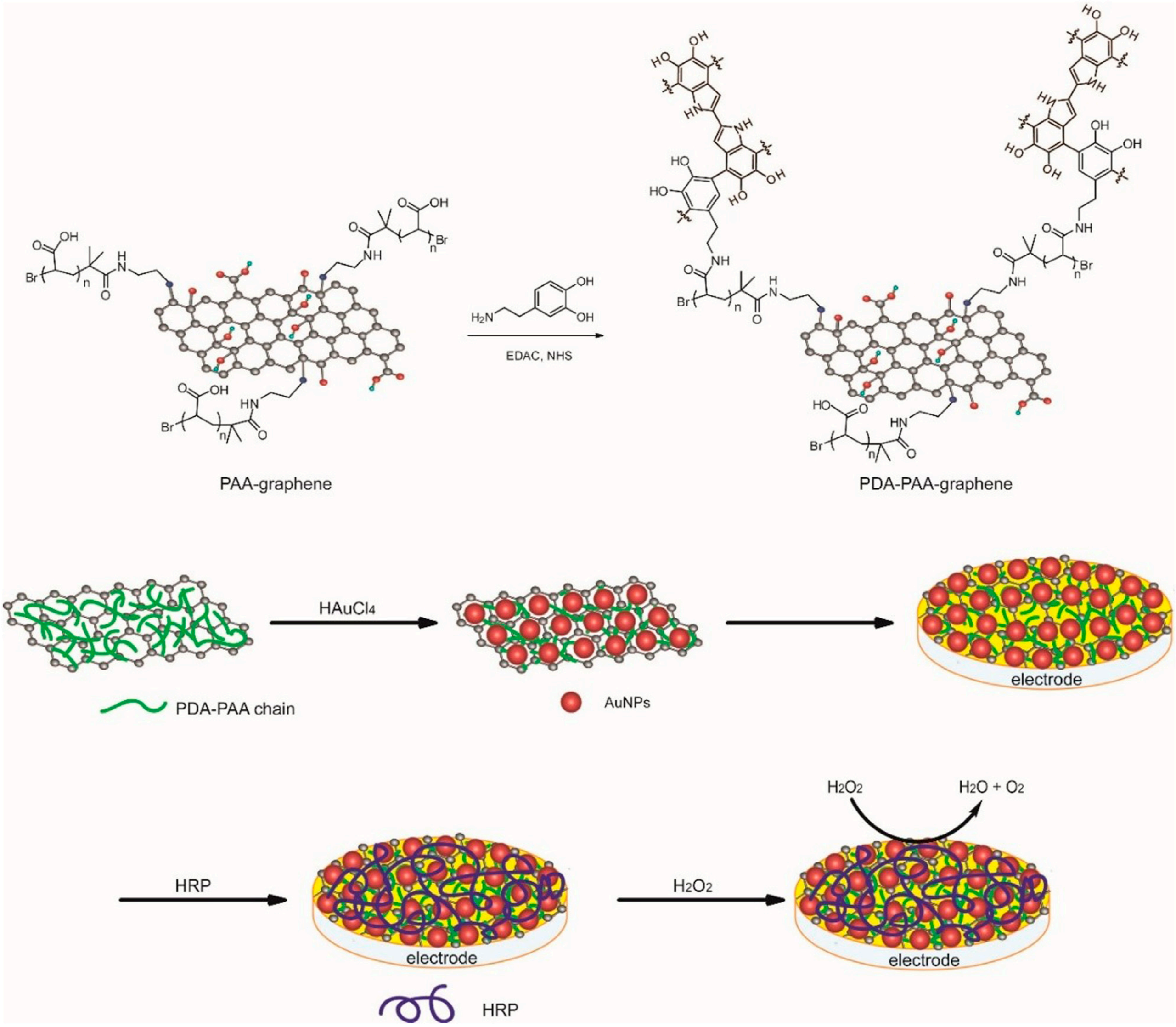

FIGURE 1 | The preparation of the Au NPs-PDA-PAA-graphene composite and the construction of enzyme electrode.

situ methods are concerned, Au nanoparticles are closely linked with each other for the sake of the reduction process and also to small quantities of agglomerations or even bigger particles are expected to have deposited on the graphene surface. The crystalline XRD pattern of Au NPs-PDA-PAA-graphene nanohybrid (**Figure 2F**) show a peak at 24.3 indexed to the (002) crystal face of graphene, and the peaks at 38.1, 44.3, 64.5, and 77.6 correspond to the (111) (200), (220), and 311) crystal faces of Au nanoparticles (JCPDS 4–0,783) (Li et al., 2012). Quantitative measurements of Au NPs on Au NPs-PDA-PAA-graphene surface are materialized by EDX, pointing out the presence of 58 wt% of Au NPs (**Supplementary Figure S2**).

SEM and TEM are used to undertake the characterization of the morphology of the Au NPs-PDA-PAA-graphene composites. **Figures 3A,B**, represent the random distribution of Au NPs PDA-PAA-graphene surface. These also show the fact that the nanoparticles are well embedded on the interior of the surface, highlighting a close interaction among the NPs and PDA-PAA modified graphene sheets. The distribution of Au NPs is believed to be relatively uniform with no severe aggregations. TEM images signify samples to be composed of nanoparticles having diameters averaging nearly 18 nm and the size distribution ranging between 5 and 30 nm. The diameter of most of the found particles is between 12 and 20 nm (**Figures 3C,D**).

The novel nanostructure of the Au NPs-PDA-PAA-graphene inspires us to investigate it as enzyme biosensor. **Figure 4** is the CV representation of differently modified electrodes in 50 mm PBS (pH = 7.4), with 50 mV s^{-1} scan rate. In the CVs of Au NPs-PDA-PAA-graphene and PDA-PAA-graphene electrodes, no observable redox peak appeared which is indicative of their electrochemical inactivity at the specific potential range (−0.8 + 0.1 V). A clearly distinguishable couple of redox peaks in the

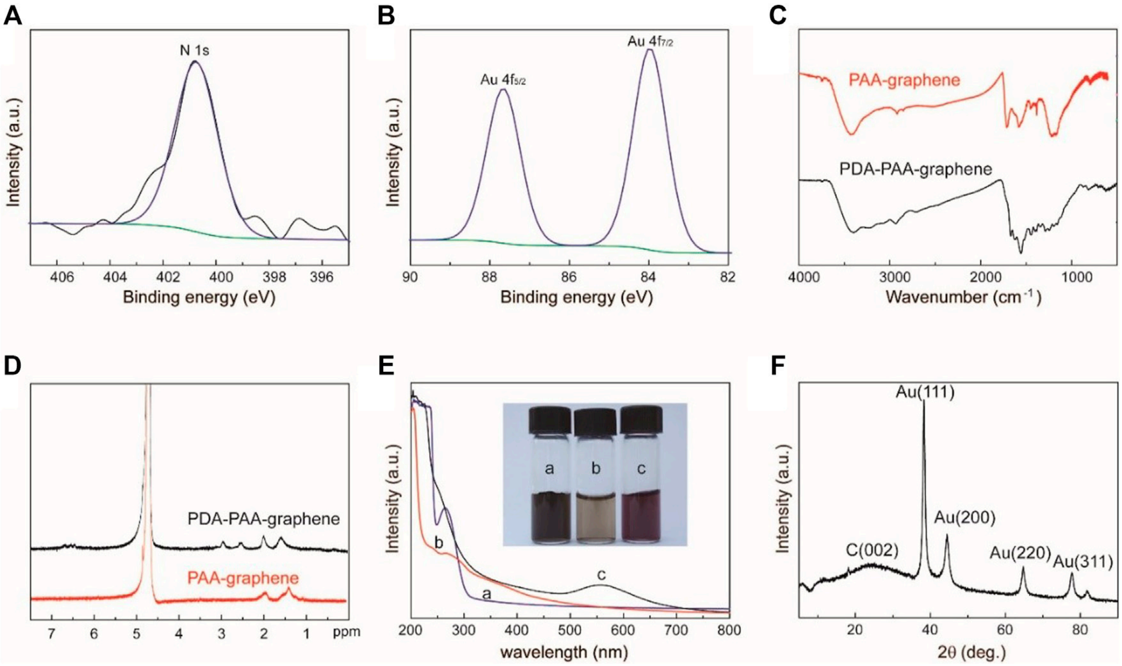

FIGURE 2 | (A) The N1s XPS spectra of Au NPs-PDA-PAA-graphene **(B)** The Au4f XPS spectra of Au NPs-PDA-PAA-graphene **(C)** FT-IR spectra for PAA-graphene and PDA-PAA-graphene) **(D)** 1H NMR spectrum of PDA-PAA-graphene and PAA-graphene in D_2O **(E)** UV-vis absorption spectra and photographs (inset) of PAA-graphene **(A)**, PDA-PAA-graphene **(B)** and Au NPs-PDA-PAA-graphene **(C)** solutions **(F)** XRD pattern of Au NPs-PDA-PAA-graphene composite.

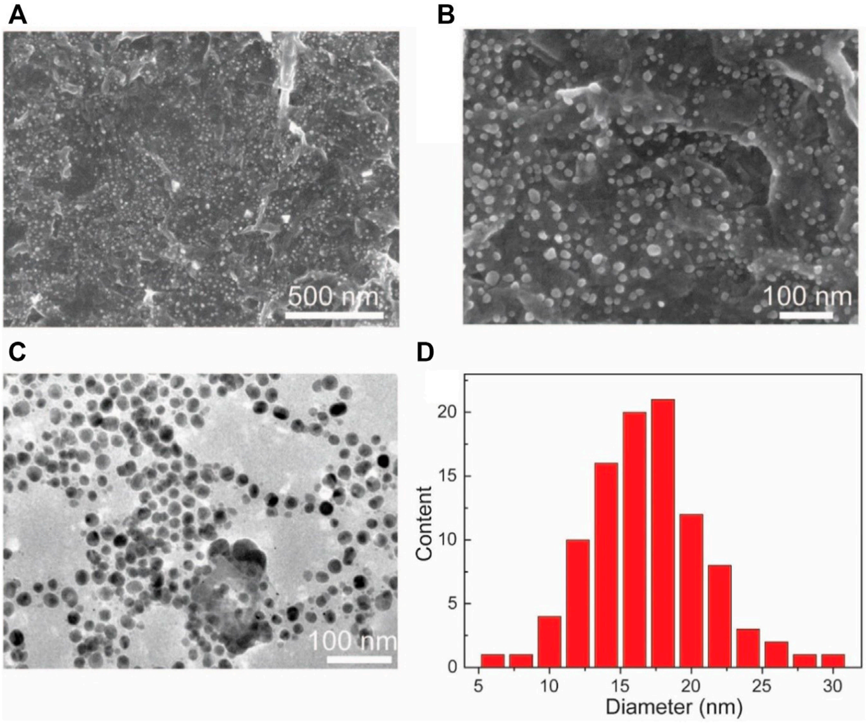

FIGURE 3 | (A,B) SEM based images of Au NPs-PDA-PAA-graphene with varying magnification **(C)** TEM image of Au NPs-PDA-PAA-graphene **(D)** Size and distribution of Au nanoparticles in statistics.

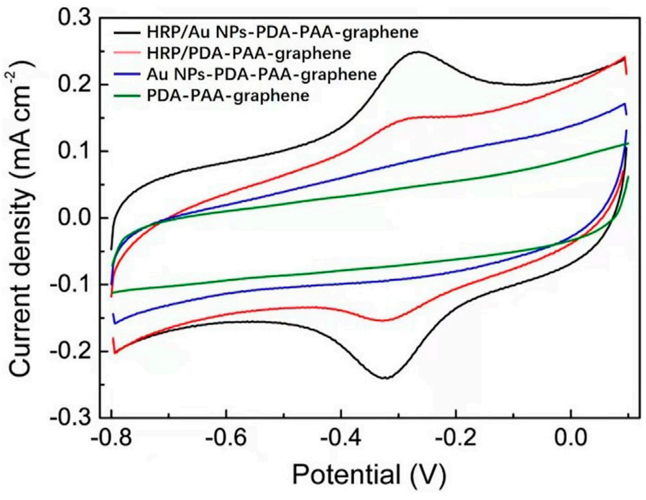

FIGURE 4 | CV curves of HRP/Au NPs-PDA-PAA-graphene, HRP/PDA-PAA-graphene, Au NPs-PDA-PAA-graphene and PDA-PAA-graphene in 0.1 M PBS (pH 7.4) having 1 mM H_2O_2 at the Scan rate of (50 mV s^{-1}).

CVs of HRP/PDA-PAA-graphene are attributed to the Fe^{III}/Fe^{II} redox coupling related to the heme protein for HRP (Liu et al., 2012). While in the CV curve of HRP/Au NPs-PDA-PAA-graphene, the Fe^{III}/Fe^{II} redox couple is more distinct with the cathodic peak potential (−0.320 V) and anodic peak potentials (−0.267 V). Considering the conventional potential [$E_{o'}$ = (Epa + Epc)/2] of −0.294 V, and peak point separation (ΔEp) ~53 mV at the scan rate of (50 mV/s), indicating a reversible electrochemical behavior of HRP, which is much better than other HRP-based biosensors known so far (Zong et al., 2006; Tang et al., 2008). This phenomenon is the proof of uninterrupted transfer of electrons between HRP and GCE, initiated by Au NPs as a promoter. The chemistry behind the direct electron transportation between the HRP and GCE is based on the Au NPs, which not only reduce the space for the center of activation for the immobilized HRP and the GCE, but also effectively boost up the electrochemical conductance of the fabricated electrode, in turn, encourages direct electron transportation between the HRP and glassy carbon electrode. As the active sites of HRP mostly buried deep inside the center and make it harder to exchange electrons with the electrode surface (Li et al., 2011), so Au NPs act as a mediator to carry out the fast electron transfer rate which in turn greatly enhanced the electrochemical performance of the synthesized electrode.

To further clarify the catalytic activity between the HRP and the electrode we used the Au NPs-PDA-PAA-graphene modified electrode immobilized with HRP to study the thoroughgoing current response by applying a different scan rate. As represented in **Figure 5A**, although the redox current gradually increased with an increase in the scan rate, the peak potential did not change obviously. **Figure 5B** shows the excellent linear relation between the redox peak current values and increased scanning rate, ranged from 0.1—1 V/s. Here the regression equation;

$$i_{pa} = 1.00 \times 10^{-4} + 0.122\mathrm{v}\,(\mathrm{R} = 0.999)$$
$$i_{pc} = -9.33 \times 10^{-5} - 0.103\mathrm{v}\,(\mathrm{R} = 0.999)$$

Here, v represents the scan rate while i_{pa}, i_{pc} are the peak current density of anode and cathode. This suggests that the redox reaction of HRP is a typical facet constrained reversible phenomenon. With the assimilation of current (reduction peak) and Faraday's law, the electrochemically active HRP can be calculated from HRP/Au NPs-PDA-PAA-graphene surface from the equation. (Zhang et al., 2010),

$$i_{pa} = \frac{n^2F^2A\Gamma\nu}{4RT}$$

where ipa signifies the reduction peak current, n denotes the total amount of electrons, A stands for the electrode surface area, v is the scan rate, and Γ is the value which needs to be calculated. The estimated Γ value was 9.57×10^{-11} mol cm^{-2}. The Au NPs-PDA-PAA-graphene composite matrix gives remarkable higher surface concentration value for the immobilization of HRP as compared to the previously published literature using different types of matrix, such as colloidal Au (7.5×10^{-11} mol cm^{-2}) (Liu and Ju, 2002)], 3-mercaptopropionic acid monolayer-modified gold surface (5×10^{-11} mol cm^{-2}) (Li and Dong, 1997).

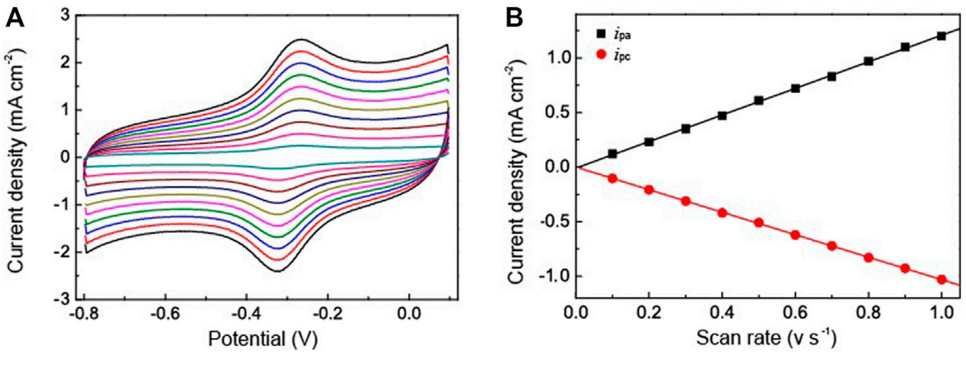

FIGURE 5 | (A) CV curves of HRP/Au NPs-PDA-PAA-graphene at various scan rate ranged from 0.1—1V/s in PBS (pH 7.4) **(B)** is the plot of cathodic/anodic peak current vs. scan rate.

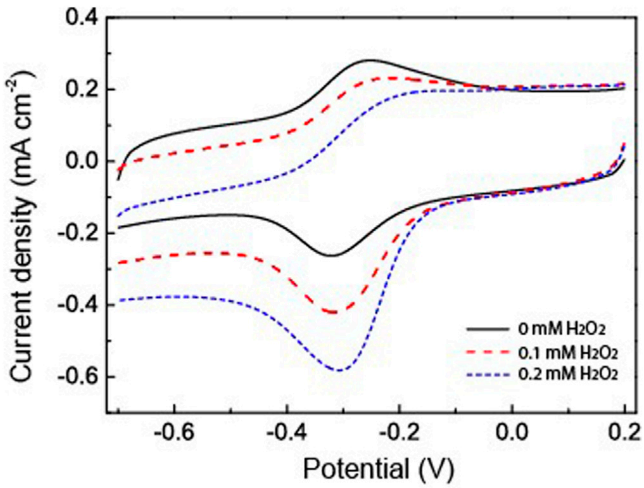

FIGURE 6 | CV curves of HRP/Au NPs-PDA-PAA-graphene with and without H_2O_2 in PBS (pH 7.4). Scan rate: 50 mV/s.

H_2O_2 has been used as an analyte to study the catalytic applications of the fabricated HRP/Au NPs-PDA-PAA-graphene films. **Figure 6** explained the catalytic behavior of the fabricated material in the presence and absence of H_2O_2. When the different concentrations of H_2O_2 were injected into PBS, there was a clear rise in the reduction peak current with a gradual decrease in the oxidation peak current. This phenomenon well explains the remarkable electrocatalytic process for the HRP oxidation *via* H_2O_2 which in turn was reduced. H_2O_2 oxidized the HRP_{re} to HRP_{ox} which was further reduced through electron transfer upon the electrode surface. As H_2O_2 concentration increased it encouraged a large cathodic peak current value, in turn there was a fast rate of electron transfer between the quantities of electrode surface and immobilized HRP.

The amperometric response of the HRP/Au NPs-PDA-PAA-graphene film electrode with sequential injection of H_2O_2 in PBS at −0.32 V is shown in **Figure 7**. The fabricated electrode gives a quick response towards any change in the H_2O_2 concentration and attains a steady state within 5 s, which is credited to the rise in electron transfer from the embedded Au NPs. The lowest limit of detection (0.02 μM S/N = 3) and an excellent linearity range from 0.1 μm to 20 mm (R = 0.999) is better than that in similar systems previously reported (Lin et al., 2007; Lu et al., 2011; Liu et al., 2012). These results suggest that HRP/Au NPs-PDA-PAA-graphene nanoarchitectures pave the way for the synthesis of enzymatic biosensors for the sensitive detection of H_2O_2.

The repeatability parameter was evaluated by taking 10 repeated measurements with the consecutive amount of 1.0 mm H_2O_2 with a same electrode which produces relative standard deviation (RSD) of ~3%. Furthermore, the RSD for the current responses for more than 10 sensors obtained by following the similar protocol is ~5%. For the stability evaluation of the HRP/Au NPs-DA-PAA-graphene film electrode preserved at 4°C, it gives 90% response even after 2 months of refrigeration (**Supplementary Figure S3**). The application of Au NPs-PDA-PAA-graphene composite enhances the biocompatibility and provides a favorable microenvironment for HRP, which aids the retention of the biological activity of HRP. Meanwhile, we speculate that the hydrophilic character of Au NPs-PDA-PAA-graphene would also improve the HRP catalytic performance it does not gets denaturation as well as no reduction in catalytic functioning has been observed at low temperature. Conversely, the sensor sensitivity get reduced quickly at room temperature which may be the reason for the swift deactivation of HRP.

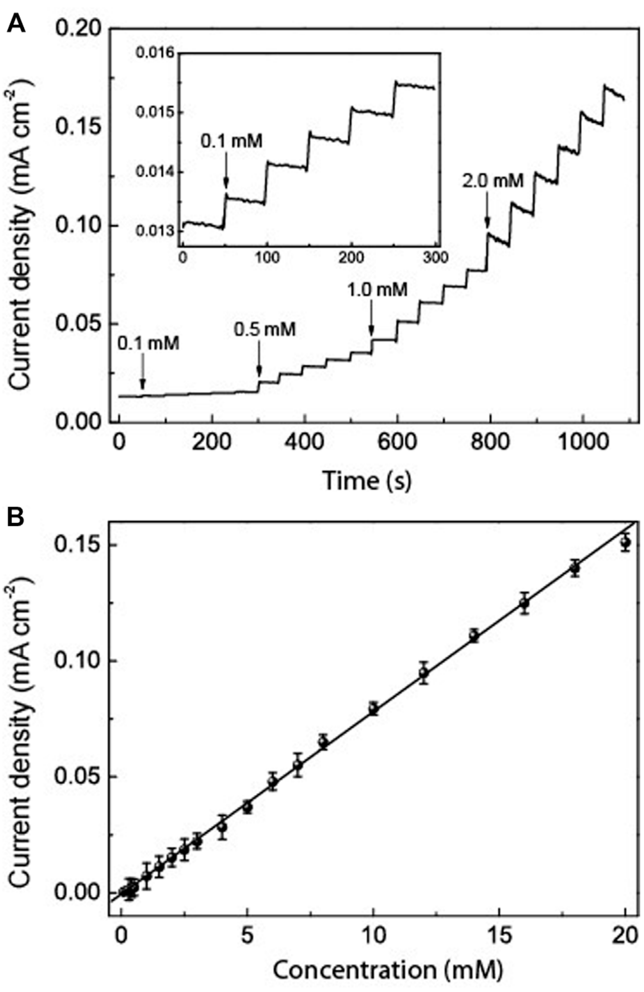

FIGURE 7 | (A) Typical amperometric response of HRP/Au NPs-PDA-PAA-graphene film electrode after the sequential adding various concentrations of H_2O_2. The inset is the enlarged response with the lowest concentration of H_2O_2 **(B)** The linear calibration curves of HRP/Au NPs-PDA-PAA-graphene film electrode for H_2O_2 determination.

By keeping in mind all the advantages of the excellent catalytic performances of the fabricated electrode such as lowest limit of detection, enhanced sensitivity, and quick response, it is noteworthy to say that the as-fabricated biosensor can be used for the determination of the extracellular H_2O_2 released by macrophage cells. The used macrophages offer a pivotal role against the different kind of microorganisms and tumors in there host cells (Niedel et al., 1979). However, these two special properties (tumoricidal and microbicidal) of the chemotactically

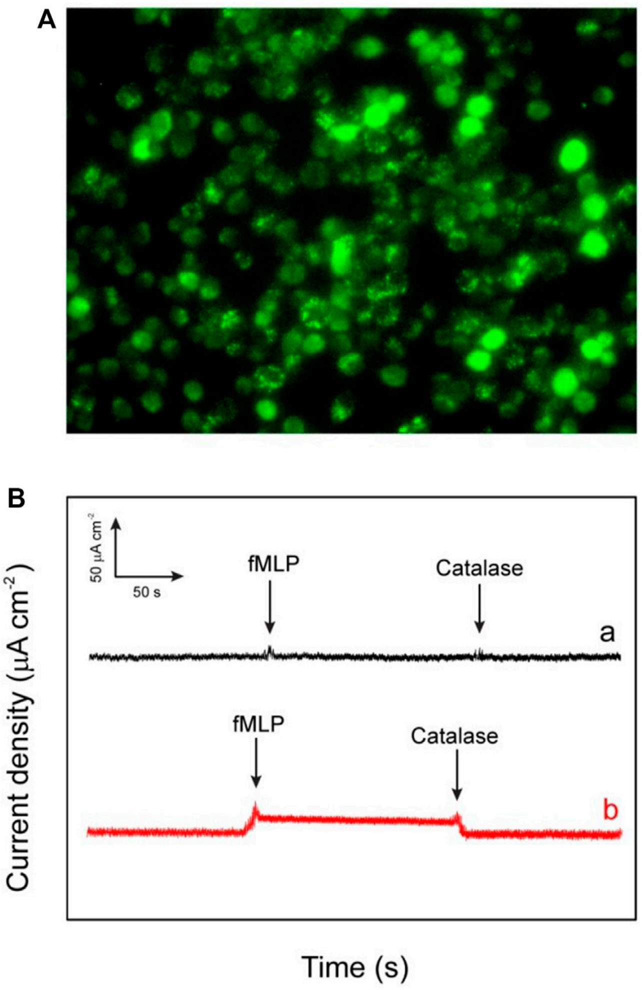

FIGURE 8 | (A) The dark field image of the macrophages (RAW264.7 murine) investigated for the *in vitro* applications **(B)** Amperometric response of HRP/Au NPs-PDA-PAA-graphene electrode for measuring the reducibility of H_2O_2 released macrophage cells induced upon the addition of 0.3 mm fMLP **(A)** and without addition of 50 ml of catalase (300 UmL^{-1}) **(B)**. The electrode was checked at bias value of a consistent potential of −320 mV (versus SCE).

responsive macrophages required some types of agents like bacterial products, cytokines, synthetic peptide, and some chemotherapeutic drugs for their activation. The stimulator N-formyl-methionyl-leucyl-phenylalanine (fMLP) used in this work is a synthetic peptide which is structurally identical to oligopeptide products of bacterial metabolism (Holian and Daniele, 1981). The chemistry behind the use of fMLP as a stimulator is not only its chemotactic properties but it also facilitates the adhering of PMN to endothelium cells. Moreover it also stimulates the release of many kind of molecules such as reactive oxygen intermediates (ROI), lysosomal enzymes, nitric oxide, interleukin 1 (IL-1), and tumor necrosis factor. In this work, the cell macrophages regarding 80% confluency are subjected to release H_2O_2 after injecting fMLP. In the experiment of real-time sensing of H_2O_2 secretion by macrophages, calcein-AM is used to stain the live cells. The dark field microscopic images refer to the fact that the stained macrophages cells are well-spread and healthy (**Figure 8A**). According to the experimental results, after the addition of each 10 μm concentration of fMLP a clear current increase (2.8 μA cm^{-2}) has been observed on the HRP/Au NPs-PDA-PAA-graphene film electrode at the applied potential (−0.32 V), which then further decreases as the H_2O_2 scavenger catalase was spiked. The same procedure was carried out with control well plates (without macrophages) which showed no response as depicted by **Figure 8B**). Therefore, we can conclude that the reported rise in cathode current at HRP/Au NPs-PDA-PAA-graphene film electrode placed near the cells is endorsed to H_2O_2oxidation. All the above discussed results markedly validate that the as-fabricated biosensor can initiate a new opening in biosensing platforms for the unswerving determination of extracellular as well as intracellular H_2O_2 and could well be effectively helpful for advanced physiological and pathological related studies.

CONCLUSION

In summary, new Au NPs-PDA-PAA-graphene composite films have been synthesized by loading highly active enzyme immobilization. The material is introduced onto the electrode surface, and serves as biosensor for extracellular and intracellular H_2O_2 detection. The biosensor exhibits remarkable results in terms of extraordinary sensitivity, wider linear range (0.1 μm–20 mm), noble stability, lowest limit of detection (0.02 mm), and reproducibility for H_2O_2 detection, which is superior to previously constructed biosensing podiums. Hence, this work brings up an advanced biosensing platform for the determination of H_2O_2 *in vivo* and *in vitro*, which can be of utmost advantage for bioelectroanalytical chemistry, cellular biology, and pathophysiological studies.

DATA AVAILABILITY STATEMENT

The original contributions presented in the study are included in the article/**Supplementary Material**, further inquiries can be directed to the corresponding author.

AUTHOR CONTRIBUTIONS

PT: Methodology, Investigation, Data curation, Formal analysis, Writing. MAS: helped in editing, conceptualization. MAJ: helped in editing, conceptualization. AA: helped in editing, conceptualization. YS: Conceptualization, Writing-review and editing, Funding acquisitions.

FUNDING

This work is supported by the Scientific Research Fund of Hubei Provincial Department of Education (B2021075), National

Natural Science Foundation of China (No. 51504168), Postdoctoral Innovation Research for Department of Human Resources and Social Security of Hubei Province, and Scientific Research Fund of Wuhan Institute of Technology (WIT) (No. K2021046).

REFERENCES

Ashraf, G., Asif, M., Aziz, A., Dao, A. Q., Zhang, T., Iftikhar, T., et al. (2020). Facet-energy Inspired Metal Oxide Extended Hexapods Decorated with Graphene Quantum Dots: Sensitive Detection of Bisphenol A in Live Cells. *Nanoscale* 12, 9014–9023. doi:10.1039/C9NR10944G

Asif, M., Aziz, A., Ashraf, G., Wang, Z., Wang, J., Azeem, M., et al. (2018a). Facet-Inspired Core-Shell Gold Nanoislands on Metal Oxide Octadecahedral Heterostructures: High Sensing Performance toward Sulfide in Biotic Fluids. *ACS Appl. Mat. Interfaces* 10, 36675–36685. doi:10.1021/acsami.8b12186

Asif, M., Aziz, A., Azeem, M., Wang, Z., Ashraf, G., Xiao, F., et al. (2018b). A Review on Electrochemical Biosensing Platform Based on Layered Double Hydroxides for Small Molecule Biomarkers Determination. *Adv. Colloid Interface Sci.* 262, 21–38. doi:10.1016/j.cis.2018.11.001

Asif, M., Aziz, A., Wang, H., Wang, Z., Wang, W., Ajmal, M., et al. (2019). Superlattice Stacking by Hybridizing Layered Double Hydroxide Nanosheets with Layers of Reduced Graphene Oxide for Electrochemical Simultaneous Determination of Dopamine, Uric Acid and Ascorbic Acid. *Microchim. Acta.* 186, 1–11. doi:10.1007/s00604-018-3158-y

Asif, M., Haitao, W., Shuang, D., Aziz, A., Zhang, G., Xiao, F., et al. (2017). Metal Oxide Intercalated Layered Double Hydroxide Nanosphere: With Enhanced Electrocatalyic Activity towards H 2 O 2 for Biological Applications. *Sensors Actuators B Chem.* 239, 243–252. doi:10.1016/j.snb.2016.08.010

Aziz, A., Asif, M., Ashraf, G., Azeem, M., Majeed, I., Ajmal, M., et al. (2019a). Advancements in Electrochemical Sensing of Hydrogen Peroxide, Glucose and Dopamine by Using 2D Nanoarchitectures of Layered Double Hydroxides or Metal Dichalcogenides. A Review. *Microchim. Acta* 186, 1–16. doi:10.1007/s00604-019-3776-z

Aziz, A., Asif, M., Azeem, M., Ashraf, G., Wang, Z., Xiao, F., et al. (2019b). Self-stacking of Exfoliated Charged Nanosheets of LDHs and Graphene as Biosensor with Real-Time Tracking of Dopamine from Live Cells. *Anal. Chim. Acta* 1047, 197–207. doi:10.1016/j.aca.2018.10.008

Badhulika, S., Terse-Thakoor, T., Villarreal, C., and Mulchandani, A. (2015). Graphene Hybrids: Synthesis Strategies and Applications in Sensors and Sensitized Solar Cells. *Front. Chem.* 3, 38. doi:10.3389/fchem.2015.00038

Bao-Kai, M., Mian, L., Ling-Zhi, C., Xin-Chu, W., Cai, S., and Qing, H. (2019). Enzyme-MXene Nanosheets: Fabrication and Application in Electrochemical Detection of H2O2. *J. Inorg. Mater.* 35, 18–138. doi:10.15541/jim20190139

Bui, H. L., Nguyen, C. T. V., Lee, W.-Y., Huang, S.-C., Chen, P.-F., Lan, M.-Y., et al. (2021). Dopamine-Initiated Photopolymerization for a Versatile Catechol-Functionalized Hydrogel. *ACS Appl. Bio Mater* 4, 6268–6279. doi:10.1021/acsabm.1c00564

Darabdhara, G., Das, M. R., Singh, S. P., Rengan, A. K., Szunerits, S., and Boukherroub, R. (2019). Ag and Au Nanoparticles/reduced Graphene Oxide Composite Materials: Synthesis and Application in Diagnostics and Therapeutics. *Adv. Colloid Interface Sci.* 271, 101991. doi:10.1016/j.cis.2019.101991

Gao, X.-G., Cheng, L.-X., Jiang, W.-S., Li, X.-K., and Xing, F. (2021). Graphene and its Derivatives-Based Optical Sensors. *Front. Chem.* 9, 615464. doi:10.3389/fchem.2021.615164

He, F.-A., Fan, J.-T., Song, F., Zhang, L.-M., and Lai-Wa Chan, H. (2011). Fabrication of Hybrids Based on Graphene and Metal Nanoparticles by *In Situ* and Self-Assembled Methods. *Nanoscale* 3, 1182–1188. doi:10.1039/C0NR00672F

Holian, A., and Daniele, R. P. (1981). Release of Oxygen Products from Lung Macrophages by N-Formyl Peptides. *J. Appl. Physiology* 50, 736–740. doi:10.1152/jappl.1981.50.4.736

SUPPLEMENTARY MATERIAL

The Supplementary Material for this article can be found online at: https://www.frontiersin.org/articles/10.3389/fchem.2022.874965/full#supplementary-material

Huang, X., Yin, Z., Wu, S., Qi, X., He, Q., Zhang, Q., et al. (2011). Graphene-Based Materials: Synthesis, Characterization, Properties, and Applications. *Small* 7, 1876–1902. doi:10.1002/smll.201002009

Ibrahim, A., Klopocinska, A., Horvat, K., and Hamid, Z. A. (2021). Graphene-Based Nanocomposites: Synthesis, Mechanical Properties, and Characterizations. *Polymers* 13, 2869. doi:10.3390/polym13172869

Kausar, A. (2020). Poly(acrylic Acid) Nanocomposites: Design of Advanced Materials. *J. Plastic Film Sheeting* 37, 409–428. doi:10.1177/8756087920981615

Li, J., and Dong, S. (1997). The Electrochemical Study of Oxidation-Reduction Properties of Horseradish Peroxidase. *J. Electroanal. Chem.* 431, 19–22. doi:10.1016/S0022-0728(97)00158-7

Li, J., Liu, C.-Y., and Liu, Y. (2012). Au/graphene Hydrogel: Synthesis, Characterization and its Use for Catalytic Reduction of 4-nitrophenol. *J. Mat. Chem.* 22, 8426–8430. doi:10.1039/C2JM16386A

Li, J., Wen, M. X., Zhang, W., Chen, Y. P., Xiao, Y., Xiong, C. X., et al. (2015). Reinforcing Epoxy Resin with Polydopamine-Coated $Al(OH)_3$: A Biomimetic Method to Constructing Organic-Inorganic Hybrid Materials. *Adv. Mat. Res.* 1082, 65–68. doi:10.4028/www.scientific.net/AMR.1082.65

Li, Q., Yu, D., Fan, C., Huang, Q., Tang, Y., Guo, R., et al. (2021). Gold Nanoparticles Adsorbed on Graphene as Nanozymes for the Efficient Elimination of Dye Pollutants. *ACS Appl. Nano Mat.* 5, 94–100. doi:10.1021/acsanm.1c03287

Li, W.-T., Wang, M.-H., Li, Y.-J., Sun, Y., and Li, J.-C. (2011). Linker-free Layer-By-Layer Self-Assembly of Gold Nanoparticle Multilayer Films for Direct Electron Transfer of Horseradish Peroxidase and H2O2 Detection. *Electrochimica Acta* 56, 6919–6924. doi:10.1016/j.electacta.2011.06.023

Liao, G., Hu, J., Chen, Z., Zhang, R., Wang, G., and Kuang, T. (2018). Preparation, Properties, and Applications of Graphene-Based Hydrogels. *Front. Chem.* 6, 450. doi:10.3389/fchem.2018.00450

Lin, J., Qu, W., and Zhang, S. (2007). Disposable Biosensor Based on Enzyme Immobilized on Au-Chitosan-Modified Indium Tin Oxide Electrode with Flow Injection Amperometric Analysis. *Anal. Biochem.* 360, 288–293. doi:10.1016/j.ab.2006.10.030

Liu, S.-Q., and Ju, H.-X. (2002). Renewable Reagentless Hydrogen Peroxide Sensor Based on Direct Electron Transfer of Horseradish Peroxidase Immobilized on Colloidal Gold-Modified Electrode. *Anal. Biochem.* 307, 110–116. doi:10.1016/S0003-2697(02)00014-3

Liu, X., Feng, H., Zhang, J., Zhao, R., Liu, X., and Wong, D. K. Y. (2012). Hydrogen Peroxide Detection at a Horseradish Peroxidase Biosensor with a Au Nanoparticle-Dotted Titanate Nanotube|hydrophobic Ionic Liquid Scaffold. *Biosens. Bioelectron.* 32, 188–194. doi:10.1016/j.bios.2011.12.002

Lu, C.-C., Zhang, M., Li, A.-J., He, X.-W., and Yin, X.-B. (2011). 3,4-Dihydroxy-L-phenylalanine for Preparation of Gold Nanoparticles and as Electron Transfer Promoter in H2O2 Biosensor. *Electroanalysis* 23, 2421–2428. doi:10.1002/elan.201100291

Mangadlao, J. D., Cao, P., Choi, D., and Advincula, R. C. (2017). Photoreduction of Graphene Oxide and Photochemical Synthesis of Graphene-Metal Nanoparticle Hybrids by Ketyl Radicals. *ACS Appl. Mat. Interfaces* 9, 24887–24898. doi:10.1021/acsami.7b06275

Mawlud, S. Q., Ameen, M. M., Sahar, M. R., and Ahmed, K. F. (2017). Plasmon-enhanced Luminescence of Samarium Doped Sodium Tellurite Glasses Embedded with Gold Nanoparticles: Judd-Ofelt Parameter. *J. Luminescence* 190, 468–475. doi:10.1016/j.jlumin.2017.06.004

Nan, H., Chen, Z., Jiang, J., Li, J., Zhao, W., Ni, Z., et al. (2018). The Effect of Graphene on Surface Plasmon Resonance of Metal Nanoparticles. *Phys. Chem. Chem. Phys.* 20, 25078–25084. doi:10.1039/C8CP03293A

Niedel, J., Wilkinson, S., and Cuatrecasas, P. (1979). Receptor-mediated Uptake and Degradation of 125I-Chemotactic Peptide by Human Neutrophils. *J. Biol. Chem.* 254, 10700–10706. doi:10.1016/S0021-9258(19)86577-8

Perumal, S., Atchudan, R., and Cheong, I. W. (2021). Recent Studies on Dispersion of Graphene-Polymer Composites. *Polymers* 13, 2375. doi:10.3390/polym13142375

Ren, S., Wang, H., Zhang, Y., Sun, Y., Li, L., Zhang, H., et al. (2016). Convenient and Controllable Preparation of a Novel Uniformly Nitrogen Doped Porous graphene/Pt Nanoflower Material and its Highly-Efficient Electrochemical Biosensing. *Analyst* 141, 2741–2747. doi:10.1039/c5an02654g

Sellami, K., Couvert, A., Nasrallah, N., Maachi, R., Abouseoud, M., and Amrane, A. (2022). Peroxidase Enzymes as Green Catalysts for Bioremediation and Biotechnological Applications: A Review. *Sci. Total Environ.* 806, 150500. doi:10.1016/j.scitotenv.2021.150500

Song, J., Cheng, L., Liu, A., Yin, J., Kuang, M., and Duan, H. (2011). Plasmonic Vesicles of Amphiphilic Gold Nanocrystals: Self-Assembly and External-Stimuli-Triggered Destruction. *J. Am. Chem. Soc.* 133, 10760–10763. doi:10.1021/ja204387w

Sun, X., Huang, C., Wang, L., Liang, L., Cheng, Y., Fei, W., et al. (2020). Recent Progress in Graphene/Polymer Nanocomposites. *Adv. Mat.* 33, 2001105. doi:10.1002/adma.202001105

Sun, Y., He, K., Zhang, Z., Zhou, A., and Duan, H. (2015). Real-time Electrochemical Detection of Hydrogen Peroxide Secretion in Live Cells by Pt Nanoparticles Decorated Graphene-Carbon Nanotube Hybrid Paper Electrode. *Biosens. Bioelectron.* 68, 358–364. doi:10.1016/j.bios.2015.01.017

Sun, Y., Zeng, W., Sun, H., Luo, S., Chen, D., Chan, V., et al. (2018). Inorganic/polymer-graphene Hybrid Gel as Versatile Electrochemical Platform for Electrochemical Capacitor and Biosensor. *Carbon* 132, 589–597. doi:10.1016/j.carbon.2018.02.099

Sun, Y., Zheng, H., Wang, C., Yang, M., Zhou, A., and Duan, H. (2016). Ultrasonic-electrodeposition of PtPd Alloy Nanoparticles on Ionic Liquid-Functionalized Graphene Paper: towards a Flexible and Versatile Nanohybrid Electrode. *Nanoscale* 8, 1523–1534. doi:10.1039/c5nr06912b

Tang, D., Yuan, R., and Chai, Y. (2008). Ultrasensitive Electrochemical Immunosensor for Clinical Immunoassay Using Thionine-Doped Magnetic Gold Nanospheres as Labels and Horseradish Peroxidase as Enhancer. *Anal. Chem.* 80, 1582–1588. doi:10.1021/ac702217m

Wang, T., Wu, Y., She, J., Xu, Y., Zhang, Y., Zhao, A., et al. (2021). 3D Nitrogen-Doped Carbon Nanofoam Arrays Embedded with PdCu Alloy Nanoparticles: Assembling on Flexible Microelectrode for Electrochemical Detection in Cancer Cells. *Anal. Chim. Acta* 1158, 338420. doi:10.1016/j.aca.2021.338420

Wen, M., Liu, M., Xue, W., Yang, K., Chen, G., and Zhang, W. (2018). Simple and Green Strategy for the Synthesis of "Pathogen-Mimetic" Glycoadjuvant@AuNPs by Combination of Photoinduced RAFT and Bioinspired Dopamine Chemistry. *ACS Macro Lett.* 7, 70–74. doi:10.1021/acsmacrolett.7b00837

White, D. L., Burkert, S. C., Hwang, S. I., and Star, A. (2019). Holey Graphene Metal Nanoparticle Composites via Crystalline Polymer Templated Etching. *Nano Lett.* 19, 2824–2831. doi:10.1021/acs.nanolett.8b04755

Wu, J., Zhang, L., Wang, Y., Long, Y., Gao, H., Zhang, X., et al. (2011). Mussel-Inspired Chemistry for Robust and Surface-Modifiable Multilayer Films. *Langmuir* 27, 13684–13691. doi:10.1021/la2027237

Xi, J., Zhang, Y., Wang, Q., Xiao, J., Chi, K., Duan, X., et al. (2018). Multi-element Doping Design of High-Efficient Carbocatalyst for Electrochemical Sensing of Cancer Cells. *Sensors Actuators B Chem.* 273, 108–117. doi:10.1016/j.snb.2018.06.039

Xiao, F., Song, J., Gao, H., Zan, X., Xu, R., and Duan, H. (2012). Coating Graphene Paper with 2D-Assembly of Electrocatalytic Nanoparticles: A Modular Approach toward High-Performance Flexible Electrodes. *ACS Nano* 6, 100–110. doi:10.1021/nn202930m

Yuan, H., Zhao, J., Wang, Q., Manoj, D., Zhao, A., Chi, K., et al. (2020). Hierarchical Core-Shell Structure of 2D VS2@VC@N-Doped Carbon Sheets Decorated by Ultrafine Pd Nanoparticles: Assembled in a 3D Rosette-like Array on Carbon Fiber Microelectrode for Electrochemical Sensing. *ACS Appl. Mat. Interfaces* 12, 15507–15516. doi:10.1021/acsami.9b21436

Zeng, W., Manoj, D., Sun, H., Yi, R., Huang, X., and Sun, Y. (2019). One-pot Synthesis of High-Density Pd Nanoflowers Decorated 3D Carbon Nanotube-Graphene Network Modified on Printed Electrode as Portable Electrochemical Sensing Platform for Sensitive Detection of Nitroaromatic Explosives. *J. Electroanal. Chem.* 833, 527–535. doi:10.1016/j.jelechem.2018.12.028

Zhang, Y., Lv, Q., Chi, K., Li, Q., Fan, H., Cai, B., et al. (2020). Hierarchical Porous Carbon Heterojunction Flake Arrays Derived from Metal Organic Frameworks and Ionic Liquid for H2O2 Electrochemical Detection in Cancer Tissue. *Nano Res.* 14, 1335–1343. doi:10.1007/s12274-020-3176-z

Zhang, Y., Xiao, J., Lv, Q., Wang, L., Dong, X., Asif, M., et al. (2017). *In Situ* Electrochemical Sensing and Real-Time Monitoring Live Cells Based on Freestanding Nanohybrid Paper Electrode Assembled from 3D Functionalized Graphene Framework. *ACS Appl. Mat. Interfaces* 9, 38201–38210. doi:10.1021/acsami.7b08781

Zhang, Y., Yuan, R., Chai, Y., Xiang, Y., Hong, C., and Ran, X. (2010). An Amperometric Hydrogen Peroxide Biosensor Based on the Immobilization of HRP on Multi-Walled Carbon Nanotubes/electro-Copolymerized Nano-Pt-Poly(neutral Red) Composite Membrane. *Biochem. Eng. J.* 51, 102–109. doi:10.1016/j.bej.2010.06.001

Zhang, Z., Zhang, J., Zhang, B., and Tang, J. (2013). Mussel-inspired Functionalization of Graphene for Synthesizing Ag-Polydopamine-Graphenenanosheets as Antibacterial Materials. *Nanoscale* 5, 118–123. doi:10.1039/c2nr32092d

Zhao, A., She, J., Manoj, D., Wang, T., Sun, Y., Zhang, Y., et al. (2020). Functionalized Graphene Fiber Modified by Dual Nanoenzyme: Towards High-Performance Flexible Nanohybrid Microelectrode for Electrochemical Sensing in Live Cancer Cells. *Sensors Actuators B Chem.* 310, 127861. doi:10.1016/j.snb.2020.127861

Zhao, A., She, J., Xiao, C., Xi, J., Xu, Y., Manoj, D., et al. (2021). Green and Controllable Synthesis of Multi-Heteroatoms Co-doped Graphene Fiber as Flexible and Biocompatible Microelectrode for *In Situ* Electrochemical Detection of Biological Samples. *Sensors Actuators B Chem.* 335, 129683. doi:10.1016/j.snb.2021.129683

Zong, L.-P., Ruan, L.-Y., Li, J., Marks, R. S., Wang, J.-S., Cosnier, S., et al. (2021). Fe-MOGs-based Enzyme Mimetic and its Mediated Electrochemiluminescence for *In Situ* Detection of H2O2 Released from Hela Cells. *Biosens. Bioelectron.* 184, 113216. doi:10.1016/j.bios.2021.113216

Zong, S., Cao, Y., Zhou, Y., and Ju, H. (2006). Zirconia Nanoparticles Enhanced Grafted Collagen Tri-Helix Scaffold for Unmediated Biosensing of Hydrogen Peroxide. *Langmuir* 22, 8915–8919. doi:10.1021/la060930h

Conflict of Interest: The authors declare that the research was conducted in the absence of any commercial or financial relationships that could be construed as a potential conflict of interest.

frontiers | Frontiers in Chemistry

ORIGINAL RESEARCH
published: 12 May 2022
doi: 10.3389/fchem.2022.911170

Gas Sensing Mechanism and Adsorption Properties of C_2H_4 and CO Molecules on the Ag_3–$HfSe_2$ Monolayer: A First-Principle Study

Lufen Jia[1], Jianxing Chen[1], Xiaosen Cui[1], Zhongchang Wang[2,3], Wen Zeng[4]* and Qu Zhou[1]*

[1]College of Engineering and Technology, Southwest University, Chongqing, China, [2]Department of Quantum and Energy Materials, International Iberian Nanotechnology Laboratory (INL), Braga, Portugal, [3]School of Materials and Energy, Southwest University, Chongqing, China, [4]College of Materials Science and Engineering, Chongqing University, Chongqing, China

The detection of dissolved gases in oil is an important method for the analysis of transformer fault diagnosis. In this article, the potential-doped structure of the Ag_3 cluster on the $HfSe_2$ monolayer and adsorption behavior of CO and C_2H_4 upon Ag_3–$HfSe_2$ were studied theoretically. Herein, the binding energy, adsorption energy, band structure, density of state (DOS), partial density of state (PDOS), Mulliken charge analysis, and frontier molecular orbital were investigated. The results showed that the adsorption effect on C_2H_4 is stronger than that on CO. The electrical sensitivity and anti-interference were studied based on the bandgap and adsorption energy of gases. In particular, there is an increase of 55.49% in the electrical sensitivity of C_2H_4 after the adsorption. Compared to the adsorption energy of different gases, it was found that only the adsorption of the C_2H_4 system is chemisorption, while that of the others is physisorption. It illustrates the great anti-interference in the detection of C_2H_4. Therefore, the study explored the potential of $HfSe_2$-modified materials for sensing and detecting CO and C_2H_4 to estimate the working state of power transformers.

Keywords: the first-principle study, $HfSe_2$ monolayer, Ag_3 doping, gas adsorption, transformer oil

Edited by:
Muhammad Asif,
Wuhan Institute of Technology, China

Reviewed by:
Shenqi Wang,
Huazhong University of Science and Technology, China
Abdul Rahman Rahman,
Zhejiang University, China

***Correspondence:**
Qu Zhou
zhouqu@swu.edu.cn
Wen Zeng
wenzeng@cqu.edu.cn

Specialty section:
This article was submitted to Nanoscience,
a section of the journal
Frontiers in Chemistry

Received: *02 April 2022*
Accepted: *13 April 2022*
Published: *12 May 2022*

Citation:
Jia L, Chen J, Cui X, Wang Z, Zeng W and Zhou Q (2022) Gas Sensing Mechanism and Adsorption Properties of C_2H_4 and CO Molecules on the Ag_3–$HfSe_2$ Monolayer: A First-Principle Study.
Front. Chem. 10:911170.
doi: 10.3389/fchem.2022.911170

INTRODUCTION

Two-dimensional transition metal dichalcogenides (TMDs) have recently emerged as a focus of the scientific community in virtue of their versatile and tunable physical properties (Xu et al., 2013; Duerloo et al., 2014; Si et al., 2020; Ju et al., 2021). Layered transition metal disulfides (LTMDs) own the properties of large specific surface value, high electronic activity, and sensitivity (Choi and Kim, 2018). The properties mentioned previously contribute to the great potential of the chemical sensors. Hafnium dichalcogenides (HfX_2, X = S, Se, or Te) belong to middle-gap semiconductors and have a high chemical reactivity and various energy dispersions (Yue et al., 2015; Mirabelli et al., 2016; Mleczko et al., 2017; Cruzado et al., 2021). As a consequence, all the excellent properties mentioned previously embody their future applications in optoelectronics and electronics.

As the most important and valuable piece of equipment, the operation status of the oil-immersed power transformers affects the safety and stability of the electric power system operation directly (Gui et al., 2020). The malfunction that occurred in oil or the insulating paper is inevitable during the long-running process of the transformer. The malfunction mainly includes overheating of oil or the insulating paper, arc discharge, partial discharge, and spark discharge (Tang et al., 2020). Under the effect of electricity and heat, the transformer oil will undergo a chemical reaction and generate gases. The gases generated are mostly hydrocarbons and some other related gases, such as CH_4, C_2H_4, CO_2, and CO. Their composition and contents are closely linked to the type and severity of the transformer faults (Singh and Bandyopadhyay, 2010). Dissolved gas analysis (DGA) could discover the hidden faults sensitively. DGA mainly includes infrared spectroscopy, gas chromatography, Raman spectroscopy, and the gas sensor method (Tran et al., 2018). Due to its simple structure, high reaction sensitivity, low cost, and low power consumption, the gas sensor method is proposed to be applied for detecting gases by more and more scientists (Wei et al., 2020).

$HfSe_2$ has the atomic stacking structure with a layer of Hf atoms stuck in the middle of two layers of Se atoms. Cui et al. explored the adsorption behavior of Pd-doped and Pt-doped $HfSe_2$ monolayers upon several kinds of gases, such as NO_2, SO_2, and SOF_2 (Cui et al., 2020a; Cui et al., 2020c). It is found that the Pd-doped monolayer behaves better for NO_2, while the Pt-doped $HfSe_2$ monolayer behaves better for SO_2. Wang et al. studied the adsorption nature and behavior of Rh-doped $HfSe_2$, and it shows a stronger interaction between the SO_2 molecule and the monolayer than SO_2F_2 (Wang and Liao, 2019). Wu et al. studied the doping behavior of Pd atoms and the sensing character of the Pd-doped $HfSe_2$ (Pd–$HfSe_2$) monolayer upon CO and C_2H_2 (Wu et al., 2022). They found that the Pd-$HfSe_2$ monolayer possesses a better adsorption behavior on CO. Yang et al. investigated the adsorption of CO, C_2H_2, and C_2H_4 based on the Cu-doped Se-vacant $MoSe_2$ (Cu–$MoSe_2$) monolayer (Yang et al., 2020). But Cu–$MoSe_2$ is not selective for the detection of C_2H_4. Xu et al. explored four characteristic dissolved gases in transformer oil: H_2, CH_4, C_2H_2, and C_2H_4 (Xu et al., 2020). It was found that the adsorption effects on C_2H_2 and C_2H_4 are stronger than those of the others. Speaking of the methods of modifying the material monolayer, Asif et al. integrated positively charged semiconductive sheets of Zn-NiAl LDH and negatively charged layers of rGO to modify the glassy carbon electrode (Asif et al., 2019a). The modified electrode exhibited excellent electrocatalytic activity. The doping formation of the Ag_3 cluster and the adsorption behavior of C_2H_4 and CO were not explored yet. In this article, the adsorption of C_2H_4 and CO of Ag_3-doped $HfSe_2$ monolayers was investigated. The doping formation adopted is the Ag_3 cluster, and three atoms contribute to the formation of a stable triangle structure. The results showed that the Ag_3-doped $HfSe_2$ monolayer behaves better for C_2H_4 adsorption but is inactive for CO.

COMPUTATIONAL DETAILS

The first-principle calculations based on the DFT (density functional theory) framework emerged as an important and dominant method in quantum mechanics simulation (Delley, 2000). All the calculations in this article adopted the $DMol^3$ package in Materials Studio software to establish the adsorption model of pristine and Ag_3-doped $HfSe_2$ upon C_2H_4 and CO. Moreover, Perdew–Burke–Ernzerhof (PBE) functional with a generalized gradient approximation (GGA) was used for the electron exchange and correlation function (Chen et al., 2019b). To better deal with the van der Waals interactions and the relativistic effect of doped atoms, Tkatchenko and Scheffler's (TS) method and the DFT semi-core pseudopotential (DSSP) method were employed, respectively. The atomic orbital basis set was described by the double numerical plus polarization (DNP) method (Cui et al., 2020b). The supercell geometry optimizations were calculated under the Monkhorst-Pack k-point mesh of 5 × 5 × 1, while 7 × 7 × 1 was sampled for the more accurate electronic structure calculations. To ensure the precision of total energy, smearing was set as 0.005Ha, and the energy tolerance accuracy, maximum force, and displacement were set as 10^{-5} Ha, 2×10^{-3} Ha/Å, and 5×10^{-3} Å, respectively (Topsakal et al., 2009; Sharma et al., 2018). To mimic a free-standing graphene sheet of $HfSe_2$, a periodic 4 × 4 × 1 $HfSe_2$ supercell was established with a 20-Å vacuum region imposed in the direction where the sheet is not periodic, and the vacuum region is large enough to ensure the doping and gas adsorption processes, as well as eliminate the interaction between adjacent units (Yang et al., 2020).

The binding energy E_b, which plays an important role in estimating the most stable configuration, is calculated as follows.

$$E_b = E_{Ag_3-HfSe_2} - E_{Ag_3} - E_{HfSe_2}. \qquad (2-1)$$

The aforementioned equation represents the total energy of the Ag_3-$HfSe_2$ monolayer subtracting the total energies of the free-standing sheet of the $HfSe_2$ and Ag_3 cluster. Comparing the binding energy of different doping sites, the configuration with the lowest binding energy is defined as the most stable one (Asif et al., 2022).

The adsorption energy E_{ad} generated during the adsorption process is calculated as follows.

$$E_{ad} = E_{gas/Ag_3-HfSe_2} - E_{gas} - E_{Ag_3-HfSe_2}. \qquad (2-2)$$

Here, in the aforementioned equation, E_{gas/Ag_3-HfSe_2} represents the total energy of the system of the Ag_3-doped $HfSe_2$ monolayer with the adsorbed gas molecule. E_{gas/Ag_3-HfSe_2} and $E_{Ag_3-HfSe_2}$ mean the energy of the adsorbed gas molecule and the energy of the Ag_3-doped $HfSe_2$ monolayer, respectively. By comparing the value of the adsorption energy E_{ad} with 0.8, the type of the adsorption can be judged. If greater than 0.8, it is defined as chemisorption, otherwise, it is physisorption (Liu et al., 2021).

RESULTS AND DISCUSSION

Analysis of Pristine and the Ag_3-Doped $HfSe_2$ Monolayer

First, the geometric structure of the free-standing $HfSe_2$ monolayer was optimized to obtain the most stable configuration, as shown in **Figures 1A,B**. It holds the atomic stacking structure with a layer of Hf atoms stuck in the middle of two layers of Se atoms (Wang and Liao, 2019). The Hf–Se bond in the intrinsic $HfSe_2$ monolayer is measured as 2.70 Å, which is

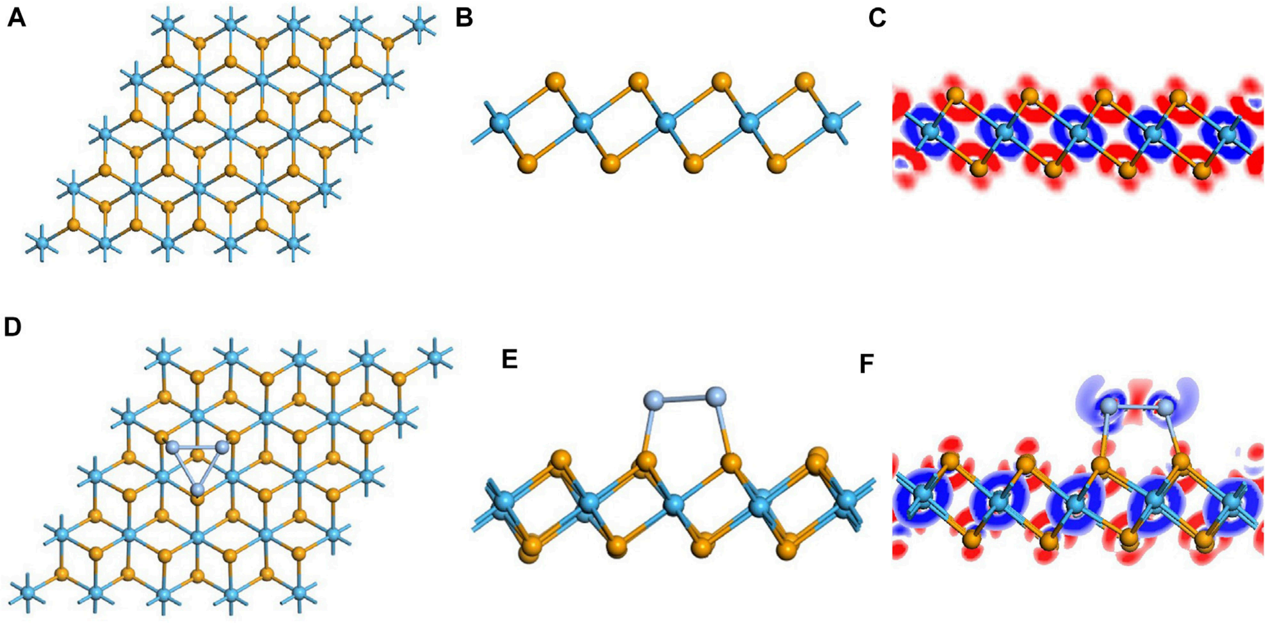

FIGURE 1 | Optimized configuration and electronic structures of the pristine and doped monolayer. **(A–C)** pristine system and **(D–F)** doped system. In DCD, red and blue regions represent electron accumulation and deletion.

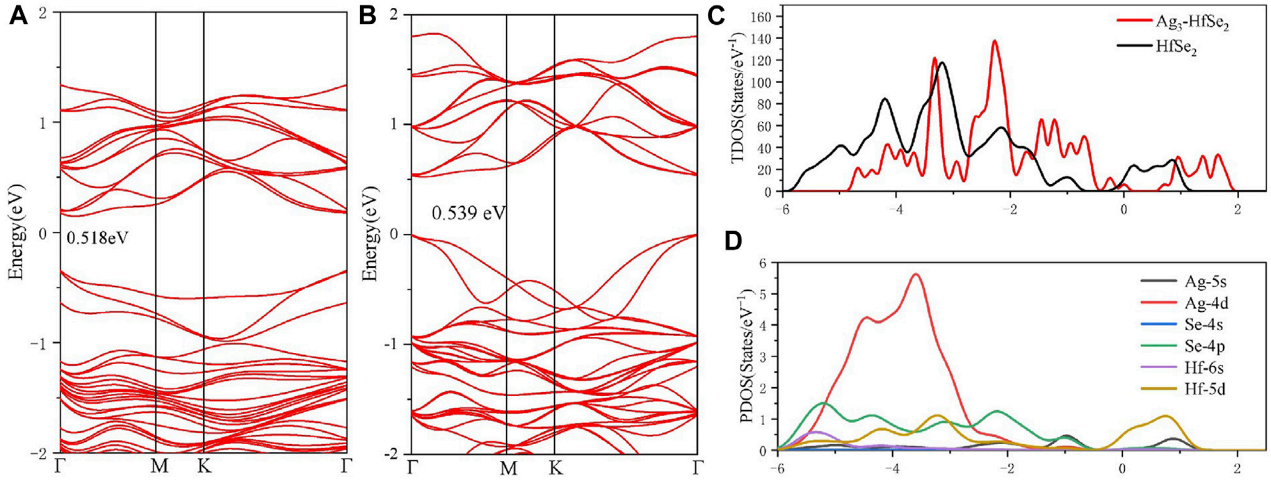

FIGURE 2 | Band structure and the TDOS and PDOS of the pristine and doped monolayers. **(A)** Band structure of the pristine $HfSe_2$ monolayer. **(B–D)** Band structure, TDOS, and PDOS of the Ag_3–$HfSe_2$ monolayer.

consistent with the articles published previously. Speaking of the performance of Ag_3 doping on the $HfSe_2$ monolayer, three doped sites were taken into account. They are named T_{se1} (a tripod site right upside the lower-layer Se atoms), T_{se2} (right upside the upper-layer Se atoms), and T_{Hf} (a tripod site right upside the mid-layer Hf atoms) (Ambrusi et al., 2017; Ju et al., 2017; Mi et al., 2021). As far as the most stable doped configuration, the lower the binding energy (E_b), the more stable is the structure. E_b is calculated as shown in **Eq. 2-1**, and the lowest one was chosen as the most stable doping system in this article. The Ag_3 cluster favored to be doped through the T_{se1} site with the numerical value of −2.512 eV, of which the E_b is lower than −1.347 and −1.155 eV for T_{se2} and T_{Hf}, respectively.

As is depicted in **Figures 1D,E**, there is a slight deformation after the doping of the Ag_3 cluster in the $HfSe_2$ monolayer, of which the Ag–Se bonds are 2.646, 2.628, and 2.648 Å, respectively. From the result of the Mulliken method (Chen et al., 2019a), it can be seen that the Ag_3 cluster is positively charged by 0.267 e after doping. As is shown in **Figure 1F**, Ag atoms are surrounded by blue areas, in which the red and blue

TABLE1 | Adsorption characteristic parameters of CO and C_2H_4 on the pristine monolayer.

Adsorbed gas	Bond length (Å)		Mulliken charge (e)		Q(e)	E_{ads} (eV)	d(Å)
CO	C-O	1.141	C	0.108	0.004	−0.159	4.055
			O	−0.104			
C_2H_4	C_1-C_2	1.337	C_1	−0.194	0.028	−0.344	3.389
	C_1-H_1	1.092	C_2	−0.186			
	C_1-H_2	1.092	H_1	0.102			
	C_2-H_3	1.092	H_2	0.101			
	C_3-H_4	1.092	H_3	0.101			
			H_4	0.101			

regions indicate electron accumulation and deletion independently (Cui et al., 2019). As a consequence, the analysis of the Mulliken method is in good accordance with the DCD, showing that the Ag_3 cluster is an electron donator. Compared with the bandgap obtained as 0.539 eV of the pristine $HfSe_2$ monolayer in **Figure 2A**, Ag_3–$HfSe_2$ is 0.553 eV with a decrease of 0.14 eV in **Figure 2B**. In comparison of the pristine and Ag_3-doped $HfSe_2$'s TDOS, it can be seen that there is a right shift, which is keeping with the result of the bandgap analysis.

As illustrated in **Figure 2D**, it can be seen from the PDOS that there are several overlapping regions among the Ag-4d, Se-4p, and Hf-5d orbitals at −6 ~ −1 eV, coincidently between the Hf-5d and Ag-5s orbitals at 0–1.5 eV. The PDOS verifies the conclusion that there are strong interactions existing among Ag, Se, and Hf atoms (Hu et al., 2019; Gao et al., 2020). As a consequence, due to the doping performance of the Ag_3 cluster, it is among the Ag-4d, Hf-5d, and Se-4p orbitals that the main orbital hybridization occurs. In addition, compared with the TDOS and PDOS mentioned previously, it can be seen that it is on the Ag, Se, and Hf atoms that the bottom of the conduction band and the top of the valence band are localized, and it also verifies the charge transfers from the Ag_3 cluster to the Se and Hf atoms (Yang et al., 2019).

Analysis of Gas Adsorption on the Pristine $HfSe_2$ Monolayer

After investigating the doping performance of the Ag_3 cluster, the adsorption behaviors of the pristine $HfSe_2$ monolayer upon CO and C_2H_4 were investigated as follows. In terms of the adsorption site of different gases upon the pristine $HfSe_2$ monolayer and Ag_3–$HfSe_2$ monolayer, all the possible adsorption sites were taken into account, but only the site with the lowest adsorption energy was adopted for further study (Zhang et al., 2009).

As for the adsorption of CO molecules on the pristine $HfSe_2$ monolayer, three different adsorption directions were simulated. The molecule accessed the Se atoms *via* C and O atoms vertically and parallelly to the monolayer, respectively (Ma et al., 2016). As shown in **Table 1**, C atoms tend to be adsorbed by Se atoms in the upper layer of the pristine $HfSe_2$ monolayer, with a distance of 4.055 Å between C and Se atoms. The length is significantly longer than the sum of the C and Se atoms' covalent radii, verifying the inexistence of the C–Se bond (Zhou et al., 2018b). For the adsorption of CO on the pristine $HfSe_2$ monolayer, the adsorption energy is 0.159 eV, which is less than 0.8 eV and to be defined as physisorption. The amount of charge transfer Q_T between the monolayer and CO molecule is very weak, with a value of 0.004 e. It includes 0.019 e of the C atom and −0.0105 e of the O atom (Late et al., 2014). Similarly, the DCD shown in **Figure 3C** reveals that the C atom and O atom are surrounded by blue and red areas, which is consistent with the Mulliken analysis. Furthermore, the bandgap, calculated as 0.691 eV, has an increase of 0.067 eV. As a consequence, based on the analysis mentioned previously, the adsorption effect of CO on the pristine monolayer is poor.

For the adsorption sites on the pristine monolayer of C_2H_4, two possible sites were investigated to simulate, with C_2H_4 being vertical and parallel to the upper layer (Qian et al., 2020). According to the calculated adsorption energy, it is the site that in a parallel direction holds the lowest energy. The C_2H_4 molecule is arrested by the Se atom, with a distance of 3.39 Å between C and Se atoms, which is longer than the sum of their covalent radii (Gao et al., 2019). The charge transfer Q_T generated by the CO molecule is −0.015 e, including −0.378 e of C atoms and 0.363 e of H atoms, which is consistent with the DCD shown in **Figure 3F**. Compared with the monolayer before the adsorption, there is an increase of 0.067 eV for the bandgap. In terms of the adsorption energy, it is 0.3437 eV that reveals the property of physisorption, which is below the standard of 0.8 eV (Zhou et al., 2018a). By reason of the foregoing analysis, the adsorption capacity of the pristine monolayer for C_2H_4 is not very well either.

Adsorption of the CO Molecule on the Ag_3-Doped $HfSe_2$ Monolayer

With regard to the adsorption of the doped monolayer, the adsorption of CO upon the Ag_3-doped monolayer was investigated first. The most stable adsorption configuration is as same as the pristine one. As is depicted in **Figure 4A**, there is a slight deformation in the configuration after doping, manifesting the reduction of the distance between the C atom and dopant, elongated from that of 4.055 Å in the pristine system to 3.65 Å. But the distance measured as 3.65 Å is still similarly longer than the sum of the covalent radii, representing that there is no chemical effect (Cortés-Arriagada et al., 2018). Although E_{ad} is raised to 0.388 eV, its property is still defined as physisorption.

Figure 5B exhibits the total TDOS distribution of the adsorption system of CO, where a right shift is observed for the TDOS state of the CO adsorbed system after adsorption. By

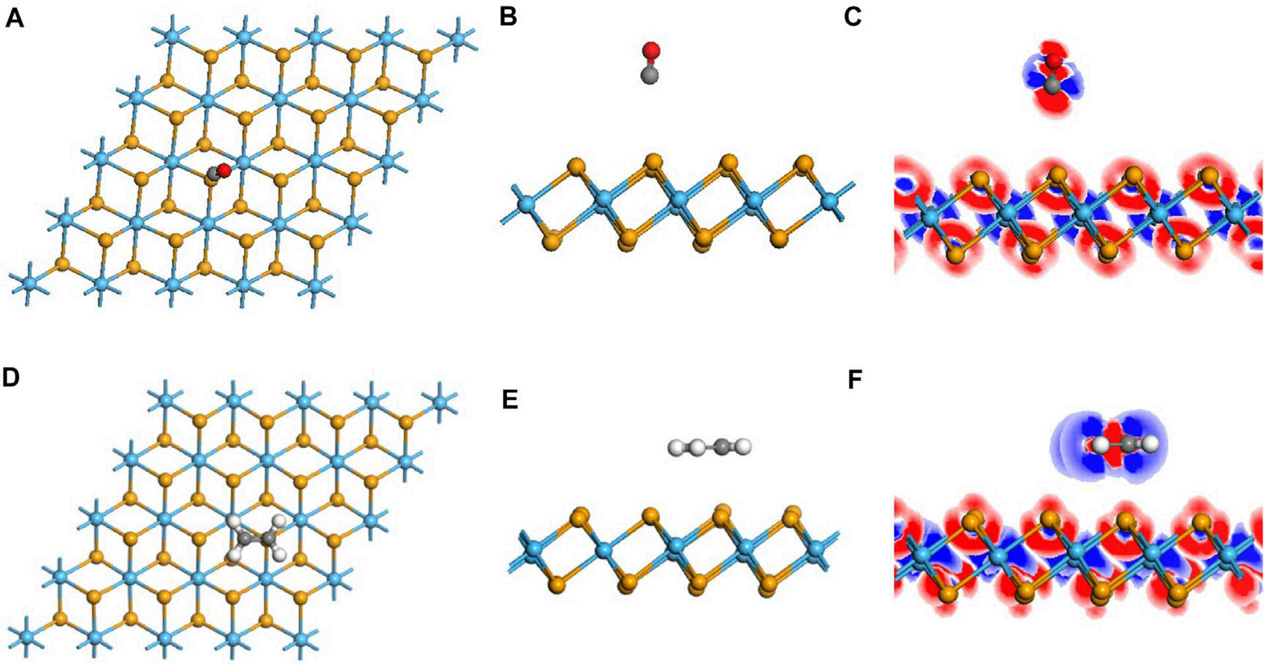

FIGURE 3 | Geometric and electronic structures of the adsorption system of CO and C_2H_4 on the intrinsic monolayer. **(A–C)** Adsorption system of CO and related DCD. **(D–F)** Adsorption system of C_2H_4 and related DCD.

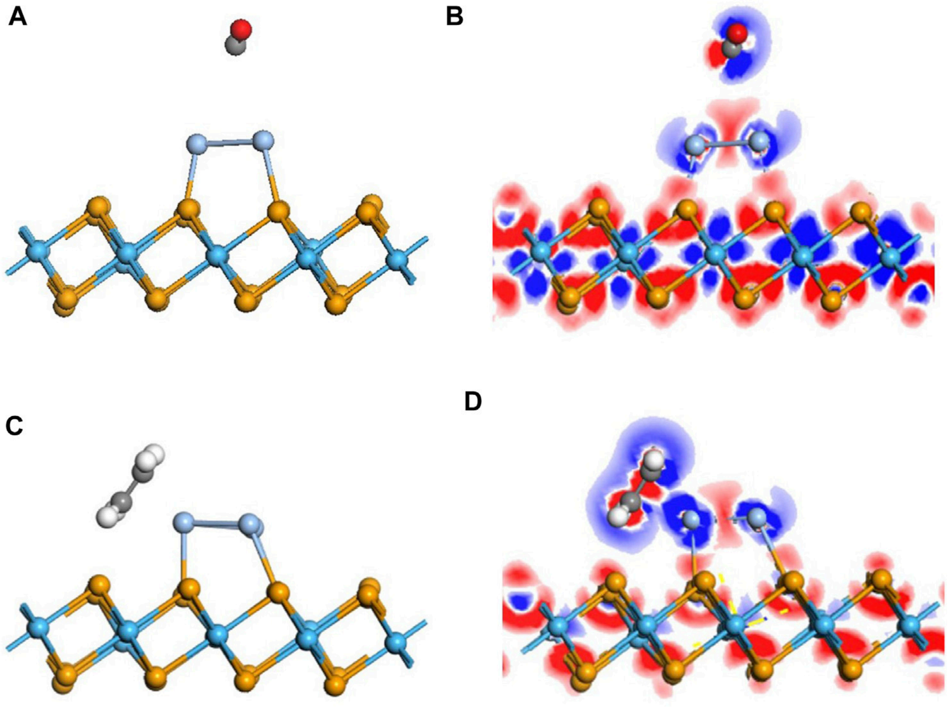

FIGURE 4 | Geometric and electronic structures of the adsorption system of CO and C_2H_4 on the doped Ag_3–$HfSe_2$ monolayer. **(A,B)** Adsorption system of CO and related DCD. **(C,D)** Adsorption system of C_2H_4 and related DCD.

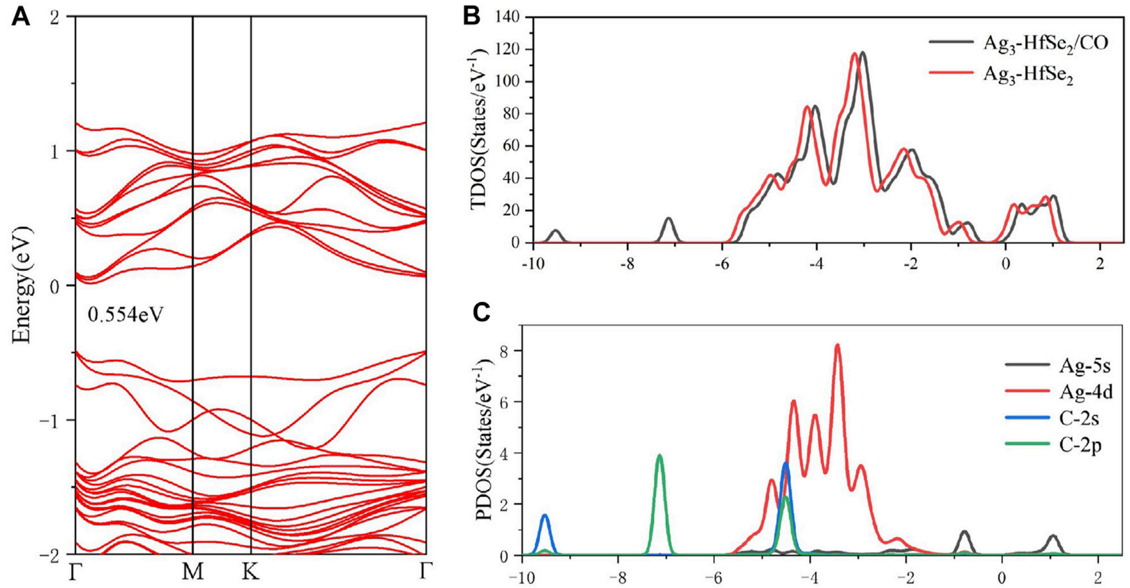

FIGURE 5 | (A) Band structure, **(B)** TDOS and **(C)** PDOS of CO molecules' adsorption on the Ag_3-doped $HfSe_2$ monolayer.

TABLE2 | Adsorption characteristic parameters of CO and C_2H_4 on the doped monolayer.

Adsorbed gas	Bond length (Å)		Mulliken charge (e)		Q(e)	E_{ads} (eV)	d(Å)
CO	C-O	1.143	C	0.0491	−0.031	−0.388	3.652
			O	−0.0801			
C_2H_4	C_1-C_2	1.367	C_1	−0.191	0.221	−0.912	2.400
	C_1-H_1	1.092	C_2	−0.188			
	C_1-H_2	1.092	H_1	0.152			
	C_2-H_3	1.092	H_2	0.162			
	C_3-H_4	1.091	H_3	0.143			
			H_4	0.143			

analyzing the band structure of the system after the adsorption of CO, it was found that the bandgap is 0.554 eV, which is shown in **Figure 5A**. Furthermore, as is shown in **Table 2**, there is 0.014 e transferred from the doped system to the CO molecule based on the analysis of Mulliken atomic charges (Allian et al., 2011). Combined with the Mulliken analysis, the demonstration of the DCD shown in **Figure 5B** is logical, in which the Ag atoms are surrounded by blue areas. In other words, the dopant Ag_3 cluster plays an important role as an electron donator in the system. According to the PDOS in **Figure 5C**, it can be found that the Ag-4d orbital is highly hybrid with the C-2s and C-2p orbitals at −5 ~ −4 eV, whereas the Ag-5s orbital is hybrid with the C-2p orbital at −1 ~ −0.5 eV (Khan Musa et al., 2020). Also, after the adsorption of the CO molecule, the bandgap of the adsorbed system is raised to 0.554 eV, which has an increase of 0.015 eV.

As a consequence, compared with the pristine system, there is a rise in the absolute value of the change in the bandgap. The change of the electronic parameters of the monolayer after the adsorption of CO molecules could be observed. Compared to the adsorption energy, adsorption distance, and charge transfer with those of pristine mentioned before, it can be seen that the adsorption performance of CO has been improved to a certain extent but is not ideal (Zhang et al., 2017). To draw a conclusion, it is not suitable for Ag_3-doped $HfSe_2$ either as a sensor material or as an adsorbent.

Adsorption of the C_2H_4 Molecule on the Ag_3-Doped $HfSe_2$ Monolayer

To better investigate the property of the adsorption of the C_2H_4 molecule upon the doped monolayer, three possible adsorption sites and directions were considered. They are as follows, approaching the Ag_3 cluster in a parallel way and in a vertical way but in two different directions, respectively. Compared with the results of the adsorption energy for different sites, it is the parallel way that holds the lowest value, which is calculated as −0.911 eV. After adsorption, it can be seen that the gas molecule is arrested by the dopant Ag_3 cluster. The detailed adsorption performance may be depicted, as in **Figure 4C**, in which the distance between the C atom and Ag atom is measured as 2.400 Å. It confirms that the interaction exists between the C and Ag atoms, and the structure has an obvious change. From the DCD

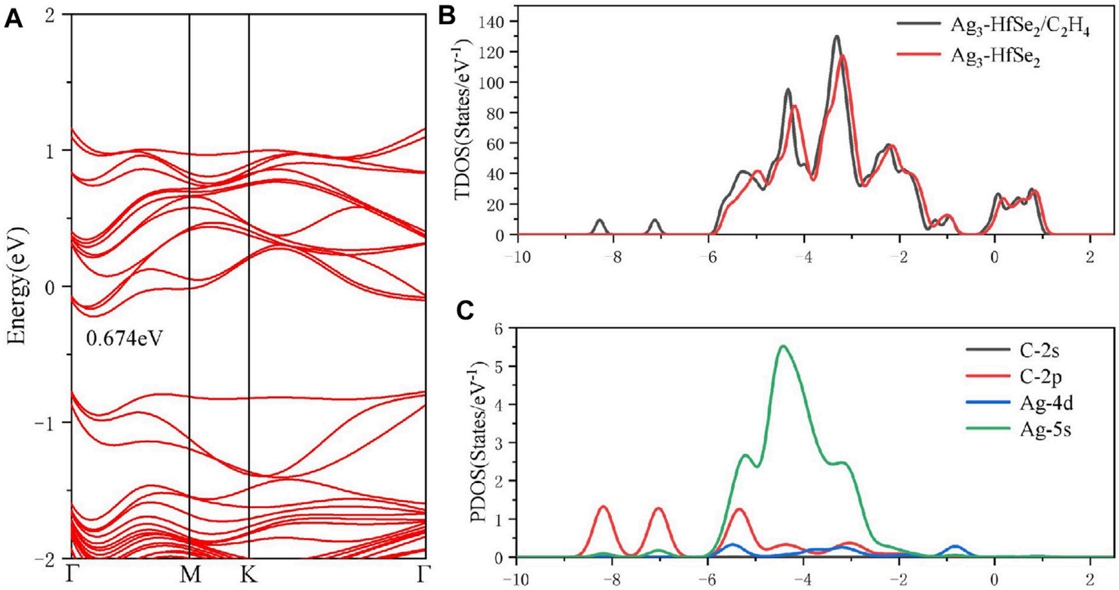

FIGURE 6 | (A) Band structure, **(B)** TDOS and **(C)** PDOS of C_2H_4 molecules' adsorption on the Ag_3-doped $HfSe_2$ monolayer.

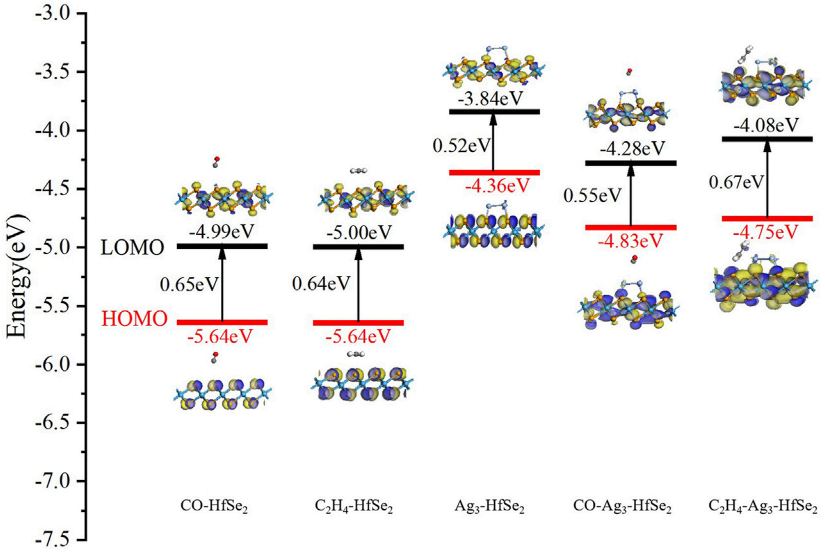

FIGURE 7 | Frontier molecular orbital distributions of CO and C_2H_4 adsorption on pristine and Ag_3–$HfSe_2$ monolayers, respectively.

in **Figure 4D**, it can be observed that the C atoms are surrounded by red areas, and the H atoms are surrounded by blue areas. It means that the H and Ag atoms act as electron donators (Wang et al., 2020). As is shown in **Figure 6A**, the band structure reveals that the bandgap of the adsorption system is 0.674 eV, which has an increase of 0.156 eV. Compared with the band structure before the adsorption, it can be found that it becomes denser and adds more impurity tracks. It widens the impurity band of the adsorption system, makes the transfer of electrons more conducive, and presents a better adsorption effect (Wu et al., 2017). The result obtained from the TDOS in **Figure 6B** demonstrates that there is a slight right shift, which is coincident with the analysis of the bandgap mentioned earlier. As demonstrated in **Figure 6C**, the PDOS reveals that there is a hybridization between the C-2p orbital and Ag-5s and Ag-4d orbitals at −6 ~ −2 eV. On the basis of the analysis of Mulliken atomic charges, there is 0.221 e transferred from the C_2H_4 molecule to the doped system.

TABLE 3 | Desorption time (s) of the adsorbed gas under different test temperatures.

Temperature(K)	CO–$HfSe_2$	CO–Ag_3–$HfSe_2$	C_2H_4–$HfSe_2$	C_2H_4–Ag_3–$HfSe_2$
298	4.79×10^{-10}	3.59×10^{-6}	6.47×10^{-7}	2,603.7408
358	1.70×10^{-10}	2.86×10^{-7}	6.87×10^{-8}	6.7917
418	8.15×10^{-11}	4.71×10^{-8}	1.39×10^{-8}	0.09774

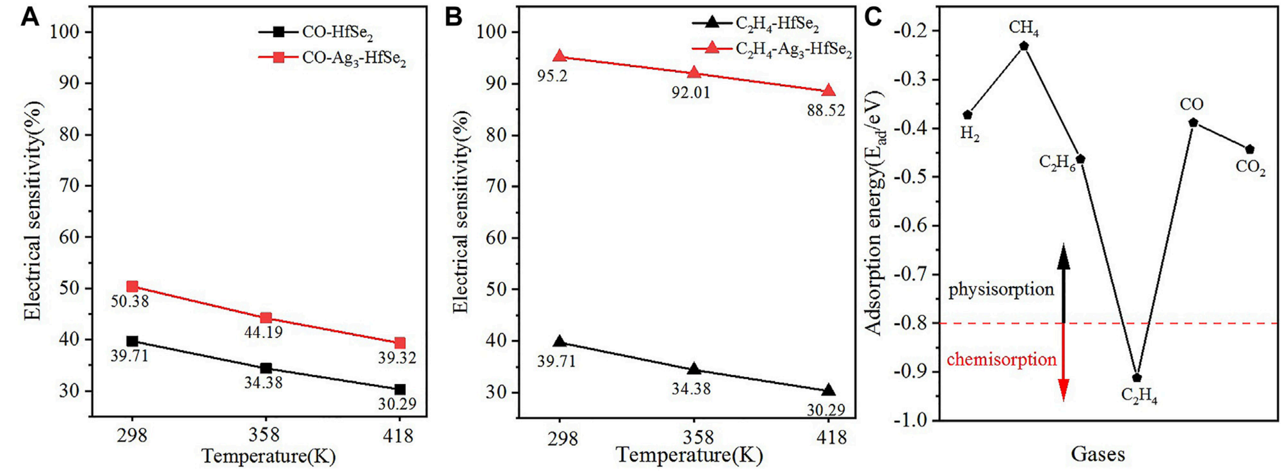

FIGURE 8 | Electrical sensitivity of **(A)** CO and **(B)**C_2H_4 on pristine and doped adsorption systems. **(C)** Comparison of the adsorption energy of different gases.

Moreover, according to the adsorption of the two gases, it can be concluded that the doped Ag_3–$HfSe_2$ monolayer is more selective for C_2H_4 gas molecules. Compared to the electronic properties of the monolayer after the adsorption of CO and C_2H_4, it can be seen that the latter holds lower adsorption energy, a wider bandgap, and a higher charge transfer capacity. All the properties mentioned previously contribute to its better performance of adsorption. As a consequence, from the aspect of electron property, it is the C_2H_4 system that holds the stronger interaction compared with the CO system. This also indicates its strong potential for applying gas sensing for detecting C_2H_4 gas molecules (Chen et al., 2020).

Analysis of the Frontier Molecular Orbital Theory

On the basis of the electronic mechanism, the dopant changes the electrostatic potential on the $HfSe_2$ monolayer because of its different electron affinities. It contributes to a change in the height of the surface potential barrier or a corresponding change in the resistance value of the semiconductor. Gas molecules are trapped on the monolayer by the Ag_3 cluster, and the dopant could be defined as a catalyst during the adsorption process (Asif et al., 2019b). It means the dopant can enhance the adsorption nature of gas molecules and accelerate the sensing electron exchange. Based on the frontier molecular orbital theory, the reasons that affect the conductivity change can be reacted directly (Liao et al., 2021). As is known, the resistive gas sensor demonstrates the effect of adsorption on different gas molecules by detecting the resistance change of the material (Asif et al., 2018). As is depicted in **Figure 7**, it shows the highest occupied orbital (HOMO) and the lowest free orbital (LOMO) before and after the adsorption of C_2H_4 and CO molecules on pristine and doped $HfSe_2$. Compared with the pristine substrate material, the difference value between the LOMO and HOMO has a slight increase, which is 0.11 and 0.10 eV, respectively. **Figure 7** shows the frontier molecular orbital of the doped system, in which the corresponding bandgap between the LOMO and HOMO is 0.52 eV. Moreover, the LOMO and HOMO orbitals are mainly distributed on the side of the doped sites of the Ag_3 cluster. However, the distribution of the LOMO and HOMO is stretched to the C_2H_4 and CO molecules obviously after the interaction between Ag_3–$HfSe_2$ and adsorbed gas molecules. During the adsorption process of the doped system, there have been incremental changes to various extents, which are 0.15 and 0.03 eV for C_2H_4 and CO systems, respectively.

In accordance with the molecular orbital theory, the decrease in the bandgap means that the charge transfer of the system is harder. In other words, at a constant temperature, the wider the forbidden band, the harder it is for the electrons to be transferred from the valence band to the conduction band. As a result, from a macro point of view, it is demonstrated as an increase in the resistance but a decrease in the conductivity (Wu et al., 2022). The relation between resistivity and bandgap can be described as follows.

$$\sigma \propto e^{-E_g / 2K_BT}. \qquad (3-1)$$

Here, σ and E_g are the conductivity and bandgap of the sensing material, and T and K_B mean the Boltzmann constant and the temperature, respectively.

ANALYSIS OF RECOVERY CHARACTERISTICS AND ELECTRICAL SENSITIVITY

Last but not the least, it is the recovery properties that must be considered for the sensing materials, in which the recovery time is an important reference. Recovery time, also regarded as desorption time, refers to the desorption rate of the adsorbed gas molecules on a gas sensor. Generally speaking, the faster the recovery time, the better is the performance of the gas sensor. The desorption time is defined as **formula (4-1)**.

$$T = A^{-1} e^{\frac{E_{ad}}{K_B T}}. \qquad (4-1)$$

Here, τ and A represent the desorption time and apparent frequency factor 10^{12} s^{-1}, and E_{ad} and T mean the absolute value of the adsorption energy and different test temperatures, respectively. In this article, the test temperatures were defined as 289 K, 358 K, and 418 K, respectively, and the Boltzmann constant is 8.62×10^{-5} eV/K (Gui et al., 2020). According to the equation given previously, the desorption time of the adsorbed gas C_2H_4 and CO under different test temperatures is demonstrated in **Table 3**. It can be seen that the desorption time reduces gradually with the increase in the test temperature. In other words, to a certain degree, the higher the ambient temperature of the gas sensing elements, the faster the gas detaches from the gas sensing material. The results calculated are consistent with the previous analysis, including the physisorption of CO and the chemisorption of C_2H_4 on the Ag_3–$HfSe_2$ monolayer.

In addition to the desorption time analyzed previously, it is the electrical sensitivity (E_S) that must be considered, which is defined in the following equation.

$$E_S = \left(\sigma_{gas}^{-1} - \sigma_{Ag_3-HfSe_2}^{-1}\right) \Big/ \sigma_{Ag_3-HfSe_2}^{-1}, \qquad (4-2)$$

Here, σ_{gas}^{-1} and $\sigma_{Ag_3-HfSe_2}^{-1}$ represent the electrical conductivity of the Ag_3–$HfSe_2$ monolayer before and after adsorption, respectively. The electrical conductivity could be calculated as in **Eq. 4–2**. The results of the electrical sensitivity are drawn in **Figure 8**, from which can be seen that after the doping of the Ag_3 cluster, there are obvious promotions for the electrical sensitivity of two gases. In particular, for the adsorption of C_2H_4, the electrical sensitivity changes from 39.71 to 95.2%, revealing its good performance of adsorption (Aziz et al., 2022).

To elucidate the anti-interference for the detection of the C_2H_4 molecule, the adsorption energy of different dissolved gases in oil was compared. The gases are H_2, CH_4, C_2H_6, C_2H_4, CO, and CO_2 respectively. As is shown in **Figure 8C**, it can be seen that C_2H_4 is below the boundary at −0.8 eV, while other gases are above the boundary. In other words, only the adsorption of C_2H_4 is chemisorption while others are defined as physisorption. As a consequence, it can be concluded that the detection of C_2H_4 based on the Ag3–$HfSe_2$ monolayer is of great anti-interference (Aziz et al., 2019).

CONCLUSION

In this article, the adsorption properties of the transformer oil decomposition gases (CO and C_2H_4) upon Ag_3–$HfSe_2$ are investigated theoretically on the basis of the first principle. The electronic behavior of Ag_3–$HfSe_2$ before and after the adsorption is analyzed and discussed by the band structure, DOS, DCD, and the Mulliken analysis. However, the desorption time is calculated through the adsorption energy, and the electrical sensitivity is analyzed through the bandgap and the frontier molecular orbital theory (Das and Shoji, 2011). After analyzing the adsorption behaviors and the response mechanisms of CO and C_2H_4, the main conclusions obtained are as follows. For the doping of the Ag_3 cluster, the simulation results show that the Ag_3 cluster is more inclined to be doped at the site T_{se1}. There are different adsorption interactions between the gases CO, C_2H_4, and the Ag_3–$HfSe_2$ monolayer, including the strong chemical adsorption of C_2H_4 and the weak physisorption of CO, respectively. In the adsorption process, C_2H_4 was attracted to transfer electrons to the monolayer of Ag_3–$HfSe_2$, whereas CO was just the reverse. After adsorption, the increase in the bandgap contributes to the increase in resistivity of Ag_3–$HfSe_2$, which corresponds to a decrease in conductivity. The resistivity relationship corresponding to the two adsorption systems is as follows: C_2H_4 > CO. After the doping of the Ag3 cluster, the electrical sensitivity has a great change for both the gases, including the change from 39.71 to 50.78% for CO and the change from 39.71 to 95.2% for C_2H_4, respectively. Speaking of the anti-interference of the detection for C_2H_4, the adsorption energy of different gases was compared. The results illustrate that the detection for C_2H_4 based on Ag3–$HfSe_2$ is of great anti-interference. Our investigation highlights the high selectivity and better adsorption performance of C_2H_4 on the Ag_3–$HfSe_2$ monolayer. It provides guidance for expanding the application range of $HfSe_2$ to the sensing materials and analyzes its feasibility to detect transformer oil decomposition theoretically.

DATA AVAILABILITY STATEMENT

The original contributions presented in the study are included in the article/supplementary material; further inquiries can be directed to the corresponding authors.

AUTHOR CONTRIBUTIONS

All authors listed have made a substantial, direct, and intellectual contribution to the work and approved it for publication.

FUNDING

This work has been supported in part by the National Natural Science Foundation of China (Nos. 52077177 and 51507144) and the Fundamental Research Funds for the Central Universities (No. XDJK 2019B021).

REFERENCES

Allian, A. D., Takanabe, K., Fujdala, K. L., Hao, X., Truex, T. J., Cai, J., et al. (2011). Chemisorption of CO and Mechanism of CO Oxidation on Supported Platinum Nanoclusters. *J. Am. Chem. Soc.* 133, 4498–4517. doi:10.1021/ja110073u

Ambrusi, R. E., Luna, C. R., Sandoval, M. G., Bechthold, P., Pronsato, M. E., and Juan, A. (2017). Rhodium Clustering Process on Defective (8,0) SWCNT: Analysis of Chemical and Physical Properties Using Density Functional Theory. *Appl. Surf. Sci.* 425, 823–832. doi:10.1016/j.apsusc.2017.07.070

Asif, M., Aziz, A., Wang, H., Wang, Z., Wang, W., Ajmal, M., et al. (2019a). Superlattice Stacking by Hybridizing Layered Double Hydroxide Nanosheets with Layers of Reduced Graphene Oxide for Electrochemical Simultaneous Determination of Dopamine, Uric Acid and Ascorbic Acid. *Mikrochim. Acta* 186, 61. doi:10.1007/s00604-018-3158-y

Asif, M., Aziz, A., Ashraf, G., Iftikhar, T., Sun, Y. M., Xiao, F., et al. (2022). Unveiling Microbiologically Influenced Corrosion Engineering to Transfigure Damages into Benefits: A Textile Sensor for H_2O_2 Detection in Clinical Cancer Tissues. *Chem. Eng. J.* 427, 11. doi:10.1016/j.cej.2021.131398

Asif, M., Aziz, A., Ashraf, G., Wang, Z., Wang, J., Azeem, M., et al. (2018). Facet-Inspired Core-Shell Gold Nanoislands on Metal Oxide Octadecahedral Heterostructures: High Sensing Performance toward Sulfide in Biotic Fluids. *ACS Appl. Mat. Interfaces* 10, 36675–36685. doi:10.1021/acsami.8b12186

Asif, M., Aziz, A., Wang, Z., Ashraf, G., Wang, J., Luo, H., et al. (2019b). Hierarchical CNTs@CuMn Layered Double Hydroxide Nanohybrid with Enhanced Electrochemical Performance in H2S Detection from Live Cells. *Anal. Chem.* 91, 3912–3920. doi:10.1021/acs.analchem.8b04685

Aziz, A., Asif, M., Ashraf, G., Iftikhar, T., Hu, J. L., Xiao, F., et al. (2022). Boosting Electrocatalytic Activity of Carbon Fiber@fusiform-like Copper-Nickel LDHs: Sensing of Nitrate as Biomarker for NOB Detection. *J. Hazard. Mater.* 422, 11. doi:10.1016/j.jhazmat.2021.126907

Aziz, A., Asif, M., Azeem, M., Ashraf, G., Wang, Z., Xiao, F., et al. (2019). Self-stacking of Exfoliated Charged Nanosheets of LDHs and Graphene as Biosensor with Real-Time Tracking of Dopamine from Live Cells. *Anal. Chim. Acta* 1047, 197–207. doi:10.1016/j.aca.2018.10.008

Chen, D., Zhang, X., Tang, J., Cui, H., Li, Y., Zhang, G., et al. (2019a). Density Functional Theory Study of Small Ag Cluster Adsorbed on Graphyne. *Appl. Surf. Sci.* 465, 93–102. doi:10.1016/j.apsusc.2018.09.096

Chen, D., Zhang, X., Xiong, H., Li, Y., Tang, J., Xiao, S., et al. (2019b). A First-Principles Study of the SF6 Decomposed Products Adsorbed over Defective WS2 Monolayer as Promising Gas Sensing Device. *IEEE Trans. Device Mat. Relib.* 19, 473–483. doi:10.1109/tdmr.2019.2919773

Chen, W. L., Gui, Y. G., Li, T., Zeng, H., Xu, L. N., and Ding, Z. Y. (2020). Gas-sensing Properties and Mechanism of Pd-GaNNTs for Air Decomposition Products in Ring Main Unit. *Appl. Surf. Sci.* 531, 7. doi:10.1016/j.apsusc.2020.147293

Choi, S.-J., and Kim, I.-D. (2018). Recent Developments in 2D Nanomaterials for Chemiresistive-type Gas Sensors. *Electron. Mat. Lett.* 14, 221–260. doi:10.1007/s13391-018-0044-z

Cortés-Arriagada, D., Villegas-Escobar, N., and Ortega, D. E. (2018). Fe-doped Graphene Nanosheet as an Adsorption Platform of Harmful Gas Molecules (CO, CO_2, SO_2 and H_2S), and the Co-adsorption in O_2 Environments. *Appl. Surf. Sci.* 427, 227–236. doi:10.1016/j.apsusc.2017.08.216

Cruzado, H. N., Dizon, J. S. C., Macam, G. M., Villaos, R. A. B., Huynh, T. M. D., Feng, L.-Y., et al. (2021). Band Engineering and Van Hove Singularity on HfX_2 Thin Films (X = S, Se, or Te). *ACS Appl. Electron. Mat.* 3, 1071–1079. doi:10.1021/acsaelm.0c00907

Cui, H., Jia, P. F., and Peng, X. Y. (2020a). Adsorption of SO_2 and NO_2 Molecule on Intrinsic and Pd-Doped $HfSe_2$ Monolayer: A First-Principles Study. *Appl. Surf. Sci.* 513, 7. doi:10.1016/j.apsusc.2020.145863

Cui, H., Jia, P. F., Peng, X. Y., and Li, P. (2020b). Adsorption and Sensing of CO and C_2H_2 by S-Defected SnS_2 Monolayer for DGA in Transformer Oil: A DFT Study. *Mater. Chem. Phys.* 249, 7. doi:10.1016/j.matchemphys.2020.123006

Cui, H., Zhang, X., Zhang, G., and Tang, J. (2019). Pd-doped MoS_2 Monolayer: A Promising Candidate for DGA in Transformer Oil Based on DFT Method. *Appl. Surf. Sci.* 470, 1035–1042. doi:10.1016/j.apsusc.2018.11.230

Cui, H., Zhu, H. L., and Jia, P. F. (2020c). Adsorption and Sensing of SO_2 and SOF_2 Molecule by Pt-Doped $HfSe_2$ Monolayer: A First-Principles Study. *Appl. Surf. Sci.* 530, 7. doi:10.1016/j.apsusc.2020.147242

Das, N. K., and Shoji, T. (2011). A Density Functional Study of Atomic Oxygen and Water Molecule Adsorption on Ni(111) and Chromium-Substituted Ni(111) Surfaces. *Appl. Surf. Sci.* 258, 442–447. doi:10.1016/j.apsusc.2011.08.107

Delley, B. (2000). From Molecules to Solids with the $DMol^3$ Approach. *J. Chem. Phys.* 113, 7756–7764. doi:10.1063/1.1316015

Duerloo, K. A., Li, Y., and Reed, E. J. (2014). Structural Phase Transitions in Two-Dimensional Mo- and W-Dichalcogenide Monolayers. *Nat. Commun.* 5, 4214. doi:10.1038/ncomms5214

Gao, X., Zhou, Q., Wang, J., Xu, L., and Zeng, W. (2020). Performance of Intrinsic and Modified Graphene for the Adsorption of H_2S and CH_4: A DFT Study. *Nanomater. (Basel)* 10, 15. doi:10.3390/nano10020299

Gao, X., Zhou, Q., Lu, Z. R., Xu, L. N., Zhang, Q. Y., and Zeng, W. (2019). Synthesis of Cr_2O_3 Nanoparticle-Coated SnO_2 Nanofibers and C_2H_2 Sensing Properties. *Front. Mater.* 6, 8. doi:10.3389/fmats.2019.00163

Gui, X. X., Zhou, Q., Peng, S. D., Xu, L. N., and Zeng, W. (2020). Dissolved Gas Analysis in Transformer Oil Using Sb-Doped Graphene: A DFT Study. *Appl. Surf. Sci.* 533, 11. doi:10.1016/j.apsusc.2020.147509

Hu, X. Y., Liu, M., Liu, X. Y., Ma, Y. X., Nan, H. S., Bi, D. M., et al. (2019). Sensing and Absorbing of Sulfur Mustard Using Pt-Decorated Graphene from First-Principles Calculations. *Phys. E-Low-Dimensional Syst. Nanostructures* 114, 6. doi:10.1016/j.physe.2019.113634

Ju, W., Li, T., Su, X., Li, H., Li, X., and Ma, D. (2017). Au Cluster Adsorption on Perfect and Defective MoS_2 Monolayers: Structural and Electronic Properties. *Phys. Chem. Chem. Phys.* 19, 20735–20748. doi:10.1039/c7cp03062b

Ju, W. W., Zhang, Y., Li, T. W., Wang, D. H., Zhao, E. Q., Hu, G. X., et al. (2021). A type-II WSe_2/$HfSe_2$ van der Waals heterostructure with adjustable electronic and optical properties. *Results Phys.* 25, 10. doi:10.1016/j.rinp.2021.104250

Khan Musa, M. R., Zhang, C., Alruqui, A. B. A., Zhao, R., Jasinski, J. B., Sumanasekera, G., et al. (2020). Insight the Process of Hydrazine Gas Adsorption on Layered WS_2: a First Principle Study. *Nanotechnology* 31, 495703. doi:10.1088/1361-6528/abb337

Late, D. J., Doneux, T., and Bougouma, M. (2014). Single-layer $MoSe_2$ Based NH_3 Gas Sensor. *Appl. Phys. Lett.* 105, 4. doi:10.1063/1.4903358

Liao, Y. M., Peng, R. C., Peng, S. D., Zeng, W., and Zhou, Q. (2021). The Adsorption of H_2 and C_2H_2 on Ge-Doped and Cr-Doped Graphene Structures: A DFT Study. *Nanomaterials* 11, 13. doi:10.3390/nano11010231

Liu, Y. P., Zhou, Q., Mi, H. W., Wang, J. X., and Zeng, W. (2021). Gas-sensing Mechanism of Cr Doped SnP_3 Monolayer to SF_6 Partial Discharge Decomposition Components. *Appl. Surf. Sci.* 546, 9. doi:10.1016/j.apsusc.2021.149084

Ma, D., Wang, Q., Li, T., He, C., Ma, B., Tang, Y., et al. (2016). Repairing Sulfur Vacancies in the MoS_2 Monolayer by Using CO, NO and NO_2 Molecules. *J. Mat. Chem. C* 4, 7093–7101. doi:10.1039/c6tc01746k

Mi, H. W., Zhou, Q., and Zeng, W. (2021). A Density Functional Theory Study of the Adsorption of Cl_2, NH_3, and NO_2 on Ag_3-Doped WSe_2 Monolayers. *Appl. Surf. Sci.* 563, 9. doi:10.1016/j.apsusc.2021.150329

Mirabelli, G., Mcgeough, C., Schmidt, M., Mccarthy, E. K., Monaghan, S., Povey, I. M., et al. (2016). Air Sensitivity of MoS_2, $MoSe_2$, $MoTe_2$, HfS_2, and $HfSe_2$. *J. Appl. Phys.* 120, 9. doi:10.1063/1.4963290

Mleczko, M. J., Zhang, C., Lee, H. R., Kuo, H. H., Magyari-Köpe, B., Moore, R. G., et al. (2017). $HfSe_2$ and $ZrSe_2$: Two-Dimensional Semiconductors with Native High-κ Oxides. *Sci. Adv.* 3, e1700481. doi:10.1126/sciadv.1700481

Qian, G. C., Peng, Q. J., Zou, D. X., Wang, S., Yan, B., and Zhou, Q. (2020). First-Principles Insight into Au-Doped MoS_2 for Sensing C_2H_6 and C_2H_4. *Front. Mater.* 7, 9. doi:10.3389/fmats.2020.00022

Sharma, A., AnuKHAN, M. S., Khan, M. S., Husain, M., Khan, M. S., and Srivastava, A. (2018). Sensing of CO and NO on Cu-Doped MoS_2Monolayer-Based Single Electron Transistor: A First Principles Study. *IEEE Sensors J.* 18, 2853–2860. doi:10.1109/jsen.2018.2801865

Si, K. Y., Ma, J. Y., Lu, C. H., Zhou, Y. X., He, C., Yang, D., et al. (2020). A two-dimensional MoS_2/WSe_2 van der Waals heterostructure for enhanced photoelectric performance. *Appl. Surf. Sci.* 507, 11. doi:10.1016/j.apsusc.2019.145082

Singh, S., and Bandyopadhyay, M. (2010). Dissolved Gas Analysis Technique for Incipient Fault Diagnosis in Power Transformers: A Bibliographic Survey. *IEEE Electr. Insul. Mag.* 26, 41–46. doi:10.1109/mei.2010.5599978

Tang, S. R., Chen, W. G., Jin, L. F., Zhang, H., Li, Y. Q., Zhou, Q., et al. (2020). SWCNTs-based MEMS Gas Sensor Array and its Pattern Recognition Based on Deep Belief Networks of Gases Detection in Oil-Immersed Transformers. *Sensors Actuators B-Chemical* 312, 12. doi:10.1016/j.snb.2020.127998

Topsakal, M., Akturk, E., and Ciraci, S. (2009). First-principles Study of Two- and One-Dimensional Honeycomb Structures of Boron Nitride. *Phys. Rev. B* 79, 11. doi:10.1103/physrevb.79.115442

Tran, D., Mac, H., Tong, V., Tran, H. A., and Nguyen, L. G. (2018). A LSTM Based Framework for Handling Multiclass Imbalance in DGA Botnet Detection. *Neurocomputing* 275, 2401–2413. doi:10.1016/j.neucom.2017.11.018

Wang, J. X., Zhou, Q., Xu, L. N., Gao, X., and Zeng, W. (2020). Gas Sensing Mechanism of Dissolved Gases in Transformer Oil on Ag-MoS_2 Monolayer: A DFT Study. *Phys. E-Low-Dimensional Syst. Nanostructures* 118, 9. doi:10.1016/j.physe.2019.113947

Wang, X., and Liao, Y. L. (2019). Selective Detection of SO_2 in SF_6 Insulation Devices by Rh-Doped $HfSe_2$ Monolayer: a First-Principles Study. *Appl. Phys. a-Materials Sci. Process.* 125, 8. doi:10.1007/s00339-019-2759-6

Wei, Z., Xu, L., Peng, S., and Zhou, Q. (2020). Application of WO_3 Hierarchical Structures for the Detection of Dissolved Gases in Transformer Oil: A Mini Review. *Front. Chem.* 8, 188. doi:10.3389/fchem.2020.00188

Wu, H. L., Zhang, B., Li, X. X., and Hu, X. X. (2022). First-principles Screening upon Pd-Doped HfSe2 Monolayer as an Outstanding Gas Sensor for DGA in Transformers. *Comput. Theor. Chem.* 1208, 7. doi:10.1016/j.comptc.2021.113553

Wu, P., Yin, N., Li, P., Cheng, W., and Huang, M. (2017). The Adsorption and Diffusion Behavior of Noble Metal Adatoms (Pd, Pt, Cu, Ag and Au) on a MoS_2 Monolayer: a First-Principles Study. *Phys. Chem. Chem. Phys.* 19, 20713–20722. doi:10.1039/c7cp04021k

Xu, L., Zhu, H., Gui, Y., Long, Y., Wang, Q., and Yang, P. (2020). First-Principles Calculations of Gas-Sensing Properties of Pd Clusters Decorated AlNNTs to Dissolved Gases in Transformer Oil. *Ieee Access* 8, 162692–162700. doi:10.1109/access.2020.3020636

Xu, M., Liang, T., Shi, M., and Chen, H. (2013). Graphene-Like Two-Dimensional Materials. *Chem. Rev.* 113, 3766–3798. doi:10.1021/cr300263a

Yang, G. F., Yan, P. F., Zhu, C., Gu, Y., Lu, N. Y., Xue, J. J., et al. (2019). Selenium Vacancy-Enhanced Gas Adsorption of Monolayer Hafnium Diselenide ($HfSe_2$) from a Theoretical Perspective. *Adv. Theory Simulations* 2, 8. doi:10.1002/adts.201900052

Yang, S., Chen, X., Gu, Z., Ling, T., Li, Y., and Ma, S. (2020). Cu-Doped $MoSe_2$ Monolayer: A Novel Candidate for Dissolved Gas Analysis in Transformer Oil. *Acs Omega* 5, 30603–30609. doi:10.1021/acsomega.0c04572

Yue, R., Barton, A. T., Zhu, H., Azcatl, A., Pena, L. F., Wang, J., et al. (2015). HfS_{e2} Thin Films: 2D Transition Metal Dichalcogenides Grown by Molecular Beam Epitaxy. *Acs Nano* 9, 474–480. doi:10.1021/nn5056496

Zhang, D., Sun, Y. E., Jiang, C., Yao, Y., Wang, D., and Zhang, Y. (2017). Room-temperature Highly Sensitive CO Gas Sensor Based on Ag-Loaded Zinc Oxide/molybdenum Disulfide Ternary Nanocomposite and its Sensing Properties. *Sensors Actuators B Chem.* 253, 1120–1128. doi:10.1016/j.snb.2017.07.173

Zhang, Y. H., Chen, Y. B., Zhou, K. G., Liu, C. H., Zeng, J., Zhang, H. L., et al. (2009). Improving Gas Sensing Properties of Graphene by Introducing Dopants and Defects: a First-Principles Study. *Nanotechnology* 20, 185504. doi:10.1088/0957-4484/20/18/185504

Zhou, Q., Lu, Z., Wei, Z., Xu, L., Gui, Y., and Chen, W. (2018a). Hydrothermal Synthesis of Hierarchical Ultrathin NiO Nanoflakes for High-Performance CH4 Sensing. *Front. Chem.* 6, 194. doi:10.3389/fchem.2018.00194

Zhou, Q., Xu, L., Umar, A., Chen, W., and Kumar, R. (2018b). Pt Nanoparticles Decorated SnO_2 Nanoneedles for Efficient CO Gas Sensing Applications. *Sensors Actuators B Chem.* 256, 656–664. doi:10.1016/j.snb.2017.09.206

Conflict of Interest: The authors declare that the research was conducted in the absence of any commercial or financial relationships that could be construed as a potential conflict of interest.

frontiers | Frontiers in Chemistry

ORIGINAL RESEARCH
published: 25 May 2022
doi: 10.3389/fchem.2022.899672

Synthesis of Fluorescent Copper Nanomaterials and Detection of Bi^{3+}

Rihan Wu[1], *Jun Ai*[1]* *and Lu Ga*[2]*

[1]Inner Mongolia Key Laboratory of Environmental Chemistry, College of Chemistry and Enviromental Science, Inner Mongolia Normal University, Hohhot, China, [2]College of Pharmacy, Inner Mongolia Medical University, Hohhot, China

Based on the aggregation-induced luminescence of glutathione-protected non-noble metal copper nanoparticles (GSH-CuNPs), a fluorescence method for the rapid detection of bismuth (Bi^{3+}) was developed. The fluorescence intensity of GSH-CuNP solution is good, and the fluorescence can be quenched in the presence of Bi^{3+}. Based on this principle, a fluorescence mean for the admeasurement of $Bi^{3+}$was built. The linear range was 0–100 mmol/L, and the detection limit was 10 mmol/L. The method is simple, rapid, and selective and can be used for the qualitative detection of Bi^{3+}.

Keywords: Bi^{3+}, detection, copper nanomaterials, fluorescence, glutathione

Edited by:
Muhammad Asif,
Wuhan Institute of Technology, China

Reviewed by:
Shuyun Zhu,
Qufu Normal University, China
Xia Li,
Liaocheng University, China

****Correspondence:***
Jun Ai
imacaj01@163.com
Lu Ga
13404832082@163.com

Specialty section:
This article was submitted to
Analytical Chemistry,
a section of the journal
Frontiers in Chemistry

Received: *19 March 2022*
Accepted: *31 March 2022*
Published: *25 May 2022*

Citation:
Wu R, Ai J and Ga L (2022) Synthesis of Fluorescent Copper Nanomaterials and Detection of Bi^{3+}.
Front. Chem. 10:899672.
doi: 10.3389/fchem.2022.899672

INTRODUCTION

Due to the serious impact of metal ions on the environment and human health, the detection of metal ions has been a hot research topic. (Brower et al., 1997; Aragay et al., 2011). These species come from anthropological and natural resources and are found in soil, reservoir water, and marine environments (Yoshizaki and Tomida, 2000; Gans et al., 2005; Ghaedi et al., 2009). They accumulate in plants, meat, and other foods (Gill, 1983; Oyaro et al., 2007; Sud et al., 2008). Through these different absorption channels, these ions can gather in the developing brain, destroy the secondary structure of proteins/peptides, and lead to debilitating diseases (Stohs and Bagchi, 1995; Järup, 2003; Sharma and Dietz, 2009). Specifically, the local accumulation of Zn^{2+} in the brain leads to the rapid induction of the amyloid structure in Alzheimer's disease (Bush et al., 1994; Lee et al., 2004). Due to the obstinacy of heavy metal ions in the environment and the resistance to conventional filtration methods, heavy metal ion pollution has plagued most developed countries (Fu and Wang, 2011). The harmful effects of heavy metal ions have prompted extensive research on their sensitive detection (Alexander et al., 2000; Ferreira et al., 2004; Korolczuk et al., 2005; Lee et al., 2008; Li et al., 2012). Acute bismuth poisoning is mainly due to oral entry; the patient will have nausea, vomiting, salivation, tongue and throat pain, abdominal pain, diarrhea, black stool with blood, skin and mucous membrane bleeding, headache, spasm, etc. Liver and kidney damage can lead to jaundice, urine protein and tube type, and even acute liver and kidney failure. For those allergic to bismuth salt, fever, rash, acute hemolysis, and exfoliative dermatitis may occur after intramuscular injection. Long-term application of bismuth can cause multiple neuritis, stomatitis, gingival swelling, pigmentation of the oral mucosa, and a black line on the gingiva. The X-ray film of the long bone end of the patient showed a white band, which was similar to that of lead poisoning cases.

As the next generation of materials, nanomaterials have shown great application prospects in many fields, such as catalysis, photonics, environmental detection, biomedical diagnosis, and treatment (Nie et al., 2010; Chen et al., 2012; Lu and Yin, 2012; Schroeder et al., 2012). This prospect comes from the unique properties of these nanomaterials, such as their plasma and quantum confinement effects, which are largely dependent on morphology (such as shape and surface structure) (Xia et al., 2009). Fluorescent metal nanoclusters (Au, Ag, and CuNCs) have attracted much attention due to their ultra-small size, quantum confinement, high photostability, and biocompatibility (Zheng et al., 2004; Burda et al., 2005; Zhu et al., 2008; Xie et al., 2009; Bain et al., 2015; Barman et al., 2016; Jin et al., 2016; Bain et al., 2017; Chakraborty and Pradeep, 2017; Kundu and Patra, 2017; Cao et al. 2014). Water soluble CuNCs were prepared from tannic acid, and the fluorescence quenching induced by the electron transfer mechanism was used to realize the high sensitivity detection of $Fe^{3\ +}$. At present, the detection of metal ions by fluorescent nanoclusters is mostly based on the fluorescence quenching mechanism. Since there are many substances that inhibit fluorescence, fluorescence quenching is a common phenomenon and has a great influence on selectivity or sensitivity (Chen et al., 2016). Fluorescence AgNCs were synthesized with glutathione (GSH) as a protective agent, and S^{2-} quenched the fluorescence of silver nanomaterials to detect S^{2-}. In the work by Feng et al. (2015), branched polyethyleneimine (bpei)-terminated CuNCs were synthesized by using bpei as the template and ascorbic acid as the reducing agent. The results display that the luminous intensity of CuNCs reaches its maximum value at 360 and 430 nm. Even in a high-salt medium, it has great water solubility, high stability, and photostability. The results show that Fe^{3+}can significantly quench the fluorescence of bpei CuNCs by electron transfer, while other common anions and cations have little effect on the luminous intensity of CuNCs. Based on these, an ultrasensitive and super selective Fe^{3+}fluorescence sensor was built and applied for measure of Fe^{3+} in human urine and water.

In this experiment, Cu nanoparticles were prepared by an easy template method. GSH is used as the protective agent and template of CuNPs, and the synthesized high fluorescence CuNPs can detect bismuth ions. When bismuth ions were added into the system, the fluorescence of Cu nanoparticles was inhibited. Moreover, among the common inorganic metal cations and anions, only Bi^{3+} can trigger the significant fluorescence quenching effect of copper nanomaterials. The nanomaterial sensor has good linear range, stability, and high selectivity and has great potential in the field of metal ion sensing and detection.

MATERIALS AND METHODS

Materials

Glutathione (GSH), $CuSO_4$, Cu $(NO_3)_2$ $3H_2O$, $ZnSO_4·7H_2O$ (Analytically Pure, Tianjin FengChuan Chemical Reagent Technology Co., Ltd.), $FeCl_2·4H_2O$ (Analytical Pure, Beijing Shangle Chemical Plant), $Bi(NO_3)_3·3H_2O$, NaCl, KCl (Analytical Pure, Tianjin Beilian Fine Chemicals Development Co., Ltd.), Ni $(NO_3)_2·6H_2O$ (Analytical Pure, Beijing 5671 Chemical Plant), NaOH (Analytically Pure, Tianjin Shengao Chemical Reagent Co., Ltd.), $MnSO_4·H_2O$ (Analytical Reagent, No.4 Chemical Plant, Chaoyang District, Beijing), $Cd(NO_3)_2$ (Analytical Pure, Beijing Chemical Plant), NH_4Cl (Analytical Pure, Tianjin People's Chemical Plant), $Na_2SiO_3·9H_2O$ (Analytical Pure, Chemical Plant of Beijing Yizhuang Middle School), $NaNO_2$ (Analytical Reagent, Tianjin Public Private Joint Venture Chemical Reagent Factory No.1), KI (Analytical Reagent, Baoding Chemical Reagent Factory, Hebei Province), $Na_2SiO_3·9H_2O$ (Analytical Pure, Chemical Plant of Beijing Yizhuang Middle School), $CoCl_2·6H_2O$ (Analysys, Shanghai Public Private Joint Venture China Trade Factory), NaF (Analytical Pure, Beijing Public and Private Chemical Plant), and ultrapure water (about 18.25 m Ω).

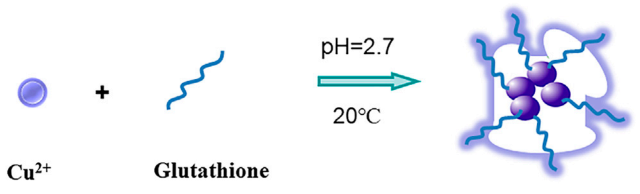

FIGURE 1 | Sketch map of the GSH-CuNPs.

Instruments

JEOL-2100f high resolution transmission electron microscope (equipped with xflash, Bruker, Germany), 5030t X-ray spectrometer (Japan Electronics Co., Ltd.), F-4600 fluorescence spectrophotometer (Hitachi high tech company), PHS-3c pH meter (Shanghai Yidian Scientific Instrument Co., Ltd.), d1008 series handheld centrifuge (Beijing Dalong Xingchuang Experimental Instrument Co., Ltd.), zf-7a portable UV detection lamp (Shanghai Guanghao analyzer Co., Ltd.), manual (adjustable and fixed) pipette (Beijing Dalong Xingchuang Experimental Instrument Co., Ltd.), and HJ-4A constant temperature magnetic heating agitator (Jiangsu Jintan Honghua instrument factory).

Synthesis of Copper Nanomaterials

Cu nanoparticles were prepared by blending 0.5 ml $50 \times 10–^{3}$ M Cu $(NO_3)_2$ $·3H_2O$ with 2.5 ml of $50 \times 10–^{3}$ M glutathione (GSH) and 2.0 ml of water, adjusting to pH 2.7 with 2 M NaOH, and centrifuging for 20 min to obtain GSH-CuNPs. Finally, it was stored at 4°C for subsequent experiments.

Detection of a Trivalent Bismuth Ion

The prepared GSH-CuNPs were put into a 1.5 ml centrifuge tube at 450 μ L, and then 50 μ L Bi^{3+} ion solutions with different levels were added. The reaction time was 15 min at room temperature. The fluorescence intensity at 471 nm was measured.

RESULTS AND DISCUSSION

Synthesis Principle of GSH-CuNPs

In this test, the synthesis method of GSH-CuNPs is shown in **Figure 1**. GSH-CuNPs with hyperfluorescence were prepared at room temperature with glutathione as the protective agent and reducing agent. When Bi^{3+} was added into the GSH-CuNP system, Bi^{3+} would destroy GSH-CuNPs and cause aggregation of GSH-CuNPs, resulting in fluorescence fading. Therefore, based

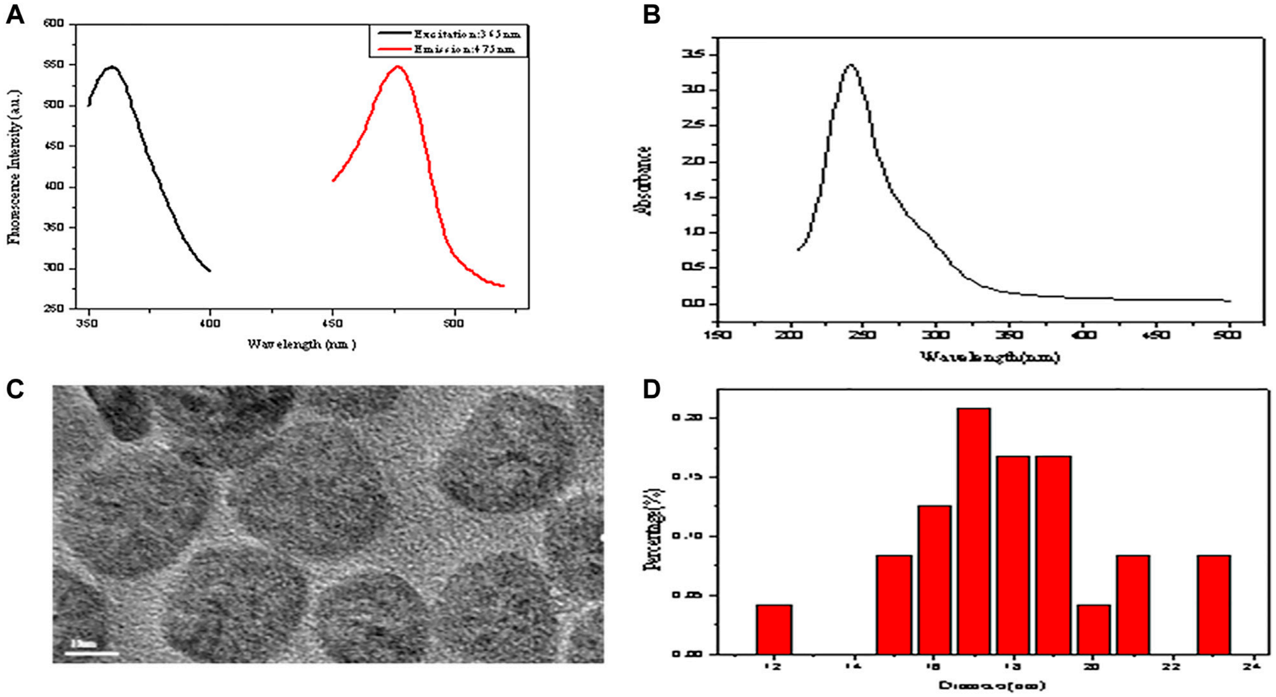

FIGURE 2 | (A) Fluorescence spectra of GSH-CuNPs; **(B)** UV–vis spectra of GSH-CuNPs; **(C)** TEM image of GSH-CuNPs; **(D)** size-distribution histogram of GSH-CuNPs.

on the trivalent bismuth ions, we can effectively inhibit the fluorescence of GSH-CuNPs so as to realize the detection of bismuth ions.

Characterization of Copper Nanomaterials

The fluorescence spectra of GSH-CuNPs are shown in **Figure 2A**. The emission and excitation of GSH-CuNPs are at 475 and 365 nm, respectively. As shown in **Figure 2B**, Cu nanoparticles have a small UV absorption spectrum, which also proves the successful synthesis of copper nanomaterials. **Figure 2C** exhibits the TEM image of GSH-CuNPs with small particle size and uniform distribution. **Figure 2D** exhibits the particle size spreading of GSH-CuNPs. The average diameter of GSH-CuNPs is about 17.0 ± 0.2 nm. These findings suggest that the synthesized GSH-CuNPs have the characteristics of great fluorescence, equality, dispersibility, and granule dimensions, indicating the successful synthesis of hyperfluorescence GSH-CuNPs.

Stability of Copper Nanomaterials

We study the stability of GSH-CuNPs under different conditions. As revealed in **Figure 3A**, the fluorescence magnitude of GSH-CuNPs remains unchanged when a sodium chloride solution of different concentrations is added. As exhibited in **Figure 3B**, when the pH value of CuNPs was adjusted, it was found that the fluorescence magnitude of CuNPs was affected by pH. When pH is 2.7, GSH-CuNPs have a higher fluorescence magnitude. As shown in **Figure 3C**, the fluorescence intensity of GSH-CuNPs remains unchanged with time. As we can see, compound GSH-CuNPs can be stored for about 45 days at 4°C. The aforementioned data prove that GSH-CuNPs have good storage stability and good optical stability.

Selectivity and Sensing Properties of Copper Nanomaterials

A series of different cations (such as CO^{2+}, Mg^{2+}, Cd^{2+}, K^{+}, Na^{+}, Bi^{3+}, and Fe^{3+}) and anions (such as I^{-} and F^{-}) with identical concentration (100 mmol L^{-1}) were tested. As shown in **Figures 4A, B**, Bi^{3+} can quench GSH-CuNPs, and the other ions have little effect on GSH-CuNPs. The results show that the technique has higher selectivity for the gauging of Bi^{3+}.

Analysis of Sensing Properties of Copper Nanomaterials

In this trial run, a few bismuth ions with different levels were used for sensor analysis. As revealed in **Figure 5A**, the fluorescence of GSH-CuNPs was found by inch inhibition with the increase of bismuth ion concentration (0 mmol l^{-1}–100 μ mol L^{-1}). As revealed in **Figure 5B**, Bi^{3+} concentration has a good linear relationship in the range of 0 μ mol l^{-1}–100 μ mol L^{-1} (R = 0.9495), and the detection limit is 10 mmol L^{-1}.

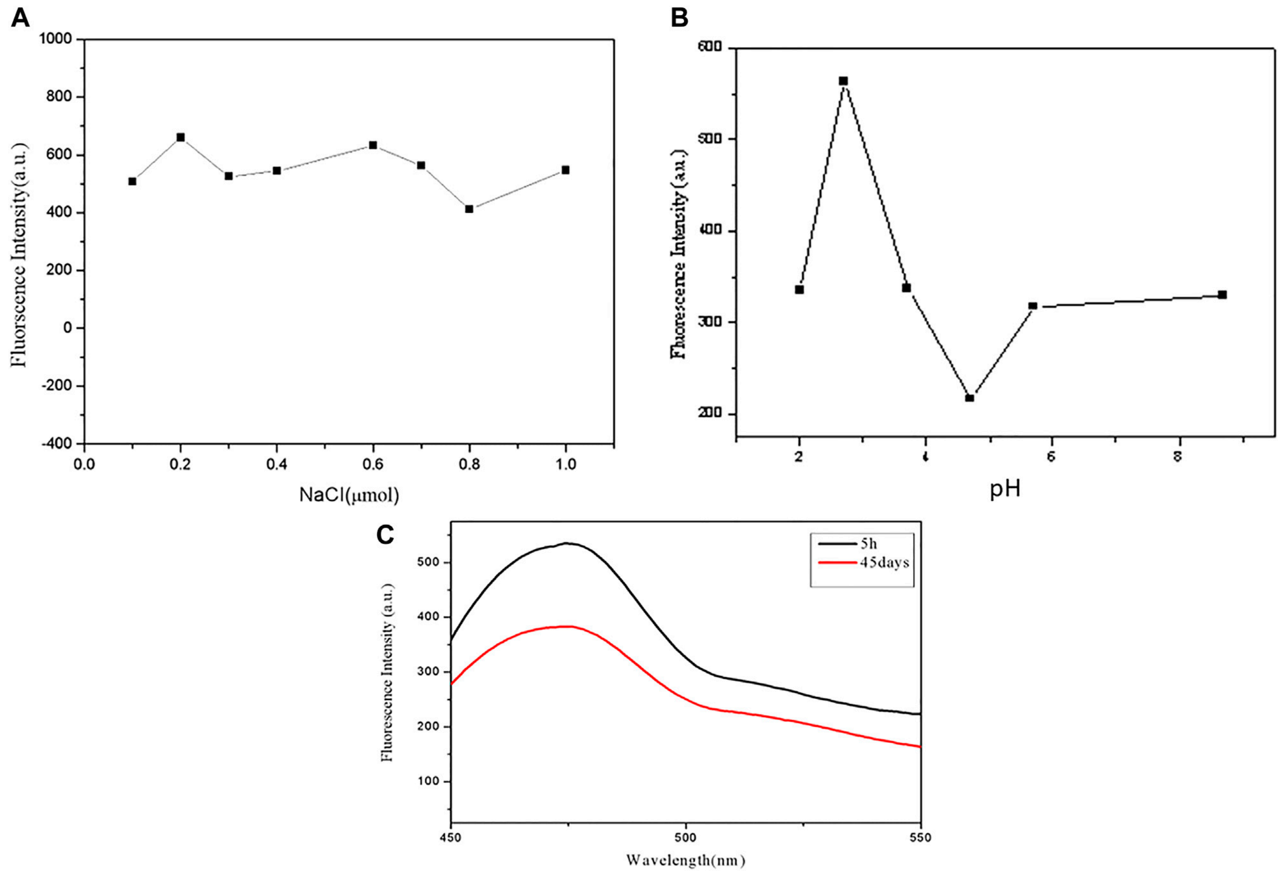

FIGURE 3 | (A) Fluorescence magnitude of GSH-CuNPs; **(B)** effect of pH value on GSH-CuNP fluorescence intensity; **(C)** GSH-CuNPs can be stored for 1 month at 4°C.

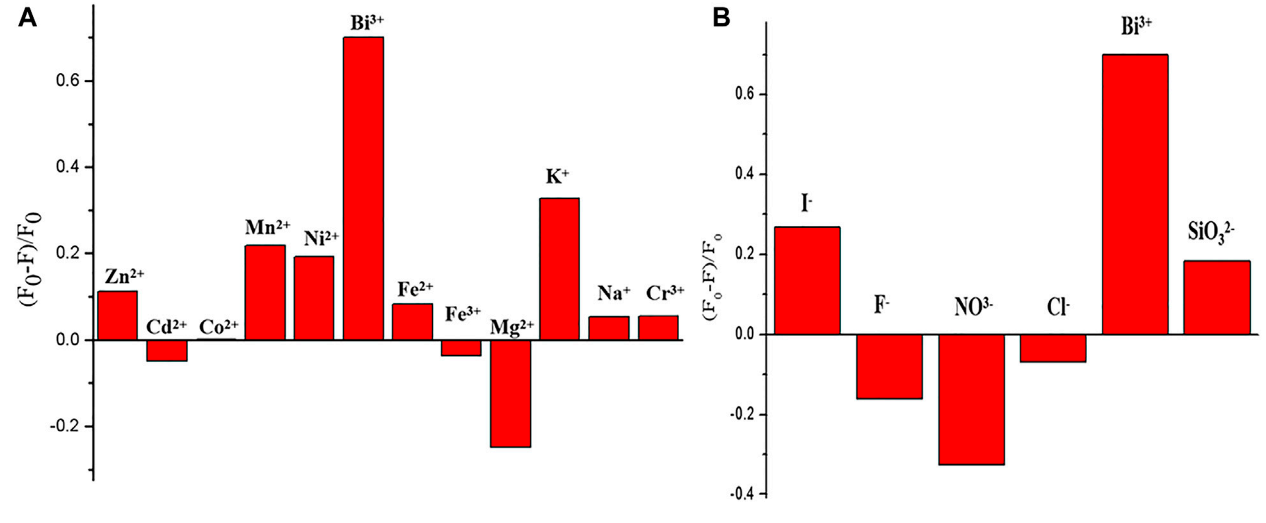

FIGURE 4 | Fluorescence intensity of GSH-CuNPs at 475 nm under the existence of various cations **(A)** and anions **(B)**.

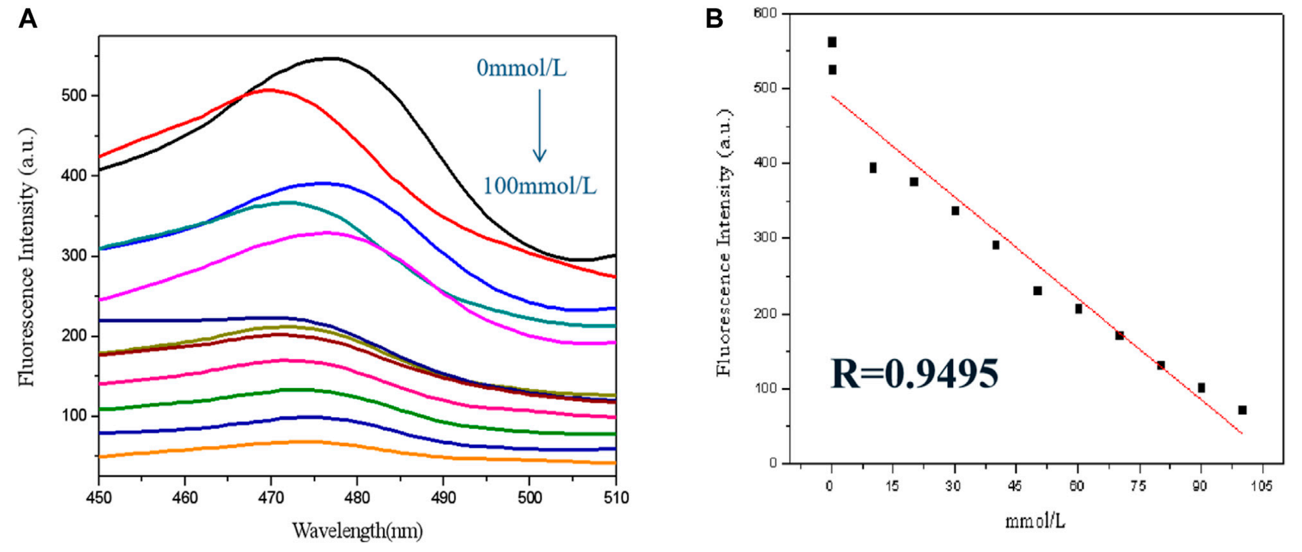

FIGURE 5 | (A) GSH-CuNP fluorescence spectra with different concentration of bismuth ions; **(B)** linear relationship between fluorescence intensity of GSH-CuNPs and concentration of Bi^{3+}.

CONCLUSION

In view of the fluorescence inhibition mechanization, a fluorescent analysis means for the detection of Bi^{3+} was built by using GSH-CuNPs as the fluorescence probe and Bi^{3+} as the quenching agent. With the increase of Bi^{3+} concentration, the fluorescence of Cu nanoparticles is inhibited in diverse degrees. The results showed that the fluorescence quenching linear relationship was good in the range of $0\,\mu$ mol l^{-1}–$100\,\mu$ mol L^{-1} (R = 0.9495). The GSH-CuNPs can be used for selective detection of bismuth ions.

DATA AVAILABILITY STATEMENT

The original contributions presented in the study are included in the article/Supplementary Material, further inquiries can be directed to the corresponding authors.

AUTHOR CONTRIBUTIONS

RW: preparation and characterization of materials and writing of the manuscript. LG: detection of bismuth ions and theoretical guidance. JA: writing and revising of the manuscript.

FUNDING

This work was supported by the National Natural Science Foundation of China (Grant No. 21864020), the Natural Science Foundation of Inner Mongolia (Grant No. 2018MS02012), the Collaborative Innovation Center for Water Environmental Security of Inner Mongolia Autonomous Region, China, (Grant No. XTCX003), and the Inner Mongolia Innovation Guide Project and Research Project of Higher School, Department of Education of Inner Mongolia Autonomous Region (Grant No. NJZC16047).

REFERENCES

Alexander, D. C., Costanzo, M. A., Guzzo, J., Cai, J., Charoensri, N., Diorio, C., et al. (2000). Blazing towards the Next Millennium: Luciferase Fusions to Identify Genes Responsive to Environmental Stress. *Water Air Soil Pollut.* 123, 81–94. doi:10.1007/978-94-011-4369-1_8

Aragay, G., Pons, J., and Merkoçi, A. (2011). Recent Trends in Macro-, Micro-, and Nanomaterial-Based Tools and Strategies for Heavy-Metal Detection. *Chem. Rev.* 111, 3433–3458. doi:10.1021/cr100383r

Bain, D., Paramanik, B., and Patra, A. (2017). Silver(I)-Induced Conformation Change of DNA: Gold Nanocluster as a Spectroscopic Probe. *J. Phys. Chem. C* 121, 4608–4617. doi:10.1021/acs.jpcc.6b10560

Bain, D., Paramanik, B., Sadhu, S., and Patra, A. (2015). A Study into the Role of Surface Capping on Energy Transfer in Metal Cluster-Semiconductor Nanocomposites. *Nanoscale* 7, 20697–20708. doi:10.1039/c5nr06793f

Barman, M. K., Paramanik, B., Bain, D., et al. (2016). Light Harvesting and White-Light Generation in a Composite of Carbon Dots and Dye-Encapsulated BSA-Protein-Capped Gold Nanoclusters. *Chem. Eur. [J]* 22, 11699–11705. doi:10.1103/physrevlett.93.077402

Brower, J. B., Ryan, R. L., and Pazirandeh, M. (1997). Comparison of Ion-Exchange Resins and Biosorbents for the Removal of Heavy Metals from Plating Factory Wastewater. *Environ. Sci. Technol.* 31, 2910–2914. doi:10.1021/cr100383r

Burda, C., Chen, X., Narayanan, R., and El-Sayed, M. A. (2005). Chemistry and Properties of Nanocrystals of Different Shapes. *Chem. Rev.* 105, 1025–1102. doi:10.1021/cr030063a

Bush, A., Pettingell, W., Multhaup, G., d Paradis, M., Vonsattel, J., Gusella, J., et al. (1994). Rapid Induction of Alzheimer A Beta Amyloid Formation by Zinc. *Science* 265, 1464–1467. doi:10.1126/science.8073293

Cao, H., Chen, Z., Zheng, H., and Huang, Y. (2014). Copper Nanoclusters as a Highly Sensitive and Selective Fluorescence Sensor for Ferric Ions in Serum and Living Cells by Imaging. *Biosens. Bioelectron.* 62, 189–195. doi:10.1016/j.bios.2014.06.049

Chakraborty, I., and Pradeep, T. (2017). Atomically Precise Clusters of Noble Metals: Emerging Link between Atoms and Nanoparticles. *Chem. Rev.* 117, 8208–8271. doi:10.1021/acs.chemrev.6b00769

Chen, D. J., Li, S. X., and Zheng, F. Y. (2016). Water Soluble Sulphur Quantum Dots for Selective Ag+ Sensing Based on the Ion Aggregation-Induced Photoluminescence Enhancement. *Biosens. Bioelectron.* 8, 632–636. doi:10.1016/j.bios.2014.06.049

Chen, X.-J., Sanchez-Gaytan, B. L., Qian, Z., and Park, S.-J. (2012). Noble Metal Nanoparticles in DNA Detection and Delivery. *WIREs Nanomed Nanobiotechnol* 4, 273–290. doi:10.1002/wnan.1159

Fan, J. A., Wu, C., Bao, K., Bao, J., Bardhan, R., Halas, N. J., et al. (2010). Self-Assembled Plasmonic Nanoparticle Clusters. *Science* 328, 1135–1138. doi:10.1126/science.1187949

Feng, J., Ju, Y., Liu, J., Zhang, H., and Chen, X. (2015). Polyethyleneimine-templated Copper Nanoclusters via Ascorbic Acid Reduction Approach as Ferric Ion Sensor. *Analytica Chim. Acta* 854 (22), 153–160. doi:10.1016/j.aca.2014.11.024

Ferreira, S. L. C., dos Santos, H. C., Costa, A. C. S., and de la Guardia, M. (2004). Procedures of Separation and Pre-concentration for Molybdenum Determination Using Atomic Spectrometry-A Review. *Appl. Spectrosc. Rev.* 39, 457–474. doi:10.1081/asr-120037147

Fu, F., and Wang, Q. (2011). Removal of Heavy Metal Ions from Wastewaters: A Review. *J. Environ. Manage.* 92, 407–418. doi:10.1016/j.jenvman.2010.11.011

Gans, J., Wolinsky, M., and Dunbar, J. (2005). Computational Improvements Reveal Great Bacterial Diversity and High Metal Toxicity in Soil. *Science* 309, 1387–1390. doi:10.1126/science.1112665

Ghaedi, M., Shokrollahi, A., Niknam, K., et al. (2009). Cloud point Extraction and Flame Atomic Absorption Spectrometric Determination of Cadmium (II), lead (II), Palladium (II) and Silver (I) in Environmental Samples. *Hazard. Mater.* 168, 1022–1390. doi:10.1126/science.1112665

Gill, P. G. K. (1983). Surface Interaction Model for Tracemetal Toxicity to Fishes: Role of Complexation, pH, and Water Hardness. *Environ. Sci. Technology* 17, 342–347.

Järup, L. (2003). Hazards of Heavy Metal Contamination. *Br. Med. Bull.* 68, 167–182. doi:10.1093/bmb/ldg032

Jin, R., Zeng, C., Zhou, M., and Chen, Y. (2016). Atomically Precise Colloidal Metal Nanoclusters and Nanoparticles: Fundamentals and Opportunities. *Chem. Rev.* 116, 10346–10413. doi:10.1021/acs.chemrev.5b00703

Korolczuk, M., Moroziewicz, A., and Grabarczyk, M. (2005). Determination of Subnanomolar Concentrations of Cobalt by Adsorptive Stripping Voltammetry at a Bismuth Film Electrode. *Anal. Bioanal. Chem.* 382, 1678–1682. doi:10.1007/s00216-005-3358-2

Kundu, S., and Patra, A. (2017). Nanoscale Strategies for Light Harvesting. *Chem. Rev.* 117, 712–757. doi:10.1021/acs.chemrev.6b00036

Lee, J.-Y., Friedman, J. E., Angel, I., Kozak, A., and Koh, J.-Y. (2004). The Lipophilic Metal Chelator DP-109 Reduces Amyloid Pathology in Brains of Human β-amyloid Precursor Protein Transgenic Mice. *Neurobiol. Aging* 25, 1315–1321. doi:10.1016/j.neurobiolaging.2004.01.005

Lee, J. H., Wang, Z., Liu, J., and Lu, Y. (2008). Highly Sensitive and Selective Colorimetric Sensors for Uranyl (UO22+): Development and Comparison of Labeled and Label-free DNAzyme-Gold Nanoparticle Systems. *J. Am. Chem. Soc.* 130, 14217–14226. doi:10.1021/ja803607z

Li, N., Zhang, L., Chen, Y., Fang, M., Zhang, J., and Wang, H. (2012). Highly Efficient, Irreversible and Selective Ion Exchange Property of Layered Titanate Nanostructures. *Adv. Funct. Mater.* 22 (4), 835–841. doi:10.1002/adfm.201102272

Lu, Z., and Yin, Y. (2012). Colloidal Nanoparticle Clusters: Functional Materials by Design. *Chem. Soc. Rev.* 41, 6874–6887. doi:10.1039/c2cs35197h

Nie, Z., Petukhova, A., and Kumacheva, E. (2010). Properties and Emerging Applications of Self-Assembled Structures Made from Inorganic Nanoparticles. *Nat. Nanotech* 5, 15–25. doi:10.1038/nnano.2009.453

Oyaro, N., Juddy, O., Murago, E., et al. (2007). The Contents of Pb, Cu, Zn and Cd in Meat in Nairobi, Kenya. *Int. Food Agric. Environ.* 5, 119–121.

Schroeder, A., Heller, D. A., Winslow, M. M., Dahlman, J. E., Pratt, G. W., Langer, R., et al. (2012). Treating Metastatic Cancer with Nanotechnology. *Nat. Rev. Cancer* 12, 39–50. doi:10.1038/nrc3180

Sharma, S. S., and Dietz, K.-J. (2009). The Relationship between Metal Toxicity and Cellular Redox Imbalance. *Trends Plant Sci.* 14, 43–50. doi:10.1016/j.tplants.2008.10.007

Stohs, S., and Bagchi, D. (1995). Oxidative Mechanisms in the Toxicity of Metal Ions. *Free Radic. Biol. Med.* 18, 321–336. doi:10.1016/0891-5849(94)00159-h

Sud, D., Mahajan, G., and Kaur, M. (2008). Agricultural Waste Material as Potential Adsorbent for Sequestering Heavy Metal Ions from Aqueous Solutions - A Review. *Bioresour. Technology* 99, 6017–6027. doi:10.1016/j.biortech.2007.11.064

Xia, Y., Xiong, Y., Lim, B., and Skrabalak, S. E. (2009). Shape-Controlled Synthesis of Metal Nanocrystals: Simple Chemistry Meets Complex Physics? *Angew. Chem. Int. Ed.* 48, 60–103. doi:10.1002/anie.200802248

Xie, J., Zheng, Y., and Ying, J. Y. (2009). Protein-Directed Synthesis of Highly Fluorescent Gold Nanoclusters. *J. Am. Chem. Soc.* 131, 888–889. doi:10.1021/ja806804u

Yoshizaki, S., and Tomida, T. (2000). Principle and Process of Heavy Metal Removal from Sewage Sludge. *Environ. Sci. Technol.* 34, 1572–1575. doi:10.1021/es990979s

Zheng, J., Zhang, C., and Dickson, R. M. (2004). Highly Fluorescent, Water-Soluble, Size-Tunable Gold Quantum Dots. *Phys. Rev. Lett.* 93, 077402. doi:10.1103/PhysRevLett.93.077402

Zhu, M., Aikens, C. M., Hollander, F. J., Schatz, G. C., and Jin, R. (2008). Correlating the Crystal Structure of A Thiol-Protected Au25 Cluster and Optical Properties. *J. Am. Chem. Soc.* 130, 5883–5885. doi:10.1021/ja801173r

Conflict of Interest: The authors declare that the research was conducted in the absence of any commercial or financial relationships that could be construed as a potential conflict of interest.

frontiers | Frontiers in Chemistry

ORIGINAL RESEARCH
published: 31 May 2022
doi: 10.3389/fchem.2022.920468

Derivative Matrix-Isopotential Synchronous Spectrofluorimetry and Hantzsch Reaction: A Direct Route to Simultaneous Determination of Urinary δ-Aminolevulinic Acid and Porphobilinogen

*Muhammad Ajmal, Jia-Wen Wei, Yan Zhao, Yi-Hong Liu, Ping-Ping Wu and Yao-Qun Li**

Department of Chemistry and the MOE Key Laboratory of Spectrochemical Analysis and Instrumentation, College of Chemistry and Chemical Engineering, Xiamen University, Xiamen, China

Early and sensitive detection of δ-aminolevulinic acid (δ-ALA) and porphobilinogen (PBG) is the cornerstone of diagnosis and effective treatment for acute porphyria. However, at present, the quantifying strategies demand multiple solvent extraction steps or chromatographic approaches to separate δ-ALA and PBG prior to quantification. These methods are both time-consuming and laborious. Otherwise, in conventional spectrofluorimetry, the overlapping spectra of the two analytes cause false diagnosis. To overcome this challenge, we present a two-step approach based on derivative matrix-isopotential synchronous fluorescence spectrometry (DMISFS) and the Hantzsch reaction, realizing the simple and simultaneous detection of δ-ALA and PBG in urine samples. The first step is chemical derivatization of the analytes by Hantzsch reaction. The second step is the determination of the target analytes by combining MISFS and the first derivative technique. The proposed approach accomplishes following advantages: 1) The MISFS technique improves the spectral resolution and resolves severe spectral overlap of the analytes, alleviating tedious and complicated pre-separation processes; 2) First derivative technique removes the background interference of δ-ALA on PBG and vice versa, ensuring high sensitivity; 3) Both the analytes can be determined simultaneously via single scanning, enabling rapid detection. The obtained detection limits for δ-ALA and PBG were 0.04 µmol L^{-1} and 0.3 µmol L^{-1}, respectively. Within-run precisions (intra and inter-day CVs) for both the analytes were <5%. Further, this study would serve to enhance the availability of early and reliable quantitative diagnosis for acute porphyria in both scientific and clinical laboratories.

Keywords: matrix-isopotential synchronous fluorescence spectrometry, δ-aminolevulinic acid, porphobilinogen, simultaneous detection, derivative technique

Edited by:
Muhammad Asif,
Wuhan Institute of Technology, China

Reviewed by:
Muhammad Wajid Ullah,
Jiangsu University, China
Dilshad Hussain,
University of Karachi, Pakistan

****Correspondence:***
Yao-Qun Li
yaoqunli@xmu.edu.cn

Specialty section:
This article was submitted to Analytical Chemistry, a section of the journal Frontiers in Chemistry

Received: *14 April 2022*
Accepted: *13 May 2022*
Published: *31 May 2022*

Citation:
Ajmal M, Wei J-W, Zhao Y, Liu Y-H, Wu P-P and Li Y-Q (2022) Derivative Matrix-Isopotential Synchronous Spectrofluorimetry and Hantzsch Reaction: A Direct Route to Simultaneous Determination of Urinary δ-Aminolevulinic Acid and Porphobilinogen. Front. Chem. 10:920468. doi: 10.3389/fchem.2022.920468

INTRODUCTION

Porphyrins play a pivotal role in chlorophyll, hemoglobin, and certain enzymes (Killiny et al., 2020). For human bodies, their synthetic sequence leads to the production of haem. However, any abnormality in the haem biosynthetic pathway can give rise to a class of genetic disorders, known as the porphyrias (Ajmal et al., 2019; Fujiwara et al., 2020; Jaramillo-Calle et al., 2021). The porphyrias are broadly categorized as either acute or non-acute. Amongst acute intermittent porphyria (AIP), hereditary coproporphyria (HP) and variegate porphyria (VP), AIP is the most common type of acute porphyria. It is caused by reduced activity of porphobilinogen deaminase (PBGD), which is the third enzyme in the haem pathway (Bechara et al., 2021). The disease (AIP) is characterized by deadly episodes of neurovisceral attacks featured by hypertension, autonomic dysfunction, and abdominal pain (Lin et al., 2011). As δ-aminolevulinic acid (δ-ALA) and porphobilinogen (PBG) are the well documented precursors for the biosynthetic pathway of haem, disorders of their urinary concentrations bear remarkable diagnostic and therapeutic significance for acute porphyria. However, unlike AIP, HP, and VP, where the urinary concentrations for both δ-ALA and PBG are raised, elevated concentration of δ-ALA alone without raising PBG marks the presence of diseases like ALA-D deficiency porphyria (ADP), hereditary tyrosinaemia type I, and lead toxicity (van't Klooster et al., 2017). Although PBG concentration in urine is recommended as the first identification test for an acute attack (Herrick and McColl, 2005), yet simultaneous detection of δ-ALA and PBG is essential for the differential screening of the aforementioned conditions.

The classical method for the qualitative determination of urinary PBG constitutes the colorimetric analysis after reaction with Ehrlich's reagent (p-dimethylaminobenzaldehyde, DMAB) in acid solution forming a red compound. In this process, equal amounts of urine and Ehrlich's reagent are mixed and PBG is obtained in the aqueous phase (Watson and schwartz, 1941). This method was later revised and simplified by Hoesch (Lamon and Redeker, 1974). However, these methods lack adequate selectivity and sensitivity for quantitative measurements, as the interfering compounds are extracted from the urinary sample before initiating the reaction. As the most prevalent alternative, Mauzerall and Granick's method allows the quantification of both δ-ALA and PBG with the help of multiple sample extraction steps. In this method, urinary samples are purified by using different cation and anion-exchange columns before derivatization with Ehrlich's reagent and precise spectrophotometric determination at 553 nm (Mauzerall and Granick, 1956). Driven by these methods, a plethora of assays (Zhang et al., 2011; Benton et al., 2012; Carichon et al., 2014) have been introduced to achieve simple and speedy quantification of δ-ALA and PBG. Despite their huge contribution towards the detection, the existing screening methods still meet the challenge to separately determine δ-ALA and PBG in complex environments with interference from plentiful coexisting compounds reacting with Ehrlich's reagent (Marver et al., 1966; Pierach et al., 1977). Therefore, complicated and lengthy purification processes to reduce background interference from coexisting components become unavoidable, which deprives most hospitals of rapid detection for acute porphyria in patients with neuropathic abdominal issues. This delay usually results in awfully misdirected treatment (Bissell, 2015). Clearly, a simple, rapid and reliable method for direct and simultaneous determination of δ-ALA and PBG is of important significance.

Chemical derivatization is widely used to enhance the detection sensitivity and retain δ-ALA and/or PBG on columns in chromatography-based approaches (Hijaz and Killiny, 2016). Modified Hantzsch reaction is reckoned as one of the most frequently employed derivatization agent for δ-ALA, as it entails the detection based on fluorescence (Tomokuni et al., 1992; Oishi et al., 1996; Donnelly et al., 2006; Kanto et al., 2013). Fluorescence spectrometry has been a powerful tool for the identification, monitoring, and quantification of various analytes in a broad range of environments, on account of high selectivity and sensitivity (Ou-Yang et al., 2018; Tsumura et al., 2018; Cheng et al., 2019; Zhai et al., 2020; Ding et al., 2022; Remolina et al., 2022; Wang et al., 2022). Despite the extensive use, the considerable background fluorescence and the spectral overlap contributed by the interfering components are liable to pose a formidable diagnostic challenge for conventional fluorescence spectrometry in case of complex multi-component analysis. The technological advancement of synchronous fluorescence spectrometry (SFS) in biological applications shows great promise in solving this problem by taking advantage of spectral simplification, band narrowing, and minimized scattering interference (Lecrenier et al., 2018; Elmas et al., 2019; Kumar, 2019; Ouyang et al., 2019; Zhao et al., 2020). SFS exploits simultaneous scanning for excitation and emission wavelengths. With the passage of time, SFS has been transformed into a number of branches, including conventional constant-wavelength SFS (defined with constant $\Delta\lambda$), constant-energy SFS, variable angle SFS, and matrix-isopotential SFS. Constant-energy SFS deals with maintaining a constant energy difference of the excitation and emission photons (Li et al., 2010). In variable-angle SFS, the excitation and emission wavelengths are varied simultaneously but at different rates (Samokhvalov, 2020).

Matrix-isopotential synchronous fluorescence spectrometry (MISFS), a branch of SFS, specializes in eliminating the unknown fluorescence matrix background and determining the individual compounds in complex matrices simultaneously (Pulgarín and Molina, 1994). This technique proceeds by establishing a cut in the combined fluorescence spectrum for maintaining a constant matrix background. Subsequently, the cut is accompanied by the matrix-isopotential trajectory, which joins together the points of equal fluorescence intensity. Most importantly, as the selected trajectory passes all through the emission and excitation wavelength maxima of the target components in the matrix, the sensitivity is increased markedly (Li et al., 2010). Derivative spectrofluorimetry serves as an analytical tool which can transform the normal spectrum of a spectral curve into a derivative spectrum. Finally, MISFS in combination with the first derivative technique emerges as an ideal platform for multi-component detections by minimizing the unknown and unspecific background fluorescence from urine, and by resolving the spectra of adjacently overlapping mixtures, without resorting to pre-analytical purification processes (Pulgarín et al., 2014).

Capitalizing on our previous knowledge regarding the porphyrins and the porphyria (Huang et al., 2010; Shindi et al., 2010; Liu et al., 2012; Ajmal et al., 2019), we combine derivative matrix-isopotential synchronous fluorescence spectrometry (DMISFS) and the Hantzsch reaction to eliminate the long-standing problems of interference and laborious pre-analytical purifications for the simple, speedy and simultaneous determination of δ-ALA and PBG in the urine. While it is common to use the Hantzsch reaction for the fluorescent detection of δ-ALA, to our knowledge, there exists no precedent for either the detection of PBG alone or simultaneously with δ-ALA involving Hantzsch reaction or DMISFS. Thus, our work is envisioned to serve as a novel diagnostic tool for patients with severe abdominal pain in both clinical and scientific applications. This work also displays great promise as potential alternative to the present day kits for quantitative detection of δ-ALA/PBG.

EXPERIMENTAL

Materials and Reagents

δ-ALA hydrochloride, acetylacetone reagent, and Formaldehyde (37%, V/V in water) were provided by Aladdin-Reagent (Shanghai, China). Porphobilinogen was purchased from Sigma-Aldrich (St. Louis, MO, United States). Methanol HPLC grade, glacial acetic acid, and hydrochloric acid were supplied by J&K (China). The aqueous solutions were prepared by purified water. The ultrapure water was obtained from a Millipore Milli-Q water purifying system (Millipore, Bedford, MA, United States), with a specific resistance of 18.2 MΩ cm.

Stock solutions for δ-ALA and PBG were prepared as 3 and 1 mM, respectively, in amber-colored volumetric flasks and were preserved in the refrigerator until use. Samples for both the analytes were prepared following a procedure reported previously (Ajmal et al., 2019). Calibration plots were obtained by spiking different solutions with concentrations as 0–5 μM for δ-ALA and 0–15 μM for PBG. Acetylacetone reagent was formulated by mixing acetylacetone, ethanol, and water in a ratio of 15:10:75, respectively. Formaldehyde solution was prepared by 3.7–fold dilution of commercially available formaldehyde solution and was stored in darkness (Oishi et al., 1996).

Urine Samples

Urine specimens from apparently healthy individuals were collected, anonymized, stored in dark containers, and refrigerated at −20°C. The obtained samples were generally analyzed within an hour from their collection time. This research was carried out according to the regulations and guidelines of the National Ethics Committee for the Biomedical Research in China. All experiments complied with the institutional guidelines and relevant laws approved by the Medical Ethics Committee of Xiamen University. Informed consent was obtained from the volunteers participating in this study.

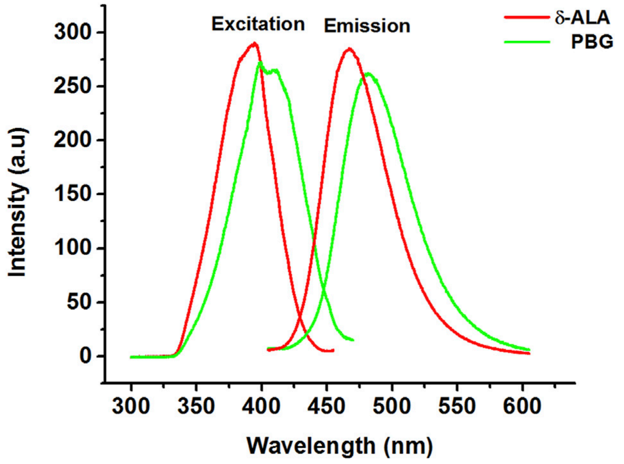

FIGURE 1 | Excitation and emission spectra of δ-ALA (2.5 μmol L^{-1}, red solid lines, λex = 394.4 nm; λem = 467.3 nm) and PBG (6.5 μmol L^{-1}, green solid lines, λex = 399.7 nm; λem = 481.6 nm).

Fluorescence Study

All the fluorimetric experiments were conducted on a laboratory-assembled MYF spectrofluorometer (Huang et al., 2010; Liu et al., 2016; Ajmal et al., 2019). The instrument was equipped with 150-W xenon lamp as the excitation source. For the two monochromators, the slits were fixed at 5 nm band passes. To control the monochromators and obtain the excitation and emission spectra, a software package framed in Turbo C 2.0 was used. This software permits the export of the obtained fluorescence data into the format of ASCII file. ASCII file is employed in the FTOTAL program, which is written on Visual BASIC (Pulgarín and Molina, 1993). This program favors the representation of three-dimensional (3D) spectra of the individual compounds from their corresponding excitation and emission spectra. These 3D spectra can also be displayed as a contour map or an isometric projection. For recording the MISF spectrum, FTOTAL achieves the intensity values for the excitation wavelengths by applying the specific function which combines points of identical intensity on the matrix comprehensive fluorescence spectrum (Wu et al., 1999). This combination of equal intensity points is called the isopotential scanning trajectory. The first derivative spectra were then acquired directly via electronic differential device equipped with the spectrofluorometer without a phase converter. A quartz cuvette with a path length of 1.0 × 1.0 cm was utilized for all the fluorescence measurements.

RESULTS AND DISCUSSION

Conventional Fluorescence Spectra

We commenced our study by obtaining conventional fluorescence spectra for δ-ALA and PBG. **Figure 1** exhibits

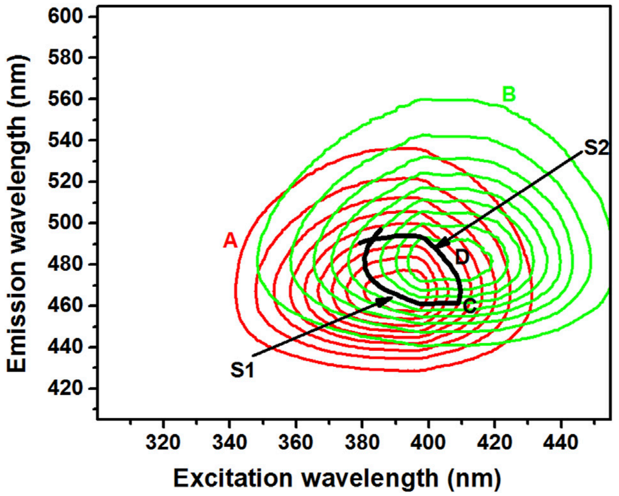

FIGURE 2 | Contour maps of δ-ALA [**(A)**, 2.5 μmol L^{-1}, red solid line], PBG [**(B)**, 6.5 μmol L^{-1}, green solid line], point of contact **(C)** and the selected isopotential scanning route [**(D)**, black solid line].

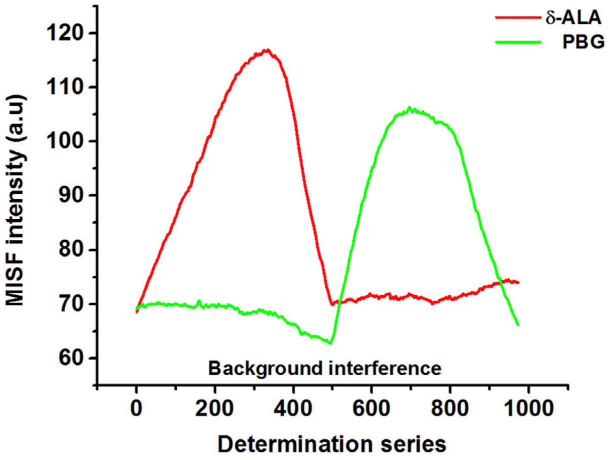

FIGURE 3 | MISF spectra of δ-ALA (2.5 μmol L^{-1}, red solid line) and PBG (6.5 μmol L^{-1}, green solid line).

the location of the excitation maxima of δ-ALA and PBG at 394.4 and 399.7 nm, respectively. And the corresponding emission maxima of δ-ALA and PBG at 467.3 and 481.6 nm, respectively. However, in this case, fluorescence bands of δ-ALA and PBG were closely overlapped on account of their almost identical molecular structures, indicating the fact that the presence of one component would overwhelmingly influence the other and hence their simultaneous quantitative detection using the conventional fluorescence spectrometry might well be difficult without resorting to the tedious and lengthy pre-separation processes.

Total Fluorescence Spectra

Theoretical three-dimensional (3D) spectra for both δ-ALA and PBG were obtained for selecting suitable scanning path of MISF. 3D spectra not only provide wide scope and comprehensive structural information, but can also furnish spectral features invisible in the conventional fluorescence spectra. These spectra were extracted from pair of emission and excitation spectra of both δ-ALA and PBG by using a home-made program (FTOTAL) and projected as the isometric presentation, where the emission spectra were plotted at corresponding increments of the excitation wavelengths. Subsequently, 3D spectra were efficiently transformed into two-dimensional contour plots by connecting the points of identical fluorescence intensity of the emission and excitation wavelengths. As shown in **Figure 2**, the superposition of the contour plots of δ-ALA and PBG leads to the overlapping in the maximum intensity regions of the analytes. This serious overlap disabled the individual detections owing to the spectral interference from the background signal.

Optimum Scanning Route Selection

The careful evaluation of the 2D contour plots of δ-ALA and PBG favored the selection of an optimum matrix-isopotential scanning trajectory by making a cut in the total fluorescence spectra of the two analytes. The selection of this trajectory was critically significant in establishing the suitable DMISFS method for the rapid and simultaneous detection of δ-ALA and PBG, since it could offer the DMISF spectra with the maximum fluorescence and minimum interference. In the selected trajectory, from left to right, the first section (S1) was a part of PBG contour lines, while the second section (S2) belonged to δ-ALA contour lines. Section1 (PBG) of the isopotential trajectory was chosen to pass through the highest possible wavelengths of δ-ALA: ex = 391 nm, em = 465.4 nm. Similarly, section 2 (δ-ALA), was selected to go through the highest possible wavelengths of PBG: ex = 403.6 nm, em = 484.3 nm. Later, these sections were combined at the crossing point, highlighted by the "C" sign to establish a complete scanning path as a matrix isopotential synchronous fluorescence (MISF) scanning route for the simultaneous detection of δ-ALA and PBG (**Figure 2**). The trajectory was highlighted by the sign "D". This isopotential scanning route was used for both MISF and DMISF based detections. When this selected path was used for acquiring luminescence spectra of δ-ALA and PBG in the presence of urinary fluorescent matrix, the same spectrum was obtained for the targets as in complete isolation, thereby, maintaining high sensitivity.

Figure 3 shows MISF spectra for δ-ALA and PBG. For appropriate presentation and quantitative determinations, the MISF spectra were outlined with the determination series plotted as the *x*-axis, while the MISF intensity set as the *y*-axis. Moreover, the determination series demonstrate the coordinate orders of all the positions (ex, em) employed for the selection of the isopotential scanning path, beginning from the extreme left up to the extreme right.

Although the spectral bands of δ-ALA and PBG were satisfactorily resolved, their quantitative measurement using MISFS technique alone might still not be precise owing to the background interference of one component on the other. First-derivative technique has been an effective tool of background

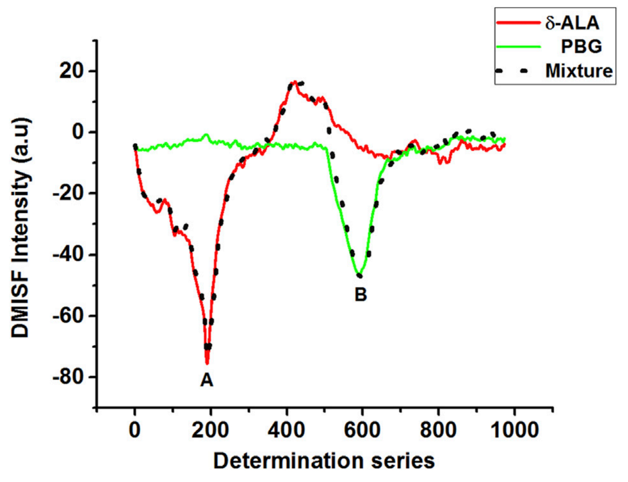

FIGURE 4 | DMISF spectra of δ-ALA (2.5 μmol L^{-1}, red solid line), PBG (6.5 μmol L^{-1}, green solid line), and their mixture, black dotted line. **(A,B)** refer to the detection points of δ-ALA and PBG respectively.

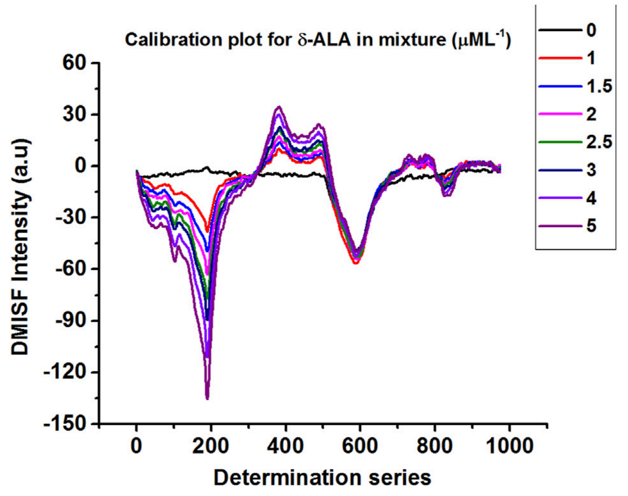

FIGURE 5 | DMISF spectra of 8 μmol L^{-1} PBG with increasing amount of δ-ALA 0–5 μmol L^{-1}.

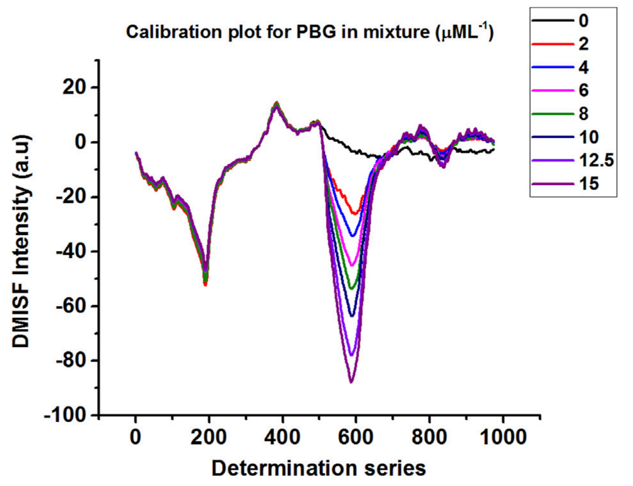

FIGURE 6 | DMISF spectra of 1.5 μmol L^{-1} δ-ALA with increasing amount of PBG 0–15 μmol L^{-1}.

elimination and spectrum enhancement, which can improve resolution ability of fine spectral structures and identify subtle spectral changes. Considering the fact that the scanning path was selected isopotentially, this issue was resolved by using the first-derivative technique in which the baseline involvement of both analytes in the normal MISF spectrum offered no interference in the first-derivative MISF spectrum. Coupling MISF technique with the first-derivative, it was possible to resolve the interference caused by the spectral overlap and determine both δ-ALA and PBG separately with high sensitivity and selectivity (**Figure 4**). **Figure 4** displays the elimination of PBG signal in the first section while retaining the net-derivative signal of δ-ALA, and vice versa for the second section. DMISF spectra of δ-ALA and PBG were scanned by the selected scanning path. The measurements corresponding to the peak maxima in the DMISF spectra of δ-ALA and PBG, highlighted as “A and B” on **Figure 4**, were applied for setting up their calibration plots.

Calibration plots for both δ-ALA and PBG were constructed by diluting appropriate aliquots of each analyte to verify their mutual independence at the selected detection points. The independence of δ-ALA detection point was displayed by obtaining DMISF spectra in mixtures having 0–5 μmol L^{-1} δ-ALA while the PBG concentration was fixed as 8 μmol L^{-1}. Likewise, the independence of PBG detection point was exhibited by conducting the DMISF spectra in mixtures with 0–15 μmol L^{-1} PBG while δ-ALA concentration was fixed, as 1.5 μmol L^{-1} (**Figures 5**, **6**). As portrayed by **Figures 5**, **6**, the DMISF spectra for δ-ALA and PBG at their respective detection points were mutually independent and well resolved, thereby, could well be quantified simultaneously in just a single scan within 90s. Moreover, the calibration plots were prepared by employing the linear regression method. The relationship between the analyte concentration and the DMISF signal at their respective detection points was linear up to the concentrations of 5 and 15 μmol L^{-1} for δ-ALA and PBG, respectively. The achieved correlation coefficient, 0.998 for both the analytes separately and individually, indicated good linearity.

Limits of Detection and Quantification

In compliance with IUPAC definition, the limits of detection were estimated as 0.04 and 0.31 μmol L^{-1} for δ-ALA and PBG respectively. The results were obtained with the equation C_{LOD} = 3Sb/m, where Sb symbolizes the standard deviation of the blank measurements (n = 16) and m refers to the slope of the calibration curve for the corresponding analyte. For the limits of quantification, the equation 10Sb/m, was used. The limits of quantification was found as 0.15 μmol L^{-1} for δ-ALA and 1.04 μmol L^{-1} for PBG. The detection limits achieved by the proposed method are satisfactory for the routine analysis of δ-ALA and PBG in urine samples.

TABLE 1 | Urine samples spiked with δ-ALA and PBG and obtained concentrations.

Sample no.	Spiked ALA (μmol L^{-1})	Spike PBG (μmol L^{-1})	Found ALA (μmol L^{-1})	Found PBG (μmol L^{-1})
1	1	6	1.0	5.0
2	3	11	2.8	9.7
3	1	10	0.9	8.8
4	3	4	2.8	2.8
5	4	7	3.8	5.5

Here, the found concentrations refer to the net concentrations of δ-ALA and PBG obtained after subtracting the signal of unspiked urine samples.

Application of the Method to Spiked Urine Samples

In order to investigate the potentiality of the proposed method towards the quantitative determination of δ-ALA and PBG, the DMISF spectra for a number of urine samples spiked with the target analytes with contrasting ratios were obtained at the isopotential scanning path. Previously constructed calibration plots were used for obtaining the concentrations of both components. The findings of these assays indicate the applicability of the present method for the precise quantification of δ-ALA and PBG in their mixtures (**Table 1**, **Supplementary Figures S1A–E**, ESI).

Precision of the Method

The within-run precision for the present method was demonstrated by repeatedly analyzing δ-ALA and PBG in a randomly obtained urine sample, from an apparently healthy subject. To be precise, the random urinary sample was analyzed for intra-day CVs (ten times a day) and inter-day CVs (six times during 6 days). The used sample was stored at −20°C. The between-run precision for intra-day CVs turned out be 3.0 and 3.1% for δ-ALA and PBG, respectively (**Supplementary Figure S2A**, ESI). However for inter-day, the CVs were 4.3 and 4.0% for δ-ALA and PBG, respectively (**Supplementary Figure S2B**, ESI).

CONCLUSION

Based on the combination of Hantzsch reaction, MISFS and the first-derivative technique, a direct and straightforward strategy was proposed aiming at the simultaneous quantification of δ-ALA and PBG in urinary samples for early diagnosis and treatment of acute porphyria. Compared with the previously reported methods, DMISFS effectively removed the spectral overlap and minimized the influence of unknown background fluorescence, making a seminal contribution as a highly sensitive technique which demanded no pre-analytical purification processes, no complicated operations and could rapidly quantify both the analytes in a single scanning within 90 s. Moreover, the present method offered improved recovery, selectivity, and limits of detections. The present method was also examined for the detection of δ-ALA and PBG in urine samples without any significant interference. This work stands out as a successful effort to not only furnish a reliable alternative for the laboratory-based diagnosis of δ-ALA and PBG but also for the commercially available screening kits with a number of added advantages. The present method is also believed to strengthen the international strives against the acute porphyria by providing prompt analysis of δ-ALA and PBG.

DATA AVAILABILITY STATEMENT

The original contributions presented in the study are included in the article/**Supplementary Material**, further inquiries can be directed to the corresponding author.

ETHICS STATEMENT

The studies involving human participants were reviewed and approved by The Medical Ethics Committee of Xiamen University, Xiamen University. The patients/participants provided their written informed consent to participate in this study.

AUTHOR CONTRIBUTIONS

MA performed the design, experiments, data analysis, and manuscript writing for this work. J-WW contributed to discussions, suggestions and writing. YZ provides supports in lab instruments and experiments. Y-HL contributed to suggestions in experimental methodology. P-PW provided technical support and lab management during the study. Y-QL supervised the project, provided advices in the research, and made writing revisions.

FUNDING

This work was financially supported by the National Natural Science Foundation of China (No. 21874110).

SUPPLEMENTARY MATERIAL

The Supplementary Material for this article can be found online at: https://www.frontiersin.org/articles/10.3389/fchem.2022.920468/full#supplementary-material

REFERENCES

Ajmal, M., Shindi, A. A. F., Liu, Y.-H., Zhao, Y., Wu, P.-P., Wei, J.-W., et al. (2019). Derivative Matrix-Isopotential Synchronous Spectrofluorimetry: A Solution for the Direct Determination of Urinary δ-aminolevulinic Acid. *New J. Chem.* 43 (46), 18092–18097. doi:10.1039/c9nj04261j

Bechara, E. J. H., Ramos, L. D., and Stevani, C. V. (2021). 5-Aminolevulinic Acid: A Matter of Life and Caveats. *J. Photochem. Photobiol.* 7, 100036. doi:10.1016/j.jpap.2021.100036

Benton, C. M., Couchman, L., Marsden, J. T., Rees, D. C., Moniz, C., and Lim, C. K. (2012). Direct and Simultaneous Determination of 5-aminolaevulinic Acid and Porphobilinogen in Urine by Hydrophilic Interaction Liquid Chromatography-Electrospray Ionisation/tandem Mass Spectrometry. *Biomed. Chromatogr.* 26 (8), 1033–1040. doi:10.1002/bmc.2770

Carichon, M., Pallet, N., Schmitt, C., Lefebvre, T., Gouya, L., Talbi, N., et al. (2014). Urinary Metabolic Fingerprint of Acute Intermittent Porphyria Analyzed by 1H NMR Spectroscopy. *Anal. Chem.* 86 (4), 2166–2174. doi:10.1021/ac403837r

Cheng, T., Huang, W., Gao, D., Yang, Z., Zhang, C., Zhang, H., et al. (2019). Michael Addition/S,N-Intramolecular Rearrangement Sequence Enables Selective Fluorescence Detection of Cysteine and Homocysteine. *Anal. Chem.* 91 (16), 10894–10900. doi:10.1021/acs.analchem.9b02814

Ding, S., Hu, H., Yue, X., Feng, K., Gao, X., Dong, Q., et al. (2022). A Fluorescent Biosensor Based on Quantum Dot-Labeled Streptavidin and Poly-L-Lysine for the Rapid Detection of Salmonella in Milk. *J. Dairy Sci.* 105 (4), 2895–2907. doi:10.3168/jds.2021-21229

Donnelly, R. F., Morrow, D. I. J., McCarron, P. A., Juzenas, P., and Woolfson, A. D. (2006). Pharmaceutical Analysis of 5-aminolevulinic Acid in Solution and in Tissues. *J. Photochem. Photobiol. B Biol.* 82 (1), 59–71. doi:10.1016/j.jphotobiol.2005.08.007

Fujiwara, H., Takahara, N., Tateishi, K., Tanaka, M., Kanai, S., Kato, H., et al. (2020). 5-Aminolevulinic Acid-Mediated Photodynamic Activity in Patient-Derived Cholangiocarcinoma Organoids. *Surg. Oncol.* 35, 484–490. doi:10.1016/j.suronc.2020.10.011

Herrick, A. L., and McColl, K. E. L. (2005). Acute Intermittent Porphyria. *Best Pract. Res. Clin. Gastroenterology* 19 (2), 235–249. doi:10.1016/j.bpg.2004.10.006

Hijaz, F., and Killiny, N. (2016). A Gas Chromatography-Mass Spectrometry Method for the Determination of Delta-Aminolevulinic Acid in Plant Leaves. *J. Chromatogr. A* 1447, 57–63. doi:10.1016/j.chroma.2016.04.041

Huang, W., Liu, Q., Zhu, E.-Y., Shindi, A. A. F., and Li, Y.-Q. (2010). Rapid Simultaneous Determination of Protoporphyrin IX, Uroporphyrin III and Coproporphyrin III in Human Whole Blood by Non-linear Variable-Angle Synchronous Fluorescence Technique Coupled with Partial Least Squares. *Talanta* 82 (4), 1516–1520. doi:10.1016/j.talanta.2010.07.034

Jaramillo-Calle, D. A., Martinez, Y. A., Balwani, M., Fernandez, C., and Toro, M. (2021). Porphyria Attacks in Prepubertal Children and Adolescents. *Mol. Genet. Metabolism* 133 (3), 242–249. doi:10.1016/j.ymgme.2021.04.008

Kanto, U., Jutamanee, K., Osotsapar, Y., Chai-arree, W., Jintanawich, W., Promdang, S., et al. (2013). Quantification of 5-aminolevulinic Acid in Swine Manure Extract by HPLC-Fluorescence. *J. Liq. Chromatogr. Relat. Technol.* 36 (19), 2731–2748. doi:10.1080/10826076.2012.725693

Karuk Elmas, Ş. N., Arslan, F. N., Akin, G., Kenar, A., Janssen, H.-G., and Yilmaz, I. (2019). Synchronous Fluorescence Spectroscopy Combined with Chemometrics for Rapid Assessment of Cold-Pressed Grape Seed Oil Adulteration: Qualitative and Quantitative Study. *Talanta* 196, 22–31. doi:10.1016/j.talanta.2018.12.026

Killiny, N., Nehela, Y., Hijaz, F., Gonzalez-Blanco, P., Hajeri, S., and Gowda, S. (2020). Knock-down of δ-aminolevulinic Acid Dehydratase via Virus-Induced Gene Silencing Alters the microRNA Biogenesis and Causes Stress-Related Reactions in Citrus Plants. *Plant Sci.* 299, 110622. doi:10.1016/j.plantsci.2020.110622

Kumar, K. (2019). Application of Akaike Information Criterion Assisted Probabilistic Latent Semantic Analysis on Non-trilinear Total Synchronous Fluorescence Spectroscopic Data Sets: Automatizing Fluorescence Based Multicomponent Mixture Analysis. *Anal. Chim. Acta* 1062, 60–67. doi:10.1016/j.aca.2019.03.009

Lamon, J., With, T. K., and Redeker, A. G. (1974). The Hoesch Test: Bedside Screening for Urinary Porphobilinogen in Patients with Suspected Porphyria. *Clin. Chem.* 20 (11), 1438–1440. doi:10.1093/clinchem/20.11.1438

Lecrenier, M.-C., Baeten, V., Taira, A., and Abbas, O. (2018). Synchronous Fluorescence Spectroscopy for Detecting Blood Meal and Blood Products. *Talanta* 189, 166–173. doi:10.1016/j.talanta.2018.06.076

Li, Y. Q., Li, X. Y., Shindi, A. A. F., Zou, Z. X., Liu, Q., Lin, L. R., et al. (2010). "Synchronous Fluorescence Spectroscopy and its Applications in Clinical Analysis and Food Safety Evaluation," in *Reviews in Fluorescence 2010* (Berlin,Germany: Springer), 95

Lin, C. S.-Y., Lee, M.-J., Park, S. B., and Kiernan, M. C. (2011). Purple Pigments: The Pathophysiology of Acute Porphyric Neuropathy. *Clin. Neurophysiol.* 122 (12), 2336–2344. doi:10.1016/j.clinph.2011.07.036

Liu, Q., Huang, W., Shindi, A. A. F., and Li, Y.-Q. (2012). A Novel Rapid Method for Simultaneous Determination of Three Diagnostically Important Porphyrins in Erythrocytes Using Hyphenated Synchronous Fluorescence Techniques. *Talanta* 88, 663–668. doi:10.1016/j.talanta.2011.11.057

Liu, Y.-H., Wu, P.-P., Liu, Q., Luo, H.-D., Cao, S.-H., Lin, G.-C., et al. (2016). A Simple Fluorescence Spectroscopic Approach for Simultaneous and Rapid Detection of Four Polycyclic Aromatic Hydrocarbons (PAH4) in Vegetable Oils. *Food Anal. Methods* 9, 3209–3217. doi:10.1007/s12161-016-0515-5

Marver, H. S., Tschudy, D. P., Perlroth, M. G., Collins, A., and Hunter, G., Jr (1966). The Determination of Aminoketones in Biological Fluids. *Anal. Biochem.* 14, 53–60. doi:10.1016/0003-2697(66)90055-8

Mauzerall, D., and Granick, S. (1956). The Occurrence and Determination of Δ-Aminolevulinic Acid and Porphobilinogen in Urine. *J. Biol. Chem.* 219 (1), 435–446. doi:10.1016/s0021-9258(18)65809-0

Montgomery Bissell, D. (2015). "The Porphyrias," in *Rosenberg's Molecular and Genetic Basis of Neurological and Psychiatric Disease* (Netherlands: Elsevier), 731–749. doi:10.1016/b978-0-12-410529-4.00066-8

Oishi, H., Nomiyama, H., Nomiyama, K., and Tomokuni, K. (1996). Fluorometric HPLC Determination of Δ-Aminolevulinic Acid (ALA) in the Plasma and Urine of Lead Workers: Biological Indicators of Lead Exposure. *J. Anal. Toxicol.* 20 (2), 106–110. doi:10.1093/jat/20.2.106

Ou-Yang, J., Li, Y., Jiang, W.-L., He, S.-Y., Liu, H.-W., and Li, C.-Y. (2018). Fluorescence-Guided Cancer Diagnosis and Surgery by a Zero Cross-Talk Ratiometric Near-Infrared γ-Glutamyltranspeptidase Fluorescent Probe. *Anal. Chem.* 91 (1), 1056–1063. doi:10.1021/acs.analchem.8b04416

Ouyang, X., Wang, S.-Y., Liu, T., Ren, Y.-A., Wang, M.-F., Chen, F.-F., et al. (2019). Functional Modulation of Cytochrome C upon Specific Binding to DNA Nanoribbons. *Chem. Commun.* 55 (93), 14074–14077. doi:10.1039/c9cc05427h

Pierach, C. A., Cardinal, R., Bossenmaier, I., and Watson, C. J. (1977). Comparison of the Hoesch and the Watson-Schwartz Tests for Urinary Porphobilinogen. *Clin. Chem.* 23 (9), 1666–1668. doi:10.1093/clinchem/23.9.1666

Pulgarín, J. A. M., Bermejo, L. F. G., and Rodríguez, S. B. (2014). Matrix Isopotential Synchronous Fluorescence Spectrometry for the Determination of Gibberellic Acid in Watermelon after Ultraviolet-Irradiation. *RSC Adv.* 4 (11), 5671

Pulgarín, J. M., and Molina, A. (1994). Determination of Nafcillin and Methicillin by Different Spectrofluorimetric Techniques. *Talanta* 41 (1), 21–30.

Pulgarín, J. M., and Molina, A. (1993). FTOTAL, A Program to Process Total Luminescence Spectra. *Comput. Chem.* 17 (4), 341

Remolina, M. C. R., Li, Z., and Peleato, N. M. (2022). Application of Machine Learning Methods for Rapid Fluorescence-Based Detection of Naphthenic Acids and Phenol in Natural Surface Waters. *J. Hazard. Mater.* 430, 128491. doi:10.1016/j.jhazmat.2022.128491

Samokhvalov, A. (2020). Analysis of Various Solid Samples by Synchronous Fluorescence Spectroscopy and Related Methods: A Review. *Talanta* 216, 120944. doi:10.1016/j.talanta.2020.120944

Shindi, A. A. F., Zhou, P.-C., Zou, Z.-X., and Li, Y.-Q. (2010). A Novel, Selective, and Rapid Fluorimetric Method for the Simultaneous Analysis of Coproporphyrin and Uroporphyrin in Urine. *Anal. Chim. Acta* 664 (1), 89–94. doi:10.1016/j.aca.2010.01.062

Tomokuni, K., Ichiba, M., and Hirai, Y. (1992). Measurement of Urinary Delta-Aminolevulinic Acid (ALA) by Fluorometric HPLC and Colorimetric Methods. *Ind. Health* 30 (3-4), 119–128. doi:10.2486/indhealth.30.119

Tsumura, S., Enoki, T., and Ooyama, Y. (2018). A Colorimetric and Fluorescent Sensor for Water in Acetonitrile Based on Intramolecular Charge Transfer: D-(π-A)2-type Pyridine-Boron Trifluoride Complex. *Chem. Commun.* 54 (72), 10144–10147. doi:10.1039/c8cc06257a

van 't Klooster, C. C., Uil, J. J., van der Leeuw, J., Eppens, E. F., and Marczinski, S. C. (2017). Unusual Cause of Abdominal Pain and Anemia. *Clin. Chem.* 63 (12), 1806–1809. doi:10.1373/clinchem.2016.267823

Wang, M., Ateia, M., Hatano, Y., Miyanaga, K., and Yoshimura, C. (2022). Novel Fluorescence-Based Method for Rapid Quantification of Live Bacteria in River Water and Treated Wastewater. *Environ. Sci. Adv.* 10, 1039. doi:10.1039/d1va00017a

Watson, C. J., and Schwartz, S. (1941). A Simple Test for Urinary Porphobilinogen. *Exp. Biol. Med.* 47 (2), 393–394. doi:10.3181/00379727-47-13152p

Wu, C., Sui, W., and Li, Y. (1999). FPATH, a Program to Design the Optimum Scanning Route for Non-linear Variable-Angle Synchronous Fluorescence. *Chem. J. Chin. Univ.* 20, 422.

Zhai, Y.-Y., Liu, Q., Cai, W.-P., Cao, S.-H., Zhang, L.-X., and Li, Y.-Q. (2020). Metallic Nanofilm Enhanced Fluorescence Cell Imaging: A Study of Distance-Dependent Intensity and Lifetime by Optical Sectioning Microscopy. *J. Phys. Chem. B* 124 (14), 2760–2768. doi:10.1021/acs.jpcb.9b11390

Zhang, J., Yasuda, M., Desnick, R. J., Balwani, M., Bishop, D., and Yu, C. (2011). A LC-MS/MS Method for the Specific, Sensitive, and Simultaneous Quantification of 5-aminolevulinic Acid and Porphobilinogen. *J. Chromatogr. B* 879 (24), 2389–2396. doi:10.1016/j.jchromb.2011.06.034

Zhao, Y., Liu, Y.-H., Cao, S.-H., Ajmal, M., Zhai, Y.-Y., Pan, X.-H., et al. (2020). Excitation-Emission Synchronization-Mediated Directional Fluorescence: Insight into Plasmon-Coupled Emission at Vibrational Resolution. *J. Phys. Chem. Lett.* 11 (7), 2701–2707. doi:10.1021/acs.jpclett.0c00403

Conflict of Interest: The authors declare that the research was conducted in the absence of any commercial or financial relationships that could be construed as a potential conflict of interest.

frontiers | Frontiers in Chemistry

ORIGINAL RESEARCH
published: 06 July 2022
doi: 10.3389/fchem.2022.932985

Novel Synthesis of Sensitive Cu-ZnO Nanorod–Based Sensor for Hydrogen Peroxide Sensing

Muhammad Arsalan[1,2], Imram Saddique[3]*, Miao Baoji[1]*, Azka Awais[1], Ilyas Khan[4], Mohamed A. Shamseldin[5] and Sadok Mehrez[6,7]

[1]Henan International Joint Laboratory of Nano-Photoelectric Magnetic Materials, Henan University of Technology, Zhengzhou, China, [2]Office of Research Innovation and Commercialization, University of Management and Technology, Lahore, Pakistan, [3]Department of Mathematics, University of Management and Technology, Lahore, Pakistan, [4]Department of Mathematics, College of Science Al-Zulfi, Majmaah University, Al-Majmaah, Saudi Arabia, [5]Mechanical Engineering, Faculty of Engineering and Technology, Future University in Egypt, New Cairo, Egypt, [6]Department of Mechanical Engineering, College of Engineering at Al Kharj, Prince Sattam Bin Abdulaziz University, Al Kharj, Saudi Arabia, [7]Department of Mechanical Engineering, University of Tunis El Manar, ENIT, Tunis, Tunisia

We aimed to synthesize sensitive electrochemical sensors for hydrogen peroxide sensing by using zinc oxide nanorods grown on a fluorine-doped tin oxide electrode by using the facial hydrothermal method. It was essential to keep the surface morphology of the material (nanorods structure); due to its large surface area, the concerned material has enhanced detection ability toward the analyte. The work presents a non-enzymatic H_2O_2 sensor using vertically grown zinc oxide nanorods on the electrode (FTO) surfaces with Cu nanoparticles deposited on zinc oxide nanorods to enhance the activity. Scanning electron microscopy (SEM), X-ray photoelectron spectroscopy (XPS), energy-dispersive X-Ray (EDX), X-ray diffraction (XRD), and electrochemical methods were used to characterize copper–zinc oxide nanorods. In addition to the high surface area, the hexagonal Cu-ZnO nanorods exhibited enhanced electrochemical features of H_2O_2 oxidation. Nanorods made from Cu-ZnO exhibit highly efficient sensitivity of 3415 $\mu AmM^{-1}cm^{-2}$ low detection limits (LODs) of 0.16 μM and extremely wide linear ranges (0.001–11 mM). In addition, copper-zinc oxide nanorods demonstrated decent reproducibility, repeatability, stability, and selectivity after being used for H_2O_2 sensing in water samples with an RSD value of 3.83%. Cu nanoparticles decorated on ZnO nanorods demonstrate excellent potential for the detection of hydrogen peroxide, providing a new way to prepare hydrogen peroxide detecting devices.

Keywords: hydrothermal method, Cu-ZnO nanorods, electrochemical sensor, H_2O_2 detection, sensing

OPEN ACCESS

Edited by:
Muhammad Asif,
Wuhan Institute of Technology, China

Reviewed by:
Dolat Khan,
King Mongkut's University of Technology Thonburi, Thailand
Tayyaba Iftikhar,
Huazhong University of Science and Technology, China

****Correspondence:***
Imram Saddique
imransmsrazi@gmail.com
Miao Baoji
mbjhaut@163.com

Specialty section:
This article was submitted to Nanoscience, a section of the journal Frontiers in Chemistry

Received: *30 April 2022*
Accepted: *26 May 2022*
Published: *06 July 2022*

Citation:
Arsalan M, Saddique I, Baoji M, Awais A, Khan I, Shamseldin MA and Mehrez S (2022) Novel Synthesis of Sensitive Cu-ZnO Nanorod–Based Sensor for Hydrogen Peroxide Sensing. Front. Chem. 10:932985. doi: 10.3389/fchem.2022.932985

INTRODUCTION

Hydrogen peroxide (H_2O_2), a reactive oxygen species (ROS) formed by biological processes, is an important biomolecule found in environmental and biological systems and has been used in a wide range of fields such as green energy (fuel cells), medicine (Asif et al., 2022a), food industry, and environmental protection (Chen et al., 2018). In contrast, several studies have indicated that excessive concentrations of H_2O_2 adversely affect the body's normal physiological functions and can cause several diseases in a living organism, such as cardiovascular disease, Alzheimer's, Parkinson's, tumors, and cancer (Arsalan et al., 2020; Wu et al., 2020). It is, therefore, vital for

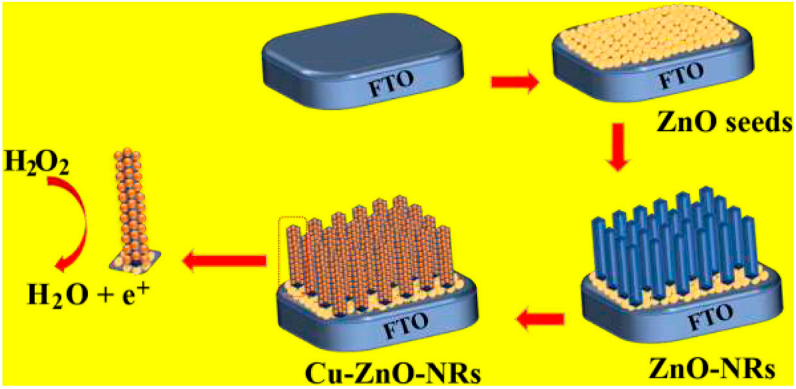

SCHEME 1 | Synthesis and manufacturing of zinc oxide nanorods on the electrode surface, followed by the deposition of Cu nanoparticles for hydrogen peroxide detection, are depicted schematically.

both industrial and academic purposes to be able to quickly, easily, and reliably carry out determination of H_2O_2 (Arsalan et al., 2021a). The detection of H_2O_2 has been accomplished by a number of analytical techniques, including titrometers, spectrophotometers, fluorescence, phosphorescence, chromatographies, and electrochemical techniques (Li et al., 2016; Waqas et al., 2022). The electrochemical technique is a superior alternative to the other methods because of its inherent sensitivity, wide detection range, rapid response, low cost, and good selectivity (Lin et al., 2010; Aziz et al., 2022a). Materials with metal-oxide properties have proven to be effective in the field of electrochemical sensing (Arsalan et al., 2019; Sooppy Nisar et al., 2019; Awais et al., 2021a; Arsalan et al., 2021b). There are many metal oxides with good performance in the biosensor and chemical sensor fields, including tin oxide, tungsten oxide, copper oxide, titanium dioxide, magnesium oxide, cuprous oxide, and zinc oxide (ZnO) (Khan et al., 2019; Awais et al., 2021b; Awais et al., 2021c; Khan et al., 2022). ZnO is an excellent candidate for applications in such environments due to its good catalytic efficiency, biocompatibility, chemical stability, and nontoxicity. In the past few years, ZnO nanostructures have been used in biosensors to detect urate, glucose, and phenolic compounds.

Electrochemical hydrogen peroxide sensors can be split into two classes based on the electrocatalyst utilized as sensor electrodes. The first group uses non-enzymatic electrocatalysts, while the second group uses enzymes, such as GDH and GOx (Zhang et al., 2012). Enzyme-based hydrogen peroxide sensors were first created by Leland C. Clark, also known as the "Father of Biosensors" (Drmosh et al., 2019). Enzyme-based sensors for hydrogen peroxide exhibit high sensitivity, selectivity, and a low detection limit. The operating temperature, relative humidity, and pH value, on the other hand, have a significant impact on the stability of enzyme-based hydrogen peroxide sensors (Asif et al., 2017). Furthermore, these sensors have a higher fabrication cost than non-enzyme–based hydrogen peroxide sensors. Due to the aforementioned limitations associated with enzyme-based hydrogen peroxide sensors, many attempts have been undertaken to produce non-enzymatic hydrogen peroxide sensors. As with enzyme-based sensors, the mechanism of sensing hydrogen peroxide non-enzymatically is entirely different from that of enzyme-based sensors, where electrocatalysts must fulfill several important criteria, including high electrocatalytic activity, large specific surfaces, strong conductivity, efficient electron transport from electrocatalysts to conductive substrates, stability, and repeatability (Khan et al., 2018; Aziz et al., 2022b). The noble metals (Au, Pd, and Pt) and their composites have been investigated as hydrogen peroxide sensor materials (Zhou et al., 2016; Jiao et al., 2017). Although noble metals are useful as hydrogen peroxide sensors, their high cost limits their practical application (Iftikhar et al., 2021). Many metal oxides have been investigated for their potential in fabrication and hydrogen peroxide sensor applications, including Co_3O_4, SnO_2, Ag_2O, Fe_2O_3, MnO_2, NiOx, Cu_2O, CoOx, and CuOx (Palanisamy et al., 2012; Xie et al., 2013; Bhati et al., 2018; Wang et al., 2018). Due to its abundance in nature, low fabrication costs, and favorable electrochemical and catalytic properties, ZnO is considered the best metal oxide for hydrogen peroxide sensors. Zinc oxide has been intensively explored due to its intriguing features, in addition to electrochemical sensors, photoelectric devices, gas sensors, and lithium-ion batteries (Ding et al., 2018). As a result of the superior catalytic properties of zinc oxide nanostructures compared to those of other metal oxide nanostructures, manufacture of low-cost hydrogen peroxide sensors based on ZnO nanostructures grown on conducting copper foil is possible (Asif et al., 2022b). Nanocombs, nanorods, nanotubes, and nanodisks, among all zinc oxide nanostructures, have more adsorption sites and a more significant surface area than nanoparticles and nanolayers. Recent research has focused on improving the electron transfer rate of ZnO nanostructures and the analyte sensing capability of the catalyst. Modifying ZnO nanostructures with Pt, Co, Ni, etc., nanoparticles increases their catalysis efficiency (Shen et al., 2020). In the preparation of active materials for sensors, several tedious steps must be completed, mostly by synthesizing nanomaterials individually and coating

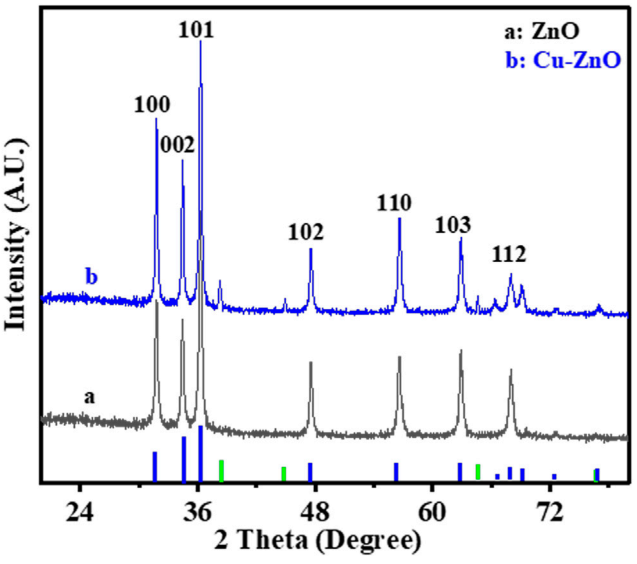

FIGURE 1 | XRD spectral analysis of Cu-modified zinc oxide nanorods before (a) and after (b) deposition of Cu nanoparticles.

them on electrode surfaces. The reduction of active sites of the manufactured nanocomposite, spin coating, or drop-casting of the material on electrodes diminish electrocatalytic activity, resulting in low reproducibility and stability of the prepared electrode. As a result, high-performance nanostructures must be prepared by growing directly on the concerned electrode. This strategy will enhance the speed of electron transfer.

Thus, we present a facile chemical method of obtaining Cu-doped ZnO nanorods by modifying the electrode surface. The electrode was constructed and electrochemically analyzed in detail to obtain a large specific surface area, good electrical conductivity, and self-support structure to allow catalytic activities. As a result of this current investigation, the electrochemical sensor prepared expresses high electro-analytical performance and can be used as a sensing material for the next generation of sensors.

Using hydrothermal methods, we grew ZnO nanorods directly on FTO electrodes at low temperatures to identify an easy and feasible way of connecting nanoparticles to electrodes. In order to boost hydrogen peroxide sensing electrochemical activity, we prepared ZnO nanorods/FTO surfaces and deposited Cu nanoparticles on them (with larger surface areas and more active sites). Electrochemical activity for hydrogen peroxide sensing was increased as a result of the electron transfer. The morphological characterization of the copper–zinc oxide nanorods confirms that the Cu nanoparticles are attached to the zinc oxide nanorods in a uniform manner. With excellent stability, selectivity, repeatability, and reproducibility, Cu–ZnO nanorods exhibited excellent electrochemical results for hydrogen peroxide sensing. In addition, the modified electrochemical sensor yielded superior results for hydrogen peroxide detection in tap water and industrial water samples.

EXPERIMENTAL RESULTS

Chemicals

Zinc acetate dihydrate ($C_4H_6O_4Zn.2H_2O$, 99%), zinc nitrate hexahydrate [Zn $(NO_3)_2.6H_2O$, 98%], copper nitrate [Cu $(NO_3)_2$], hexamethylenetetramine ($C_6H_{12}N_4$, 99%), ethanol (98%), hydrogen peroxide (H_2O_2), fluorine doped Tin-oxide (FTO), acetone (98%), alanine (Ala), dopamine (DA), citric acid (CA), penicillamine (Pen), glycine (Gly), ascorbic acid (AA), uric acid (UA), valine (Val), phenylalanine (Phe), and fructose, all analytical grade reagents, were purchased from Aladdin. The reagents were used in the analysis without any further purification. For the preparation of all solutions, deionized distilled water (18 MΩ cm) was used. The 0.1 mol/L PBS (pH = 7.0) electrolyte was used in all the experiments.

Apparatus

Special instruments are used for morphological and chemical characterization. Scanning electron microscopy (SEM) measurements were taken with the JEOL, Japan (JSM-6390) and PHI-500 and Ulvac-Phi were used to perform X-ray photoelectron spectroscopy (XPS) (Japan). X-ray diffraction (XRD) measurements were taken with the D/MAX-3C (Japan), DPV (differential pulse voltammetry), EIS (electrochemical impedance spectroscopy), and CV (cyclic voltammetry), measurements were taken with the electrochemical work station (Gamry Reference 3000, Japan). As a working electrode, fluorine-doped tin-oxide (electrode area = 0.50 cm^2 (active area = 0.30 cm^2) was used. Pt wire was used as a counter electrode, and for the reference electrode, Ag/AgCl was used in the conventional three-electrode system.

Modification of the Sensor

For the preparation of the sensor, FTO electrodes (geometric area = 0.50 cm^2) were cleaned three times with an acetone-ethanol solution and then dried. Following the cleaning of the electrode surface, an insulating layer was placed, with only 0.30 cm^2 of the electrode surface remaining uninsulated for modification and electrocatalytic activities. The working area can be adjusted using this insulating layer, as stated in the literature (Baruah et al., 2021). The ultra-thin layer of zinc oxide seeds (45–55 nm) on the electrode surface was deposited using an optimal procedure that included soaking the electrode (FTO) surface with zinc acetate dihydrate (0.005 M) solution, washing it with methanol, and drying it with Ar gas. The process is performed four to six times for preparing uniform seed growth on the electrode surface. The zinc acetate substance put on the electrode was then heated for 15 min at 300 (˚C) degrees Celsius. The method is repeated two more times to ensure that the ZnO seeds are deposited in a uniform layer on the electrode surface. Hydrothermal ZnO nanorod development was achieved after uniformly coating ZnO seeds. The electrode was suspended inversely in a glass dish with a standard mixture of a fixed concentration of hexamethylenetetramine (0.06 M) and zinc nitrate dihydrate (0.04 M) at a fixed 90˚C temperature for 2.5 h. When the reaction was finished, the zinc oxide

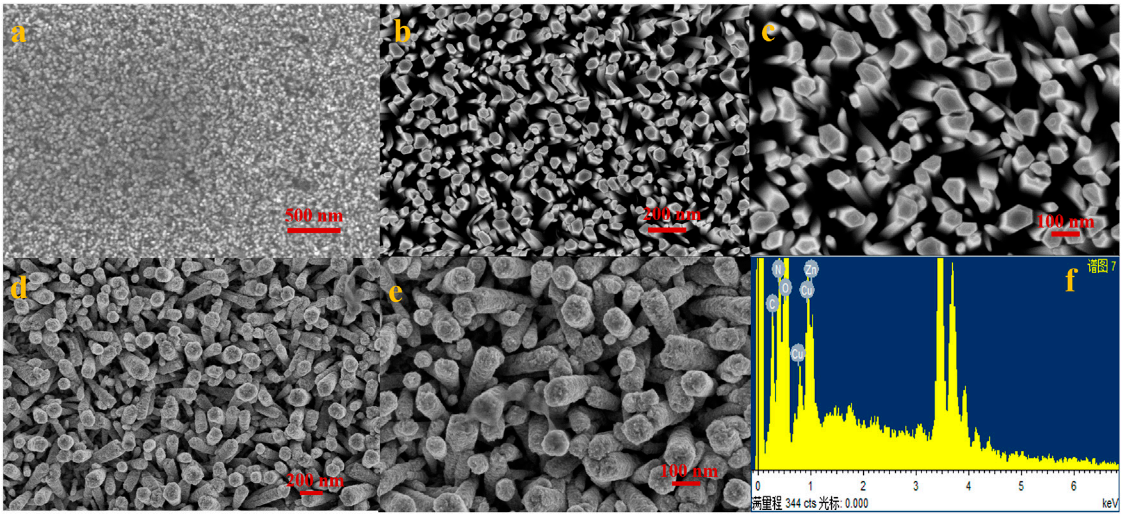

FIGURE 2 | (A) Uniformly distributed ZnO nanoseeds on the substrate; **(B,C)** show the vertically developed zinc oxide nanorods on the concerned electrode surface; **(D,E)** shows the SEM images of fabricated copper-zinc oxide nanorods at low and high resolution; and **(F)** shows the EDS spectral analysis of copper–zinc oxide nanorods.

nanorods generated on the specific electrode were cleaned to eradicate any impurities. The Cu nanoparticles were deposited on the ZnO nanorods grown in a prepared solution of 15 ml deionized distilled water, 0.5 ml methanol (as a reducing agent), and 0.03 g/ml of $[Cu(NO_3)_2]$. The mixture was transferred to an autoclave after 30 min outside and kept at 120°C for 80 min. The electrode was thoroughly cleaned with distilled water and absolute ethanol after the reaction was completed and allowed to cool to room temperature.

Scheme 1 depicted the preparation and manufacturing of Cu–ZnO nanorods. We demonstrate the production and modification of an effective hydrogen peroxide sensor by hydrothermally growing zinc oxide nanorods directly on the concerned FTO electrode. The excellent hydrogen peroxide sensing results were obtained by depositing Cu nanoparticles on zinc oxide nanorods with enhanced surface area.

RESULTS AND DISCUSSION

Physical and Chemical Characterization

EIS, EDS, XPS, XRD, and SEM were used to characterize the morphology of the prepared and modified electrodes. **Figure 1** depicts the zinc oxide nanostructure or morphology before and after the deposition of Cu nanoparticles. The XRD spectral analysis of manufactured zinc oxide nanorods before and after the synthesis of Cu nanoparticles is shown in **Figure 1**. The various peaks of zinc oxide nanorods indicated the hexagonal form of the nanorods. The Cu-ZnO nanorod spectra were also expressed after the modification with Cu nanoparticles, displaying all of the diffraction peaks and extra peaks of corresponding Cu nanoparticles. The hexagonal form of the prepared material was demonstrated by corresponding peaks at (100°), (101°), (102°), (103°), (002°), (110°), and (112°) planes, as indicated in literature (Kelly et al., 2019). The maximum peak intensity for the (101°) plane was measured at $2\theta = 36.2°$, with further peaks confirming the hexagonal form. **Figure 1** shows the blue and green peaks, representing ZnO and Cu nanoparticles, respectively.

Figure 2 shows the results of SEM analysis of the manufactured electrode (A–E). **Figure 2A** shows an SEM image of ZnO nanoseeds that were equally scattered across the electrode surface. The zinc oxide nanorods were vertically generated and uniformly spread across the substrate's surface, as shown in **Figures 2B,C**. The modified Cu-ZnO nanorods are shown in low- and high-resolution SEM images in **Figures 2D,E**. The Cu-Zn oxide nanorod rough surface was noticed when compared to the smooth surface of ZnO nanorods due to the production of Cu nanoparticles. Cu-ZnO nanorods had a diameter of about 100–150 nm. **Figure 2F**, which included the EDS analysis, was used to determine the composition of Cu-ZnO nanorods. EDS spectral analysis reveals the chemical composition of Cu, Zn, and O components in Cu-ZnO nanorods.

XPS analysis was used to further characterize the chemical properties of Cu-ZnO nanorods and ZnO nanorods, as shown in **Figure 3**. **Figure 3A** shows a comparison of the entire XPS spectra of ZnO nanorods and Cu-ZnO nanorods. The whole scan reveals the presence of zinc, carbon, and oxygen atoms in zinc oxide nanorods. In contrast, the spectra of Cu-ZnO nanorods corroborated the presence of Cu, Zn, C, and O elements, indicating that Cu nanoparticles were successfully modified on ZnO nanorods. **Figure 3B** shows an expanded XPS spectrum of O 1s, which reveals a peak at 532.1 eV with a slightly higher binding capacity due to the modification of the surface of zinc oxide with copper (Al-Dairy et al., 2021). The Zn 2p peaks in Cu-ZnO nanorods were discovered to be at 1043.9 and 1021.2 eV, respectively, matching the Zn $2p_{3/2}$ and Zn $2p_{1/2}$, suggesting that the Zn valence state is 2^+ (Kelly et al., 2019; Mishra et al.,

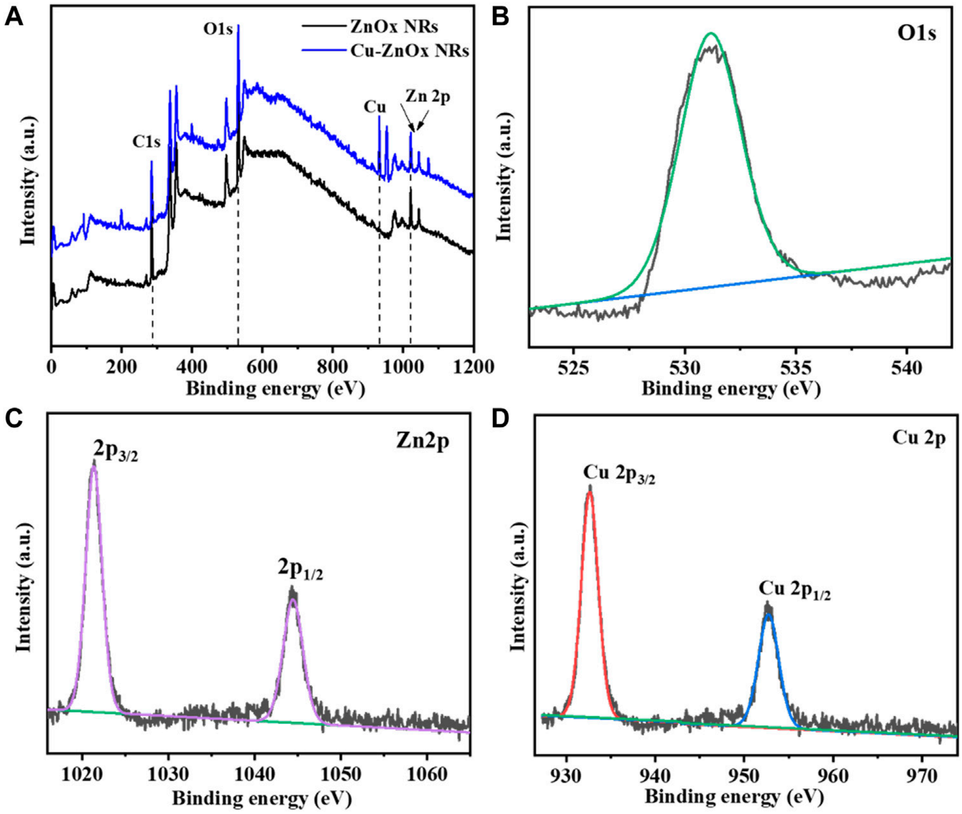

FIGURE 3 | (A) Compare the XPS spectra of Cu-ZnO nanorods to the spectra of ZnO nanorods. It was also reported that the simplified peaks for oxygen **(B)** O1s, **(C)** zinc Zn 2p, and deposited material Cu 2p **(D)** elements with their magnified spectra were also mentioned.

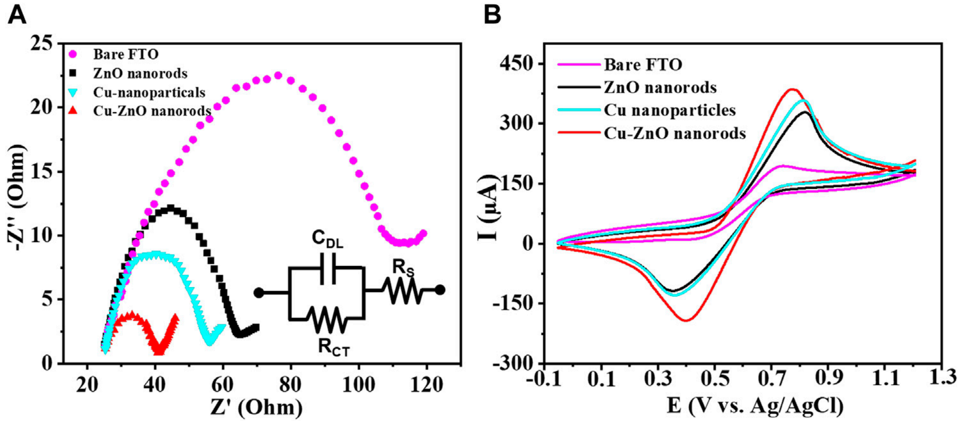

FIGURE 4 | (A) Resistance capacity of Cu-ZnO nanorods, zinc oxide nanorods, Cu nanoparticles, and blank FTO, was best described by plotting Nyquist semicircle in standard 0.1 mol/L KCl containing a 0.1 M K_4 [Fe(CN)$_6$] and K_3 [Fe(CN)$_6$] solution. **(B)** CV results of blank FTO with further modified electrodes zinc oxide nanorods, Cu nanoparticles, and Cu-ZnO nanorods were mentioned in standard KCl containing K_4 [Fe(CN)$_6$] and K_3 [Fe(CN)$_6$] solution.

2019). As illustrated in **Figure 3**, the addition of copper nanoparticles or fabrication of copper on zinc oxide nanorods results in binding energy shifts of 932.5 and 952.3 eV for Cu $2p_{3/2}$ and $2p_{1/2}$, respectively (d). It was also shown that when compared to bulk Cu (953 eV), Cu $2p_{3/2}$ had a binding energy shift of 0.51 eV (Awais et al., 2021a; Fariba Beigmoradi and Hadi Beitollahi, 2021). The binding energy shifting in the negative direction was observed due to electron transfer from zinc oxide to

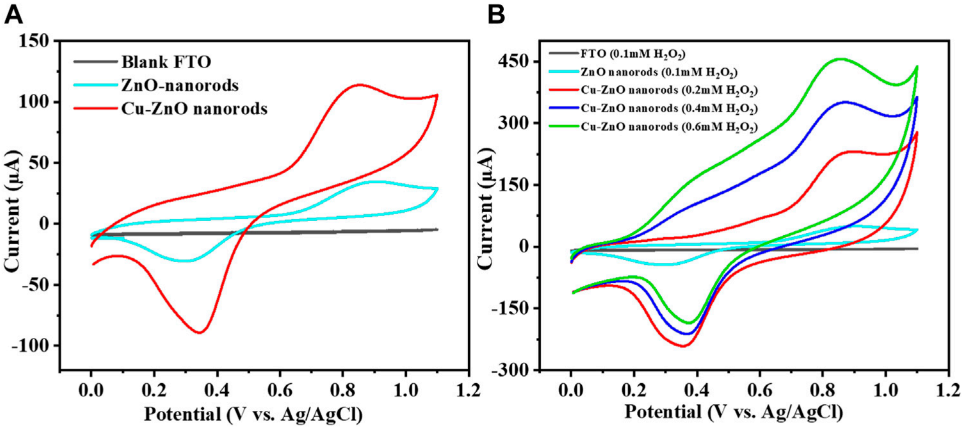

FIGURE 5 | (A) Expressed that at a fixed scan rate of 50 mVs^{-1}, and the CV curve of zinc oxide nanorods, Cu-ZnO NRs, and blank FTO in 0.1 mol/L phosphate buffer containing 0.2 mM hydrogen peroxide was mentioned. **(B)** Shows the various hydrogen peroxide concentrations, the CV curves of blank FTO, zinc oxide nanorods, and produced Cu-ZnO nanorods are compared.

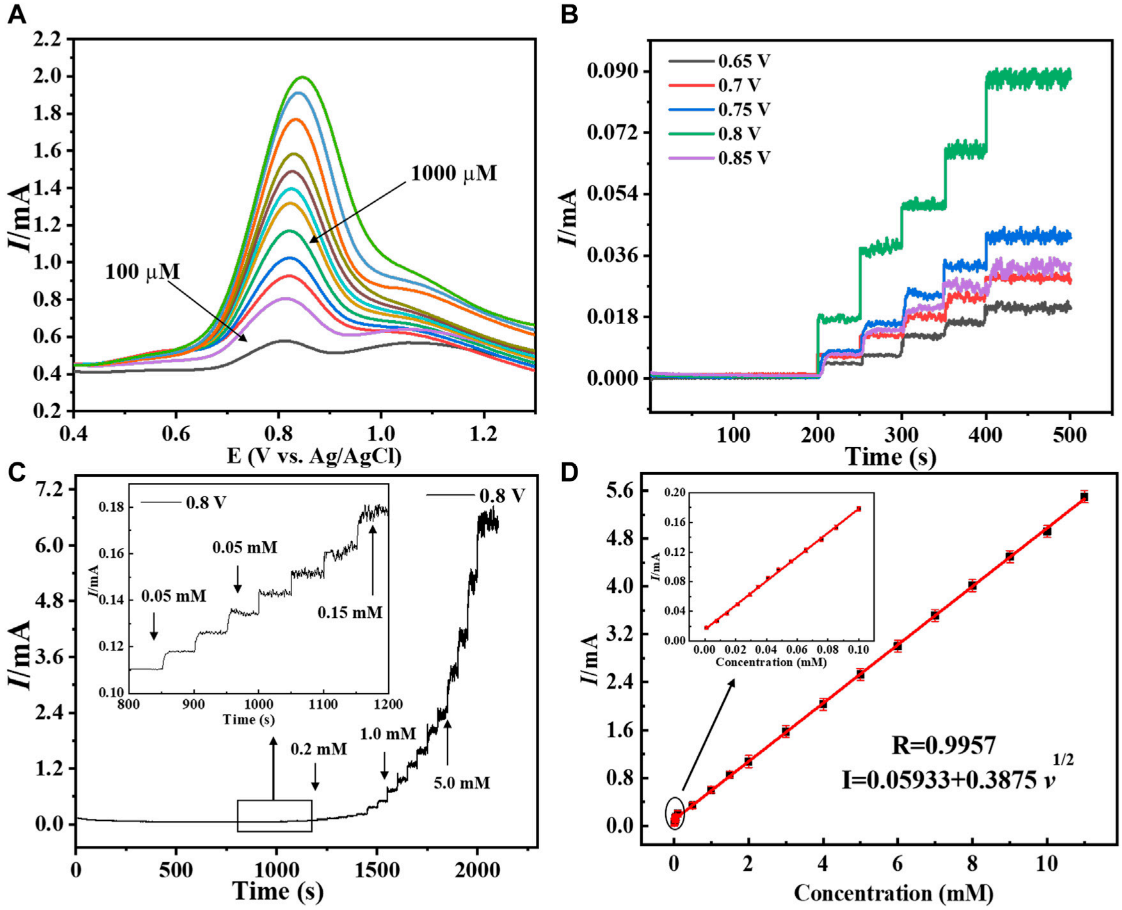

FIGURE 6 | (A) Depicted the DPV graph of Cu-ZnO nanorods at various hydrogen peroxide concentrations. **(B)** Amperometric response of copper-zinc oxide nanorods in 0.1 mol/L phosphate electrolyte with varied potentials ranging from (0.65–0.85 V) was discussed. The I-T graph of Cu-ZnO nanorods, with various hydrogen peroxide concentrations, is shown at a specific potential of +0.8 V **(C)**. The insert shows a magnified I-T graph of Cu-ZnO nanorods. For Cu-ZnO nanorods, the corresponding linear graph of current vs. hydrogen peroxide concentration is displayed in **(D)**. Insert mentioned the magnified linear graph.

copper, which could have been produced by the intensive attraction of copper nanoparticles with zinc oxide (Chen et al., 2018).

Electrochemical Studies

Some analysis was carried out to better understand the electrochemical characteristics of the produced nanostructure. **Figure 4A** expressed the EIS spectral analysis of each electrode in standard potassium chloride solution containing K_4 [Fe $(CN)_6$] and K_3 [Fe $(CN)_6$] solution (for blank FTO, zinc oxide nanorods, Cu nanoparticles, and Cu-ZnO nanorods). The impedance findings were evaluated using the Rct values (as mentioned in the insert of **Figure 4A**). The Rct value of blank FTO (purple color) is the highest, with a value of Rct = 92, compared to ZnO nanorods (black color) with Rct = 40.5 and copper nanoparticles (light blue color) with Rct = 32.7. When compared to bare FTO, the Rct values reduced, indicating an enhanced electron transfer rate. We used prepared ZnO nanorods with Cu nanoparticle deposition in order to select the more competent electrode. The Rct value was further decreased after copper nanoparticle modification on ZnO nanorods, and Cu-ZnO nanorods (red color) exhibit low resistance when compared to all other electrodes, with Rct = 15.8. The fabricated copper–zinc oxide nanorod electrode exhibits the lowest resistance rate for electron transfer when related to other modified electrodes. For the additional electrochemical study, a Cu-ZnO nanorod electrode was used. In 0.1 mol/L KCl solution containing 0.1 mol/L K_3 [Fe $(CN)_6$]/K_4 [Fe $(CN)_6$], cyclic voltammetry analysis was conducted to investigate the electrochemical reaction of blank FTO with different modified electrodes such as zinc oxide nanorods, Cu nanoparticles, and Cu–ZnO nanorods. **Figure 4B** illustrates the current responses for oxidation peaks determined from cyclic voltammetry analysis for blank FTO, zinc oxide nanorods, Cu nanoparticles, and Cu–ZnO nanorod electrodes. The Cu–ZnO nanorod electrode had the largest redox peak current, while other ZnO nanorods, Cu nanoparticles, and blank FTO electrodes had less current value. When modified ZnO nanorod, Cu nanoparticle, and Cu-ZnO nanorod electrode comparison was carried out in CV experiments, the blank FTO had the lowest redox potential current. From the CV study, it was concluded that Cu-ZnO nanorods were a good contender for detecting the analyte in the study.

The simplest and most suitable method to investigate the electrochemical performance is the cyclic voltammetry method. CV results of different electrodes were analyzed in an electrochemical cell with specific potential ranges from 0 to +1.15 V to select the best potential electrode. **Figure 5A** shows the CV results at a fixed scan rate of 50 mVs^{-1} of produced Cu–ZnO nanorods in 0.1 mol/L phosphate buffer electrolyte containing 0.2 mM hydrogen peroxide. Fabricated Cu–ZnO nanorods were shown to have good current activity. As compared to CVs of various electrodes in 0.2 mM, hydrogen peroxide was also conducted, demonstrating a higher oxidation current. As shown in **Figure 5B**, the modified Cu–ZnO nanorods have outstanding catalytic properties when compared to those of blank FTO and zinc oxide nanorods. Modified Cu-ZnO nanorods exhibited a well-defined oxidation peak at +0.8 V in 0.2 mM hydrogen peroxide. The results of fabricated Cu-ZnO nanorods suggested that the electrode might be used for hydrogen peroxide electro-oxidation. **Figure 5B** clearly shows that as the hydrogen peroxide concentration rises, the current increases as well, indicating that the electrode has potential for detecting hydrogen peroxide. **Supplementary Figure S1** depicted a schematic example of hydrogen peroxide sensing. In the absence and presence of 0.2 mM hydrogen peroxide, CV measurements of a fabricated copper–zinc oxide nanorod electrode in 0.1 mol/L phosphate electrolyte at various scan speeds from 20 to 200 mVs^{-1} were mentioned (**Supplementary Figures S1A,B**). The current response increased in the presence of hydrogen peroxide, indicating the catalytic activity of the fabricated material, according to CV data.

Detection Results of Modified Cu-ZnO Nanorod Electrode

The modified electrode’s for hydrogen peroxide sensing activity was tested in order to exhibit analytical parameters such as linear range, response time, detection limit, and sensitivity. **Figure 6A**, shows the sensing performance of the prepared electrode to evaluate its sensing activity using DPV. It was discovered that as the concentration increased, the current increased as well, implying that the fabricated copper–zinc oxide nanorod catalyst is suited for hydrogen peroxide sensing. In addition, as indicated in the literature (Hu et al., 2022), amperometric studies with modified Cu-ZnO nanorods were conducted at various potential ranges between +0.65 and +0.85 V to evaluate the suitable potential for hydrogen peroxide detection. With continued addition of standard hydrogen peroxide concentrations, at a fixed scan rate of 50 mVs^{-1}, the amperometric response in 0.1 mol/L phosphate electrolyte was evaluated at various applied potentials. **Figure 6B** demonstrates that when compared to other applied potentials, the Cu-ZnO nanorods were chosen for long-term current-time study because it has the highest potential at +0.8 V. The Randles–Sevcik equation was used to calculate the active surface area of the sensing electrode, and the CV technique is used to investigate it in a deoxidized mixture containing standard potassium chloride solution containing K_4 [Fe $(CN)_6$] and K_3 [Fe $(CN)_6$] solution, at various scan rates, as shown in **Supplementary Figure S2**. The active surface areas of ZnO nanorods (0.328 cm^2), Cu nanoparticles (0.319 cm^2), and Cu-ZnO nanorods (0.369 cm^2) were observed. After carefully observing the surface area, the optimum pH of the electrolyte was also obtained for better sensing activity. To evaluate the optimum pH of the electrolyte, the amperometric analysis was conducted at a fixed scan rate of 50 mVs^{-1} in 0.1 mol/L PBS (at different pH) electrolyte at a fixed current of +0.8 V, and their linear graph is expressed in **Supplementary Figure S3**. The linear graph of different pH values from pH 6.0 to pH 8.0 was mentioned. The results show that the optimum pH of the electrolyte which shows maximum current or sensitivity is at pH 7.0. So, pH 7.0 is considered optimum pH for concerning materials and is used in all amperometric analyses.

TABLE 1 | Comparison of different electrodes for hydrogen peroxide sensing.

Electrode	Sensitivity ($\mu A\ mM^{-1}\ cm^{-2}$)	Linear range (mM)	Lower detection limit (μM)	Reference
CuO nanofibers	431.3	0.006–2.5	0.8	Hussain et al. (2016)
ZnO composite	2961.7	Up to 8.45	0.4	Kannadasan et al. (2014)
CuO nanosphere	404.53	0–2.55	1	Li et al. (2019)
ZnO nanocombs	1533	0.02–4.5	20	Rashed et al. (2021)
GOD/ZnO	30	0.001–0.76	0.7	Al-Hardan et al. (2016)
ZnO-Ag	3.85	0.015–6.5	1.5	Shahkhatuni et al. (2019)
ZnO-Ni	61.78	0.5–8	2.5	Xu et al. (2020)
ZnO-Co	13.3	0–4	20	Xie et al. (2013)
ZnO nanocrystal	1091.1	0.6–1.4	0.22	Zang et al. (2007)
Cu-ZnO nanorods	3415	0.001–11	0.16	This work

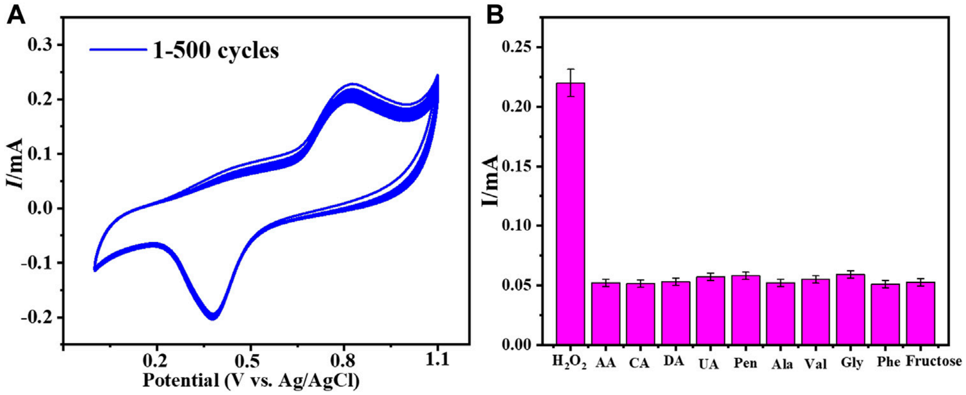

FIGURE 7 | (A) Cu-ZnO nanorod stability was evaluated for 500 cycles in 0.2 mM hydrogen peroxide in phosphate electrolyte at a fixed scan rate of 50 mVs^{-1}. **(B)** Anti-interference results for all probable interfering compounds such as fructose, Phe, Ala, Gly, Val, DA, CA, UA, AA, and Pen were expressed.

The long I-T analysis was conducted at a fixed scan rate of 50 mVs^{-1} in 0.1 mol/L PBS (pH = 7.0) electrolyte at a fixed current of +0.8 V. The current response developed slowly at lower concentrations but rapidly at higher concentrations, as shown in **Figure 6C**. The linear range of 0.001–11 mM of Cu-ZnO nanorod modified electrode for hydrogen peroxide sensing was observed. For comparison, the current-time responses of Cu nanoparticles@FTO and ZnO nanorods@FTO electrodes were also examined. According to the findings, Cu-ZnO nanorods have substantially higher responsiveness than other electrodes. The enlarged current response of all electrodes at lower concentrations is shown in the insert. With increasing concentration, the current response increases linearly. The amperometric studies for linearity for hydrogen peroxide current vs. concentration are shown in **Figure 6D**. The limit of detection was found to be 0.16 M, and the coefficient of correlation (R_2) value was observed to be $R_2 = 0.9957$. Furthermore, the current was shown to increase linearly with the increase in hydrogen peroxide concentration from 0.001 to 11 mM. The hydrogen peroxide detection sensitivity of a modified Cu-ZnO nanorod electrode was measured to be 3415 $\mu AmM^{-1}cm^{-2}$ as mentioned in **Table 1**. In **Table 1**, we compare the detecting activity of our modified Cu-ZnO nanorod electrode to that of various previously published hydrogen peroxide electrodes. **Table 1** demonstrates that the fabricated Cu-ZnO nanorods have a significantly higher sensing activity of 3415 $\mu AmM^{-1}cm^{-2}$ than previously reported electrodes and a lower LOD and a much wider linear range. The Cu-ZnO nanorod sensor that was prepared has a large linear range and a good reaction time. Chronoamperometry was used to determine the reaction time of the manufactured electrode. The chronoamperogram revealed that Cu-ZnO nanorods have a good reaction time. The reaction time of Cu-ZnO nanorods was 1.49 s, which is decent when compared to that of previous sensors. In addition, our fabricated electrode performed better in terms of sensing since it was grown directly on ZnO nanorods with a larger surface area for Cu deposition. The modified Cu-ZnO nanorod electrode showed a high electron transfer rate in an electrochemical method for hydrogen peroxide oxidation. The use of a hydrothermal approach to modify a non-enzymatic sensor results in an outstanding nanostructure with a cost-effective, stable, and larger surface area for hydrogen peroxide sensor modification.

Reproducibility, Reusability, Anti-Interference Activity, and Stability

The fabricated electrode's reusability and repeatability were assessed in order to assess its performance. To assess the performance of Cu–ZnO nanorods, a reproducibility and

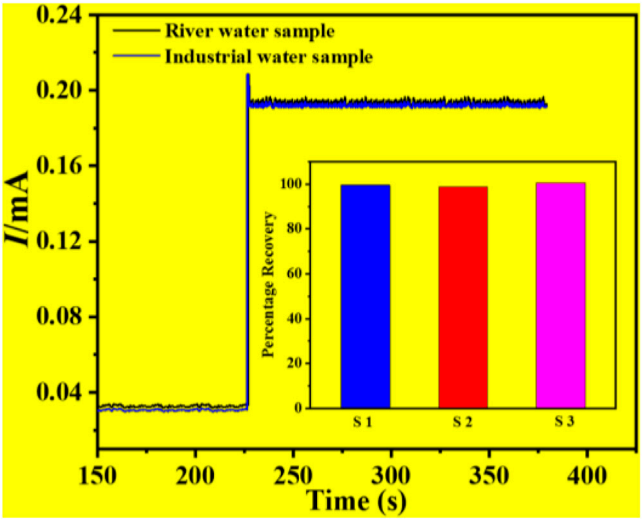

FIGURE 8 | Percentage of recovery results in an actual water sample test of a water sample and an industrial water sample, with a histogram graph was mentioned.

reusability test was carried out on ten samples, each of which contained the same amount of hydrogen peroxide. The CV response was evaluated in 0.1 mol L^{-1} PBS (pH = 7.0) vs. Ag/AgCl at a fixed scan rate of 50 mVs^{-1}. After numerous uses, the produced electrode retains up to 98.2 percent of its sensing ability; this indicates that the produced electrode is repeatable and reusable. The RSD was estimated to be approximately 3.83 %. CV analysis responding in 0.2 mM hydrogen peroxide at a fixed scan rate of 50 mVs^{-1} in phosphate buffer was used to examine the stability of fabricated Cu-ZnO nanorods. The stability graph of Cu-ZnO nanorods during 500 cycles is shown in **Figure 7A**. The electrode's stability is improved by nanorods generated directly on the electrode surface. The long-term durability of the manufactured electrode was also examined after 15 days, and there were few changes; as illustrated in **Supplementary Figure S4**, the modified electrode remained stable for a long time. The ability to distinguish between the target analyte and interfering species with similar electrocatalytic activity is one of the most significant analytical skills of electrochemical sensors. Major interferences which can impact hydrogen peroxide sensing include fructose, citric acid (CA), ascorbic acid (AA), dopamine (DA), and uric acid (UA). The anti-interference ability of the fabricated electrode for hydrogen peroxide detection was tested using aline (Val), fructose, alanine (Ala), citric acid (CA), phenylalanine (Phe), glycine (Gly), ascorbic acid (AA), dopamine (DA), uric acid (UA), and penicillamine (Pen). The amperometric response was evaluated at a fixed scan rate of 50 mVs^{-1} in the presence of 0.2 mM hydrogen peroxide in 0.1 mol/L phosphate electrolyte, by adding 0.1 mM of each interfering chemical. **Figure 7B** shows the result of those interfering substances as a graphical form. Fabricated Cu-ZnO nanorods results expressed that it has no obvious response to all other interfering substances, showing excellent selectivity for amperometric hydrogen peroxide detection. Due to the nature of the material, the Cu-ZnO nanorods display extremely few interferences at relatively high potential.

Hydrogen Peroxide Detection in Water Samples

Some studies were carried out in order to determine the use of the constructed Cu-ZnO nanorod electrode for hydrogen peroxide detection. The I-T graphical result of Cu-ZnO nanorods was obtained by adding 2 ml of the water sample or industrial water sample into 8 ml of 0.1 mol/L phosphate at a fixed current of +0.8 V as shown in **Figure 8**. The results of water samples were compared and mentioned. The findings of many samples were gathered and displayed in a histogram graph in **Figure 8**. When compared to analytically measured values, the results demonstrated that hydrogen peroxide detection in water samples was excellent, having various kinds of substances present in the water sample (Bhati et al., 2018), and the water sample has a 2.5 percent lower detection activity for hydrogen peroxide. The findings suggested that the manufactured Cu-ZnO nanorod sensor might be used in real-environment water samples.

CONCLUSION

Finally, vertically growing copper–zinc oxide nanorods on the electrode surface were successfully constructed for excellent hydrogen peroxide detection. Physiochemical and electrochemical approaches were used to characterize the Cu–ZnO nanorods. The hexagonal Cu–ZnO nanorods had a large surface area and excellent electrochemical properties for hydrogen peroxide detection. The non-enzymatic electrochemical sensor that was created has a large linear range, a low detection limit, strong selectivity, and a good response toward hydrogen peroxide. The reaction time, stability, repeatability, and reproducibility of the Cu–ZnO nanorods were all excellent. Furthermore, the hydrogen peroxide sensing activity in a real water sample demonstrated the sensor's excellent results with a recovery percentage of 98%. The fabricated copper–zinc oxide nanorod electrode outperformed ZnO nanorods, copper nanoparticles, and other electrodes in terms of electrochemical performance. The manufactured Cu-ZnO nanorods proved to be a viable candidate for hydrogen peroxide sensing in the actual world with excellent real-environment detection of the concerned analyte.

DATA AVAILABILITY STATEMENT

The original contributions presented in the study are included in the article/**Supplementary Material**; further inquiries can be directed to the corresponding authors.

AUTHOR CONTRIBUTIONS

Conceptualization, MA, MB, AA, and IK; methodology, IS, IK, MS, and SM; investigation, SM and IK; writing—original draft preparation, MA and AA; writing—review and editing, IS; validation, MS; funding acquisition, MS and SM; resources, MB and AA; supervision, IS and MB. All authors have read and agreed to the published version of the manuscript.

REFERENCES

Al-Dairy, A. R., Albiss, B., and Jaradat, A. A. (2021). Computational Modeling of ZnO-NRs and Graphene Nanostructure as a Glucose Biosensor. *Sens. Imaging* 22 (1), 1–13. doi:10.1007/s11220-021-00353-3

Al-Hardan, N., Abdul Hamid, M., Shamsudin, R., Othman, N., and Kar Keng, L. (2016). Amperometric Non-enzymatic Hydrogen Peroxide Sensor Based on Aligned Zinc Oxide Nanorods. *Sensors* 16 (7), 1004. doi:10.3390/s16071004

Arsalan, M., Awais, A., Chen, T., Sheng, Q., and Zheng, J. (2019). Development of PANI/BN-based Absorbents for Water Remediation. *Water Qual. Res. J.* 54 (4), 290–298. doi:10.2166/wqrj.2019.048

Arsalan, M., Awais, A., Qiao, X., Sheng, Q., and Zheng, J. (2020). Preparation and Comparison of Colloid Based Ni50Co50(OH)2/BOX Electrocatalyst for Catalysis and High Performance Nonenzymatic Glucose Sensor. *Microchem. J.* 159, 105486. doi:10.1016/j.microc.2020.105486

Arsalan, M., Babar, N.-U. -A., Sadiqa, A., Mansha, S., Baig, N., Nisar, L., et al. (2021). Surface-assembled Fe-Oxide Colloidal Nanoparticles for High Performance Electrocatalytic Water Oxidation. *Int. J. Hydrogen Energy* 46 (7), 5207–5222. doi:10.1016/j.ijhydene.2020.11.035

Arsalan, M., Qiao, X., Awais, A., Wang, Y., Yang, S., Sheng, Q., et al. (2021). Enhanced Sensitive Electrochemical Sensor for Simultaneous Catechol and Hydroquinone Detection by Using Ultrasmall Ternary Pt-based Nanomaterial. *Electroanalysis* 33 (6), 1528–1538. doi:10.1002/elan.202100026

Asif, M., Aziz, A., Ashraf, G., Iftikhar, T., Sun, Y., and Liu, H. (2022). Turning the Page: Advancing Detection Platforms for Sulfate Reducing Bacteria and Their Perks. *Chem. Rec.* 22 (1), e202100166. doi:10.1002/tcr.202100166

Asif, M., Aziz, A., Ashraf, G., Iftikhar, T., Sun, Y., Xiao, F., et al. (2022). Unveiling Microbiologically Influenced Corrosion Engineering to Transfigure Damages into Benefits: A Textile Sensor for H2O2 Detection in Clinical Cancer Tissues. *Chem. Eng. J.* 427, 131398. doi:10.1016/j.cej.2021.131398

Asif, M., Liu, H., Aziz, A., Wang, H., Wang, Z., Ajmal, M., et al. (2017). Core-shell Iron Oxide-Layered Double Hydroxide: High Electrochemical Sensing Performance of H 2 O 2 Biomarker in Live Cancer Cells with Plasma Therapeutics. *Biosens. Bioelectron.* 97, 352–359. doi:10.1016/j.bios.2017.05.057

Awais, A., Arsalan, M., Qiao, X., Yahui, W., Sheng, Q., Yue, T., et al. (2021). Facial Synthesis of Highly Efficient Non-enzymatic Glucose Sensor Based on Vertically Aligned Au-ZnO NRs. *J. Electroanal. Chem.* 895, 115424. doi:10.1016/j.jelechem.2021.115424

Awais, A., Arsalan, M., Sheng, Q., and Yue, T. (2021). A Non-enzymatic Hydrogen Peroxide Sensor with Enhanced Sensitivity Based on Pt Nanoparticles. *Anal. Sci.* 37 (10), 1419–1426. doi:10.2116/analsci.20p456

Awais, A., Arsalan, M., Sheng, Q., Zheng, J., and Yue, T. (2021). Rational Design of Highly Efficient One-pot Synthesis of Ternary PtNiCo/FTO Nanocatalyst for Hydroquinone and Catechol Sensing. *Electroanalysis* 33 (1), 170–180. doi:10.1002/elan.202060166

Aziz, A., Asif, M., Ashraf, G., Iftikhar, T., Ajmal, M., Liu, H., et al. (2022). Showcasing Advanced Electrocatalytic Behavior of Layered Double Hydroxide Wrapped on Carbon Nanotubes: Real-Time Monitoring of L-Cysteine in Biological Matrices. *Chem. Eng. J.* 440, 135985. doi:10.1016/j.cej.2022.135985

Aziz, A., Asif, M., Ashraf, G., Iftikhar, T., Hu, J., Xiao, F., et al. (2022). Boosting Electrocatalytic Activity of Carbon Fiber@fusiform-like Copper-Nickel LDHs: Sensing of Nitrate as Biomarker for NOB Detection. *J. Hazard. Mater.* 422, 126907. doi:10.1016/j.jhazmat.2021.126907

Baruah, S., Maibam, B., Borah, C. K., Agarkar, T., Kumar, A., and Kumar, S. (2021). A Highly Receptive ZnO-Based Enzymatic Electrochemical Sensor for Glucose Sensing. *IEEE Sensors J.* 21 (13), 14601–14608. doi:10.1109/jsen.2021.3069303

Bhati, V. S., Ranwa, S., Fanetti, M., Valant, M., and Kumar, M. (2018). Efficient Hydrogen Sensor Based on Ni-Doped ZnO Nanostructures by RF Sputtering. *Sensors Actuators B Chem.* 255, 588–597. doi:10.1016/j.snb.2017.08.106

Chen, L., Xu, X., Cui, F., Qiu, Q., Chen, X., and Xu, J. (2018). Au Nanoparticles-ZnO Composite Nanotubes Using Natural Silk Fibroin Fiber as Template for Electrochemical Non-enzymatic Sensing of Hydrogen Peroxide. *Anal. Biochem.* 554, 1–8. doi:10.1016/j.ab.2018.05.020

Ding, H., Zhang, L., Tang, Z., Dong, Y., and Chu, X. (2018). Black Phosphorus Quantum Dots Doped ZnO Nanoparticles as Efficient Electrode Materials for Sensitive Hydrogen Peroxide Detection. *J. Electroanal. Chem.* 824, 161–168. doi:10.1016/j.jelechem.2018.07.055

Drmosh, Q. A., Yamani, Z. H., Hendi, A. H., Gondal, M. A., Moqbel, R. A., Saleh, T. A., et al. (2019). A Novel Approach to Fabricating a Ternary rGO/ZnO/Pt System for High-Performance Hydrogen Sensor at Low Operating Temperatures. *Appl. Surf. Sci.* 464, 616–626. doi:10.1016/j.apsusc.2018.09.128

Fariba Beigmoradi, B., and Hadi Beitollahi, B. (2021). MXene/La3+ Doped ZnO/Hb Nanocomposite Modified Glassy Carbon Electrode as Novel Voltammetric Sensor for Determination of Hydrogen Peroxide. *Surf. Engin. Appl.Electrochem.* 57 (6), 708–714. doi:10.3103/s106837552106003x

Hu, X., Liu, J., Jin, H., Huang, F., Wang, Z., Wang, F., et al. (2022). Ultrasensitive Determination of Intracellular Hydrogen Peroxide by Equipping Quantum Dots with a Sensing Layer via Self-Passivation. *Nano Res.* 15 (5), 4350–4356. doi:10.1007/s12274-022-4099-7

Hussain, M., Sun, H., Karim, S., Nisar, A., Khan, M., ul Haq, A., et al. (2016). Noble Metal Nanoparticle-Functionalized ZnO Nanoflowers for Photocatalytic Degradation of RhB Dye and Electrochemical Sensing of Hydrogen Peroxide. *J. Nanoparticle Res.* 18 (4), 1–14. doi:10.1007/s11051-016-3397-y

Iftikhar, T., Asif, M., Aziz, A., Ashraf, G., Jun, S., Li, G., et al. (2021). Topical Advances in Nanomaterials Based Electrochemical Sensors for Resorcinol Detection. *Trends Environ. Anal. Chem.* 31, e00138. doi:10.1016/j.teac.2021.e00138

Jiao, M., Van Duy, N., Chien, N. V., Hoa, N. D., Van Hieu, N., Hjort, K., et al. (2017). On-chip Growth of Patterned ZnO Nanorod Sensors with PdO Decoration for Enhancement of Hydrogen-Sensing Performance. *Int. J. Hydrogen Energy* 42 (25), 16294–16304. doi:10.1016/j.ijhydene.2017.05.135

Kannadasan, N., Shanmugam, N., Sathishkumar, K., Cholan, S., Poonguzhali, R., and Viruthagiri, G. (2014). Synthesis of Ce4+ Ions Doped ZnO Electrode as a Sensor for Hydrogen Peroxide. *J. Mater Sci. Mater Electron* 25 (11), 5137–5143. doi:10.1007/s10854-014-2283-6

Kelly, S. R., Shi, X., Back, S., Vallez, L., Park, S. Y., Siahrostami, S., et al. (2019). ZnO as an Active and Selective Catalyst for Electrochemical Water Oxidation to Hydrogen Peroxide. *ACS Catal.* 9 (5), 4593–4599. doi:10.1021/acscatal.8b04873

Khan, A., Khan, D., Khan, I., Ali, F., Karim, F. U., and Imran, M. (2018). MHD Flow of Sodium Alginate-Based Casson Type Nanofluid Passing through a Porous Medium with Newtonian Heating. *Sci. Rep.* 8 (1), 8645–8712. doi:10.1038/s41598-018-26994-1

Khan, A., Khan, D., Khan, I., Ali, F., Karim, F. u., and Nisar, K. S. (2019). MHD Flow of Brinkman Type H_2O-Cu, Ag, TiO_2 and Al_2O_3 Nanofluids with Chemical Reaction and Heat Generation Effects in a Porous Medium. *Jmag* 24 (2), 262–270. doi:10.4283/jmag.2019.24.2.262

Khan, D., Kumam, P., Watthayu, W., and Khan, I. (2022). Heat Transfer Enhancement and Entropy Generation of Two Working Fluids of MHD Flow with Titanium Alloy Nanoparticle in Darcy Medium. *J. Therm. Analysis Calorim.*, 1–12. doi:10.1007/s10973-022-11284-w

Li, W., Wu, X., Han, N., Chen, J., Tang, W., and Chen, Y. (2016). Core-shell Au@ZnO Nanoparticles Derived from Au@MOF and Their Sub-ppm Level Acetone Gas-Sensing Performance. *Powder Technol.* 304, 241–247. doi:10.1016/j.powtec.2016.08.028

SUPPLEMENTARY MATERIAL

The Supplementary Material for this article can be found online at: https://www.frontiersin.org/articles/10.3389/fchem.2022.932985/full#supplementary-material

Li, X., Zhu, G., Dou, J., Yang, J., Ge, Y., and Liu, J. (2019). Electrospun Au Nanoparticle-Containing ZnO Nanofiber for Non-enzyme H2O2 Sensor. *Ionics* 25 (11), 5527–5536. doi:10.1007/s11581-019-03118-x

Lin, C.-Y., Lai, Y.-H., Balamurugan, A., Vittal, R., Lin, C.-W., and Ho, K.-C. (2010). Electrode Modified with a Composite Film of ZnO Nanorods and Ag Nanoparticles as a Sensor for Hydrogen Peroxide. *Talanta* 82 (1), 340–347. doi:10.1016/j.talanta.2010.04.047

Mishra, A. K., Mukherjee, B., Kumar, A., Jarwal, D. K., Ratan, S., Kumar, C., et al. (2019). Superficial Fabrication of Gold Nanoparticles Modified CuO Nanowires Electrode for Non-enzymatic Glucose Detection. *RSC Adv.* 9 (4), 1772–1781. doi:10.1039/c8ra07516f

Palanisamy, S., Chen, S.-M., and Sarawathi, R. (2012). A Novel Nonenzymatic Hydrogen Peroxide Sensor Based on Reduced Graphene oxide/ZnO Composite Modified Electrode. *Sensors Actuators B Chem.* 166-167, 372–377. doi:10.1016/j.snb.2012.02.075

Rashed, M. A., Faisal, M., Harraz, F. A., Jalalah, M., Alsaiari, M., and Alsareii, S. A. (2021). A Highly Efficient Nonenzymatic Hydrogen Peroxide Electrochemical Sensor Using Mesoporous Carbon Doped ZnO Nanocomposite. *J. Electrochem. Soc.* 168 (2), 027512. doi:10.1149/1945-7111/abe44b

Shahkhatuni, G. H., Aroutiounian, V. M., Arakelyan, V. M., Aleksanyan, M. S., and Shahnazaryan, G. E. (2019). Investigation of Sensor Made of ZnO:La for Detection of Hydrogen Peroxide Vapours by Impedance Spectroscopy Method. *J. Contemp. Phys.* 54 (2), 188–195. doi:10.3103/s1068337219020117

Shen, C.-L., Zheng, G.-S., Wu, M.-Y., Wei, J.-Y., Lou, Q., Ye, Y.-L., et al. (2020). Chemiluminescent Carbon Nanodots as Sensors for Hydrogen Peroxide and Glucose. *Nanophotonics* 9 (11), 3597–3604. doi:10.1515/nanoph-2020-0233

Sooppy Nisar, K., Khan, D., Khan, A., Khan, W. A., Khan, I., and Aldawsari, A. M. (2019). Entropy Generation and Heat Transfer in Drilling Nanoliquids with Clay Nanoparticles. *Entropy* 21 (12), 1226. doi:10.3390/e21121226

Wang, L., Wu, T., Wu, H., Zhong, J., Wang, N., and Wang, R. (2018). A Novel Non-enzymatic Hydrogen Peroxide Sensor Based on Co:ZnO Modified Electrodes. *Prog. Nat. Sci. Mater. Int.* 28 (1), 24–27. doi:10.1016/j.pnsc.2017.12.001

Waqas, M., Liu, C., Huang, Q., Zhang, X., Fan, Y., Jiang, Z., et al. (2022). Zn2+ Induced Self-Assembled Fabrication of Marigold-like ZnO microflower@ Ni(OH)2 Three-Dimensional Nanosheets for Nonenzymatic Glucose Sensing. *Electrochimica Acta* 410, 140040. doi:10.1016/j.electacta.2022.140040

Wu, H., Chung, H. Y., Tsang, D. C. W., Huang, N. M., Xie, Z., Lim, H. N., et al. (2020). Scavenger-free and Self-Powered Photocathodic Sensing System for Aqueous Hydrogen Peroxide Monitoring by CuO/ZnO Nanostructure. *Chem. Eng. Sci.* 226, 115886. doi:10.1016/j.ces.2020.115886

Xie, L., Xu, Y., and Cao, X. (2013). Hydrogen Peroxide Biosensor Based on Hemoglobin Immobilized at Graphene, Flower-like Zinc Oxide, and Gold Nanoparticles Nanocomposite Modified Glassy Carbon Electrode. *Colloids Surfaces B Biointerfaces* 107, 245–250. doi:10.1016/j.colsurfb.2013.02.020

Xu, H., Wei, Z., Verpoort, F., Hu, J., and Zhuiykov, S. (2020). Nanoscale Au-ZnO Heterostructure Developed by Atomic Layer Deposition towards Amperometric H2O2 Detection. *Nanoscale Res. Lett.* 15 (1), 41. doi:10.1186/s11671-020-3273-7

Zang, J., Li, C. M., Cui, X., Wang, J., Sun, X., Dong, H., et al. (2007). Tailoring Zinc Oxide Nanowires for High Performance Amperometric Glucose Sensor. *Electroanalysis* 19 (9), 1008–1014. doi:10.1002/elan.200603808

Zhang, W., Xie, G., Li, S., Lu, L., and Liu, B. (2012). Au/CeO2-chitosan Composite Film for Hydrogen Peroxide Sensing. *Appl. Surf. Sci.* 258 (20), 8222–8227. doi:10.1016/j.apsusc.2012.05.025

Zhou, F., Jing, W., Shi, J., Jiang, Z., Cheng, Y., and Gao, K. (2016). Effects of Etching Parameters on ZnO Nanotubes Evolved from Hydrothermally Synthesized ZnO Nanorods. *Ceram. Int.* 42 (4), 4788–4796. doi:10.1016/j.ceramint.2015.11.164

Conflict of Interest: The authors declare that the research was conducted in the absence of any commercial or financial relationships that could be construed as a potential conflict of interest.

The reviewer DK declared a past co-authorship with the author IK to the handling editor.

frontiers | Frontiers in Chemistry

TYPE Editorial
PUBLISHED 06 September 2022
DOI 10.3389/fchem.2022.992793

OPEN ACCESS

EDITED AND REVIEWED BY
Parikshit Sahatiya,
Birla Institute of Technology and
Science, India

*CORRESPONDENCE
Muhammad Asif,
asif83chemist@gmail.com
Fei Xiao,
xiaofei@hust.edu.cn
Yimin Sun,
ymsun@wit.edu.cn

SPECIALTY SECTION
This article was submitted to
Nanoscience,
a section of the journal
Frontiers in Chemistry

RECEIVED 13 July 2022
ACCEPTED 21 July 2022
PUBLISHED 06 September 2022

CITATION
Asif M, Xiao F, Govindasamy M and Sun Y
(2022), 2D Nanoarchitectures
for Sensing/Biosensing Applications.
Front. Chem. 10:992793.
doi: 10.3389/fchem.2022.992793

2D Nanoarchitectures for Sensing/Biosensing Applications

Muhammad Asif[1]*, Fei Xiao[2]*, Mani Govindasamy[3] and Yimin Sun[1]*

[1]Hubei Key Laboratory of Plasma Chemistry and Advanced Materials, School of Materials Science and Engineering, Wuhan Institute of Technology, Wuhan, China, [2]Key Laboratory of Material Chemistry for Energy Conversion and Storage, Ministry of Education, School of Chemistry and Chemical Engineering, Huazhong University of Science & Technology, Wuhan, China, [3]Department of Materials Engineering, Ming-Chi University of Technology, New Taipei City, Taiwan

KEYWORDS

sensors, biosensors, 2D nanomaterials, pollutants, biomolecules, point-of-care

Editorial on the Research Topic
2D Nanoarchitectures for Sensing/Biosensing Applications

In analytical chemistry, sensing and biosensing are among the most important research areas for carrying out the analysis of a number of target analytes (Hermawan et al., 2021). The growing number of analytes that can be detected using various approaches, along with the large number of sensing platforms that produce analytically beneficial outcomes, highlight the significance of sensing techniques (Asif et al., 2018). Sensing and biosensing techniques are regarded as highly sensitive, specific, and capable of multitasking as shown in Graphical abstract (Zhang et al., 2020).

In comparison to other nanomaterials, 2D nanostructures exhibit encouraging application potential for the *in vitro* detection of small biological molecules, neurotransmitters, and proteins, which in turn are used as biomarkers. These nanostructures are cost-effective and easy to synthesize, and they offer rapid response times in terms of the screening and monitoring of various disorders, including potentially fatal cancers (Iftikhar et al., 2021). They also play a role in improving the sensitivity, selectivity, and stability of the sensing platforms (Aziz et al., 2019). Moreover, 2D nanoarchitectures, when coupled with emerging types of nanostructures and advanced nanotechnology, not only improve sensing capabilities for the real-time detection of gases, pollutants, and small biomolecules but also help these technologies execute *in vitro* and *in vivo* diagnosis (Dral and Johan, 2018). The introduction of point-of-care testing devices, in particular, has revolutionized sensing systems. These devices offer portability, flexibility, non-invasiveness (Asamoah et al., 2021), low cost, time-effectiveness, improved sampling frequency, and implantability (Xu et al., 2019). Meanwhile, trials involving the wireless transmission of analytical data to medical centers for processing have been successful, while the development of ready-to-use and

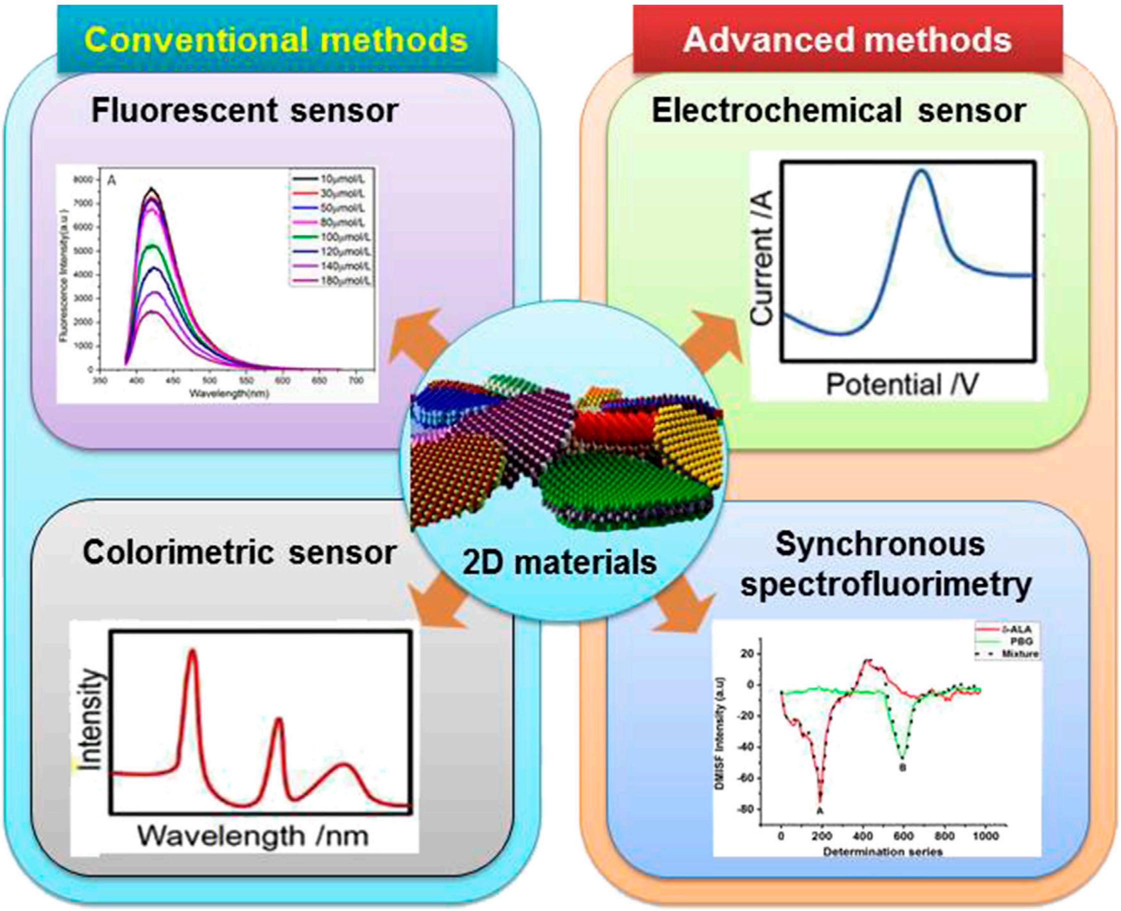

GRAPHICAL ABSTRACT
Schematic illustration of 2D materials based sensors for the detection of various analytes.

reusable sensors continues to lag behind due to the complexity and high cost of these devices (Asif et al., 2021).

In short, the research field is quite broad, which makes it a bit difficult to represent all the exciting developments in sensing platforms explored in these articles. This Research Topic covers a total of eleven articles, ten of which represent original research and one of which is a review. All articles were contributed by experts in the sensing and biosensing field.

To date, a great deal of effort has been devoted to improving the efficiency and biocompatibility of sensors. In this regard, Wang et al. successfully fabricated a composite material through the polymerization of indole-5-carboxylic acid into poly-5-carboxyindole nanostructures (PI-5-CA), which were further hybridized with carboxylated single-walled carbon nanotubes (C-SWCNTs). The electrode modified with PI-5-CA/C-SWCNTs was used as an electrochemical immunosensor to detect *E. coli* O157:H7, demonstrating a wide linear concentration range of 2.98×10^1 to 2.98×10^7 CFU/ml and a limit of detection (LOD) of 2.5 CFU/ml. Interestingly, the sensor was also used to detect bacteria in water specimens, with decent accuracy.

Colorimetric assays are considered quick and easy to use because they involve a color change phenomenon (Asif et al., 2020). Zhang et al. have developed a rapid and highly sensitive colorimetric method for the detection of L-Histidine (L-His) that uses Cu^{2+} ions, which inhibit the oxidation of the 3,3′,5,5′-tetramethylbenzidine (TMB)-H_2O_2 system. The as-constructed sensor showed two linear concentration ranges of 60 nM–1 μM and 1 μM–1 mM, with a LOD of 50 nM, and proved to be efficient for the detection of L-His in urine samples.

Wang et al. fabricated fluorescent copper-based nanoarchitectures of 5–6 nm in size and employed them as sensors for the detection of NO_2^- and temperature. The copper nanomaterials produced fluorescence, which was selectively quenched by nitrite ions. The intensity of the fluorescence also correlated well with temperatures ranging between 20 and 60°C. These nanomaterials are good enough to be used in nanothermometers, devices that, with their high degree of sensitivity and specificity, are considered necessary for, e.g., the detection of dissolved gases in oil, and therefore capable of, e.g., diagnosing faults in power transformers. Keeping this in mind, HYPERLINK Jia et al. constructed a gas sensor based on an Ag_3-$HfSe_2$ monolayer for the detection of C_2H_4 and CO molecules and explored their mechanisms and adsorption behaviors. The adsorption effect on C_2H_4 was greater than that on CO. The electrical sensitivity of C_2H_4 was found to increase up to 55.49% after adsorption, a phenomenon known as chemisorption. This sensor has the potential to efficiently monitor the working status of power transformers.

Tang et al. prepared MnO_2 nanosheets with glutathione (GSH) to detect Cu^{2+} ions using a simple colorimetric assay. The fabricated sensor exhibited a wide linearity range of 10–300 nM, with an LOD of 6.9 nM, and demonstrated superb anti-interference capability in Cu^{2+} detection from tap water samples. The sensor performed efficiently without any additional H_2O_2 or complicated modification processes.

Furthermore, Wu et al. developed a fluorescence sensor for the detection of Bi^{3+} ions. The authors prepared glutathione-protected non-noble transition metal copper nanoparticles (GSH-CuNPs) that carried out their sensing applications via aggregation-induced luminescence. Mechanistically, the fluorescence of the CuNPs was inhibited upon the addition of Bi^{3+} ions. The fabricated sensor was simple, fast, and selective, displaying a linearity range of 0 mmol/L–100 mmol/L, with an LOD of 10 mmol/L. HYPERLINK Ajmal et al.presented a two-step approach, based on derivative matrix-isopotential synchronous fluorescence spectrometry (DMISFS) and the Hantzsch reaction, for the rapid, reliable, and simultaneous detection of δ-aminolevulinic acid (δ-ALA) and porphobilinogen (PBG) in urinary samples. The authors envision their sensor as a novel diagnostic tool for patients with severe abdominal pain and as a potential alternative to the δ-ALA/PBG detection kits currently in use, with both clinical and scientific applications.

Yang et al. discussed the recent progress on electrocatalysts based on metal–organic frameworks (MOFs) in the context of electrochemical sensing applications. In this review, the authors briefly present different types of MOFs-based nanomaterials by classifying them into metal-based, carbon-based, and other MOF-based nanostructures. They also elaborate on the structure–activity–performance relationships between these catalysts and extensively discuss the effects of metal cations and synthetic ligands.

Tong et al. and Huang et al. differentiated between cancerous and normal cells by precisely and accurately detecting H_2O_2 via sensors based on an Au nanoparticles-polydopamine-poly acrylic acid-graphene (Au NPs-PDAPAA-graphene) nanohybrid, and on a $Cu_2(OH)_3NO_3$-wrapped ZnO nanorod assembly [$Cu_2(OH)_3NO_3$@ZnO], respectively. Owing to the synergistic effects of multicomponent systems, the former electrochemical sensor offered higher sensitivity (LOD of 0. 02 μM) than the latter (LOD of 1 μM). Both sensors were successfully employed in real-time tracking of H_2O_2 excreted by different types of live cells.

The last contribution to this Research Topic was by Siddique et al. The authors fabricated Cu-ZnO nanorods, which were used in the electrochemical sensing of H_2O_2. The constructed sensor exhibited good reproducibility, stability, and selectivity, with a linearity range up to 11 mM and an LOD of 0.16 μM.

In summary, this Research Topic highlights the development of nanomaterials, their structure–activity–performance correlations, their improvements to sensing platforms, their performances, and their various potential applications.

Author contributions

MA drafted the manuscript. MA, FX, MG, and YS edited and proofread the manuscript.

Conflict of interest

The authors declare that the research was conducted in the absence of any commercial or financial relationships that could be construed as a potential conflict of interest.

Publisher's note

References

Asamoah, B. O., Uurasjärvi, E., Räty, J., Koistinen, A., Roussey, M., and Peiponen, K. E. (2021). Towards the development of portable and *in situ* optical devices for detection of micro-and nanoplastics in water: A review on the current status. *Polymers* 13, 730. doi:10.3390/polym13050730

Asif, M., Ajmal, M., Ashraf, G., Muhammad, N., Aziz, A., Iftikhar, T., et al. (2020). The role of Biosensors in coronavirus disease-2019 outbreak. *Curr. Opin. Electrochem.* 23, 174–184. doi:10.1016/j.coelec.2020.08.011

Asif, M., Aziz, A., Azeem, M., Wang, Z., Ashraf, G., Xiao, F., et al. (2018). A review on electrochemical biosensing platform based on layered double hydroxides for small molecule biomarkers determination. *Adv. Colloid Interface Sci.* 262, 21–38. doi:10.1016/j.cis.2018.11.001

Asif, M., Xu, Y., Xiao, F., and Sun, Y. (2021). Diagnosis of COVID-19, vitality of emerging technologies and preventive measures. *Chem. Eng. J.* 423, 130189. doi:10.1016/j.cej.2021.130189

Aziz, A., Asif, M., Ashraf, G., Azeem, M., Majeed, I., Ajmal, M., et al. (2019). Advancements in electrochemical sensing of hydrogen peroxide, glucose and dopamine by using 2D nanoarchitectures of layered double hydroxides or metal dichalcogenides. A review. *Microchim. Acta* 186, 671. doi:10.1007/s00604-019-3776-z

Dral, A. P., and Johan, E. (2018). 2D metal oxide nanoflakes for sensing applications: Review and perspective. *Sensors Actuators B Chem.* 272, 369–392. doi:10.1016/j.snb.2018.05.157

Hermawan, A., Amrillah, T., Riapanitra, A., Ong, W. J., and Yin, S. (2021). Prospects and challenges of MXenes as emerging sensing materials for flexible and wearable breath-based biomarker diagnosis. *Adv. Healthc. Mat.* 10, 2100970. doi:10.1002/adhm.202100970

Iftikhar, T., Asif, M., Aziz, A., Ashraf, G., Jun, S., Li, G., et al. (2021). Topical advances in nanomaterials based electrochemical sensors for resorcinol detection. *Trends Environ. Anal. Chem.* 31, 00138. doi:10.1016/j.teac.2021.e00138

Xu, K., Lu, Y., and Takei, K. (2019). Multifunctional skin-inspired flexible sensor systems for wearable electronics. *Adv. Mat. Technol.* 4, 1800628. doi:10.1002/admt.201800628

Zhang, R., Belwal, T., Li, L., Lin, X., Xu, Y., and Luo, Z. (2020). Nanomaterial-based Biosensors for sensing key foodborne pathogens: Advances from recent decades. *Compr. Rev. Food Sci. Food Saf.* 19, 1465–1487. doi:10.1111/1541-4337.12576

Advantages of publishing in Frontiers

OPEN ACCESS
Articles are free to read
for greatest visibility
and readership

FAST PUBLICATION
Around 90 days
from submission
to decision

HIGH QUALITY PEER-REVIEW
Rigorous, collaborative,
and constructive
peer-review

TRANSPARENT PEER-REVIEW
Editors and reviewers
acknowledged by name
on published articles

Frontiers
Avenue du Tribunal-Fédéral 34
1005 Lausanne | Switzerland

Visit us: www.frontiersin.org
Contact us: frontiersin.org/about/contact

REPRODUCIBILITY OF RESEARCH
Support open data
and methods to enhance
research reproducibility

DIGITAL PUBLISHING
Articles designed
for optimal readership
across devices

FOLLOW US
@frontiersin

IMPACT METRICS
Advanced article metrics
track visibility across
digital media

EXTENSIVE PROMOTION
Marketing
and promotion
of impactful research

LOOP RESEARCH NETWORK
Our network
increases your
article's readership